Heralded generation of concurrent quantum resource states via photon-subtraction from frequency nondegenerate squeezed light

Author:
Kuntz, Katanya

Publication Date:
2013

DOI:
https://doi.org/10.26190/unsworks/16576

Heralded generation of concurrent quantum resource states via photon-subtraction from frequency nondegenerate squeezed light

Katanya Brianne Kuntz

A thesis submitted in fulfilment
of the requirements of the degree of
Doctor of Philosophy

School of Engineering and Information Technology
University of New South Wales
Canberra

Submitted
September 3, 2013
Revised
November 27, 2013

COPYRIGHT STATEMENT

Katanya Brianne Kuntz
27.November.2013

AUTHENTICITY STATEMENT

I certify that the Library deposit digital copy is a direct equivalent of the final officially approved version of my thesis. No emendation of content has occurred and if there are any minor variations in formatting, they are the result of the conversion to digital format.

Katanya Brianne Kuntz
27.November.2013

Statement of Originality

I hereby declare that this submission is my own work and to the best of my knowledge it contains no materials previously published or written by another person, or substantial proportions of material which have been accepted for the award of any other degree or diploma at UNSW or any other educational institution, except where due acknowledgement is made in the thesis. Any contribution made to the research by others, with whom I have worked at UNSW or elsewhere, is explicitly acknowledged in the thesis. I also declare that the intellectual content of this thesis is the product of my own work, except to the extent that assistance from others in the project's design and conception or in style, presentation and linguistic expression is acknowledged.

Katanya Brianne Kuntz
27.November.2013

Acknowledgements

There is a saying ‘it takes a village to raise a child’, and I think this can be extended to finishing a doctorate. I have many people to thank for their continued support. First and foremost, I would like to thank my supervisors Prof Elanor Huntington and A/Prof Charles Harb. Their patience, encouragement, and guidance throughout my doctoral degree has been invaluable. In particular I would like to thank Elanor for the indispensable discussions that contributed to this thesis. Her support during the tough times (boy were there a few!), and especially during those moments of triumph encouraged me to continue working until the goal was accomplished. I am grateful for having her as a supervisor and a role model.

For continued support throughout the project, I would like to extend heartfelt gratitude to Prof Tim Ralph. His endless patience and uncanny ability to explain complicated concepts simply are muchly appreciated. He also came to the rescue when nothing made sense, and I am very grateful for the time he spent helping solve the mystery. It was a pleasure working with him.

I would also like to express my sincere gratitude to my group members for their help. Special thanks goes to Dr Michéle Heurs and Dr James Webb for introducing me to experimental quantum optics, and teaching me invaluable skills in the lab. I would like to thank Trevor Wheatley for the numerous fruitful discussions troubleshooting problems in the experiment, and for helping us to get a new laser ASAP. I am grateful to Dr Aleks Davidovic for his continued support, advice, and consolation after I suffered a *second* not-at-fault car accident, and had to ship the laser overseas for repairs *again*. I would also like to thank Dr Hongbin Song for her encouragement and support during the latter part of my PhD. It has been a pleasure working with her, and I look forward to future collaborations! Thanks also to Dr Mohammed Mabrok for his advice throughout this journey, and for being there to solve tricky math problems. Finally, thank you to the past and present officemates in room 309 for making our office a fun and friendly place.

Also, I would like to express my sincere appreciation for the assistance of the electronics and mechanics workshop staff. In particular, I would like to thank Phil Hestbeck, Rick Whyte, Darryl Budarick, and Shane Brandon for making various widgets that helped make the experiment a success. I would also like to thank

Mitchell Sinclair for his assistance in designing and building the optical table enclosure system. It was a pleasure working with you all.

On a personal note, I would like to thank Dr David Fry, Pat Irwin, and Dr Anna Harding for taking my spark of interest in physics and nurturing it into a wildfire. Words cannot properly express my gratitude for how your early influences have shaped my life. All those hours spent teaching calculus and quantum physics, and letting me play in a university laboratory paved the way to this doctorate. I would also like to thank Prof Alexander Lvovsky for his influential role on my early career. Thank you for giving me the opportunity to work in your lab all those years ago and for being my undergraduate honours project supervisor. Thank you as well to Dr Mirko Lobino for giving us the project idea of building a light sabre! I would not be where I am today if it weren't for those opportunities and guidance.

A heartfelt thank you is extended to my family for always encouraging me to pursue my dreams in science. I appreciate all those long phone calls that reminded me of your endless support and reassurance that I would finish. And thank you for supporting my decision to study in Australia! Finally, thank you to my partner Ben and my extended Australian family for making me feel like I belong and keeping me grounded. I am so grateful to Ben for being a source of strength that kept me going, even when it seemed impossible. He always knew when I needed a big hug after a particularly difficult day in the lab. He has been so thoughtful and patient throughout this ordeal, and words cannot express my gratitude. Time for a holiday!

Abstract

For decades we have known that an optical parametric oscillator (OPO) generates a two-mode squeezed vacuum state. The interaction between the 'pump' field at the second harmonic frequency and a nonlinear medium inside the optical cavity produces entangled pairs of parametric down-converted photons. Due to the mechanics of a cavity, these photons can be generated at the optical carrier frequency (half the pump frequency), or in equally-spaced side-band frequencies symmetrically above and below the carrier. These side-band frequencies can be within the OPO linewidth centred on the carrier (spaced by kHz-MHz) or at the cavity resonance frequencies, which are evenly spaced by the free spectral range (FSR) of the cavity (spaced by MHz-GHz). The entangled photons in each correlated pair of side-bands form a two-mode squeezed vacuum state.

However, since the photons only differ by kHz-GHz in frequency, the output from an OPO is usually viewed as *degenerate*. This is due to the way a homodyne detector measures this two-mode state. Homodyne detection automatically performs a mixing operation on the upper and lower side-bands which rotates the measurement basis. In this rotated basis the two-mode state becomes two separable *single*-mode squeezed vacua. The standard homodyne detection technique cannot distinguish between these two symmetric single-mode states, therefore giving measurements that look like an OPO is a degenerate system which produces a single-mode squeezed vacuum state.

We have shown that combining the wave-like nature of homodyne detection with the particle-like nature of photon counting in a hybrid experiment can produce an asymmetric two-mode quantum state. Applying photon-subtraction to a two-mode squeezed vacuum state produces two *distinguishable* single-mode states: a photon-subtracted squeezed vacuum state and a squeezed vacuum state. These asymmetric states cannot be properly characterised by a measurement technique that cannot distinguish between them. We have applied a novel measurement that combines time-domain measurements with frequency-resolved homodyne detection for a fixed demodulation phase. The ability to control this phase gives us independent access to either single-mode state. We were able to perform quantum state tomography on our projected state and separately reconstruct each single-mode state. We also showed

that the photon-subtracted squeezed vacuum state is a quantum non-Gaussian state *without* homodyne detection efficiency correction by extracting entanglement between the first three FSRs created by the optical implementation of our projector. Therefore, by accessing the FSR side-band modes of a nondegenerate OPO we were able to generate both a squeezed vacuum state and a quantum non-Gaussian state that are independent yet travelling in the same optical mode.

To my parents and our dear friend Dr David J.I. Fry.

Contents

Glossary of terms

Term	Definition
APD	Avalanche photodiode
BS	Non-polarising beamsplitter
CV	Continuous variable
DV	Discrete variable
FBS	Frequency beamsplitter
FSR	Free spectral range
HD	Homodyne detector
LO	Local oscillator (optical)
OPO	Optical parametric oscillator
PBS	Polarising beamsplitter
PD	Photodetector
PDC	Parametric down-conversion
PMP	Polarisation-maintaining-panda optical fibre
PND	Photon number distribution
SHG	Second harmonic generator/generation
SS-NOPO	Side-band-scale nondegenerate optical parametric oscillator
WS-NPDC	Wavelength-scale nondegenerate parametric down-conversion
$\hat{A}$	Arbitrary operator
$\Delta\hat{A}$	Standard deviation of operator $\hat{A}$
$\Delta\hat{A}^2, V_A$	Variance of operator $\hat{A}$
$\langle\hat{A}\rangle = \langle\psi\vert\hat{A}\vert\psi\rangle$	Expectation value of operator $\hat{A}$
$\hat{a}, (\hat{a}^\dagger)$	Field annihilation (creation) operator
α	Coherent amplitude of $\hat{a}$, $\alpha = \langle\hat{a}\rangle$
α_{2n}	Coefficients of a pure two-mode squeezed vacuum state
β	Cavity decay rate (HWHM)
β_{2n}	Coefficients of a pure single-mode squeezed vacuum state
β_{k_B}	Thermal state constant, $\beta_{k_B} = 1/k_B T$
c	Speed of light in a vacuum (2.99792458×10^8 m/s)
γ_{FWHM}	Cavity linewidth (FWHM)

ζ	Homodyne detection interference visibility between signal and LO
ζ_{FBS}	FBS interference visibility
$\eta_e(f)$	Homodyne detection efficiency at frequency f due to raised level of electronic noise
η_{esc}	OPO escape efficiency
η_f	APD fibre coupling efficiency
η_{HD}	Optical homodyne detection efficiency, $\eta_{HD} = \eta_{QE}\eta_t\zeta^2$
η_t	Propagation efficiency to homodyne detector
η_{QE}	Quantum efficiency of a photo-diode
E_{nl}	Single-pass nonlinear conversion efficiency
$\mathcal{F}$	Cavity finesse, $\mathcal{F} = \omega_s/\gamma_{FWHM}$
L	Total cavity loss
θ	LO optical phase
$\hat{n}$	Photon-number operator, $\hat{n} \equiv \hat{a}^\dagger\hat{a}$
P_{Th}	Pump threshold power; pump power at which OPO reaches self-sustained oscillation
P_{dc}	APD dark count probability
p	Total cavity path length
ξ	Squeezing parameter
$\hat{\rho}$	Density operator (state operator)
$\hat{S}(\xi)$	Squeezing operator
R	Complex amplitude reflectance
r	Intensity reflection coefficient
T	Complex amplitude transmittance
t	Intensity transmission coefficient
τ	Temporal offset
$\mathrm{tr_b}\left[\hat{\rho}_{ab}\right]$	Partial trace of $\hat{\rho}_{ab}$ over mode b
ϕ	Demodulation phase offset
ϕ_{pump}	Pump beam optical phase
$\lvert\psi\rangle$	State vector
$\hat{U}_s$	Spatially-symmetric beamsplitter unitary
$\hat{U}_t$	Time-symmetric beamsplitter unitary
Ω_0	Optical carrier angular frequency
ω_s	Free spectral range angular frequency
ω_m	FBS measured angular frequency
$\hat{X}^+$	Amplitude quadrature
$\hat{X}^-$	Phase quadrature

List of Figures

Chapter 1

Introduction

Anyone who can contemplate quantum mechanics without getting dizzy hasn't properly understood it.

Niels Bohr

In this chapter we present a brief introduction to quantum information science, and discuss the possible platforms currently under investigation for use in various quantum technologies. We concentrate our review on optical schemes, focusing on the contrasts between the discrete and continuous variable regimes. We will then discuss various hybrid quantum optics experiments that attempt to bridge these two worlds. We will highlight a particular type of hybrid experiment that combines the wave-like nature of homodyne detection with the particle-like nature of photon counting to produce quantum non-Gaussian states. We conclude by discussing the quantum states generated by our experiment which utilises two-mode squeezed vacuum to generate concurrent quantum resource states, and how these states could play an important role in future quantum technologies.

1.1 Historical perspective

Quantum information science offers exciting possibilities to improve a wide-range of real world applications from storing and processing vast amounts of information at classically unreachable speeds and efficiencies, to transmitting codes with unbreakable security and improving the accuracy of clocks [1, 2]. Utilising various quantum properties of light and matter can lead to several advantageous abilities, including the quantum internet [3], secure information transfer protocols, such as quantum key distribution (QKD) [4], and quantum computing algorithms, such as Shor's quantum factoring algorithm [5,6] and Grover's quantum search algorithm [7–9]. As first proposed by Feynman in 1982 [10], it is believed that a quantum computer is necessary for properly simulating some physical systems [11–17]. There are several other practical applications of quantum technologies that include increasing the sensitivities of measurement techniques by employing non-classical light through quantum metrology [2, 18–21] and quantum lithography [22]. Quantum lithography is an emerging field that exploits a well-known quantum property called *entanglement* to fabricate devices with features on the order of magnitude smaller than an optical wavelength [22]. Fabrication on this scale is impossible with classical light due to the limits imposed by optical diffraction. This application has immediate implications in the current trend of miniaturisation of computer chips and the birth of nanotechnology. As the size of circuit boards becomes closer to the quantum scale, quantum effects must be considered when designing, fabricating, and operating these devices.

One significant appeal offered by quantum information science is the possibility of a quantum computer. A quantum computer can store and manipulate information in the form of quantum bits (qubits) instead of classical bits. Unlike the classical bit, which can be assigned the value 0 or 1, qubits can utilise quantum mechanical qualities, such as *superposition*, to exist in a superposition state of 0 *and* 1. The idea that a quantum system could perform computations was first explicitly commented on by Benioff in 1982 [23]. A quantum computer can also exploit *quantum parallelism* in which certain probabilistic tasks can be performed much faster compared to any classical restriction of the calculation [24]. There's little doubt that such a computing device provides the possibility for enormous computing power, which may surpass the factoring abilities of current supercomputers due to the exponential speed-up of quantum algorithms over existing classical computing algorithms [5, 11].

A basic requirement of a universal quantum computer is to consist of a system of scalable physical qubits that can be initialised, measured, and made to controllably interact with each other, while remaining well-isolated from the surrounding environment [25]. These qualities are vital for implementing a universal set of quantum logic gates [26, 27]. It is also necessary to transfer quantum information between these qubits [28], which could be implemented with the help of *quantum teleportation* [29–32]. Quantum teleportation is the transmission and reconstruction of quantum information over arbitrary distances [29]. Usually the teleported information takes the form of the state of a quantum system, such as transferring the polarisation state of one photon to another photon. A novel encoding technique called *quantum dense coding* could also be used to increase the quantum capacity of a classical information channel to facilitate more efficient communication [33–35].

There are various physical platforms which could be utilised to construct such a qubit, such as non-classical light [25, 36–39], atom- and ion-traps [40–45], impurities in diamond [46], superconducting charge and flux qubits [47], nuclear magnetic resonance (NMR) techniques [48–50], spin- and charge-based quantum dots [51–53], nuclear spin qubits in silicon and other molecules [54], cavity quantum electrodynamics [55–60], and superconducting Josephson junctions [61]. Currently, there are several international collaborations working towards creating a universal quantum computer using one or a combination of these platforms. Some schemes have clear advantages over others but all platforms have challenges to overcome.

Employing light as part of the encoding platform in quantum information processing is a logical choice as light naturally integrates into quantum computation, communication, and cryptography schemes [62–64]. One critical advantage of optical quantum systems over their atomic counterparts is the ability to transfer information *at the speed of light.* Since photons remain fairly isolated from their environment, they are potentially free from decoherence compared to atoms, causing photons to possess longer information storage times [38]. Logical photonic qubits also offer flexibility in how the information is encoded due to their multiple degrees of freedom, such as polarisation, spatial, and optical frequency modes. Optical quantum gates are relatively simple to implement as standard birefringent wave plates can act as single qubit logic gates, and polarising beamsplitters can be used to transition between polarisation and path encoding [25]. However, the inherent ability of photons to undergo non-destructive interactions with their surroundings becomes a disadvantage when an operation requires photons to interact with each other, such as in two-qubit quantum gates. There are ways to work around this problem by making nonlinear projective measurements with photodetectors [27]. However, these measurements are probabilistic whereas deterministic operations are required for a technically viable quantum computer.

There exists two distinct paradigms in quantum optics for generating resource states and demonstrating optical quantum information operations: the *discrete variable* (particle-like) regime [38] and *continuous variable* (wave-like) regime [65]. The difference between these two regimes is in the type of *measurement* performed on the state, not the state itself. Each regime utilises a different property of light by *choosing* to measure its discrete variable (DV) or continuous variable (CV) properties. Changing the nature of the measurement affects the measurement result and reveals either the CV or DV nature of light. The fact that light (and matter) behaves either wave-like or particle-like depending on the measurement technique used has been known since the birth of quantum physics and is referred to as *wave-particle duality* [66]. The DV regime stores and manipulates information in discrete levels of light [67–70]. Therefore, single photons are the carriers of DV information, which can be encoded in their polarisation or frequency degrees of freedom. Measurements are then performed by avalanche photodiodes (APDs) or by photon-number-resolving detectors (PNRDs), such as transition-edge sensors (TESs). A CV scheme exploits the continuous degrees of freedom associated with an optical field, such as its phase and amplitude quadratures, to encode information. A particular kind of CV photodetection called *homodyne detection* is utilised for state characterisation in this regime. This technique can access either the phase or amplitude quadratures of light, unlike direct CV detection which can only access the amplitude quadrature. These photodetection techniques will be further explain in chapter 2.

Both the DV and CV regimes rely on the production of entangled photon pairs [71]. The generation of correlated photons had its beginnings decades ago with the theoretical prediction [72–74], and then experimental demonstration of photons being emitted by 'parametric fluorescence' [75]. One of the first observations of this non-classical light state was from optically pumping ammonium dihydrogen phosphate and lithium niobate ($LiNbO_3$) crystals with high-powered lasers [75–77]. Then photon antibunching was observed from atomic fluorescence [78–81] using photomultiplier tubes [82, 83]. The technique of producing entangled photon pairs from nonlinear crystals is now commonly referred to as *parametric down-conversion* (PDC), and is the standard technique used in a large number of quantum optics experiments [84–95].

Parametric down-converted photons can be distinguishable or indistinguishable in all degrees of freedom (wavelength, polarisation, spatial and temporal modes), and entangled in all of these parameters. A PDC process that produces *indistinguishable* photons is usually referred to as *degenerate* PDC. Another type of PDC can generate entangled *distinguishable* photons. These photons may exit the nonlinear crystal at different spatial angles or have orthogonal polarisations, or they could be at completely different wavelengths, such as a photon at 532 nm down-converting into $532\text{nm} \mapsto 810\text{nm} + 1550\text{nm}$ [96–98]. Throughout this thesis we will refer to this type of nondegeneracy where the wavelengths of the down-converted photons differ by a few nanometres or more as *wavelength-scale* nondegenerate PDC (WS-NPDC).

In chapter 2 we will discuss another type of nondegenerate PDC that is generated by an optical cavity with a nonlinear medium inside. This type of optical system forms a *side-band-scale nondegenerate optical parametric oscillator* (SS-NOPO). The frequency transfer function of the optical cavity shapes the down-conversion spectrum of the nonlinear medium to generate a 'comb' of entangled photon pairs at frequencies above and below the optical carrier frequency. The down-converted photons can exist at frequencies within the 'baseband' cavity linewidth at frequencies equally separated by a few kilohertz or megahertz from the optical carrier frequency. Or these entangled photons can exist at correlated cavity resonance frequencies spaced by the *free spectral range* (FSR) of the cavity. Entangled side-bands spaced by one or more FSRs exist on a frequency scale of megahertz to gigahertz from the carrier frequency. Therefore, these photons are at $\Omega_0 \pm \omega_s$, where Ω_0 is the carrier angular frequency and ω_s is a particular FSR angular frequency. These side-bands can differ by only a few *hundredths* of a nanometre in wavelength. Thus this type of PDC is often thought of as *degenerate.* However, these photons (side-bands) are distinguishable, as demonstrated by the ability to spatially separate them using an empty optical cavity or unbalanced interferometer [99–101]. There are several other types of single photon sources [46, 94, 102], some of which include quantum dots in pillar microcavities [103], single atoms or ions in high-finesse cavities [104, 105], diamond nanocrystals [106], single molecules in host crystals [107], Kerr nonlinearity four-wave mixing [108], and waveguiding structures [109]. We shall focus exclusively on the states produced by a SS-NOPO in this thesis.

Discrete variable experiments commonly utilise APDs or TESs to detect one photon from an entangled pair which projects the presence of its entangled partner in the appropriate optical mode. The ability to deterministically know the success or failure of a quantum operation based on the detection of a photon is a major advantage of the DV paradigm. A well-known DV quantum computing scheme is the Knill, Laflamme, and Milburn (KLM) protocol [37]. In 2001 they illustrated theoretically that it is possible to conduct efficient linear optical quantum computing (LOQC) with the sole use of photons and linear optics. The information is encoded in two orthogonal modes of a single photon with one mode as logical *0* and the other mode as logical *1*. Since this seminal paper several groups have experimentally demonstrated the power of this technique [27, 110–112].

However, there are significant disadvantages to the KLM scheme due to the enormous resource requirements, such as the requirement of more than $10,000$ pairs of entangled photons to achieve $> 95\%$ success probability of a near-deterministic control-NOT (CNOT) gate [25]. A CNOT gate is the canonical example of an entangling logic gate which is necessary for universal quantum computation [25]. The state of the target qubit 'flips' conditional on a control qubit being in the logical state *1*. As the majority of entangled photon production is probabilistic, the experimental challenges to produce large numbers of resource states is overwhelming. Furthermore, there is a lack of fault tolerance, the requirement for photon-number-resolving measurements, and the quantum gates are probabilistic so they only succeed 1/16 of the time (with heralded fails) [27]. There have been several attempts to simplify the scheme further to create practical schemes for linear optical computing [25, 111, 113–116]. For example, the success rate of the gates can be improved by utilising quantum teleportation to transfer a non-deterministic gate that was successful onto waiting control and target qubits to ensure 100% success [31]. Quantum teleportation is a critical ingredient for quantum computing and communication networks, and was first experimentally demonstrated in DV systems by Bouwmeester *et al.* in 1997 [30]. Further proof-of-principle experiments were performed shortly afterwards by several groups [117–119].

Optical quantum information science was extended into the CV regime by the demonstration that electromagnetic fields are a natural physical representation of the formalism for quantum error correction [120–122], teleportation [123–127], and computation [128]. These experiments typically involve generating a CV non-classical state, such as *quadrature squeezed light.* The first experimental demonstration of CV quantum teleportation was of an optical coherent state using squeezed light by Furusawa *et al.* [125]. A squeezed state has a lowered noise variance in one quadrature, and therefore an increased noise level in the conjugate quadrature [129–135]. This quantum state will be further defined in chapter 2. Some of the first experimental demonstrations of quadrature squeezing were generated by four-wave mixing in an optical cavity [136] and PDC in an optical cavity using $\chi^{(2)}$ nonlinearity [137–145]. Since those seminal experiments, the quality and level of noise reduction in optical states have been significantly improved [146–157].

Continuous variable states offer efficient ways to implement essential aspects of quantum communication and computation protocols. The CV qubit, called a 'qumode', can be prepared, unitarily manipulated, measured, and entangled by utilising the continuous Gaussian noise profiles in their quadratures [65]. Gaussian states and transformations have been shown to be primary tools for analysing quantum information processing [158]. Furthermore, feed-forward techniques can be used to displace an optical mode in phase space, which is a vital operation in quantum information [65]. As mentioned earlier, homodyne detection is a well-known measurement technique that can characterise either quadrature of the CV state with high efficiency. Furthermore, efficient CV entanglement can be created by interacting two non-classical Gaussian beams on a beamsplitter [125, 159, 160]. The quality of entanglement depends directly on the amount of squeezing present in the interacting light beams, so there will always be a degree of imperfection.

However, it has been established that Gaussian states and transformations alone are insufficient for universal quantum computation [128]. The use of squeezing unitaries and linear optics only transforms Gaussian states into Gaussian states. Although quantum Gaussian states are useful for quantum communication [161–164] and one-way quantum computation with cluster states [165–170], a quantum computer consisting of fully Gaussian qubits can always be efficiently simulated by a classical computer [171]. Therefore, non-Gaussian operations or states must be included in the quantum system for universality to be achieved, and for the system to be no longer classically simulated. The cubic Hamiltonian like the $\chi^{(3)}$ Kerr nonlinearity is an example of a non-Gaussian operation [172–178]. However, due to the weak nature of this nonlinearity, it is experimentally challenging to use in a scalable quantum computer.

Experiments involving measurement-induced nonlinearities can produce quantum non-Gaussian states from Gaussian states. This technique can be easier to experimentally implement than a strong $\chi^{(3)}$-nonlinearity, and creates states that are necessary for universal quantum computing [179]. The KLM protocol is an example of a measurement-induced nonlinearity applied to a fully DV system. Another approach can generate non-Gaussian states by merging the DV and CV worlds in a new type of optical system referred to as a *hybrid* experiment. Hybrid experiments belong to a paradigm that utilises both discrete and continuous variable measurement techniques on the same optical state. Optical hybrid quantum information protocols have been proposed that attempt to overcome the various practical and fundamental limitations caused by relying solely on measurements of discrete or continuous variables while retaining the advantages of both systems [180, 181]. For example, there can be more advantages to working in the CV regime for certain tasks, such as quantum teleportation, which can be accomplished unconditionally in the CV paradigm with only linear optics [124]. The discrete nature of single photons means that they are excellent for heralding the success or failure of an event over a lossy channel, which is useful for entanglement generation [182, 183]. However, one drawback to DV detection is that APDs at certain wavelengths, like telecommunication wavelengths, have notoriously poor quantum detection efficiencies which can affect the quality of state characterisation. Whereas homodyne detection at these wavelengths uses photodiodes that have $\sim 90\%$ quantum efficiencies, and is a well-known and reliable measurement technique for CV state characterisation.

There are several other advantages to combining CV and DV measurement techniques to form a hybrid discrete-continuous photonic system [181], from the study of fundamental quantum phenomena [184–187] to a hybrid quantum repeater protocol for long-distance entanglement distribution [188–190] to heralded state generation [191]. Quantum repeaters work by first generating entanglement over shorter segments and then joining these segments by entanglement swapping and purification to achieve scalable entanglement distribution across long lossy channels [192]. A hybrid system can also generate essential resources for quantum-enhanced applications [65] such as entanglement distillation [193–195], quantum computation [178, 196], CV quantum teleportation of DV encoded photonic qubits [197–200], and highly efficient optical telecommunications [201, 202], and can allow for hybrid Bell measurements [203] and hybrid projectors using both discrete and continuous variable detection systems [204, 205].

One of the first applications of a measurement-induced nonlinearity to a hybrid system was the Gottesman, Kitaev, and Preskill (GKP) scheme. In this protocol, photon number measurements are utilised to create non-Gaussian states from Gaussian resources, which encodes logical DV states into physical CV states [179]. Recently, the various advantages provided by a hybrid quantum information system has encouraged several experimental demonstrations, especially in the area of generating single-photon states or superpositions of macroscopic states (both non-

Gaussian states). This type of hybrid experiment combines the advantages of 'deterministic' DV photon counting with high-efficiency homodyne detection to project quantum non-Gaussian states. Lvovsky *et al* was one of the first to demonstrate a non-Gaussian state by generating a one-photon Fock state, and then characterising it using CV measurements [206]. In this experiment, spatially nondegenerate PDC photons are separated into two optical modes: the trigger and signal. The trigger field is spectrally filtered before detection by a single-photon detector. A detection event of the trigger photon heralds the presence of its entangled partner in the signal field. The signal field is then characterised using homodyne detection, and quantum state tomography is conducted of the one-photon Fock state, which revealed negativity of the Wigner function near the origin in phase space.

Other quantum non-Gaussian states have been generated since this seminal experiment in which the squeezed vacuum state is used to generate a photon-subtracted squeezed vacuum state. These photon-subtracted states have photon number distributions (PNDs) that are clearly different to a single-photon Fock state. The probability of measuring a three-photon term in a photon-subtracted squeezed vacuum state is higher than for a two-photon term, which is not possible to generate with spatial or polarisation nondegenerate PDC. (We will show in chapter 3 that it *is* possible to generate such a state with nondegenerate PDC from a SS-NOPO.) This PND of odd photon number probabilities is approximate to an odd Schrödinger cat state of small amplitude [207,208]. The famous *Schrödinger cat* [209] is a gedanken experiment in quantum physics which illustrates the bizarre possibility that a macroscopic object, such as a cat, could exist simultaneously in a quantum superposition of two clearly distinguishable states, such as the cat being both 'dead' and 'alive'. The optical version of a Schrödinger cat state can be a superposition of bright coherent states with opposite phase, $|\alpha\rangle \pm |-\alpha\rangle$ [210]. However, it is experimentally difficult to generate such coherent state superpositions with a coherent amplitude of $\alpha \gg 1$. Therefore, photon-subtracted squeezed vacuum states are generated instead, which are mathematically approximate to small-amplitude Schrödinger cat states (*kitten states*) [91, 94, 95, 97, 102, 186, 193, 211–231]. For $\alpha \lesssim 1$, these kitten states can be approximated with high fidelity by squeezed single-photon states [232].

Quantum non-Gaussian states are extremely powerful resource states, as illustrated by the recent development of a quantum information scheme, called coherent state quantum computing (CSQC). This scheme utilises coherent state superpositions to encode, compute, and transmit information [232–240]. Furthermore, information could be encoded into the odd and even kitten state basis, which offers the advantage of being a more orthogonal basis compared to CSQC, which uses phase-shifted coherent states as the basis [237]. As the Gaussian squeezed vacuum state is approximate to an even kitten state, there are notably several advantages to having a system that could produce both quantum non-Gaussian and Gaussian states simultaneously. Thus far such a quantum state from a single optical cavity has not been experimentally generated.

By combining the DV nature of projective photon-counting measurements with time-and-frequency-resolved CV homodyne detection and phase-locked frequency demodulation, we have realised simultaneous generation of independent and distinct quantum resource states in a single optical mode at a telecommunication wavelength. We utilised the nondegenerate qualities of a SS-NOPO to generate a photon-subtracted two-mode squeezed vacuum state. Homodyne measurement of a two-mode state rotates the measurement basis into a basis defined as the linear combinations of the correlated upper and lower side-bands. These combinations define two distinct modes that we will refer to as the *symmetric* and *anti-symmetric* modes. Thus, the two-mode quantum state becomes two single-mode quantum states in this symmetric/anti-symmetric basis. However, only one of the two modes is affected by the photon-subtraction operation. Therefore, a quantum non-Gaussian state is created in the symmetric side-band mode that is *independent* of the single-mode squeezed vacuum state in the anti-symmetric side-band mode. Due to the nature of our measurement technique, both of these states can be accessed and manipulated independently. Furthermore, they exist in a natural basis for demonstrating universal quantum gate operations, such as displacement in the phase and amplitude quadratures.

1.2 Thesis plan

In the next chapter we review fundamental concepts in theoretical and experimental quantum optics, as well as a theoretical model for Schrödinger kitten state generation with imperfect experimental conditions. We will also discuss the standard tomographic reconstruction technique used to characterise quantum states via homodyne detection.

In chapter 3 we introduce state generation theory pertaining to our experiments with two-mode squeezed vacuum and photon-subtracted two-mode squeezed vacuum. We will define a new basis consisting of the superpositions of the upper and lower side-bands produced by a SS-NOPO (*symmetric* and *anti-symmetric* modes). This will introduce a novel way of interpreting the standard homodyne measurement in this symmetric/anti-symmetric basis. We will then mathematically derive what occurs when a frequency-resolved homodyne measurement is applied to a two-mode squeezed vacuum state, which naturally preforms a measurement in the symmetric/anti-symmetric basis. Unlike the standard homodyne measurement technique, applying this phase-locked-frequency-resolved measurement technique allows access to *both* the symmetric and anti-symmetric modes. We then predict an intriguing result by applying this measurement operator to the photon-subtracted two-mode squeezed vacuum state. We shall show that photon-subtraction will only occur on one of the two modes (e.g. the symmetric mode), leaving the squeezed vacuum state in the orthogonal mode unaffected. This produces a unique set of *independent and distinguishable* quantum states in the symmetric and anti-symmetric side-bands modes. A phase-locked-frequency-resolved homodyne measurement is necessary to fully characterise this asymmetric state.

In chapter 4 we will discuss the experiment in detail. The experiment can be run in one of two modes: *unprojected* state mode or *projected* state mode. We will discuss each of these modes, and focus on describing each component in the experiment separately. We will also introduce a novel way to characterise the frequency transfer function on an optical system up to the gigahertz frequency range *without* the need for a wide-bandwidth photodetector.

Our data acquisition techniques and results from the *unprojected* two-mode squeezed vacuum state experiment are presented in chapter 5. We will demonstrate the ability of our measurement technique to fully characterise this unprojected state at the first three FSRs of our SS-NOPO. We will also show that for the case of the unprojected state, the states at each FSR are independent squeezed vacuum states.

The true power of this measurement technique is demonstrated in chapter 6 when this method is applied in a hybrid photon-subtracting experiment. We present results that fully characterise two distinguishable and independent quantum states in the *projected* symmetric and anti-symmetric side-band modes. Due to the transmission function of our optical filtering system used in the projected state experiment, the states at each FSR are no longer independent. We establish that these states are entangled and that the quality of our reconstructed projected states improve when a frequency-dependent temporal mode function is applied which exploits this entanglement. We conclude in chapter 7 and identify possible areas of future research.

1.3 Summary of results

The novel contributions to the field discussed in this thesis are:

- We present state generation theory pertaining to our experiments with two-mode squeezed vacuum and photon-subtracted two-mode squeezed vacuum (chapter 3).
- Formulated a measurement technique to conduct frequency characterisation

of optical cavities into the gigahertz range using a standard power meter and an amplitude modulator (chapter 4).

- Experimental implementation of time-and-frequency-resolved homodyne measurements on a two-mode squeezed vacuum state which demonstrates the ability of this measurement technique to access both the symmetric and anti-symmetric side-band modes of a quantum state (chapter 5).

- Experimental demonstration of a photon-subtraction operation on a two-mode squeezed vacuum state produced by a SS-NOPO which only affects one of the side-band modes. This operation effectively destroys the symmetry that previously existed between the symmetric and anti-symmetric side-bands modes of the two-mode squeezed vacuum state (chapter 6).

- Experimental characterisation of projected states consisting of a quantum non-Gaussian state in the symmetric side-band mode and a squeezed vacuum state in the anti-symmetric mode. These states are independent and exist in a *single* optical mode at a telecommunication wavelength (chapter 6).

Chapter 2

Quantum optics basics

A careful analysis of the process of observation in atomic physics has shown that the subatomic particles have no meaning as isolated entities, but can only be understood as interconnections between the preparation of an experiment and the subsequent measurement.

Erwin Schrödinger

2.1 Quantum state representations

2.1.1 Basics

Before the introduction of quantum theory, the physics of the universe was explained using classical Newtonian mechanics. The state of an object was described by observable quantities, such as position (x) or momentum (p) variables. The state could be *directly* observed via a measurement of its *exact* position and momentum, and the uncertainty in that measurement depended on the accuracy of the measurement device. There was no theoretical limit to the accuracy of such a measurement. Therefore, according to classical physics, it is theoretically possible to perform an exact measurement on a system with an ideal measurement device, and the act of that measurement is seen as an independent event which does not affect the state of the system.

The introduction of quantum mechanics changed the concept of states and independent measurements without uncertainties. The state of a system can no longer be described by a set of exact single-valued variables, and is instead represented by a *state vector* written as a 'ket', $|\psi\rangle$. If the system is prepared perfectly then it can be described by a superposition of pure states [241],

$$|\psi\rangle = c_1|\psi\rangle_1 + c_2|\psi\rangle_2 + \dots \tag{2.1}$$

Measurements are represented by Hermitian operators $\hat{A}$ called *observables* which describe a particular action or measurement to be performed on the system. An operator is determined to be Hermitian if $\hat{A} = \hat{A}^\dagger$, where $\hat{A}^\dagger$ is the Hermitian conjugate of $\hat{A}$, and $(\hat{A}^\dagger)^\dagger = \hat{A}$ [242]. Generally the system to be measured will be in a superposition state of the possible measurement outcomes before the measurement is performed. These possible outcomes are the *eigenstates* $|a\rangle$ associated with the measurement observable $\hat{A}$. Therefore, before the act of measurement we can expand the state vector, $|\psi\rangle$, to give

$$|\psi\rangle = \sum_a \langle a|\psi\rangle |a\rangle, \tag{2.2}$$

where $\langle a|\psi\rangle$ is the complex projection of $|\psi\rangle$ onto $|a\rangle$ [243]. After the measurement has been made, the superposition collapses to just one of the eigenstates, and the numerical outcome of the measurement is a real number called an *eigenvalue*, a. The observable can be described in terms of its eigenstates and eigenvalues as

$$\hat{A} = \sum_a a|a\rangle\langle a|. \tag{2.3}$$

Each eigenstate has a probability of occurring associated with it, p_a, which is defined as

$$p_a = \frac{|\langle a|\psi\rangle|^2}{\sum_a |\langle a|\psi\rangle|^2}. \tag{2.4}$$

If we immediately repeated the measurement, we would obtain the same result, a, because the act of the first measurement collapsed the system into a single eigenstate, which gives a particular measurement result with certainty. This is called the *collapse of the state vector* or *collapsing the wavefunction*. Furthermore, the average or *expectation value*, $\langle\hat{A}\rangle$, of the measurement value a is given by [243]

$$\langle\hat{A}\rangle = \sum_a a p_a = \langle\psi|\hat{A}|\psi\rangle. \tag{2.5}$$

According to the principles of quantum mechanics, non-commuting observables such as position and momentum, cannot be simultaneously measured with absolute precision. This is because there is a minimum uncertainty relationship called the *Heisenberg uncertainty principle* [244] that is always obeyed in nature. In general the commutation relation for two arbitrary observables $\hat{A}$ and $\hat{B}$ is defined as

$$[\hat{A}, \hat{B}] = \hat{A}\hat{B} - \hat{B}\hat{A} = C, \tag{2.6}$$

where C is a complex constant. If $|C| > 0$ then observables $\hat{A}$ and $\hat{B}$ are non-commuting. The uncertainty principle states that the product of uncertainties of simultaneous measurements is bounded by a factor which depends on the commutator relation

$$\Delta\hat{A}\Delta\hat{B} \geq \frac{|[\hat{A},\hat{B}]|}{2}. \tag{2.7}$$

The variance $\Delta\hat{A}^2$ (or V_A) of a measurement is defined as the square of the uncertainty $\Delta\hat{A}$ in the measurement (standard deviation), where $\Delta\hat{A}^2 = (\Delta\hat{A})^2$ and

$$\begin{aligned}\Delta\hat{A}^2 \equiv V_A &= \langle\psi|(\hat{A} - \langle\hat{A}\rangle)^2|\psi\rangle \\ &= \langle\psi|\hat{A}^2|\psi\rangle - (\langle\psi|\hat{A}|\psi\rangle)^2 \\ &= \langle\hat{A}^2\rangle - \langle\hat{A}\rangle^2.\end{aligned} \tag{2.8}$$

2.1.2 The density matrix

It is possible for a system to exist in a statistical mixture (or ensemble) of multiple pure states, $|\psi_j\rangle$, with probabilities q_n. A single state ket cannot adequately describe such a mixed state and therefore the *density operator* (or state operator) was introduced, which is defined as

$$\hat{\rho} = \sum_j q_j|\psi_j\rangle\langle\psi_j|, \tag{2.9}$$

where $\sum_j q_j = 1$ and $\hat{\rho} = |\psi\rangle\langle\psi|$ for a pure state. The *density matrix* is defined as the representation of $\hat{\rho}$ in a given basis, $\{|\phi_k\rangle\}$,

$$\hat{\rho} = \sum_{m,n} \rho_{mn}|\phi_m\rangle\langle\phi_n|, \tag{2.10}$$

where

$$\rho_{mn} = \langle\phi_m|\hat{\rho}|\phi_n\rangle = \sum_j q_j\langle\phi_m|\psi_j\rangle\langle\psi_j|\phi_n\rangle. \tag{2.11}$$

The diagonal elements are $\rho_{nn} = \sum_j q_j|\langle\phi_n|\psi_j\rangle|^2$ and therefore non-negative. A very common density matrix representation in quantum optics is in terms of the photon-number basis called the *Fock basis* where these diagonal elements represent the photon number distribution of the quantum state. The density matrix contains complete information about any given state and can be used to calculate the expectation value of any observable as

$$\langle\hat{A}\rangle = \mathrm{tr}[\hat{A}\hat{\rho}] = \sum_{n,j} q_j\langle\phi_n|\hat{A}|\psi_j\rangle\langle\psi_j|\phi_n\rangle = \sum_j q_j\langle\psi_j|\hat{A}|\psi_j\rangle. \tag{2.12}$$

Throughout this thesis we will discuss multimode systems in which the two modes are entangled. In quantum optics a mode of a state refers to a degree of freedom of the electromagnetic field, such as frequency, polarisation, temporal, spatial, etc. A system is defined as entangled if the state vector describing the total system is a tensor product of subspaces, $|\psi\rangle = |a_1\rangle \otimes |a_2\rangle$, and cannot be factorized any further. The density matrix of mode a in such a two mode state can be found by taking a partial trace of the two-mode density matrix, $\hat{\rho}_{ab}$, over mode b as

$$\hat{\rho}_a = \mathrm{tr}_\mathrm{b}\Big[\hat{\rho}_{ab}\Big]. \tag{2.13}$$

This is equivalent to measuring one half of the two-mode state by applying a measurement operator to only mode a. The partial trace of a joint system $|\psi\rangle_C = |\psi\rangle_A \otimes |\psi\rangle_B$ where,

$$\rho^C = \rho \otimes \sigma = \begin{pmatrix} \rho_{11}\sigma & \rho_{12}\sigma \\ \rho_{21}\sigma & \rho_{22}\sigma \end{pmatrix},$$

is mathematically defined as

$$\mathrm{tr}_\mathrm{B}\Big[\rho^C\Big] = \begin{pmatrix} \rho_{11}\mathrm{tr}[\sigma] & \rho_{12}\mathrm{tr}[\sigma] \\ \rho_{21}\mathrm{tr}[\sigma] & \rho_{22}\mathrm{tr}[\sigma] \end{pmatrix} = \begin{pmatrix} \rho_{11} & \rho_{12} \\ \rho_{21} & \rho_{22} \end{pmatrix} = \rho$$

2.1.3 Quadrature operators of light fields

This mathematical formalism of operators can be applied to the quantum mechanical description of the electromagnetic field and various optical states. A quantized electromagnetic field at frequency ω can be described by a Hamiltonian which is analogous to the harmonic oscillator,

$$\hat{H} = \hbar\omega\Big(\hat{a}^\dagger\hat{a} + \frac{1}{2}\Big), \tag{2.14}$$

where $\hat{a}$ and $\hat{a}^\dagger$ are the annihilation and creation operators of field excitations, respectively. These operators satisfy the boson commutation relation

$$[\hat{a}_\nu, \hat{a}^\dagger_{\nu'}] = \delta_{\nu\nu'}, \tag{2.15}$$

and

$$[\hat{a}_\nu, \hat{a}_{\nu'}] = [\hat{a}^\dagger_\nu, \hat{a}^\dagger_{\nu'}] = 0, \tag{2.16}$$

where ν and ν' are optical modes and $\delta_{\nu\nu'}$ is the Kronecker delta. If both operators are acting on the same mode then $\nu = \nu'$ and $[\hat{a}_\nu, \hat{a}^\dagger_{\nu'}] = 1$. The annihilation and creation operators are non-Hermitian, and therefore are not measurable quantities. However, their real and imaginary parts are Hermitian, and they form the amplitude quadrature operator, $\hat{X}^{+}$, and phase quadrature operator, $\hat{X}^{-}$, which are defined as

$$\begin{aligned}\hat{X}^{+} &= \hat{a} + \hat{a}^{\dagger} \\ \hat{X}^{-} &= -i(\hat{a} - \hat{a}^{\dagger}).\end{aligned} \tag{2.17}$$

More generally any arbitrary quadrature operator, $\hat{X}(\theta)$, is defined as

$$\hat{X}(\theta) = e^{-i\theta}\hat{a} + e^{i\theta}\hat{a}^{\dagger} = \hat{X}^{+}\cos\theta + \hat{X}^{-}\sin\theta. \tag{2.18}$$

We can calculate the commutation relation between these quadratures by applying equation 2.6 to give

$$[\hat{X}^{+}, \hat{X}^{-}] = 2i. \tag{2.19}$$

And according to the uncertainty principle defined in equation 2.7,

$$\Delta\hat{X}^{+}\Delta\hat{X}^{-} \geq 1. \tag{2.20}$$

Therefore, it is impossible to simultaneously measure both the phase and amplitude quadratures of an electromagnetic field with perfect precision. This fundamental noise level in a measurement is referred to as *quantum noise* or *quantum uncertainty.* The noise levels in one quadrature can be reduced below the quantum noise limit, which results in an increased noise level in the orthogonal quadrature according to equation 2.20. Such optical states are called *squeezed states* and they will be discussed in more detail in §2.2. States that obey the equality in equation 2.20, such as *coherent states*, the *vacuum state*, and pure squeezed states are referred to as *minimum uncertainty states* and will be further discussed in §2.2.

The overlap between the eigenstates of the quadrature operators, $|X^{+}\rangle$, and a state $|\psi\rangle$ is given by the wavefunction $\psi(X^{+}) = \langle X^{+}|\psi\rangle$. The quadrature probability distribution of the given state is given by $|\psi(X^{+})|^{2}$. Therefore, the probability distribution for the general quadrature operator, $\hat{X}(\theta)$, is given by

$$\mathrm{pr}[X(\theta)] = |\langle X(\theta)|\psi\rangle|^{2}, \tag{2.21}$$

and for a general mixed state

$$\mathrm{pr}[X(\theta)] = \langle X(\theta)|\hat{\rho}|X(\theta)\rangle = \mathrm{tr}\Big[|X(\theta)\rangle\langle X(\theta)|\hat{\rho}\Big]. \tag{2.22}$$

The wavefunctions of photon-number states (called Fock states and will be further discussed in §2.2.1) for a general rotated quadrature are given by [243, 245]

$$\langle X(\theta)|n\rangle = \frac{e^{in\theta}}{\sqrt{2^n n!\sqrt{\pi}}} H_n[X(\theta)]e^{-X(\theta)/2}, \tag{2.23}$$

where $H_n(x)$ is the Hermite polynomial of order n. The wavefunction of the vacuum state where $n = 0$ is

$$|\langle X(\theta)|0\rangle|^2 = \frac{1}{\sqrt{\pi}} e^{-X(\theta)/2}, \tag{2.24}$$

which is a Gaussian function with quadratures of equal variance that satisfies the equality in the uncertainty principle (2.20), illustrating this state is a minimum uncertainty state. Only the zeroth-order of this function gives a Gaussian distribution.

2.1.4 The Wigner function

In classical physics the momentum and position of a particle trapped in a harmonic oscillator is well-defined. It can be represented as a point in phase space spanned by these variables called a phase distribution $W(x, p)$. Therefore, such a distribution allows the prediction of all statistical information about the state, and we can determine a particular pair of x and p values for a given simultaneous measurement. The equivalent distribution in classical optics would be a joint-probability distribution of the real and imaginary components of the complex amplitude α of an optical state (the amplitude and phase quadratures of the electromagnetic oscillator). However, obtaining such a distribution for a quantum state is forbidden by the uncertainty principle as it would mean that we could precisely and simultaneously know information about two non-commuting observables. Instead a *quasi*-probability distribution is defined which provides us with an intuitive representation of the state. In 1932, E. P. Wigner introduced a distribution that is now referred to as the *Wigner function*, which has become one of the most famous distributions used in quantum optics [246]. The Wigner function has a one-to-one correspondence with the density matrix and can be written as [243]

$$W(X^+, X^-) = \frac{1}{2\pi} \int_{-\infty}^{\infty} \exp(ixX^-) \Big\langle X^+ - \frac{x}{2} \Big| \hat{\rho} \Big| X^+ + \frac{x}{2} \Big\rangle dx. \tag{2.25}$$

It is normalized,

$$\int_{-\infty}^{\infty} \int_{-\infty}^{\infty} W(X^+, X^-) dX^+ dX^- = 1, \tag{2.26}$$

and its marginal distributions are the probability distributions for the amplitude and phase quadratures,

$$\int_{-\infty}^{\infty} W(X^+, X^-) dX^- = \mathrm{pr}(X^+) \tag{2.27}$$
$$\int_{-\infty}^{\infty} W(X^+, X^-) dX^+ = \mathrm{pr}(X^-).$$

More generally the amplitude quadrature probability distribution $\mathrm{pr}(X^+, \theta)$ after an arbitrary phase shift θ is [243, 247]

$$\mathrm{pr}(X^+, \theta) = \int_{-\infty}^{\infty} W(X^+ \cos\theta - X^- \sin\theta, X^+ \sin\theta + X^- \cos\theta) dX^-. \tag{2.28}$$

We can also use the Wigner function to evaluate the expectation value of an operator $\hat{A}$ by

$$\langle \hat{A} \rangle = \mathrm{tr}[\hat{\rho}\hat{A}] = 2\pi \int_{-\infty}^{\infty} \int_{-\infty}^{\infty} W(X^+, X^-) W_A(X^+, X^-) dX^+ dX^-, \tag{2.29}$$

where

$$W_A(X^+, X^-) = \frac{1}{2\pi} \int_{-\infty}^{\infty} \exp(ixX^-) \Big\langle X^+ - \frac{x}{2} \Big| \hat{A} \Big| X^+ + \frac{x}{2} \Big\rangle dx. \tag{2.30}$$

Equation 2.30 is a special case of the overlap formula [243] where

$$\mathrm{tr}[\hat{A}\hat{B}] = 2\pi \int_{-\infty}^{\infty} \int_{-\infty}^{\infty} W_A(X^+, X^-) W_B(X^+, X^-) dX^+ dX^-. \tag{2.31}$$

Most properties of the Wigner function are similar to a classical distribution except for the surprising feature that it can have *negative* values. As mentioned in the previous chapter, some optical states can have negativity in their Wigner functions, which is often considered the signature of a non-classical (quantum) state [248]. The first experimental demonstration of a system that could be characterised by a negative Wigner function was done by Leibfried *et al.* for the motional state of a trapped ion [249]. These negative values are allowed since simultaneous measurements of the amplitude and phase quadratures are forbidden. For example, using equation 2.23, the Wigner function of the single-photon Fock state $|1\rangle$ can be shown to be

$$\begin{aligned} W_{|1\rangle}(X^+, X^-) &= \frac{1}{2\pi}\int_{-\infty}^{\infty} \exp(ixX^-)\Big\langle X^+ - \frac{x}{2}\Big|1\Big\rangle\Big\langle 1\Big|X^+ + \frac{x}{2}\Big\rangle dx \qquad (2.32)\\ &= \frac{1}{\pi^{3/2}}\int_{-\infty}^{\infty} \exp(ixX^-)\Big(X^+ - \frac{x}{2}\Big)\Big(X^+ + \frac{x}{2}\Big)\\ &\times \exp\Big(-\frac{1}{2}\Big(X^+ - \frac{x}{2}\Big)^2 - \frac{1}{2}\Big(X^+ + \frac{x}{2}\Big)^2\Big)dx\\ &= \frac{1}{\pi}\exp\Big(-(X^+)^2 - (X^-)^2\Big)\Big(2(X^+)^2 + 2(X^-)^2 - 1\Big), \end{aligned}$$

which has the negative value of $-1/\pi$ within a circle of radius $1/\sqrt{2}$ around the origin. In fact there are restrictions on the maximum and minimum values the Wigner function can take, where $-1/\pi$ is the absolute minimum and $1/\pi$ is the absolute maximum. This property is another example of how the Wigner function differs from a classical probability distribution. In contrast to the single-photon state, the vacuum state has a completely positive Wigner function, which is found by integrating the Wigner function over a Gaussian with variances fulfilling equation 2.20 [250]

$$W_{|0\rangle}(X^+, X^-) = \frac{1}{\pi}\exp\Big[-(X^+)^2 - (X^-)^2\Big]. \qquad (2.33)$$

Another useful aspect of the Wigner function is the ability to calculate a state's density matrix in the Fock basis from it and vice versa. This relationship illustrates the transition between these two different ways of describing the same state: the continuous variable Wigner function and discrete variable density matrix. We can see from equation 2.29 that

$$\rho_{mn} = \mathrm{tr}\Big[\hat{\rho}|n\rangle\langle m|\Big] = 2\pi \int_{-\infty}^{\infty}\int_{-\infty}^{\infty} W(X^+, X^-)W_{mn}(X^+, X^-)dX^+dX^-, \qquad (2.34)$$

with

$$W_{mn}(X^+, X^-) = \frac{1}{2\pi}\int_{-\infty}^{\infty} \exp(ixX^-)\Big\langle X^+ - \frac{x}{2}\Big|m\Big\rangle\Big\langle n\Big|X^+ + \frac{x}{2}\Big\rangle dx. \qquad (2.35)$$

From Leonhardt [243], this function is:

for $m \geq n$,

$$W_{mn}(X^+, X^-) = \frac{1}{\pi} \exp\Big(- (X^+)^2 - (X^-)^2 \Big) (-1)^m (-X^+ + iX^-)^{m-n} \times \sqrt{2^{m-n} \frac{n!}{m!}} L_n^{m-n} \Big(2(X^+)^2 + 2(X^-)^2 \Big), \tag{2.36}$$

and for $m < n$,

$$W_{mn}(X^+, X^-) = \frac{1}{\pi} \exp\Big(- (X^+)^2 - (X^-)^2 \Big) (-1)^m (-X^+ + iX^-)^{n-m} \times \sqrt{2^{n-m} \frac{m!}{n!}} L_m^{n-m} \Big(2(X^+)^2 + 2(X^-)^2 \Big), \tag{2.37}$$

where L_k^a are generalized Laguerre polynomials. Conversely, the Wigner function can be found given a state's density matrix ρ_{mn} from equation 2.25

$$\begin{aligned} W(X^+, X^-) &= \frac{1}{2\pi} \int_{-\infty}^{\infty} \exp(ixX^-) \Big\langle X^+ - \frac{x}{2} \Big| \Big(\sum_{m,n} \rho_{mn} |m\rangle\langle n| \Big) \Big| X^+ + \frac{x}{2} \Big\rangle dx \\ &= \sum_{m,n} \rho_{mn} W_{mn}(X^+, X^-). \end{aligned} \tag{2.38}$$

Often the quality of a quantum state is described by the value at the origin of the Wigner function due to its ability to have negative values. Therefore it is interesting to note that the value $W(0,0)$ is given by a simple equation which only depends on the diagonal elements of the density matrix, since $W_{mn}(0,0) = \delta_{mn}(-1)^m/\pi$:

$$W(0,0) = \frac{1}{\pi} \sum_n (-1)^n \rho_{nn} \tag{2.39}$$

This simplicity is because all of the phase information about the state is contained in the off-diagonal elements of the density matrix. Because the phase space origin has no defined phase, the off-diagonal elements of the density matrix are not required to calculate $W(0,0)$.

2.2 Quantum states of light

2.2.1 Fock states

Photon-number states or *Fock states* are non-classical states that consist of a fixed number of photons. They are the eigenstates of the photon-number operator, $\hat{n}$, where $\hat{n} \equiv \hat{a}^\dagger \hat{a}$. As discussed in the previous chapter, Fock states such as the single photon state are highly desirable resource states in optical quantum information applications. The annihilation and creation operators are known as 'lowering' and 'raising' operators due to their ability to annihilate or create single photons when acted on a Fock state, $|n\rangle$, in the same mode,

$$\hat{a}|n\rangle = \sqrt{n}|n-1\rangle, \quad \hat{a}^\dagger|n\rangle = \sqrt{n+1}|n+1\rangle. \tag{2.40}$$

A Fock state always has a positive integer number of photons as it is not physically possible for a state to have a fractional photon number or a negative number of photons.

The quantisation of the electromagnetic field leads us to the minimum energy state of the electromagnetic oscillator, which is the *vacuum state* and is denoted by $|0\rangle$. The vacuum state is a physically meaningful state and can be measured via homodyne detection. Therefore, there is a physical limit to the action of the annihilation operator once an n-photon state $|n\rangle$ has been lowered by n steps: $\hat{a}|0\rangle = \mathbf{0}$, where $\mathbf{0}$ is the null vector and not a scalar. Furthermore, we can see that we can generate $|n\rangle$ by repeatedly acting the creation operator on the vacuum state,

$$(\hat{a}^\dagger)^n|0\rangle = \sqrt{n!}|n\rangle \tag{2.41}$$

2.2.2 Coherent states

Optical states such as *coherent states* possess Gaussian statistics and can therefore be characterised by a completely positive Gaussian Wigner function. Coherent states are perfectly coherent light states which can be produced by an ideal laser. These states best emulate the classically defined light state and are therefore often referred to as classical states. Mathematically they are defined as displaced vacuum states

$$|\alpha\rangle = \hat{D}(\alpha)|0\rangle, \tag{2.42}$$

where

$$\hat{D}(\alpha) = e^{-\frac{1}{2}|\alpha|^2} e^{\alpha\hat{a}^\dagger} e^{-\alpha^*\hat{a}}, \tag{2.43}$$

and are the eigenstates of the annihilation operator $\hat{a}$,

$$\hat{a}|\alpha\rangle = \alpha|\alpha\rangle. \tag{2.44}$$

We can express this state in the Fock basis as

$$|\alpha\rangle = e^{-\frac{1}{2}|\alpha|^2} \sum_{n=0}^{\infty} \frac{\alpha^n}{\sqrt{n!}}|n\rangle. \tag{2.45}$$

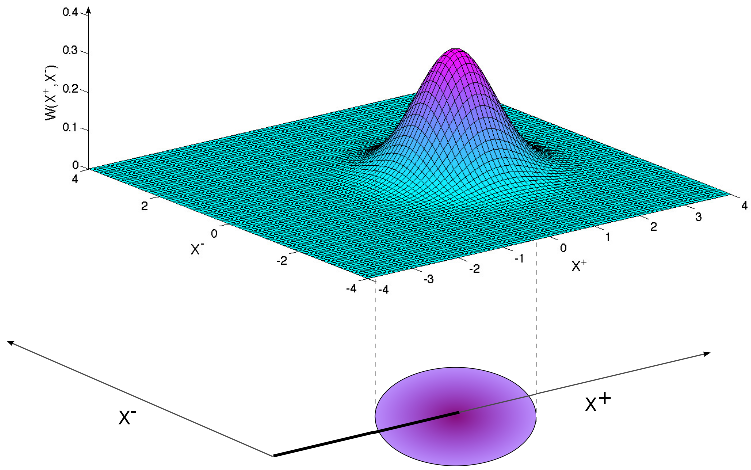

Figure 2.1: Theoretical 3-dimensional Wigner function and 2-dimensional *'ball and stick picture'* of a coherent state with $|\alpha| = 1/\sqrt{2}$.

A coherent state has equal noise levels in its amplitude and phase quadratures. This can be seen in the continuous variable Wigner function of a coherent state shown in figure 2.1. This Wigner function is defined as

$$W_\alpha(X^+, X^-) = \frac{1}{\pi} \exp\Big(-(X^+ - X^+_\alpha)^2 - (X^- - X^-_\alpha)^2 \Big) \tag{2.46}$$

with

$$\alpha = \frac{X^+_\alpha + iX^-_\alpha}{\sqrt{2}}, \tag{2.47}$$

which is a Gaussian function with minimum variance in both quadratures, making it a minimum uncertainty state. Figure 2.1 illustrates that a coherent state is simply a displaced vacuum state centred on $\alpha = (X^+_\alpha + iX^-_\alpha)/2$. The standard deviation of the contour of such a Gaussian Wigner function is an ellipse, which corresponds to the quadrature noise levels of the state. This ellipse is the 'ball' shown on the 2-dimensional X^+, X^- plot shown below the 3-dimensional Wigner function plot in figure 2.1. Also shown in the 2-dimensional plot is a 'stick' extending from the origin of the graph to the 'ball,' which represents the coherent amplitude of the state. That is why the X^+, X^- plot of a quantum state is often referred to as the *'ball and stick picture'*.

It can be shown from equation 2.45 that a coherent state has Poissonian photon statistics,

$$p_n = |\langle n|\alpha\rangle|^2 = \frac{|\alpha|^{2n}}{n!} e^{-|\alpha|^2}. \tag{2.48}$$

Equation 2.48 describes a coherent state in terms of its discrete variables (photon-

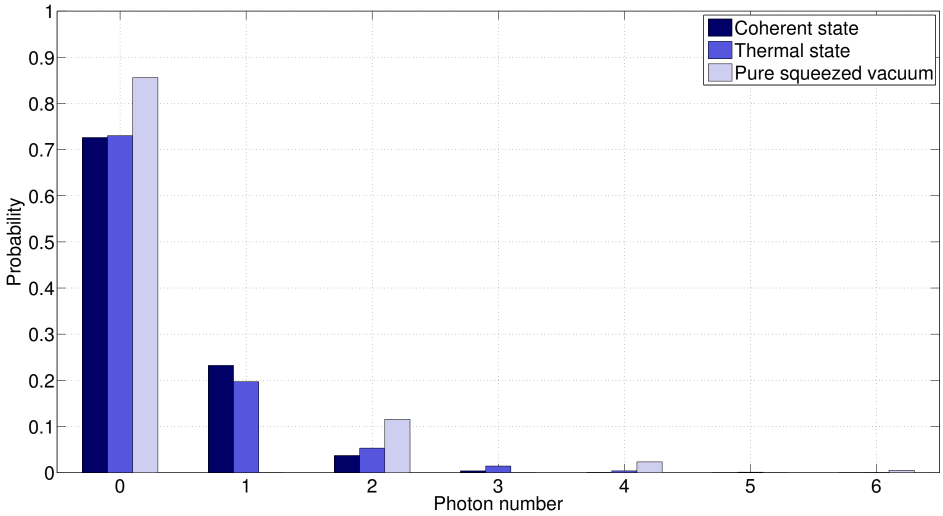

Figure 2.2: Theoretical photon number distributions for a coherent state ($|\alpha|^2 = 0.32$), a thermal state (-5 dB of squeezing), and a pure squeezed vacuum state (-5 dB of squeezing).

numbers) and this type of representation is shown in figure 2.2. By definition a state that can be described by Poissonian statistics is entirely random. Hence there are equal noise levels in the amplitude and phase quadratures.

Increasing the amplitude $|\alpha|$ only affects the displacement away from $W(0,0)$ and does not affect the height of the Wigner function or the quadrature noise distribution. This is why very large coherent states can be thought of as 'classical' states as the noise becomes negligibly small and the state becomes a point in classical phase space (i.e. if the 'stick' becomes very large compared to the size of the 'ball', then the 'ball' becomes a point). The average number of photons in the state is proportional to the intensity: $\bar{n} = \langle n \rangle = \langle \alpha | \hat{n} | \alpha \rangle = |\alpha|^2$. The standard deviation of the photon number is $\Delta n = |\alpha|$. Performing a photon counting measurement on the state will return n photon numbers with p_n probability.

2.2.3 Thermal states

Unlike a coherent state where photons occupy a single optical mode, the number of possible optical modes in a *thermal state* can exceed the number of photons, resulting in less than one photon on average per mode. The photon number distribution is dependent on the temperature of the system, as evident in black body radiation. The density matrix of this mixed state is defined as,

$$\rho_{thermal} = (1 - e^{-\beta_{k_B}\hbar\omega}) \sum_{n=0}^{\infty} e^{-n\beta_{k_B}\hbar\omega} |n\rangle\langle n|, \tag{2.49}$$

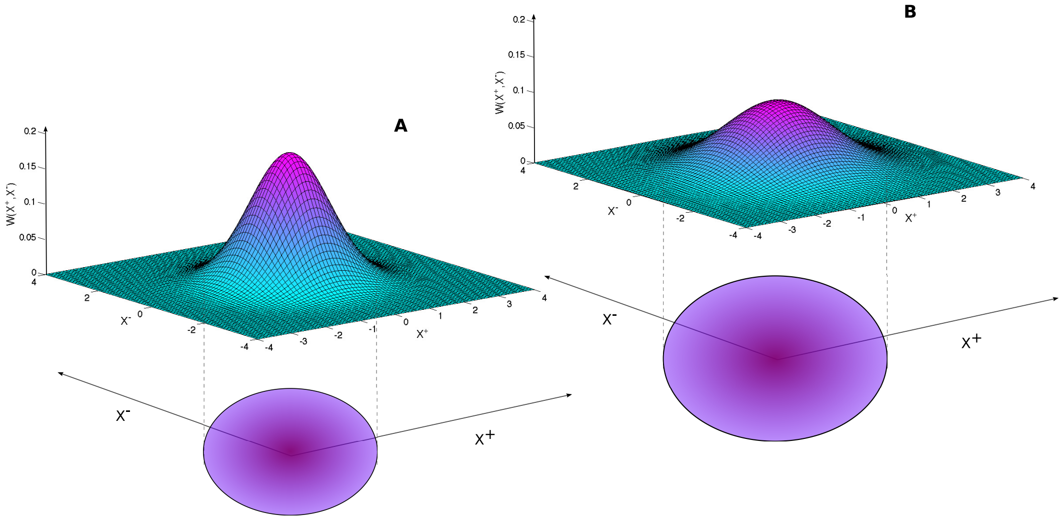

Figure 2.3: Theoretical 3-dimensional Wigner function and 2-dimensional *'ball and stick picture'* of two thermal states corresponding to A) -5 dB of squeezing, and B) -8 dB of squeezing.

where

$$\beta_{k_B} = \frac{1}{k_B T},$$

ω is the optical frequency, k_B is the Boltzmann's constant, and T is the temperature. A thermal state can result from multi-mode squeezing when some modes are not detected. In the case of two-mode squeezing where one mode is traced over, the temperature of the resultant thermal state can also be related to the amount of squeezing in the two-mode squeezed vacuum state [251]

$$T = \frac{\hbar\omega}{2k_B \ln(\coth|\xi|)}, \tag{2.50}$$

where

$$\xi = -\frac{\ln(V^\theta)}{2}$$

is the squeezing parameter for a squeezing angle of zero degree, and $V^\theta = (\Delta X(\theta))^2$ is the variance of the minimum noise quadrature, $X(\theta)$, in linear units (referred to as the squeezing level). The squeezing level can also be expressed in decibel units (dB) where $x\,\mathrm{dB} = 10\log_{10}(V^\theta)$. The photon number distribution (discrete variable representation) of a thermal state corresponding to -5 dB of squeezing is shown in figure 2.2.

The continuous variable Wigner function for a thermal state can be expressed as [243]

$$W(X^+, X^-) = \frac{1}{\pi} \tanh\left(\frac{\beta_{k_B}\hbar\omega}{2}\right) \exp\left(- (X^{+2} + X^{-2}) \tanh\left(\frac{\beta_{k_B}\hbar\omega}{2}\right)\right). \quad (2.51)$$

The Wigner functions for two thermal states that correspond to different squeezing levels are shown in figure 2.3. Unlike the Wigner function of a coherent state, these distributions are centred on $W(0,0)$, and the amount of quadrature noise and the height of the Wigner functions depends on the temperature of the state. Increasing the amount of squeezing, V_0, has the affect of increasing the temperature of the state, and therefore proportionally increasing the amount of quadrature noise evenly distributed between X^+ and X^-, which decreases the height of the Wigner function.

2.2.4 Squeezed states

A *squeezed state* is an optical state that has a reduced noise level in one quadrature which is below the *quantum noise limit* (QNL), say $\Delta X^+ < 1$, and consequently due to the uncertainty principle the noise level in the conjugate quadrature has been increased above the QNL, resulting in $\Delta X^- > 1$. For example, if the variance of the noise level of X^+ is lowered to 0.5 relative to QNL (which is normalized to 1), then $V^+ = 0.5$ in linear units or V^+ =-3 dB in decibels (squeezing). If the squeezed state is a minimum uncertainty state then the variance of the orthogonal quadrature is $V^- = 2$ in linear units or $V^- = 3$ dB (anti-squeezing), such that $\Delta X^+ \Delta X^- = 1$. However, it is experimentally challenging to produce a minimum uncertainty squeezed state as any loss in the system results in an disproportional amount of anti-squeezing to squeezing [152].

The photon number distribution of a squeezed state is given by [252]

$$p_n = |\langle n|\alpha, \phi, \xi\rangle|^2, \quad (2.52)$$

where

$$\begin{aligned}\langle n|\alpha, \phi, \xi\rangle = &\sqrt{\frac{e^{in\phi}\tanh^n \xi}{2^n n! \cosh \xi}} \exp\left(- \frac{1}{2}\Big(|\alpha|^2 + |\alpha|^{*2} e^{i\phi} \tanh \xi\Big)\right) \\ &\times H_n\left[\frac{\alpha + \alpha^* e^{i\phi} \tanh \xi}{\sqrt{2e^{i\phi}\tanh \xi}}\right],\end{aligned} \quad (2.53)$$

and ϕ is the quadrature squeezing angle. A pure single-mode squeezed vacuum state with $\phi = 0$ can be expressed as [253]

$$|\xi\rangle = \hat{S}(\xi)|0\rangle = \sum_{n=0}^{\infty} \beta_{2n}|2n\rangle, \tag{2.54}$$

where

$$\beta_{2n} = \frac{1}{\sqrt{\cosh \xi}} \frac{\sqrt{(2n)!}(-\tanh \xi)^n}{2^n n!}, \tag{2.55}$$

and $\hat{S}(\xi)$ is the single-mode squeezing operator. Note that according to equation 2.54, a squeezed vacuum state is defined as the squeezing operator acting on the vacuum state. The photon number distribution of a pure squeezed vacuum state consists of only even photon numbers (pairs of photons). The photon number distribution of a pure squeezed vacuum state corresponding to -5 dB of squeezing is shown in comparison to a coherent state and a thermal state in figure 2.2.

Another way to represent a squeezed state is by its Wigner function, which is given by

$$W_{sqz}(X^+, X^-) = \frac{1}{\pi} \exp\Bigg(- \frac{(X^+)^2}{e^{2\xi}} - \frac{(X^-)^2}{e^{-2\xi}} \Bigg), \tag{2.56}$$

which is a completely positive Gaussian with a maximum value of $1/\pi$. The variance of a squeezed vacuum state is given by,

$$\Big(\Delta X(\theta)\Big)^2 = \langle \xi | X(\theta)^2 | \xi \rangle - \langle \xi | X(\theta) | \xi \rangle^2, \tag{2.57}$$

where

$$\begin{aligned} \langle \xi | X(\theta)^2 | \xi \rangle &= \frac{1}{2} \Bigg[\langle 0 | \hat{S}^\dagger(\xi) \Big(\hat{a}^2 e^{-2i\theta} + \hat{a}\hat{a}^\dagger + \hat{a}^\dagger \hat{a} + \hat{a}^{\dagger 2} e^{2i\theta} \Big) \hat{S}(\xi) | 0 \rangle \Bigg] \\ &= \langle 0 | \hat{a}^2(\xi) e^{-2i\theta} | 0 \rangle + \langle 0 | \hat{a}(\xi) \hat{a}^\dagger(\xi) | 0 \rangle + \langle 0 | \hat{a}^\dagger(\xi) \hat{a}(\xi) | 0 \rangle \\ &+ \langle 0 | \hat{a}^{\dagger 2}(\xi) e^{2i\theta} | 0 \rangle. \end{aligned} \tag{2.58}$$

$$\because \ \hat{a}(\xi) = \hat{a} \cosh r + \hat{a}^\dagger e^{i\phi_{pump}} \sinh r \tag{2.59}$$

and

$$\hat{a}^\dagger(\xi) = \hat{a}^\dagger \cosh r + \hat{a}^\dagger e^{-i\phi_{pump}} \sinh r, \tag{2.60}$$

where ϕ_{pump} is the optical phase of the second harmonic field. Then

$$\langle \xi | X(\theta)^2 | \xi \rangle = 2 \cos(\phi_{pump} - 2\theta) \cosh r \sinh r + \cosh^2 r + \sinh^2 r. \tag{2.61}$$

When $\phi_{pump} - 2\theta = 0$,

$$\langle\xi|X(\theta)^2|\xi\rangle = e^{2r}, \tag{2.62}$$

and when $\phi_{pump} - 2\theta = \pi$,

$$\langle\xi|X(\theta)^2|\xi\rangle = e^{-2r}. \tag{2.63}$$

$\langle\xi|X(\theta)|\xi\rangle$ is given by

$$\begin{aligned}\langle\xi|X(\theta)|\xi\rangle =& \frac{1}{2}\langle\xi|\hat{a} + \hat{a}^\dagger|\xi\rangle \\ =& \frac{1}{2}\langle 0|S^\dagger(\xi)(\hat{a} + \hat{a}^\dagger)S(\xi)|0\rangle \\ =& \frac{1}{2}\langle 0|\hat{a}(\xi) + \hat{a}^\dagger(\xi)|0\rangle \\ =& 0.\end{aligned} \tag{2.64}$$

Therefore

$$\begin{aligned}\Big(\Delta X(\theta)\Big)^2 &= \langle\xi|X(\theta)^2|\xi\rangle \\ &= \frac{1}{2}\Big[e^{2r}\Big(\cos(\phi_{pump} - 2\theta) + 1\Big) + e^{-2r}\Big(1 - \cos(\phi_{pump} - 2\theta)\Big)\Big],\end{aligned} \tag{2.65}$$

When $\phi_{pump} - 2\theta = 0$,

$$\Big(\Delta X(\theta)\Big)^2 = e^{2r}, \tag{2.66}$$

which is the minor axis of the squeezing ellipse, and when $\phi_{pump} - 2\theta = \pi$,

$$\Big(\Delta X(\theta)\Big)^2 = e^{-2r}, \tag{2.67}$$

which is the major axis of the squeezing ellipse.

The Wigner function can also be expressed in terms of the optical phase of the second harmonic field, ϕ_{pump}, relative to the down-converted photon pairs at the fundamental frequency [254],

$$W(x, y) = \frac{1}{\pi\Delta X_{Sqz}\Delta X_{Asqz}} exp\left[\frac{-(x - e_0\cos\phi_{pump})^2}{(\Delta X_{Sqz})^2} - \frac{(y - e_0\sin\phi_{pump})^2}{(\Delta X_{Sqz})^2}\right] \tag{2.68}$$

where ΔX_{Sqz} is the minimum standard deviation of the quadrature fluctuations (and $(\Delta X_{Sqz})^2$ is the squeezing level in linear units), ΔX_{Asqz} is the maximum standard deviation of the quadrature fluctuations (and $(\Delta X_{Asqz})^2$ is the anti-squeezing level in linear units), e_0 is the state's amplitude ($e_0 = 0$ for squeezed vacuum state and

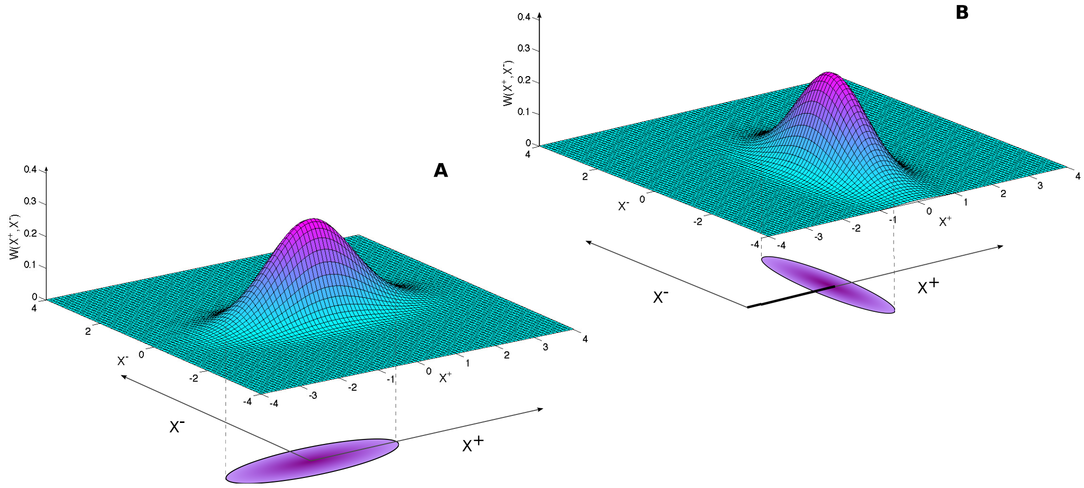

Figure 2.4: Theoretical 3-dimensional Wigner functions and 2-dimensional *'ball and stick pictures'* of minimum uncertainty squeezed states for -3 dB (6 dB) of squeezing (anti-squeezing). A) amplitude-quadrature squeezed vacuum state, and B) phase-quadrature squeezed coherent state with $|\alpha| = 1/\sqrt{2}$.

$e_0 \neq 0$ for a squeezed coherent state), and

$$\begin{aligned} x &= X^- \cos\phi_{pump} + X^+ \sin\phi_{pump} \\ y &= -X^- \sin\phi_{pump} + X^+ \cos\phi_{pump}. \end{aligned} \tag{2.69}$$

The Wigner functions for a squeezed coherent state and a squeezed vacuum state are shown in figure 2.4. A squeezed coherent state is defined as

$$|\xi\rangle_\alpha = \hat{D}(\alpha)\hat{S}(\xi)|0\rangle, \tag{2.70}$$

where $\hat{D}(\alpha)$ is the displacement operator defined in equation 2.43. The contour of the Wigner function of a squeezed state is an ellipse with semiminor and semimajor axes which correspond to the squeezed and anti-squeezed quadratures, respectively. The Wigner function of a squeezed vacuum state is centred on $W(0,0)$, whereas the Wigner function of a squeezed coherent state is displaced away from the phase-space origin by its coherent amplitude.

2.3 Propagation in quantum optics

2.3.1 Schrödinger and Heisenberg pictures

Unitary transformation operators, $\hat{U}$, are employed to model the propagation of quantum optical modes through basic optical elements, such as mirrors, cavities, and

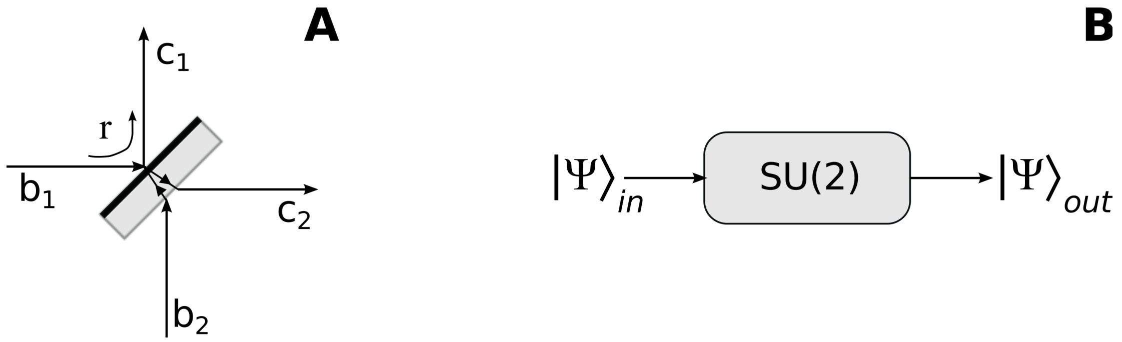

Figure 2.5: Schematic diagrams of two common models used to represent a beamsplitter. A) Physical representation of a beamsplitter with reflectivity r; Heisenberg operators $\hat{b}_1$ and $\hat{b}_2$ represent the incident modes and $\hat{c}_1$ and $\hat{c}_2$ represent the exiting modes. B) Circuit model diagram of a beamsplitter with Schrödinger picture states representing the input state $|\psi\rangle_{in}$ evolving to the output state $|\psi\rangle_{out}$ after interacting with the beamsplitter unitary $SU(2)$.

beamsplitters. Operators of elements that do not change with time are defined such that $\hat{U} = exp(-i\hat{H}\tau/\hbar)$, where $\hat{H}$ is the interaction Hamiltonian which characterises the optical element and τ characterises the strength of the interaction or the time over which it acts [242]. These operators are defined to be unitary where $\hat{U}^{-1} = \hat{U}^{\dagger}$. There are two distinct and equivalent ways to use these operators to model the evolution of light through optics: the *Schrödinger picture* and the *Heisenberg picture.* In the Schrödinger picture, the observables remain stationary while the states evolve from $|\psi\rangle_{in} \rightarrow |\psi\rangle_{out}$, which is calculated via

$$|\psi\rangle_{out} = \hat{U}|\psi\rangle_{in}. \tag{2.71}$$

Whereas in the Heisenberg picture, the state of the system remains stationary and the mode observables evolve. An operator in the Schrödinger picture, $\hat{B}$, is equivalent to an operator in the Heisenberg picture, $\hat{b}$, via

$$\hat{b} \equiv \hat{U}^{\dagger}\hat{B}\hat{U}. \tag{2.72}$$

These two pictures are also equivalent in that both techniques return the same expectation values,

$$_{out}\langle\psi|\hat{B}|\psi\rangle_{out} \equiv {}_{in}\langle\psi|\hat{U}^{\dagger}\hat{B}\hat{U}|\psi\rangle_{in} \equiv {}_{in}\langle\psi|\hat{b}|\psi\rangle_{in}. \tag{2.73}$$

Figure 2.5 illustrates how these two pictures can be applied to model a beamsplitter in two distinct yet equivalent ways. We will now use these two pictures to model the propagation of light through a beamsplitter with an arbitrary intensity reflection coefficient of r.

2.3.2 Beamsplitter model

Understanding how to model a beamsplitter plays an important role in modelling more complex optical systems, such as homodyne detection and an interferometer. The beamsplitter unitary is a 2×2 matrix ($SU(2)$) that can take one of two forms of symmetry: spatially symmetric or time symmetric [255]. The spatially symmetric beamsplitter $\hat{U}_s$ with an arbitrary intensity reflection coefficient of r is defined as

$$\hat{U}_s = \begin{pmatrix} i\sqrt{r} & \sqrt{1-r} \\ \sqrt{1-r} & i\sqrt{r} \end{pmatrix}.$$

In this model each beam acquires a $\pi/2$-phase shift upon reflection; hence it is spatially symmetric. Applying this unitary in the Heisenberg picture gives

$$\begin{aligned} \mathbf{c}_{out} &= \hat{U}_s \mathbf{b}_{in} \\ \begin{pmatrix} \hat{c}_1 \\ \hat{c}_2 \end{pmatrix} &= \begin{pmatrix} i\sqrt{r} & \sqrt{1-r} \\ \sqrt{1-r} & i\sqrt{r} \end{pmatrix} \begin{pmatrix} \hat{b}_1 \\ \hat{b}_2 \end{pmatrix}. \end{aligned} \tag{2.74}$$

It is simple to model light travelling in the opposite direction through an optical element as beam paths are reversible in quantum field theory. Since U_s is not time symmetric, its Hermitian conjugate must be used to calculate the input operators in terms of the output operators,

$$\begin{aligned} \mathbf{b}_{in} &= \hat{U}_s^\dagger \mathbf{c}_{out} \\ \begin{pmatrix} \hat{b}_1 \\ \hat{b}_2 \end{pmatrix} &= \begin{pmatrix} -i\sqrt{r} & \sqrt{1-r} \\ \sqrt{1-r} & -i\sqrt{r} \end{pmatrix} \begin{pmatrix} \hat{c}_1 \\ \hat{c}_2 \end{pmatrix}. \end{aligned} \tag{2.75}$$

However, the time symmetric beamsplitter unitary $\hat{U}_t$ can be used to calculate the output operators in terms of the input operators or vice versa, and is defined as

$$\begin{aligned} \hat{U}_t &= \begin{pmatrix} \sqrt{r} & \sqrt{1-r} \\ \sqrt{1-r} & -\sqrt{r} \end{pmatrix} \\ \mathbf{b}_{in} &= \hat{U}_t \mathbf{c}_{out} \\ \mathbf{c}_{out} &= \hat{U}_t \mathbf{b}_{in}. \end{aligned} \tag{2.76}$$

Note that this unitary is not spatially symmetric as one beam acquires a π-phase shift upon reflection while the other beam does not acquire a phase shift.

Sometimes it is more intuitive to model a system in the Schrödinger picture instead of the Heisenberg picture or vice versa. The Schrödinger picture gives a uniquely quantum mechanical view of these transformations whereas the Heisenberg

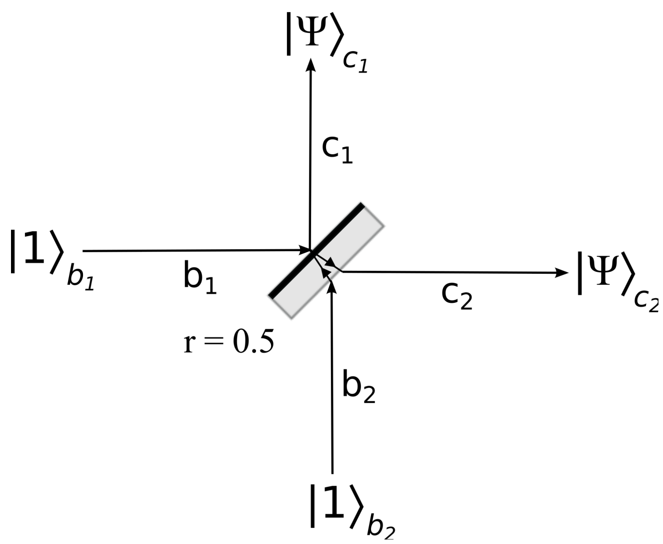

Figure 2.6: Schematic diagram of the Hong-Ou-Mandel effect modeled using both the Heisenberg and Schrödinger pictures.

picture takes a more classical approach in that canonical quantisation requires that the equations of motion of the annihilation operator $\hat{a}$ be identical to those of the classical amplitude α.

For example, Schrödinger picture is more intuitive to use to model the famous Hong-Ou-Mandel effect where two single photons incident on a beamsplitter will 'stick together' and both exit either one output or the other [256]. A schematic of how to model this effect is shown in figure 2.6. First we describe the input state as

$$\begin{aligned} |\Psi\rangle_{in} &= |\psi\rangle_{b1} \otimes |\psi\rangle_{b2} \\ &= |1\rangle_{b1} \otimes |1\rangle_{b2}. \end{aligned} \tag{2.77}$$

Using the relation described by equation 2.41 we can rewrite $|\Psi\rangle_{in}$ in terms of Schrödinger creation operators,

$$\begin{aligned} |\Psi\rangle_{in} &= \hat{B}_1^\dagger|0\rangle_{b1} \otimes \hat{B}_2^\dagger|0\rangle_{b2} \\ &= \hat{B}_1^\dagger\hat{B}_2^\dagger|0\rangle_{in}. \end{aligned} \tag{2.78}$$

Now we apply U_s to the input state to calculate the output state from a spatially symmetric beamsplitter with $r = 0.5$ (50/50 beamsplitter),

$$\begin{aligned} |\Psi\rangle_{out} &= \hat{U}_s|\Psi\rangle_{in} \\ &= \hat{U}_s\hat{B}_1^\dagger\hat{B}_2^\dagger|0\rangle_{in} \\ &= \hat{U}_s\hat{B}_1^\dagger\hat{B}_2^\dagger\hat{U}_s^\dagger\hat{U}_s|0\rangle_{in} \end{aligned} \tag{2.79}$$

Inserting $\hat{U}_s^\dagger \hat{U}_s$ in the final step of equation 2.79 is allowed because $\hat{U}_s^\dagger \hat{U}_s = 1$. We can apply the definition 2.72 to translate the Schrödinger operators into Heisenberg operators as $\hat{U}_s \hat{B}_1^\dagger \hat{U}_s^\dagger \equiv \hat{b}_1^\dagger$. We can then evolve the Heisenberg operators using the beamsplitter unitary to give $\hat{b}_1, \hat{b}_2$ in terms of $\hat{c}_1, \hat{c}_2$. By definition the vacuum mode is unaffected by unitary transformations representing linear passive optical elements. Therefore

$$|0\rangle_{out} = \hat{U}_s|0\rangle_{in}. \tag{2.80}$$

Applying the inverse equation of motion defined in equation 2.75 and using the relation 2.80 gives,

$$\begin{aligned} |\Psi\rangle_{out} &= \hat{b}_1^\dagger \hat{b}_2^\dagger \hat{U}_s |0\rangle_{in} \\ &= \frac{1}{2}\left(\hat{c}_2^\dagger + i\hat{c}_1^\dagger\right)\left(\hat{c}_1^\dagger + i\hat{c}_2^\dagger\right)|0\rangle_{out} \\ &= \frac{1}{2}\left[\hat{c}_2^\dagger\hat{c}_1^\dagger + i\hat{c}_2^\dagger\hat{c}_2^\dagger + i\hat{c}_1^\dagger\hat{c}_1^\dagger - \hat{c}_1^\dagger\hat{c}_2^\dagger\right]|0\rangle_{out} \\ &= \frac{1}{2}\left[|1\rangle_{c2}|1\rangle_{c1} + i|0\rangle_{c1}|2\rangle_{c2} + i|2\rangle_{c1}|0\rangle_{c2} - |1\rangle_{c1}|1\rangle_{c2}\right] \\ &= \frac{i}{2}\left[|0\rangle_{c1}|2\rangle_{c2} + |2\rangle_{c1}|0\rangle_{c2}\right]. \end{aligned} \tag{2.81}$$

Clearly from the output state equation $|\Psi\rangle_{out}$ we would expect both photons to exit the same output port of the beamsplitter if the two single photons reach the beamsplitter simultaneously. Therefore the number of coincidence counts between the two detectors monitoring these output ports would drop dramatically due to the interaction of the single photons with the 50/50 beamsplitter, which was experimentally confirmed by Hong *et al.* in 1987 [256]. This calculation is an example of the power of the Schrödinger picture to model quantum mechanical effects.

2.3.3 Frequency beamsplitter

Various applications in optics require the spatial separation of frequency side-bands from an optical spectrum. One example is the spatial separation of entangled side-bands from a squeezed vacuum state to demonstrate EPR entanglement between its spectral components [99, 164, 257]. Spatial separation of spectral side-bands can be achieved via an unbalanced *Mach-Zehnder interferometer* consisting of two 50/50 beamsplitters and a path length difference which adds a time delay between the two arms of the interferometer. The time delay, τ, results in a phase shift $\omega\tau$ given to the frequency side-bands and not the carrier since ω is the side-band angular frequency above or below the carrier angular frequency, Ω_0. This ability to spatially separate frequencies is the reason such an interferometer is referred as a '*frequency beamsplitter*' (FBS).

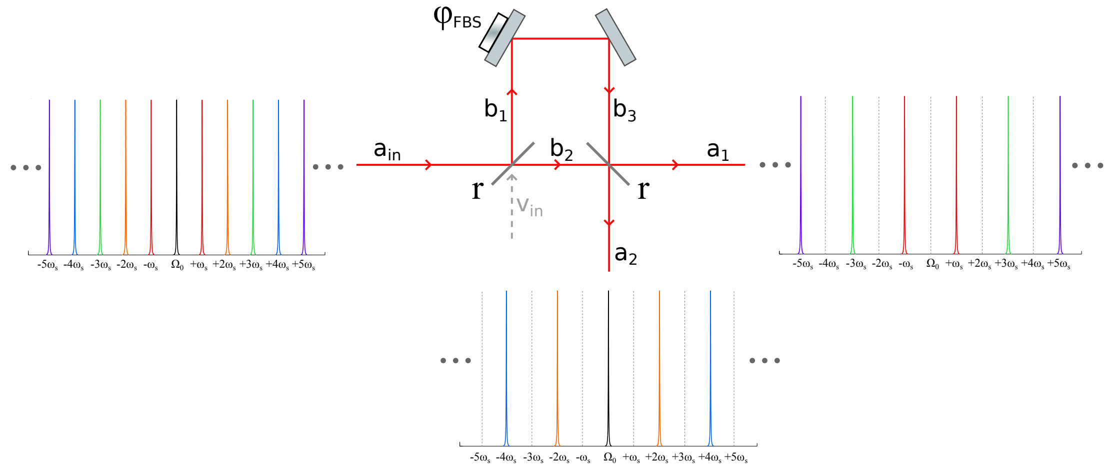

Figure 2.7: Schematic diagram of a frequency beamsplitter with the various input and output modes modelled using Heisenberg operators. The path length difference illustrated in this schematic results in the spatial separation of $\pm\omega_s, \pm 3\omega_s, \pm 5\omega_s$, etc. side-bands from the carrier at Ω_0 and side-bands at $\pm 2\omega_s, \pm 4\omega_s$, etc. Both beamsplitters have $r = 0.5$.

The path length difference can be engineered to separate the spectral components at particular side-band frequencies $\pm n\omega_s$ in a specific configuration. For example, an upper frequency side-band at $+\omega_s$ could be separated from a lower frequency side-band at $-\omega_s$ via an FBS [101]. Another possible configuration results in the spatial separation of $\pm\omega_s, \pm 3\omega_s, \pm 5\omega_s$, etc. side-bands from the carrier at Ω_0 and side-bands at $\pm 2\omega_s, \pm 4\omega_s$, etc. [100]. An FBS with this path length configuration is illustrated in figure 2.7 and will be referred to as 'configuration A.' An FBS in configuration A was used in our experiment, and will be further discussed in chapter 4. Therefore, a detailed model of an FBS in this configuration shall be the focus for the rest of this section.

It can be more intuitive to model an FBS in the Heisenberg picture, as shown in figure 2.7. Using the spatially symmetric beamsplitter convention, $\hat{U}_s$, the outputs from the first 50/50 beamsplitter are given by

$$\hat{b}_1(t) = \frac{1}{\sqrt{2}}\Big(i\hat{a}_{in}(t) + \hat{v}_{in}(t)\Big) \tag{2.82}$$

$$\hat{b}_2(t) = \frac{1}{\sqrt{2}}\Big(\hat{a}_{in}(t) + i\hat{v}_{in}(t)\Big), \tag{2.83}$$

where $\hat{v}_{in}$ models the input vacuum field. The path length difference results in a phase shift $e^{i\omega\tau}$, and the optical-scale phase shift due to the piezo-mounted mirror is $e^{i\phi_{FBS}} = e^{i\Omega_0\tau}$. Therefore

$$\hat{b}_3(t) = \hat{b}_2(t)e^{i\phi_{FBS}}e^{i\omega\tau} \tag{2.84}$$
$$= \frac{1}{\sqrt{2}}\Big(\hat{a}_{in}(t) + i\hat{v}_{in}(t)\Big)e^{i\phi_{FBS}}e^{i\omega\tau}.$$

The outputs from the second beamsplitter are

$$\hat{a}_1(t) = \frac{1}{\sqrt{2}}\Big(\hat{b}_2(t) + i\hat{b}_3(t)\Big) \tag{2.85}$$
$$\hat{a}_2(t) = \frac{1}{\sqrt{2}}\Big(i\hat{b}_2(t) + \hat{b}_3(t)\Big). \tag{2.86}$$

Substituting equations 2.83 and 2.84 into equations 2.85 and 2.86 gives,

$$\hat{a}_1(t) = \frac{1}{2}\Big[\hat{a}_{in}(t)(1 - e^{i\phi_{FBS}}e^{i\omega\tau}) + \hat{v}_{in}(t)(i + ie^{i\phi_{FBS}}e^{i\omega\tau})\Big] \tag{2.87}$$
$$\hat{a}_2(t) = \frac{1}{2}\Big[\hat{a}_{in}(t)(i + ie^{i\phi_{FBS}}e^{i\omega\tau}) + \hat{v}_{in}(t)(e^{i\phi_{FBS}}e^{i\omega\tau} - 1)\Big]. \tag{2.88}$$

The propagation mode $\hat{a}_{in}$ can be broken up into two contributions: the steady-state mean amplitude term $\bar{a}_{in}$ at the carrier frequency, Ω_0, and the fluctuating term $\delta\hat{a}_{in}$ which represents the continuum of side-band modes at ω surrounding the carrier frequency. That is

$$\hat{a}_{in}(t) = \bar{a}_{in} + \delta\hat{a}_{in}(t) \tag{2.89}$$
$$\hat{v}_{in}(t) = \bar{v}_{in} + \delta\hat{v}_{in}(t) = \delta\hat{v}_{in}(t). \tag{2.90}$$

Note that the mean amplitude of the vacuum state is zero. Therefore, equations 2.87 and 2.88 become

$$\hat{a}_1(t) = \frac{1}{2}\Big[\bar{a}_{in}(1 - e^{i\phi_{FBS}}) + \delta\hat{a}_{in}(t)(1 - e^{i\phi_{FBS}}e^{i\omega\tau}) + \delta\hat{v}_{in}(t)(i + ie^{i\phi_{FBS}}e^{i\omega\tau})\Big] \tag{2.91}$$

$$\hat{a}_2(t) = \frac{1}{2}\Big[\bar{a}_{in}(i + ie^{i\phi_{FBS}}) + \delta\hat{a}_{in}(t)(i + ie^{i\phi_{FBS}}e^{i\omega\tau}) + \delta\hat{v}_{in}(t)(e^{i\phi_{FBS}}e^{i\omega\tau} - 1)\Big]. \tag{2.92}$$

We can transform the output fields in terms of frequency components by taking the Fourier transform of the fluctuating terms $\delta\hat{a}_{in}(t) \to \delta\hat{a}_{in}(\omega)$ to give

$$\delta\hat{a}_1(\omega) = \frac{1}{2}\Big[\delta\hat{a}_{in}(\omega)(1 - e^{i\phi_{FBS}}e^{i\omega\tau}) + \delta\hat{v}_{in}(\omega)(i + ie^{i\phi_{FBS}}e^{i\omega\tau})\Big] \tag{2.93}$$
$$\delta\hat{a}_2(\omega) = \frac{1}{2}\Big[\delta\hat{a}_{in}(\omega)(i + ie^{i\phi_{FBS}}e^{i\omega\tau}) + \delta\hat{v}_{in}(\omega)(e^{i\phi_{FBS}}e^{i\omega\tau} - 1)\Big]. \tag{2.94}$$

The FBS path length difference is engineered with a particular design frequency in mind, ω_s. Thus, the path length difference between the two arms of the interferometer results in a phase shift of $\varsigma_{_{FBS}}$ given to the fluctuating terms, which is defined as

$$\varsigma_{_{FBS}} = \omega_s \tau = \frac{\omega_s \Delta l}{c}, \tag{2.95}$$

where ω_s is the design frequency of the FBS, Δl is the actual path length difference and c is the speed of light in a vacuum. Using equations 2.93 and 2.94 we can now calculate the various frequency components found in the exiting fields of the second beamsplitter for a particular $\varsigma_{_{FBS}}$ and $\phi_{_{FBS}}$. The spectral components for an FBS in configuration A ($\phi_{_{FBS}} = 0$ and $\varsigma_{_{FBS}} = \pi$) are listed in table 2.1.

FBS output $\hat{a}_1$	FBS output $\hat{a}_2$
$\bar{a}_1 = 0$	$\bar{a}_2 = \bar{a}_{in}$
$\delta\hat{a}_1(\pm\omega_s) = \delta\hat{a}_{in}(\pm\omega_s)$	$\delta\hat{a}_2(\pm\omega_s) = -\delta\hat{v}_{in}(\pm\omega_s)$
$\delta\hat{a}_1(\pm 2\omega_s) = i\delta\hat{v}_{in}(\pm 2\omega_s)$	$\delta\hat{a}_2(\pm 2\omega_s) = i\delta\hat{a}_{in}(\pm 2\omega_s)$
$\delta\hat{a}_1(\pm 3\omega_s) = \delta\hat{a}_{in}(\pm 3\omega_s)$	$\delta\hat{a}_2(\pm 3\omega_s) = -\delta\hat{v}_{in}(\pm 3\omega_s)$
$\delta\hat{a}_1(\pm 4\omega_s) = i\delta\hat{v}_{in}(\pm 4\omega_s)$	$\delta\hat{a}_2(\pm 4\omega_s) = i\delta\hat{a}_{in}(\pm 4\omega_s)$
$\delta\hat{a}_1(\pm 5\omega_s) = \delta\hat{a}_{in}(\pm 5\omega_s)$	$\delta\hat{a}_2(\pm 5\omega_s) = -\delta\hat{v}_{in}(\pm 5\omega_s)$

Table 2.1: Spectral components of output fields $\hat{a}_1$ and $\hat{a}_2$ for an FBS in configuration A ($\phi_{_{FBS}} = 0$ and $\varsigma_{_{FBS}} = \pi$).

Therefore an FBS in configuration A will result in both the upper and lower frequency side-bands at $\pm\omega_s, \pm 3\omega_s, \pm 5\omega_s$, etc. to exit from one output port of the second beamsplitter in the FBS ($\hat{a}_1$) and being spatially separated from the carrier and side-bands at $\pm 2\omega_s, \pm 4\omega_s$, etc. This result has been graphically represented in figure 2.7.

An important feature of the FBS is that for particular configurations, the side-bands are not corrupted by vacuum. To illustrate this point, we show the output modes for a different FBS phase configuration (configuration B) in tables 2.2 and 2.3 where $\phi_{_{FBS}} = \pi/2$ and $\varsigma_{_{FBS}} = \pi/2$. Note that the frequency components at $\pm 2\omega_s$ and $\pm 4\omega_s$ of both FBS output fields are corrupted by vacuum. Any corruption of a quantum state by vacuum can be detrimental to its quantum properties. The fact that configuration A does not lead to vacuum corrupted states and sends both upper and lower side-bands down the same spatial mode were necessary features for its use in our quantum optics experiment.

FBS output $\hat{a}_1$	FBS output $\hat{a}_2$
$\bar{a}_1 = \bar{a}_{in}\frac{e^{-i\pi/4}}{\sqrt{2}}$	$\bar{a}_2 = \bar{a}_{in}\frac{ie^{-i\pi/4}}{\sqrt{2}}$
$\delta\hat{a}_1(+\omega_s) = \delta\hat{a}_{in}(+\omega_s)$	$\delta\hat{a}_2(+\omega_s) = -\delta\hat{v}_{in}(+\omega_s)$
$\delta\hat{a}_1(-\omega_s) = i\delta\hat{v}_{in}(-\omega_s)$	$\delta\hat{a}_2(-\omega_s) = i\delta\hat{a}_{in}(-\omega_s)$
$\delta\hat{a}_1(+3\omega_s) = i\delta\hat{v}_{in}(+3\omega_s)$	$\delta\hat{a}_2(+3\omega_s) = i\delta\hat{a}_{in}(+3\omega_s)$
$\delta\hat{a}_1(-3\omega_s) = \delta\hat{a}_{in}(-3\omega_s)$	$\delta\hat{a}_2(-3\omega_s) = -\delta\hat{v}_{in}(-3\omega_s)$
$\delta\hat{a}_1(+5\omega_s) = \delta\hat{a}_{in}(+5\omega_s)$	$\delta\hat{a}_2(+5\omega_s) = -\delta\hat{v}_{in}(+5\omega_s)$
$\delta\hat{a}_1(-5\omega_s) = i\delta\hat{v}_{in}(-5\omega_s)$	$\delta\hat{a}_2(-5\omega_s) = i\delta\hat{a}_{in}(-5\omega_s)$

Table 2.2: Spectral components of output fields $\hat{a}_1$ and $\hat{a}_2$ at $\pm n\omega_s$ where $n = 1, 3, 5$ for an FBS in configuration B ($\phi_{_{FBS}} = \pi/2$ and $\varsigma_{_{FBS}} = \pi/2$).

FBS output $\hat{a}_1$	FBS output $\hat{a}_2$
$\delta\hat{a}_1(+2\omega_s) = \frac{1}{2}\big[\delta\hat{a}_{in}(+2\omega_s)(1+i) + i\delta\hat{v}_{in}(+2\omega_s)(1-i)\big]$	$\delta\hat{a}_2(+2\omega_s) = \frac{1}{2}\big[i\delta\hat{a}_{in}(+2\omega_s)(1-i) - \delta\hat{v}_{in}(+2\omega_s)(1+i)\big]$
$\delta\hat{a}_1(-2\omega_s) = \frac{1}{2}\big[\delta\hat{a}_{in}(-2\omega_s)(1+i) + i\delta\hat{v}_{in}(-2\omega_s)(1-i)\big]$	$\delta\hat{a}_2(-2\omega_s) = \frac{1}{2}\big[i\delta\hat{a}_{in}(-2\omega_s)(1-i) - \delta\hat{v}_{in}(-2\omega_s)(1+i)\big]$
$\delta\hat{a}_1(+4\omega_s) = \frac{1}{2}\big[\delta\hat{a}_{in}(+4\omega_s)(1-i) + i\delta\hat{v}_{in}(+4\omega_s)(1+i)\big]$	$\delta\hat{a}_2(+4\omega_s) = \frac{1}{2}\big[i\delta\hat{a}_{in}(+4\omega_s)(1+i) + \delta\hat{v}_{in}(+4\omega_s)(i-1)\big]$
$\delta\hat{a}_1(-4\omega_s) = \frac{1}{2}\big[\delta\hat{a}_{in}(-4\omega_s)(1-i) + i\delta\hat{v}_{in}(-4\omega_s)(1+i)\big]$	$\delta\hat{a}_2(-4\omega_s) = \frac{1}{2}\big[i\delta\hat{a}_{in}(-4\omega_s)(1+i) + \delta\hat{v}_{in}(-4\omega_s)(i-1)\big]$

Table 2.3: Spectral components of output fields $\hat{a}_1$ and $\hat{a}_2$ at $\pm n\omega_s$ where $n = 2, 4$ for an FBS in configuration B ($\phi_{_{FBS}} = \pi/2$ and $\varsigma_{_{FBS}} = \pi/2$).

2.4 Detecting light

2.4.1 Direct detection

One of the most important aspects of a quantum optics experiment is the ability to detect light and therefore characterise the generated quantum states. Without this ability to convert an optical signal into an electrical signal we could not quantify the resulting optical state from a nonlinear interaction or conduct photon-subtraction experiments to produce non-Gaussian quantum states. In direct detection no phase information can be retrieved about the light being measured. Instead it is a straightforward intensity measurement of the light done by generating a current which is proportional to the light's intensity. The most common measurement device used in a quantum optics laboratory for direct detection is a photodetector. A photodetector consists of a combination of electronics and a photodiode which generates a current that is directly proportional to the optical power P_{opt} in the incident light. This current is then transformed into a voltage, $\mathcal{U}$, where $P_{opt} \propto \mathcal{U}$, which can be analysed by an oscilloscope or a radio-frequency (RF) spectrum analyser. Photodiodes usually have a linear response which is important for accurate characterisation of a light field. The term *saturation* refers to when the electrical signal can no longer linearly respond to an increase in the optical power of the incident light, and should be avoided during many measurements. However, some measurement devices such as an avalanche photodiode (APD) are purposely operated in this saturation mode in order to generate a large enough electrical signal to be detectable in response to the measurement of an optical field with low photon flux. The proportionality constant of a photodiode is referred to as its *responsivity* and is expressed in units of A/W. The photodiodes that we use to detect near-infrared light at 1550 nm are standard InGaAs PIN photodiodes which have a quantum efficiency (i.e. number of electrons per photon) of 90%.

The photon flux of the optical state we wish to characterise determines the ideal method of detection. PIN photodiodes perform well at detecting more intense light when it is only necessary to generate a photo-current which is proportional to the light. However in situations where the field has a low photon flux (a few photons/sec) it is necessary to use an avalanche photodiode (APD). A single photon absorption event in an APD operating with a reverse bias above the diode breakdown voltage (Geiger mode) results in an electron avalanche which generates a macro-current that can be detected. APDs are approximate to a photon-number detector, and are commonly used in projecting experiments to generate non-classical states such as photon-subtracted squeezed vacuum states. Unfortunately the quantum efficiencies of InGaAs APDs is $10 - 20\%$, which means out of 100 photons only $10 - 20$ are actually detected by the APD. This low quantum efficiency can have detrimental effects on the quality of the projected state, which will be further discussed later in this thesis.

2.4.2 Homodyne detection

A photodetection technique that can provide both amplitude and phase information about a quantum state is balanced homodyne detection. In this detection scheme a weak signal field is interfered with a phase-coherent strong beam called an optical local oscillator (LO) at the same optical frequency on a 50/50 beamsplitter. The exiting beams are then detected by two standard PIN photodiodes, and the resulting photo-currents are subtracted via electronics. High-speed photodiodes can be combined with fast electronics to produce a wide-bandwidth homodyne detector

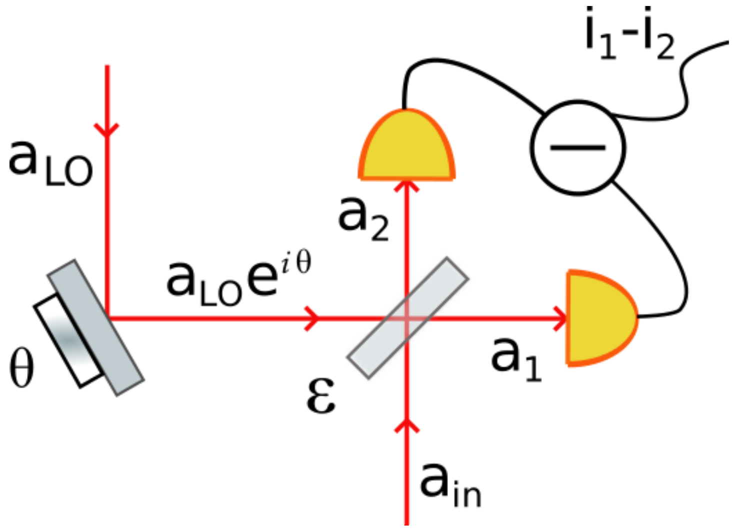

Figure 2.8: Schematic diagram of homodyne detection.

that can measure frequencies up to several gigahertz (GHz). Homodyne detection is a standard measurement technique in quantum optics and is thoroughly explained in the literature [242, 243, 258–261]. Therefore we will only discuss a brief overview of the technique.

A schematic diagram of the homodyne detection technique is shown in figure 2.8. It is more intuitive to model this system in the Heisenberg picture. The operator $\hat{a}_{in}$ denotes the input signal field to be measured and $\hat{a}_{LO}e^{i\theta}$ denotes the strong LO field with an adjustable optical phase, θ, relative to the signal, which is controlled (in our experiments) by a piezo-mounted mirror in the LO beam path.

The exiting modes $\hat{a}_1$ and $\hat{a}_2$ are given by

$$\hat{a}_1(t) = \frac{1}{\sqrt{2}}\Big(i\hat{a}_{in}(t) + \hat{a}_{LO}(t)e^{i\theta}\Big) \tag{2.96}$$

$$\hat{a}_2(t) = \frac{1}{\sqrt{2}}\Big(\hat{a}_{in}(t) + i\hat{a}_{LO}(t)e^{i\theta}\Big). \tag{2.97}$$

Since the photo-currents i_1 and i_2 are proportional to the number of photons in the detected field, $\hat{n}$, the subtracted output from the homodyne detector is

$$i_1 - i_2 \propto \hat{n}_1 - \hat{n}_2 = \hat{a}_1^\dagger\hat{a}_1 - \hat{a}_2^\dagger\hat{a}_2 \tag{2.98}$$

where

$$\hat{a}_1^\dagger\hat{a}_1 = \frac{1}{2}\Big(i\hat{a}_{LO}^\dagger\hat{a}_{in}e^{-i\theta} + \hat{a}_{LO}^\dagger\hat{a}_{LO} + \hat{a}_{in}^\dagger\hat{a}_{in} - i\hat{a}_{in}^\dagger\hat{a}_{LO}e^{i\theta}\Big) \tag{2.99}$$

$$\hat{a}_2^\dagger\hat{a}_2 = \frac{1}{2}\Big(i\hat{a}_{in}^\dagger\hat{a}_{LO}e^{i\theta} + \hat{a}_{LO}^\dagger\hat{a}_{LO} + \hat{a}_{in}^\dagger\hat{a}_{in} - i\hat{a}_{LO}^\dagger\hat{a}_{in}e^{-i\theta}\Big). \tag{2.100}$$

Having a balanced detection scheme (i.e. equal transmission and reflection on the beamsplitter) means that the subtracted output removes the direct detection components of the LO and signal fields, and leaves just the interference terms which depend on the optical phase θ,

$$\hat{a}_1^\dagger\hat{a}_1 - \hat{a}_2^\dagger\hat{a}_2 = i\hat{a}_{LO}^\dagger\hat{a}_{in}e^{-i\theta} - i\hat{a}_{in}^\dagger\hat{a}_{LO}e^{i\theta}. \tag{2.101}$$

We then use relation 2.89 and linearise the resulting equation by ignoring the second-order fluctuation terms like $\delta\hat{a}_{LO}^\dagger\delta\hat{a}_{in}$ to give

$$\begin{aligned}\hat{a}_1^\dagger\hat{a}_1 - \hat{a}_2^\dagger\hat{a}_2 \approx\, & 2\bar{a}_{LO}\bar{a}_{in}\cos\theta + \bar{a}_{LO}(\delta\hat{a}_{in}e^{-i\theta} + \delta\hat{a}_{in}^\dagger e^{i\theta}) \\ & + \bar{a}_{in}(\delta\hat{a}_{LO}e^{i\theta} + \delta\hat{a}_{LO}^\dagger e^{-i\theta}) \\ & = 2\bar{a}_{LO}\bar{a}_{in}\cos\theta + \bar{a}_{LO}\delta\hat{X}_{in}(-\theta) + \bar{a}_{in}\delta\hat{X}_{LO}(\theta).\end{aligned} \tag{2.102}$$

The term $\bar{a}_{in}$ ($\bar{a}_{LO}$) is the steady-state amplitude of the signal (local oscillator), and $\delta\hat{X}_{in}^{-\theta}$ ($\delta\hat{X}_{LO}^{\theta}$) is the quadrature measurement of fluctuations in the signal (local oscillator) field, respectively. As the signal strength of the measured fluctuations scales with the optical power, by setting $\bar{a}_{sig} \ll \bar{a}_{LO}$ in the homodyne measurement allows for the last term in equation 2.102 to be disregarded, leaving

$$\hat{a}_1^\dagger\hat{a}_1 - \hat{a}_2^\dagger\hat{a}_2 \approx\ 2\bar{a}_{LO}\bar{a}_{in}\cos\theta + \bar{a}_{LO}\delta\hat{X}_{in}(-\theta). \tag{2.103}$$

Thus, homodyne detection is capable of measuring the quadrature observable $\hat{X}(\theta) = e^{-i\theta}\hat{a} + e^{i\theta}\hat{a}^\dagger$ for any given phase of the LO.

2.5 Optical parametric oscillators

2.5.1 Parametric amplification

The amplification of an optical signal is useful in a number of applications, particularly for producing a high power laser beam. If the process is insensitive to phase then both the noise and the coherent amplitude of the state are amplified, and this amplification acts equally on all quadratures. However, it is possible to have a phase *sensitive* amplifier in which the noise in one quadrature is amplified while the noise in the other quadrature is attenuated or *de-amplified*. Consider the situation where the amplitude quadrature is amplified by amount $\sqrt{K}$ and the phase quadrature is attenuated by the same amount. We can write the annihilation operator of the output field as

$$\hat{a}_{out} = \frac{1}{2}\Big(\sqrt{K}\hat{X}^+ + \frac{i}{\sqrt{K}}\hat{X}^-\Big). \tag{2.104}$$

This transformation is legitimate and still obeys the commutation relations. Therefore, as long as the product of the gains is unity, noiseless amplification of one of the quadratures at the expense of noise amplification of the orthogonal quadrature can be achieved. In analogy with the linear amplifier, equation 2.104 can also be written in the form [242],

$$\hat{a}_{out} = \sqrt{G}\hat{a}_{in} + \sqrt{G-1}\hat{a}^{\dagger}_{in} \tag{2.105}$$

where the gain is

$$G = \frac{(K+1)^2}{4K}. \tag{2.106}$$

This classical nonlinear behaviour can be used to generated a squeezed state from a 'full' optical cavity (i.e. a cavity with a nonlinear crystal inside the resonant field). A higher amount of amplification/de-amplification of the classical field can correspond to more squeezing in the quantum state as long as the amount of loss in the system is low. We will show in §2.7 that the amount of squeezing in a system is a function of classical gain and loss, as well as the detection efficiency of the technique used to characterise the quantum state.

2.5.2 Second-order nonlinearity

Phase sensitive amplification can be achieved from a second-order nonlinearity. Classically the induced dipole polarisation $P(E)$ caused by the interaction of an optical beam's electric field E with an atomic medium can be described by

$$P(E) = \chi E + \chi^{(2)}E^2 + \chi^{(3)}E^3 + \cdots \tag{2.107}$$

An optical material can be classified as nonlinear if the higher-order terms in the $P(E)$ expansion become significant for a particular incident beam power. The invention of high-powered lasers has led to the discovery of several materials that show nonlinear behaviour. Materials that exhibit a second-order $\chi^{(2)}$ nonlinearity can be used to produce phase sensitive amplification and squeezed light due to their ability to couple a fundamental field (oscillating at ν) to a harmonic or 'pump' field (oscillating at 2ν). The interaction Hamiltonian is given by

$$\hat{H} = i\hbar\chi^{(2)}(\hat{b}^{\dagger}\hat{a}^2 - \hat{a}^{\dagger 2}\hat{b}). \tag{2.108}$$

This Hamiltonian can be interpreted in terms of photons: two photons at the fundamental frequency (mode a) are annihilated to produce a single photon at the harmonic frequency (mode b), whilst one photon at the harmonic frequency is being annihilated to produce a pair of photons at the harmonic frequency which are *entangled*. In order to achieve maximum conversion efficiency, both the energy and momentum must be conserved in either the up-conversion (fundamental to harmonic) or the down-conversion (harmonic to fundamental) process.

The conversion efficiency, E_{nl}, of a $\chi^{(2)}$-nonlinear crystal can be experimentally measured by characterising its single-pass conversion efficiency. The amount of second harmonic power, P_H, produced by the incident single-pass fundamental field, P_F, is measured as a function of crystal temperature to give $E_{nl} = P_H/P_F^2$. The nonlinear crystals employed in our experiment exhibit *quasi-phase matching* which is where alternating polarity regions of the birefringent crystal are electrostatically induced at manufacture. This structure in the crystal's refractive index is referred to as 'periodic poling' and serves to cyclically correct relative phase shifts between the fundamental and harmonic that may accumulate during the active region. The refractive indices of these regions are very sensitive to temperature. Therefore, there is a precise temperature at which maximal up- or down-conversion efficiency will be achieved.

2.5.3 Wavelength-scale v.s. side-band-scale nondegeneracy

In parametric down-conversion, a 'pump' beam at the harmonic frequency, ω_3, is down-converted into two fields of lower frequency at ω_1 and ω_2, where $\omega_1 + \omega_2 = \omega_3$. In preserving energy and momentum these down-converted photons are correlated in spatial, temporal, frequency, and polarisation degrees of freedom. Depending on the phase-matching conditions of the nonlinear medium used, the entangled photons may be *indistinguishable* and have the same polarisation, spatial mode and wavelength. This type of parametric down-conversion (PDC) is usually referred to as *degenerate* parametric down-conversion. For example, the pump beam at ω_3 is down-converted into two indistinguishable photons where $\omega_1 = \omega_2 = \omega_3/2$ [90, 91].

There is another category of parametric down-conversion where the entangled photons are *distinguishable*. For example, the down-converted pair could have completely different wavelengths, and follow from parametric down-conversion processes such as [96–98, 102, 219, 262]

$$\begin{aligned} &390\text{nm} \mapsto 521\text{nm} + 1550\text{nm} \\ &532\text{nm} \mapsto 810\text{nm} + 1550\text{nm} \\ &710\text{nm} \mapsto 1310\text{nm} + 1550\text{nm}. \end{aligned} \tag{2.109}$$

Systems that produce this type of PDC need two completely different sets of optics with different optical coatings to work with the down-converted beams because the

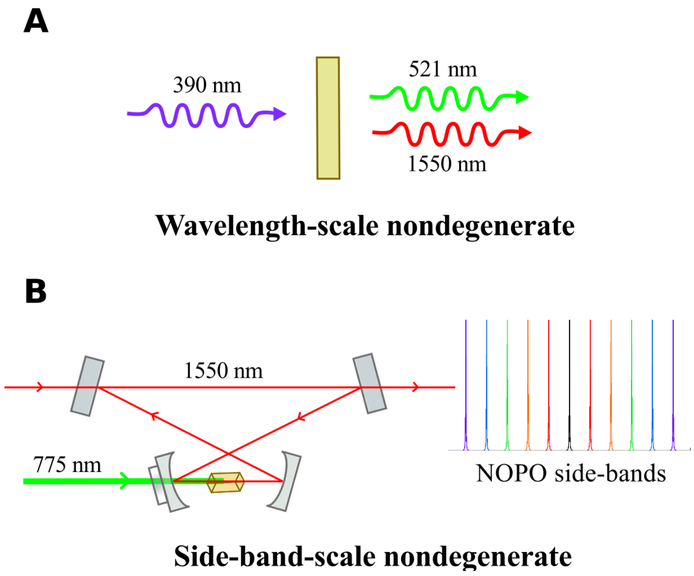

Figure 2.9: Comparison between A) wavelength-scale nondegenerate parametric down-conversion (WS-NPDC) and B) a side-band-scale nondegenerate optical parametric oscillator (SS-NOPO).

two wavelengths are in different regions of the electromagnetic spectrum. Therefore, this type of PDC can be referred to as *wavelength-scale nondegenerate PDC* (WS-NPDC) and is depicted in figure 2.9A.

There is another type of PDC which is usually referred to as degenerate even though this is not technically true. Consider the situation where a nonlinear crystal with a conversion bandwidth of 2 THz was manufactured to down-convert a 775 nm photon into two 1550 nm photons. According to the conservation of energy, there is an entire spectrum of down-converted photons with wavelengths ranging from 1542 nm to 1558 nm (i.e. within the crystal's conversion bandwidth) because a 775 nm photon could down-convert into two photons at *exactly* 1550 nm (truly *degenerate*) or into two photons at slightly different wavelengths, such as one photon at 1549 nm and the other at 1551 nm. This type of PDC has been previously demonstrated in a single-pass system where 394.5nm $\mapsto$ 789nm + 791nm [92]. Since the down-converted photons are at slightly different wavelengths they are distinguishable but the colours are not so different as to warrant the use of different optics. For that reason, this type of PDC is usually referred to as degenerate PDC even through this label is untrue.

The usual technique for generating a squeezed state is to use a nonlinear $\chi^{(2)}$-medium to produce 'degenerate' PDC. In continuous-wave experiments the $\chi^{(2)}$-material is commonly placed inside an optical cavity. An optical cavity consists of an arrangement of at least two mirrors which circulate the light in a closed path. The light inside the cavity can form a resonant field which amplifies the optical power. Since the strength of the $\chi^{(2)}$-nonlinearity scales with the optical power of the incident laser beam, a stronger beam results in more nonlinear behaviour. Placing a nonlinear crystal inside an optical cavity can amplify its nonlinear behaviour and lead to a higher up-conversion or down-conversion efficiency.

We know from classical optics that optical cavities have an infinite number (theoretically) of resonance frequencies defined by,

$$\omega_{cavity} = m\frac{2\pi c}{p} \tag{2.110}$$

where

$$m = 1, 2, 3, \ldots \tag{2.111}$$

and p is the round-trip path length of the cavity. Therefore the cavity will emit light at every resonance, and these frequencies are evenly spaced by the *free spectral range* (FSR) of the cavity, $\omega_s = 2\pi c/p$. This resonant behaviour of a cavity combined with the down-conversion bandwidth of the nonlinear crystal forms an *optical parametric oscillator* (OPO). An OPO will create a 'comb' of entangled frequency side-bands where the pump beam at ω_p is down-converted into light at $+\omega_s$ and $-\omega_s$ which are correlated symmetrically about the carrier at $\Omega_0 = \omega_p/2$, as shown in figure 2.9B. A typical cavity will have an FSR of a few hundred megahertz to a few gigahertz which means that if a pump photon at 775 nm is down-converted into the 1st FSR side-bands at ±515 MHz (as for our cavity) then the wavelengths of the down-converted photons are 1549.996 nm and 1550.004 nm. We shall refer to this type of nondegenerate system as a *side-band-scale nondegenerate optical parametric oscillator* (SS-NOPO).

2.5.4 Two-mode squeezed vacuum from a SS-NOPO

The two-mode squeezed vacuum state produced by a SS-NOPO for a particular pair of side-band frequencies, $\pm\omega_s$, where $+\omega_s$ is in mode a and $-\omega_s$ is in mode b, takes the form of

$$\begin{aligned}|\Psi\rangle_{SS-NOPO} &= \hat{S}(\xi)_{a,b}|0\rangle_a|0\rangle_b = \exp(\xi\hat{a}^\dagger\hat{b}^\dagger - \xi^*\hat{a}\hat{b})|0,0\rangle_{a,b} \\ &= \sum_{n=0}^{\infty}\alpha_{2n}|n\rangle_{+\omega_s}|n\rangle_{-\omega_s},\end{aligned} \tag{2.112}$$

where

$$\alpha_{2n} = \frac{1}{\cosh\xi}(\tanh\xi)^n. \tag{2.113}$$

Therefore the output state from a SS-NOPO can be expressed as

$$|\Psi\rangle_{SS-NOPO} = \sum_{m=0}^{\infty}\sum_{n=0}^{\infty} \alpha_{2n}|n\rangle_{+m\omega_s}|n\rangle_{-m\omega_s},$$

where m is the FSR number, ω_s is the FSR frequency for the cavity, n is the photon number, and $m = 0$ corresponds to the perfectly degenerate case at the carrier, Ω_0. The two-mode squeezed vacuum state for a pair of side-bands spaced by a single FSR (i.e. $m = 1$) can be simplified to

$$|\Psi\rangle_{SS-NOPO} \approx \alpha_0|0\rangle_{+\omega_s}|0\rangle_{-\omega_s} + \alpha_2|1\rangle_{+\omega_s}|1\rangle_{-\omega_s} + \alpha_4|2\rangle_{+\omega_s}|2\rangle_{-\omega_s} + \alpha_6|3\rangle_{+\omega_s}|3\rangle_{-\omega_s}, \tag{2.114}$$

where the Fock space of this equation has been truncated to $n = 3$. The fact that SS-NOPOs produce two-mode squeezed vacuum states with the modes consisting of the upper and lower side-bands has been known for decades [130]. However, due to the way standard homodyne detection measures a symmetric quantum state like squeezed vacuum, this nondegenerate output *looks* degenerate, as we shall show in chapters 3 and 4. We will show in the next chapter that we can no longer pretend a SS-NOPO is degenerate when we apply homodyne detection to an asymmetric quantum state, such as photon-subtracted two-mode squeezed vacuum. In fact it can be beneficial to remove the pretence and utilise the distinguishable frequency side-bands from a SS-NOPO.

2.6 Photon-subtracted state generation theory

Optical Schödinger cat states in the form of coherent state superpositions are experimentally challenging to produce. The coherent amplitude of the superposition state must be large ($\alpha \gg 1$) to make a true ‘cat’ state, which is difficult to generate as large coherent amplitude superpositions quickly decohere [263]. An alternative approach is to produce a state that is approximate to a small-amplitude cat state, called a ‘kitten’ state, by subtracting a single photon from squeezed vacuum. This photon-subtracted squeezed state is conditioned when a squeezed vacuum state is incident on a weakly reflecting beamsplitter and a photon is detected by a single-photon detector in the reflected field [207]. The detection of a single photon heralds the generation of the photon-subtracted state at the characterising detector (usually a homodyne detector) in the transmitted field. Hence these states are also referred to as ‘heralded states.’ The reflectivity of the beamsplitter is small in these experiments, which results in a low probability of more than one photon being removed. Dakna *et al* was the first to propose the concept of this ‘conditional measurement’

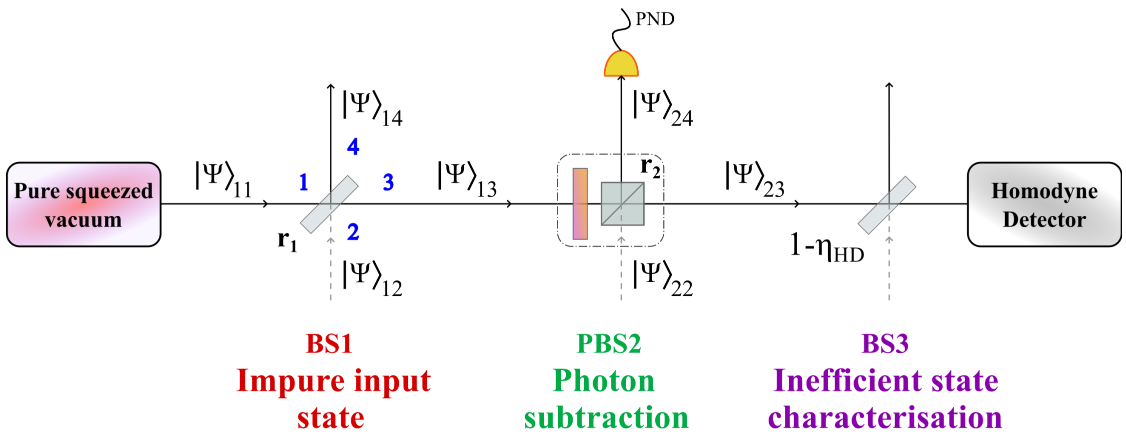

Figure 2.10: Schematic diagram of a theoretical model for Schrödinger kitten state generation with experimental imperfections. Label convention used to denote the input/output ports as '1-4' from a beamsplitter is illustrated. Note that $|\psi\rangle_{13}$ is both the output state from $BS1$ and the input state to $PBS2$. Grey beam: vacuum, BS: beamsplitter, PBS: polarising beamsplitter, PND: photon-number detector, r_1: intensity reflection coefficient of $BS1$ used to model loss, r_2: variable intensity reflection coefficient from combination half-wave plate and polarisation beamsplitter used to model the tap-off beamsplitter in a projected state experiment, η_{HD}: intensity transmission coefficient of $BS3$ used to model inefficient homodyne detection.

based on a lossless beamsplitter [207]. They developed a model by taking into account the squeezing level, beamsplitter transmission, photon-number detector inefficiency, and non-photon-number-resolving ability [207, 264, 265]. We will now discuss such a model based on photon-subtraction from a single-mode squeezed vacuum state.

A schematic diagram of a theoretical model for Schrödinger kitten state generation with experimental imperfections [227] is shown in figure 2.10. The model includes three parts: impure input state, photon subtraction, and inefficient state characterisation. We will use the following notation to denote the input and output states from the first two beamsplitters in the model: $|\psi\rangle_{jk}$ where $j = 1, 2$ denotes either the first beamsplitter, *BS1* ($j = 1$) or the second beamsplitter, *PBS2* ($j = 2$), and $k = 1, 2, 3, 4$ denotes specific beamsplitter input/output ports following the numbering convention illustrated in figure 2.10.

The input state $|\psi\rangle_{11}$ to the first beamsplitter *BS1* is a pure single-mode squeezed state. This beamsplitter has an intensity reflection coefficient of r_1 and represents a fictitious beamsplitter used to model optical loss in the experiment which results in an impure input state. Loss in a pure squeezed vacuum state manifests itself as the appearance of odd photon number components in the density matrix of the squeezed vacuum state. The output state $|\psi\rangle_{13}$ from *BS1* is the input state to the second stage of the model which simulates photon subtraction. This stage consists of a 'magic' beamsplitter composed of an arbitrarily tunable half-wave plate and a polarisation beamsplitter, *PBS2* [221,227]. The combination of half-wave plate and *PBS2* results in a variable intensity reflection coefficient, r_2. The output state $|\psi\rangle_{24}$ from *PBS2* is then detected by a photon-number detector, *PND*. Finally, an artificial beamsplitter, *BS3*, is used to model the inefficiency of the homodyne detector in the state characterisation stage.

Ideally, when an even (odd) number of photons are subtracted from a pure squeezed vacuum state, an even (odd) kitten with a negative Wigner function will be obtained. However, numerous factors can undermine the ability of such an experiment to produce a Wigner function with negativity. These factors include optical elements related to the experiment, such as the impurity of the input squeezed vacuum state, mode impurity before the *PND*, and inefficiency of the homodyne detector used to characterise the quantum state. Imperfections in the *PND* can further degrade the prepared state. Some examples of common detector imperfections are a high dark count probability, low quantum efficiency, and a non-photon-number-resolving ability of some detectors. Therefore, a quantitative analysis of all these imperfections can shed light on the practical generation of Schrödinger kitten states, particularly with regards to experiments at telecommunication wavelengths. We will now summarize a model outlined by Song *et al.* to analyse the impacts of these experimental parameters on the quality of Schrödinger kitten state generation.

2.6.1 Impure input state

Parametric down-conversion from a second-order $\chi^{(2)}$ nonlinear medium is an effective approach to generate squeezed vacuum states. As discussed in §2.2.4, a pure squeezed vacuum state consists of a photon number distribution with only even photon numbers. Impurity in the state contaminates the photon number distribution with odd photon number probabilities. This impurity can be equivalent to loss in a pure squeezed vacuum state, and can be described as a pure squeezed vacuum state defined by equation 2.54 followed by a beamsplitter, as shown in figure 2.10. Therefore, the total input state to *BS1* is written as

$$\begin{aligned}
|\Psi\rangle_{IN1} &= |\psi\rangle_{11} \otimes |\psi\rangle_{12} \\
&= \hat{S}_{11}(\xi)|0\rangle_{11}|0\rangle_{12} \\
&= \sum_{n=0}^{\infty} \beta_{2n}|2n\rangle_{11}|0\rangle_{12},
\end{aligned} \tag{2.115}$$

where β_{2n} is defined by equation 2.55. Using the definition 2.41, we get

$$|\Psi\rangle_{IN1} = \sum_{n=0}^{\infty} \frac{\beta_{2n}(\hat{a}_{11}^{\dagger})^{2n}}{\sqrt{(2n)!}}|0\rangle_{11}|0\rangle_{12}. \tag{2.116}$$

Applying the time symmetric beamsplitter matrix (2.76), $\hat{U}_t$, we can describe the total output state from *BS1* as

$$\begin{aligned}|\Psi\rangle_{OUT1} &= \hat{U}_t|\Psi\rangle_{IN1} \\ &= \sum_{n=0}^{\infty}\frac{\beta_{2n}}{\sqrt{(2n)!}}\left(\sqrt{r_1}\hat{a}^{\dagger}_{14}+\sqrt{t_1}\hat{a}^{\dagger}_{13}\right)^{2n}|0\rangle_{13}|0\rangle_{14},\end{aligned} \tag{2.117}$$

where t_1 is the intensity transmission coefficient and $r_1 + t_1 = 1$ for a lossless beamsplitter. The binomial theorem can be applied to expand equation 2.117 since $\hat{a}^{\dagger}_{13}$ and $\hat{a}^{\dagger}_{14}$ act on the same frequency mode and $[\hat{a}^{\dagger}, \hat{a}^{\dagger}] = 0$, giving

$$|\Psi\rangle_{OUT1} = \sum_{n=0}^{\infty}\sum_{k=0}^{2n}\beta_{2n}\sqrt{\frac{(2n)!}{k!(2n-k)!}}r_1^{\frac{k}{2}}t_1^{\frac{2n-k}{2}}|2n-k\rangle_{13}|k\rangle_{14}. \tag{2.118}$$

The density matrix $\hat{\rho}_{13}$ of the transmitted state $|\psi\rangle_{13}$ from *BS1* (i.e. the impure single-mode squeezed vacuum state) can be obtained by tracing the density matrix $\hat{\varrho}_{OUT1}$ of the overall output state $|\Psi\rangle_{OUT1}$ over mode *13* [266],

$$\begin{aligned}\hat{\rho}_{13} &= |\psi\rangle_{13}\,{}_{13}\langle\psi| \\ &= \mathrm{tr}_{13}\left[\hat{\varrho}_{OUT1}\right] \\ &= \sum_{n,b=0}^{\infty}\sum_{k=0}^{\min(2n,2b)}\sqrt{\frac{(2n)!(2b)!}{(2n-k)!(2b-k)!}}\frac{\beta_{2n}\beta_{2b}r_1^k t_1^{n+b-k}}{k!}|2n-k\rangle_{13}\,{}_{13}\langle 2b-k|,\end{aligned} \tag{2.119}$$

where

$$\hat{\varrho}_{OUT1} = |\Psi\rangle_{OUT1}\,{}_{OUT1}\langle\Psi|, \tag{2.120}$$

and tr[·] denotes the trace of a matrix. Figure 2.11 shows a comparison between a pure -5 dB squeezed vacuum state and an impure -5 dB squeezed vacuum state after 5% loss (i.e. $r_1 = 0.05$). Note the appearance of odd photon numbers in the impure squeezed vacuum state. The variance of an impure squeezed state is given by,

$$\begin{aligned}V^{\pm}_{imp} &= (1-r_1)V^{\pm}_{pure} + r_1 V^{\pm}_{vac} \\ &= (1-r_1)V^{\pm}_{pure} + r_1\end{aligned} \tag{2.121}$$

where $V^{\pm}_{imp}$ is the variance of the amplitude and phase quadratures of the impure squeezed state, $V^{\pm}_{pure}$ is the variance of the amplitude (V^{+}_{imp}) and phase (V^{-}_{imp}) quadratures of the pure squeezed state, and $V^{\pm}_{vac}$ is the variance of the vacuum state ($V^{\pm}_{vac} = 1$).

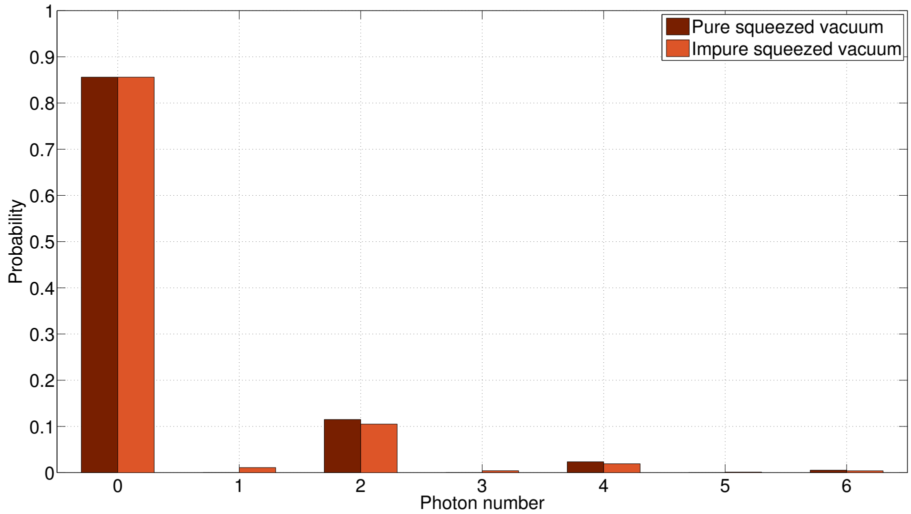

Figure 2.11: Theoretical photon number distributions of a pure squeezed vacuum state (-5 dB of squeezing) and an impure squeezed vacuum state (-5 dB of squeezing with $r_1 = 5\%$).

2.6.2 Conditional measurement based on lossless beamsplitter

According to the conditional beamsplitter operator defined in reference [264], we can express the output state $|\psi\rangle_{23}$ from *PBS2* in terms of the input state $|\psi\rangle_{13}$ as

$$|\psi\rangle_{23} = \frac{\hat{Y}|\psi\rangle_{13}}{\|\hat{Y}|\psi\rangle_{13}\|}, \tag{2.122}$$

where $\|\cdot\|$ denotes the magnitude of a state vector. The non-unitary conditional beamsplitter operator, $\hat{Y}$ is defined as

$$\begin{aligned} \hat{Y} &= {}_{24}\langle\psi|\hat{U}_r|\psi\rangle_{22} \\ &= \frac{T_2^{\hat{n}_{13}}(-R_2^*)^m(\hat{a}_{13})^m}{\sqrt{m!}}, \end{aligned} \tag{2.123}$$

where $|\psi\rangle_{22}$ ($|\psi\rangle_{24}$) is a single-port input (output) state for *PBS2*, respectively. T_2 (R_2) is the complex amplitude transmittance (reflectance) of *PBS2*, respectively, where $|R_2|^2 + |T_2|^2 = r_2 + t_2 = 1$. The number operator, $\hat{n}_{13}$, is defined as $\hat{n}_{13} = \hat{a}_{13}^\dagger\hat{a}_{13}$. This subscript notation follows the same notation scheme as used for the states where $\hat{n}_{jk} = \hat{a}_{jk}^\dagger\hat{a}_{jk}$ for $j = 1, 2$ and $k = 1, 2, 3, 4$. m is the number of detected photons by the *PND*. $\hat{U}_r$ is the standard representation of the rotation [SO(3), special orthogonal] group in three dimensions and is defined as [255]

$$\hat{U}_r = \exp\Big(-i(\phi_{T_2} - \phi_{R_2})\hat{L}_3\Big)\exp\Big(-i2\arccos(T_2)\hat{L}_2\Big)\exp\Big(-i(\phi_{T_2} + \phi_{R_2})\hat{L}_3\Big), \tag{2.124}$$

where ϕ_{T_2}, ϕ_{R_2} are the quantum mechanical counterparts to the classical Euler angles related to *PBS2*, and $\hat{L}_2, \hat{L}_3$ are angular momentum operators defined as

$$\begin{aligned}\hat{L}_2 &= \frac{1}{2i}\Big(\hat{a}_{13}^{\dagger}\hat{a}_{22} - \hat{a}_{22}^{\dagger}\hat{a}_{13}\Big) \\ \hat{L}_3 &= \frac{1}{2i}\Big(\hat{a}_{13}^{\dagger}\hat{a}_{22} - \hat{a}_{22}^{\dagger}\hat{a}_{13}\Big).\end{aligned} \tag{2.125}$$

Equation 2.124 can be rewritten as [264]

$$\hat{U}_r = T_2^{\hat{n}_{13}}\exp\Big(-R_2^*\hat{a}_{22}^{\dagger}\hat{a}_{13}\Big)\exp\Big(R_2\hat{a}_{13}^{\dagger}\hat{a}_{22}\Big)T_2^{-\hat{n}_{22}}. \tag{2.126}$$

Therefore

$$\begin{aligned}\hat{\rho}_{23}(m) &= |\psi\rangle_{23}\,{}_{23}\langle\psi| \\ &= \frac{t_2^{\frac{\hat{n}_{13}}{2}}\hat{a}_{13}^{m}\hat{\rho}_{13}\hat{a}_{13}^{\dagger m}t_2^{\frac{\hat{n}_{13}}{2}}}{\mathrm{tr}\Big[t_2^{\frac{\hat{n}_{13}}{2}}\hat{a}_{13}^{m}\hat{\rho}_{13}\hat{a}_{13}^{\dagger m}t_2^{\frac{\hat{n}_{13}}{2}}\Big]}.\end{aligned} \tag{2.127}$$

2.6.3 Impact of projecting detector's qualities on state preparation

State preparation with an ideal photon-number-resolving detector

In the case of an ideal photon-number-resolving detector (i.e. no dark counts and the quantum efficiency is 100%), we can obtain the projected state density matrix by substituting equation 2.119 into equation 2.127,

$$\begin{aligned}\hat{\rho}_{23}(m) &= |\psi\rangle_{23}\,{}_{23}\langle\psi| \\ &= \frac{\rho_A(m)}{\mathrm{tr}\Big[\rho_A(m)\Big]},\end{aligned} \tag{2.128}$$

where $\hat{\rho}_A(m)$ is the density matrix for a projected state generated with an ideal photon-number-resolving detector, which is defined as

$$\begin{aligned}\rho_A(m) = &\sum_{n=0}^{\infty}\sum_{b=0}^{\infty}\sum_{k=0}^{\min(2n,2b)-m}\frac{\beta_{2n}\beta_{2b}r_1^k r_2^m (t_1t_2)^{n+b-k}}{m!k!} \\ &\times\sqrt{\frac{(2n)!(2b)!}{(2n-k-m)!(2b-k-m)!}}|2n-k-m\rangle_{23}\,{}_{23}\langle 2b-k-m|.\end{aligned} \tag{2.129}$$

However, an ideal photon-number-resolving detector is unavailable in practical experiments. APDs are commonly used as photon-number detectors, where Si-APDs and InGaAs-APDs are used to detect near-infrared wavelengths (~ 860 nm) and telecommunication wavelengths (~ 1550 nm), respectively. Therefore, it is imperative to consider all possible imperfections of the photon-number detector, including the dark count probability, quantum efficiency, and the non-photon-number-resolving ability, and implement a quantitative analysis on the impact of all these experimental imperfections on the resultant quantum state.

State preparation with an imperfect photon-number-resolving detector

We will now discuss how to model the qualities of an imperfect photon-number-resolving detector, such as dark count probability, quantum efficiency, and non-photon-number-resolving ability.

Dark counts probability and quantum efficiency

On the one hand, the existence of dark counts causes 'false' clicks even if a photon is not actually subtracted. On the other hand, some actual clicks are missed due to the inefficiency of the detector. Therefore, m-click events may originate from $m-1, m-2, \ldots, 0$ or $m+1, m+2, \ldots$ actual photons being subtracted. Consequently, the conditional state is a statistical mixture, which can be expressed as [207, 227]

$$\hat{\rho}_B(m) = \sum_{k=0}^{\infty} Q(k|m)\hat{\rho}_{23}(k), \tag{2.130}$$

where $\hat{\rho}_B(m)$ is the density matrix for a projected state generated with an imperfect photon-number-resolving detector and $Q(k|m)$ is defined as the conditioned probability, with which m photons would have been subtracted, given that k photons are actually detected by the imperfect detector. According to the Bayes rule, we can obtain the conditional probability

$$Q(k|m) = \frac{P(m|k)S(k)}{P(m)}, \tag{2.131}$$

where

$$\begin{aligned} S(k) =& \sum_{n=k}^{\infty}\sum_{l=0}^{\infty}\sum_{b=0}^{\infty}\sum_{s=0}^{\min(2l,2b)} \beta_{2n}\beta_{2b} r_1^s t_1^{l+b-s} r_2^k t_2^{n-k} \sqrt{\frac{(2l)!(2b)!}{(2l-s)!(2b-s)!}} \\ &\times \frac{n!}{k!s!(n-k)!} \langle n|2l-s\rangle_{23\ 23}\langle 2b-s|n\rangle \end{aligned} \tag{2.132}$$

is the probability of k photons being subtracted, which is calculated based on [267] and

$$P(m|k) = \sum_{d=0}^{m} e^{-P_{dc}} \frac{(P_{dc})^d}{d!} \frac{k!\eta_{APD}^{m-d}(1-\eta_{APD})^{k-m+d}}{(m-d)!(k-m+d)!}, \tag{2.133}$$

where P_{dc} and η_{APD} are the dark count probability and quantum efficiency of the APD, respectively [268].

Non-photon-number-resolving ability

Most photon-number detectors used in experiments so far are on-off or non-photon-number-resolving detectors without the capability to distinguish the specific number of detected photons. A non-photon-number-resolving detector is different from a photon-number-resolving detector in that it accepts k clicks even though the actual number of clicks can be larger than k. Thus we have [227]

$$\hat{\rho}_C(m) = \sum_{k=m}^{\infty} \frac{Q(k)\hat{\rho}_B(k)}{\sum_{k=m}^{\infty} Q(k)}, \tag{2.134}$$

where $\hat{\rho}_C(m)$ is the density matrix for a projected state generated with an imperfect non-photon-number-resolving detector.

Mode purity of subtracted photons

The mode purity, $s^{'}$, is defined as the probability that the photons detected by the photon-number detector are mode matched to the local oscillator used in the kitten state characterisation via homodyne detection. As it is quite difficult to obtain a perfect mode purity, the detected density matrix of a projected state, $\hat{\rho}_{detect}$, would be a mixed state consisting of the actual projected state, $\hat{\rho}_{proj}$, and the unprojected state, $\hat{\rho}_{unproj}$ (i.e. the input state after experiencing loss from r_1 and r_2). Therefore, we have [211, 269]

$$\hat{\rho}_{detect} = s^{'}\hat{\rho}_{proj} + (1-s^{'})\hat{\rho}_{unproj}, \tag{2.135}$$

where $\hat{\rho}_{proj}$ could be $\hat{\rho}_A$ (density matrix for a projected state from an ideal photon-number-resolving detector), $\hat{\rho}_B$ (density matrix for a projected state from an imperfect photon-number-resolving detector), or $\hat{\rho}_C$ (density matrix for a projected state from an imperfect non-photon-number-resolving detector).

2.7 Inefficient homodyne detection

The optical homodyne detector efficiency can be calculated as [216, 221, 227]

$$\eta_{HD} = \eta_{QE} * \eta_t * \zeta^2, \tag{2.136}$$

where η_{QE} is the quantum efficiency of the two photodiodes in the homodyne detector, η_t is the propagation efficiency to the homodyne detector, and ζ is the interference visibility between the signal and local oscillator, denoting the degree of mode matching. Therefore the total efficiency, η_{HD}, quantifies various categories of loss. As shown in figure 2.10, the homodyne detection inefficiency can be simulated by a lossless beamsplitter before a perfect homodyne detector with transmission, η_{HD}, and the density matrix measured with an inefficient homodyne detector is given by [243]

$$\langle l|\hat{\rho}_{detect}(\eta_{HD})|n\rangle = \sum_{k=0}^{\infty} B_{l+k,l}(\eta) B_{l+k,l}(\eta) \langle l+k|\hat{\rho}_{detect}|n+k\rangle \tag{2.137}$$

in terms of the initial field density matrix, $\hat{\rho}_{detect}$, where

$$B_{l+k,l}(\eta) = \sqrt{\frac{(l+k)!}{k!l!}\eta_{HD}^{l}(1-\eta_{HD})^{k}} \tag{2.138}$$

2.7.1 η_{HD} affect on measured variance

Inefficient homodyne detection affects the level of detected squeezing and anti-squeezing from a squeezed state. For example, the variance of the output mode from an OPO for the anti-squeezed V^+ and squeezed V^- quadratures can be modelled as [152, 270, 271]

$$V^{\pm} = 1 \pm \left[\eta_{HD}\eta_{esc}\frac{4x}{(1 \mp x)^2 + 4\Omega^2}\right], \tag{2.139}$$

where Ω is the detuning parameter defined as the ratio between the measurement frequency (frequency shift away from FSR resonance, which is $\Omega = 0$ in our experiment) and the OPO cavity decay rate, which is defined as

$$\beta = \frac{c\Big[(1 - r_{oc}) + L\Big]}{p}, \tag{2.140}$$

and r_{oc} is the intensity reflection of the OPO output coupler mirror, L is the total intracavity loss, and p is the total cavity path length. η_{esc} is the OPO escape efficiency and x is a parameter related to the cavity, which are defined as

$$\eta_{esc} = \frac{1 - r_{oc}}{(1 - r_{oc}) + L} \tag{2.141}$$

$$x = \frac{P_{pump}}{P_{Th}}. \tag{2.142}$$

P_{pump} is the optical power of the second harmonic field ('pump'), and P_{Th} is the pump threshold power (i.e. the pump power at which the OPO reaches self-sustained oscillation) defined as

$$P_{Th} = \frac{\left[(1 - r_{oc}) + L\right]^2}{4E_{nl}} \tag{2.143}$$

The theoretical amount of classical parametric amplification, G_+, and attenuation, G_-, produced by an OPO is related to x

$$G_{\pm} = \frac{1}{1 \mp x}. \tag{2.144}$$

Therefore, given the other experimental parameters, equation 2.139 defines the minimum (maximum) amount of squeezing (anti-squeezing) that could be measured by a homodyne detector with efficiency η_{HD}. If $\eta_{HD} < 1$ then the measured variance of the squeezed quadrature will be higher (i.e. less squeezing) than the theoretical minimum defined by equation 2.139 for $\eta_{HD} = 1$.

2.7.2 Modelling electronic noise as poor quantum efficiency

All homodyne detectors are subject to non-desirable *electronic noise*, which includes a range of noise such as ambient noise, dark current noises from the detector's photodiodes, and the intrinsic noise of components in the detector's electronic circuit. Another source of noise is the electronic noise floor of the instrument being used to measure the homodyne detector signal. Kumar *et al.* have shown that the detection efficiency of a homodyne detector depends not only on detector characteristics, defined by η_{HD}, but also on the measurement conditions. A high enough noise level in the measurement conditions can affect the homodyne detection efficiency, and therefore affect the amount of measured squeezing. This concept that a raised electronic noise floor can be modelled as poor quantum efficiency can be quantified by defining a frequency-dependent *electronic* homodyne detection efficiency, $\eta_e(f)$, as [272]

$$\eta_e(f) = 1 - \frac{\langle \hat{Q}_e^2 \rangle}{\langle \hat{Q}_{meas}^2 \rangle}, \tag{2.145}$$

where Q_e represents the added noise to the measurement of the field quadrature, Q_{meas}. This electronic detection efficiency is related to the *shot noise* level of the measurement conditions, which corresponds to the noise level determined by the local oscillator's optical intensity as

$$\eta_e(f) = 1 - \frac{P_{dark}(f)}{P_{shot}(f)}, \tag{2.146}$$

where $P_{dark}(f)$ ($P_{shot}(f)$) is the power spectral density of the electronic (shot) noise at frequency, f. Ideally we would want $P_{dark}(f) \ll P_{shot}(f)$ such that $\eta_e(f) \approx 1$. However, as we will show in chapter 5, this is sometimes not possible and the measurement of a quantum state can be corrupted due to a raised electronic noise level from data aliasing affects.

2.8 Optical quantum state tomography

2.8.1 Maximum likelihood estimation

A common challenge in experimental science is estimating a model that best describes the underlying structure of the system under observation. A standard technique used to overcome this challenge is called the *maximum likelihood* method. Usually a functional relationship between the independent and dependent variables of the system are known or can be assumed where $y = f(x_1, x_2, \ldots)$ and y is the variable being measured. This model will depend on one or more parameters, $\mathbf{s}$, where $y = f(x_1, x_2, \ldots; \mathbf{s})$ and the set of observations of the system $\{y_i\}$ can be used to estimate the parameters $\mathbf{s}$. If a specified model and known parameters are given then it is straightforward to calculate the probability for an observed outcome to happen by $\mathrm{pr}(\{y_i\}|\mathbf{s})$. However, if only the observations are known and the parameters $\mathbf{s}$ are unknown then the probability becomes a function that depends on both the observations and a range of possible parameter values called the likelihood function:

$$L(\mathbf{s}) \equiv \mathrm{pr}(\{y_i\}|\mathbf{s}). \tag{2.147}$$

The basis of the maximum likelihood method is that with no other a priori information about the system other than the observed data set $\{y_i\}$, the parameters that are most likely correct are the ones that maximise the likelihood function. The parameters $\mathbf{s}_0$ which maximise the likelihood are called the *maximum likelihood (MaxLik) estimator*. The familiar least-squares method of parameter estimation is in fact just a special case of maximum likelihood estimation. This method of parameter estimation is only relevant under the assumption that the measurement outcomes are independent and normally distributed [273].

The total probability outcome for a system where the data samples $\{y_i\}$ are independent and identically distributed is given by the product of the probabilities of the individual samples. For this reason it is common to use the logarithm of the likelihood since the product turns into a sum without changing the location of the maximum,

$$\ln L(\mathbf{s}) = \ln \prod_i \mathrm{pr}(\{y_i\}|\mathbf{s}) = \sum_i \ln \mathrm{pr}(\{y_i\}|\mathbf{s}). \tag{2.148}$$

The maximisation of this function can be conducted using various techniques, such as the iterative expectation-maximisation algorithm [274]. Generally a variation of this algorithm is used to carry out parameter estimation with maximum likelihood in most quantum state applications.

2.8.2 MaxLik applied to homodyne tomography

We can estimate which quantum states of light are generated by our experiment by using the maximum likelihood method which was previously applied to quantum state reconstruction by Lvovsky [245]. We will follow the form presented by Lvovsky [245] and summarized by Neergaard-Nielsen [275]. One of the reasons this method can be applied to quantum optics experiments is that the generated state can be sampled a large number of times and these samples are independent and identically distributed. Each sample corresponds to a homodyne measurement of the experimental state for a particular measurement angle where this state can be continuously generated under the same experimental conditions. The sample distribution is determined by the density matrix through equation 2.22. Therefore the density matrix can be estimated through the maximum likelihood method where the parameters **s** are the matrix entries. The Wigner function can then be calculated from the density matrix that maximises the likelihood function. This technique has been referred to as *homodyne tomography* due to its similarities to medical tomographic imaging where 2D projections are taken at various angles and used to create a 3D model.

The continuous-valued outcomes from the homodyne measurements have to be binned to discretize the data. The probability of detecting a particular quadrature value $\hat{X}^{\theta}$ for a density matrix $\hat{\rho}$ (whether its the state's actual density matrix or one estimated by this technique) within the jth bin is

$$\begin{aligned} \mathrm{pr}_{\theta,j} &= \int_{q_j}^{q_{j+1}} \mathrm{pr}(X_\theta) dX_\theta \\ &= \int_{q_j}^{q_{j+1}} \mathrm{tr}\Big[|X_\theta\rangle\langle X_\theta|\hat{\rho}\Big] dX_\theta \\ &= \mathrm{tr}\Big[\hat{\Pi}_{\theta,j}\hat{\rho}\Big], \end{aligned} \tag{2.149}$$

where

$$\hat{\Pi}_{\theta,j} = \int_{q_j}^{q_{j+1}} |X_\theta\rangle\langle X_\theta| dX_\theta \tag{2.150}$$

is the projection operator for the jth bin. The sum of the probabilities and projectors for a specific measurement angle equals unity/identity if the bins cover the entire range of X_θ values,

$$\begin{aligned}\sum_j \mathrm{pr}_{\theta,j} &= 1 \qquad (2.151)\\ \sum_j \hat{\Pi}_{\theta,j} &= \hat{\mathrm{I}}.\end{aligned}$$

The likelihood function in terms of the density matrix $\hat{\rho}$ for $N_{\theta,j}$ observations in the jth bin is

$$\begin{aligned}\ln L(\hat{\rho}) &= \ln \prod_{\theta,j} \mathrm{pr}_{\theta,j}^{N_{\theta,j}} \qquad (2.152)\\ &= \sum_{\theta,j} N_{\theta,j} \ln \mathrm{pr}_{\theta,j}.\end{aligned}$$

This equation assumes the quadrature phase angle is kept constant while $\hat{X}_\theta$ is sampled a number of times before the angle is adjusted to a new value and the measurement is repeated. The $\sum_\theta$ denotes the summation over all sampled measurement phase angles. In our measurement procedure we allow the LO phase to randomly wander, which is a technique previously demonstrated [206, 276, 277]. The measurement angle is then determined during post-processing of the data based on measured experimental parameters, which will be further explained in chapter 4. It is important to ensure a sufficient number of measurement angles were used in order to avoid a low azimuthal resolution of the reconstructed Wigner function. For each set of measurement angles there is an entire corresponding quadrature distribution $\mathrm{pr}(X_\theta)$ and set of projectors $\{\hat{\Pi}_j\}$.

To find the ensemble $\hat{\rho}$ that maximises the likelihood function we must introduce the operator

$$\hat{R}(\hat{\rho}) \equiv \sum_\theta \frac{N_\theta}{N} \sum_j \frac{f_{\theta,j}}{\mathrm{pr}_{\theta,j}} \hat{\Pi}_{\theta,j}, \qquad (2.153)$$

where $f_{\theta,j}$ is the frequency of observations in the jth bin within the θ phase angle measurement. Note that according to definition 2.153 the distribution ρ_0 which is most likely to produce the observed data set must have its probabilities equal to the measured frequencies in all bins. As outlined in several papers [245, 278, 279], the solution to the extremal equation $\hat{R}(\hat{\rho}_0)\hat{\rho}_0 = \hat{\rho}_0$, which is equivalent to

$$\hat{R}(\hat{\rho}_0)\hat{\rho}_0\hat{R}(\hat{\rho}_0) = \hat{\rho}_0, \qquad (2.154)$$

can be found by an iterative method that can be seen as a special case of the classical expectation-maximisation algorithm [274]. Beginning from an initial guess, $\hat{\rho}^{(0)}$, the iteration continues as

$$\hat{\rho}^{(k+1)} = \mathcal{N}[\hat{R}(\hat{\rho}^{(K)})\hat{\rho}^{(K)}\hat{R}(\hat{\rho}^{(K)})], \tag{2.155}$$

where $\mathcal{N}$ denotes normalization to a unitary trace. Each step in the iteration will monotonically increase the likelihood associated with the current density matrix estimate and converge towards the fixed point $\hat{\rho}_0$. The iterations were terminated once the incremental changes to the estimated density matrix fell below an arbitrarily defined threshold given by

$$\Delta\hat{\rho} = \sum_{m,n} \left| \hat{\rho}_{mn}^{(n)} - \hat{\rho}_{mn}^{(n-1)} \right|. \tag{2.156}$$

The reconstructed density matrix is conveniently in the number state basis, where the matrix representation of the projection operator is given by

$$(\hat{\Pi}_{\theta,j})_{mn} = \int_{q_j}^{q_{j+1}} \langle m|X_\theta\rangle\langle X_\theta|n\rangle dX_\theta, \tag{2.157}$$

with $\langle m|X_\theta\rangle$ defined in equation 2.23. It is necessary to truncate the infinite Hilbert space to dimension $M+1$ where M is the maximal photon number. The choice of M must be large enough to include all photon numbers that may contribute to the state.

2.8.3 Correcting for imperfect homodyne efficiency

A significant advantage to the maximum likelihood method is its ability to explicitly include imperfect detection efficiency in the algorithm [245, 280]. As discussed in §2.7, it is common to model detection efficiency η_{HD} by a fictitious beamsplitter with transmittance η_{HD} before the homodyne detection set-up (figure 2.10). This non-unity efficiency can be incorporated into the reconstruction algorithm by exchanging the projection operator $\hat{\Pi}_{\theta,j}$ with an element of a POVM (positive operator-valued measure). A POVM is a set $\{\hat{E}_m\}$ of positive operators fulfilling the completeness relation $\sum_m \hat{E}_m = \hat{\mathrm{I}}$. Therefore we get

$$\hat{E}_{\theta,j}(\eta_{HD}) = \sum_{m,n,k} \sqrt{B_m^{m+k}(\eta_{HD})B_n^{n+k}(\eta_{HD})} \int_{q_j}^{q_{j+1}} dX_\theta \langle n|X_\theta\rangle\langle X_\theta|m\rangle|n+k\rangle\langle m+k|, \tag{2.158}$$

where

$$B_m^{m+k} = \sqrt{\binom{m+k}{m} \eta^m (1-\eta)^k}.$$

The summation of m and n runs from 0 to the truncation number M, and k from 0 to M-max(m, n). This operator now represents a detection event in the (θ, j) bin by an η_{HD}-efficiency detector. Therefore, the non-unity efficiency is incorporated into the reconstruction algorithm by exchanging the projection operator $\hat{\Pi}_{\theta,j}$ with $\hat{E}_{\theta,j}(\eta_{HD})$ everywhere it appeared in the previous discussion. This iteration algorithm will directly reconstruct the state $\hat{\rho}_{\eta_{HD}=1}$ before the imperfect detector.

Chapter 3

Theory of SS-NOPO state generation

The true sign of intelligence is not knowledge but imagination.
Albert Einstein

In this chapter a frequency-resolved measurement operator is applied to a two-mode squeezed vacuum state generated by a side-band-scale nondegenerate optical parametric oscillator (SS-NOPO). We will show that a rotation operation occurs on these two-modes if the measurement technique cannot distinguish between the upper and lower side-bands. This operation rotates the measurement basis which results in the two-mode state becoming two separable single-mode squeezed vacuum states. These single-mode states are *indistinguishable* due to their symmetry. It is because of this property that the two-mode squeezed vacuum state produced by a SS-NOPO is often treated as degenerate and therefore *single*-mode. We will show that standard homodyne detection cannot distinguish between these two single-mode states, and also cannot choose which state to characterise. Therefore this technique returns a measurement that is indistinguishable from a single-mode squeezed vacuum state.

We will then illustrate that a new measurement technique is required to fully characterise each single-mode state if the symmetry between the states is broken so that the two single-mode states become *distinguishable*. We will discuss how applying a measurement-induced nonlinearity such as photon-subtraction to a two-mode squeezed vacuum state will result in two *independent and distinguishable* quantum states. Thus producing a photon-subtracted squeezed vacuum state *and* a squeezed vacuum state in a *single* optical mode.

3.1 Two-mode squeezed vacuum

Parametric down-conversion is a well-known technique for generating entangled pairs of photons [84]. These down-converted photons will be correlated in spatial, temporal, frequency, and polarisation degrees of freedom. Since the two fields originated from the second harmonic pump field, they will also be quadrature-correlated and can form a two-mode squeezed state. The two-mode structure of the photons can take numerous forms. The down-converted photons could have orthogonal polarisations, or exit the nonlinear medium in distinguishable spatial modes. Another common form of nondegeneracy is *wavelength-scale* nondegenerate parametric down-conversion (WS-NPDC) in which the photons are created at wavelengths that may differ by tens to hundreds of nanometres (e.g. a 532 nm photon down-converting into a 810 nm photon and 1550 nm photon).

In §2.5.3 we introduced the concept of a side-band-scale nondegenerate optical parametric oscillator (SS-NOPO). It has been well established that a two-mode squeezed vacuum (twin-beam) state can be generated by a $\chi^{(2)}$-nonlinear medium inside an optical cavity [130, 281–290]. The two-mode structure can take the form of upper and lower frequency side-bands correlated symmetrically about the optical carrier. These side-bands could be separated by only a few kilohertz to megahertz above and below the optical carrier frequency Ω_0 (e.g. $\Omega_0 \pm 1$ MHz) and therefore be within the 'baseband' linewidth of the cavity centred on the carrier. Often the squeezed vacuum state produced by a SS-NOPO is investigated in this baseband frequency range. Since an optical cavity has multiple resonance frequencies (spaced by the free-spectral range, FSR), the down-converted photons could also exist at side-bands evenly spaced by an FSR frequency, which is usually in the range of megahertz to gigahertz above and below the carrier. Due to the way in which homodyne detection probes both the upper and lower side-bands simultaneously, and the fact that the wavelengths of the photons only differ by a fraction of a nanometre, the SS-NOPO output state is often treated as degenerate and single-mode.

We will show that this is 'allowed' since the standard homodyne detection technique returns a measurement result that is indistinguishable from a single-mode squeezed vacuum state. In this way, homodyne detection can be interpreted as measuring a two-mode state in a rotated measurement basis in which the state becomes two separable single-mode states. For the case of two-mode squeezed vacuum, these two states are both single-mode squeezed vacuum states that are indistinguishable.

However, this standard detection technique is no longer adequate when the degeneracy from a SS-NOPO breaks down and the two single-mode states become distinctly different (e.g. a non-Gaussian and a Gaussian state). Therefore, the upper and lower frequency side-bands produced by a SS-NOPO should be thought of as forming a two-mode state. A new measurement technique must be utilised that can individually access and characterise *either* single-mode state in this rotated basis. This measurement technique involves frequency-resolved homodyne detection and was first introduced by Ralph *et al.* [291]. We will explicitly show that having access to the frequency demodulation *phase* allows state reconstruction of either single-mode side-band state.

3.1.1 Decomposition of two-mode squeezed vacuum state

As we discussed in §2.5.3, a pure two-mode squeezed vacuum state can be described by [263, 292]

$$\begin{aligned}|\Psi\rangle_{a,b} &= \hat{S}(\xi)_{a,b}|0\rangle_a|0\rangle_b \\ &= \exp(\tanh(\xi)\hat{a}^\dagger\hat{b}^\dagger)(\cosh\xi)^{-(\hat{a}^\dagger\hat{a}+\hat{b}^\dagger\hat{b}+1)}\exp(\tanh(\xi)\hat{a}\hat{b})|0,0\rangle_{a,b} \\ &= \sum_{n=0}^{\infty}\alpha_{2n}|n,n\rangle_{a,b},\end{aligned} \tag{3.1}$$

where α_{2n} is defined by equation 2.113. The measurement result from separately characterising one mode demonstrates that modes a and b are entangled. If mode a is isolated and measured, the properties of its state will no longer have the photon statistics of a squeezed vacuum state. Direct measurement of mode a or b results in lost correlation between the entangled modes, causing the measured state to be indistinguishable from a thermal state [251, 293, 294]. We can see this result by taking the partial trace over mode a in equation 3.1, which calculates the photon number distribution in mode a

$$\begin{aligned}P^{(a)} &= \mathrm{tr_b}\Big[\hat{S}(\xi)|0,0\rangle_{a,b}\,{}_{a,b}\langle 0,0|\hat{S}^\dagger(\xi)\Big] \\ &= \mathrm{tr_b}\Big[\frac{1}{\cosh^2\xi}\sum_{n=0}^{\infty}\sum_{m=0}^{\infty}(\tanh\xi)^{n+m}|n,n\rangle_{a,b}\,{}_{a,b}\langle m,m|\Big] \\ &= \frac{1}{\cosh^2\xi}\sum_{n,m=0}^{\infty}(\tanh\xi)^{n+m}\;{}_b\langle m|n\rangle_b\;|n\rangle_a\,{}_a\langle m| \\ &= \frac{1}{\cosh^2\xi}\sum_{n,m=0}^{\infty}(\tanh\xi)^{n+m}\delta_{nm}|n\rangle_a\,{}_a\langle m| \\ &= \frac{1}{\cosh^2\xi}\sum_{n=0}^{\infty}(\tanh\xi)^{2n}|n\rangle_a\,{}_a\langle n|,\end{aligned} \tag{3.2}$$

which is a thermal state with $\langle n\rangle = \sinh^2\xi$. Measuring a thermal state by measuring one half of an entangled pair has been experimentally demonstrated in two-mode squeezed vacuum states generated from nondegenerate PDC [284,289,295]. However, single-mode squeezed vacuum states can be retrieved from the two-mode state if a mode-mixing operation is applied to the state before detection [289, 296]. For example, if modes a and b were spatial modes they could be optically mixed on a beamsplitter and the outputs would be in spatial modes c and d, which are defined as

$$\hat{c} = \frac{\hat{a} + \hat{b}}{\sqrt{2}}, \;\; \hat{d} = \frac{\hat{a} - \hat{b}}{\sqrt{2}}.$$

Homodyne detection of modes c and d results in two single-mode squeezed vacuum states with opposite squeezed quadratures. This result can be explained by expressing the two-mode squeezing operator in the rotated c, d basis as

$$\exp(\xi \hat{a}^\dagger \hat{b}^\dagger - \xi^* \hat{a}\hat{b}) = \exp\left(\frac{\xi}{2}\hat{c}^{\dagger 2} - \frac{\xi^*}{2}\hat{c}^2\right)\exp\left(-\frac{\xi}{2}\hat{d}^{\dagger 2} + \frac{\xi^*}{2}\hat{d}^2\right). \tag{3.3}$$

Therefore, the two-mode squeezing operator can be written as a product of two single-mode squeezing operators in the rotated basis [292]. Furthermore, the two-mode squeezed vacuum state becomes a product state of two single-mode squeezed vacuum states in this rotated basis

$$|\Psi\rangle_{a,b} = |\Psi\rangle_c |\Psi\rangle_d, \tag{3.4}$$

where

$$|\Psi\rangle_c = \sum_{n=0}^{\infty} \beta_{2n} |2n\rangle_c, \;\; |\Psi\rangle_d = \sum_{n=0}^{\infty} \beta_{2n} |2n\rangle_d.$$

$|\Psi\rangle_c$ and $|\Psi\rangle_d$ are single-mode squeezed vacuum states that are amplitude and phase quadrature squeezed, respectively, and β_{2n} is defined in equation 2.55. This result applies for modes of any kind, not just spatial modes and just relies on a rotation operation to move between the $\{a, b\}$ and $\{c, d\}$ bases.

3.1.2 Measuring squeezed vacuum side-band modes

The Einstein-Podolsky-Rosen (EPR) entanglement that exists between the upper and lower FSR side-bands generated by a SS-NOPO have been theoretically and experimentally investigated [99, 164, 168]. Therefore, a similar mode-mixing operator must be performed on the correlated frequency side-bands in order to retrieve the single-mode squeezed vacuum states. However, optical frequency-mixing can be experimentally challenging and damaging to fragile quantum states [297]. Luckily, the standard technique for characterising optical quantum states, homodyne detection, *automatically* performs this mixing operation on the upper and lower frequency side-bands, and can therefore be thought of as measuring in the c, d-basis. We will now summarise a measurement technique that combines homodyne detection with frequency demodulation to allow access to a single-mode state in the c, d-basis at a particular side-band frequency, ω_s.

We first define the following Hermitian operator that represents the observable measured by an ideal homodyne detector [291]

$$\hat{X}(\theta, t) = e^{-i\theta}\hat{a}(t) + e^{i\theta}\hat{a}^\dagger(t) = \int_{-\infty}^{\infty} d\omega e^{i\omega t}[e^{-i\theta}\hat{a}(\omega) + e^{i\theta}\hat{a}^\dagger(-\omega)], \tag{3.5}$$

where θ is the optical phase difference between the local oscillator and the signal field to be measured. We can isolate a pair of side-bands at a particular frequency, ω_s, from the homodyne signal by multiplying $\hat{X}(\theta, t)$ with a cosine at frequency ω_s, and doing a time integration. First we note that the time domain $\hat{a}(t)$ and frequency domain $\hat{a}(\omega)$ annihilation operators are Fourier transform pairs:

$$\hat{a}(t) = \int_{-\infty}^{\infty} \hat{a}(\omega)e^{i\omega t}d\omega \tag{3.6}$$

$$\hat{a}(\omega_s) = \int_{-\infty}^{\infty} \hat{a}(t)e^{-i\omega_s t}dt \tag{3.7}$$

$$\hat{a}(-\omega_s) = \int_{-\infty}^{\infty} \hat{a}(t)e^{i\omega_s t}dt. \tag{3.8}$$

According to the Fourier transforms defined in equations 3.6-3.8, we have

$$\hat{a}^\dagger(t) = \int_{-\infty}^{\infty} \hat{a}^\dagger(-\omega)e^{i\omega t}d\omega \tag{3.9}$$

$$\hat{a}^\dagger(\omega_s) = \int_{-\infty}^{\infty} \hat{a}^\dagger(t)e^{i\omega_s t}dt \tag{3.10}$$

$$\hat{a}^\dagger(-\omega_s) = \int_{-\infty}^{\infty} \hat{a}^\dagger(t)e^{-i\omega_s t}dt. \tag{3.11}$$

We can relate $\hat{a}(\omega)$ to $\hat{a}(\omega_s)$ by substituting equations 3.6 into equation 3.7, and substituting equation 3.9 into equation 3.10 to give

$$\hat{a}(\omega_s) = \int\int \hat{a}(\omega)e^{i(\omega-\omega_s)t}d\omega dt \tag{3.12}$$

$$\hat{a}^\dagger(\omega_s) = \int\int \hat{a}^\dagger(-\omega)e^{i(\omega+\omega_s)t}d\omega dt. \tag{3.13}$$

Similar expressions are found for $\hat{a}(-\omega_s)$ and $\hat{a}^\dagger(-\omega_s)$. Therefore, a signal at frequency ω_s can be isolated from the homodyne data by

$$\begin{aligned}\hat{X}_{\omega_s}(\theta,\phi) &= \int dt\cos(\omega_s t+\phi)\hat{X}(\theta,t) \\ &= \int\int\frac{1}{2}\Big\{e^{i(\omega+\omega_s)t}\Big[e^{-i(\theta-\phi)}\hat{a}(\omega)+e^{i(\theta+\phi)}\hat{a}^\dagger(-\omega)\Big] \\ &\quad + e^{i(\omega-\omega_s)t}\Big[e^{-i(\theta+\phi)}\hat{a}(\omega)+e^{i(\theta-\phi)}\hat{a}^\dagger(-\omega)\Big]\Big\}d\omega dt,\end{aligned} \tag{3.14}$$

where ϕ is the rf demodulation phase. Solving equation 3.14 by utilising equation 3.12 and equation 3.13 gives [291]:

$$\hat{X}_{\omega_s}(\theta,\phi) = \frac{1}{2}\Big[e^{-i(\theta+\phi)}\hat{a}_{+\omega_s}+e^{i(\theta+\phi)}\hat{a}^\dagger_{+\omega_s}+e^{-i(\theta-\phi)}\hat{a}_{-\omega_s}+e^{i(\theta-\phi)}\hat{a}^\dagger_{-\omega_s}\Big]. \tag{3.15}$$

This measurement operator can be experimentally implemented by combining high-frequency homodyne detection with frequency demodulation. We will now show that applying this measurement technique to the two-mode squeezed vacuum state generated by a SS-NOPO allows us to extract two single-mode squeezed vacuum states from the homodyne signal.

3.1.3 Symmetric & anti-symmetric basis

We define the symmetric and anti-symmetric side-band modes at a particular side-band frequency ω_s in terms of the upper and lower side-bands:

$$\hat{a}_S = \frac{1}{\sqrt{2}}\Big[\hat{a}_{+\omega_s}+\hat{a}_{-\omega_s}\Big] \tag{3.16}$$

$$\hat{a}_A = \frac{1}{\sqrt{2}}\Big[\hat{a}_{+\omega_s}-\hat{a}_{-\omega_s}\Big]. \tag{3.17}$$

We can use these definitions to transform equation 2.114 into the symmetric/anti-symmetric (S,A) basis:

$$\begin{aligned}|\Psi\rangle_{SS-NOPO} &= \alpha_0|0\rangle_S|0\rangle_A+\frac{\alpha_2}{\sqrt{2}}\Big[|2\rangle_S|0\rangle_A-|0\rangle_S|2\rangle_A\Big] \\ &+\frac{\alpha_4}{4}\Big[\sqrt{6}|4\rangle_S|0\rangle_A-2|2\rangle_S|2\rangle_A+\sqrt{6}|0\rangle_S|4\rangle_A\Big] \\ &+\frac{\alpha_6}{\sqrt{48}}\Big[\sqrt{15}|6\rangle_S|0\rangle_A-3|4\rangle_S|2\rangle_A+3|2\rangle_S|4\rangle_A-\sqrt{15}|0\rangle_S|6\rangle_A\Big].\end{aligned} \tag{3.18}$$

Substituting the α-coefficients of a pure two-mode squeezed vacuum state (equation

2.113) into equation 3.18 gives

$$\begin{aligned}|\Psi\rangle_{SS-NOPO} =\; & \frac{1}{\cosh\xi}|0\rangle_S|0\rangle_A + \frac{\tanh\xi}{\sqrt{2}\cosh\xi}\Big[|2\rangle_S|0\rangle_A - |0\rangle_S|2\rangle_A\Big] \\ & + \frac{(\tanh\xi)^2}{\cosh\xi}\Big[\frac{\sqrt{6}}{4}|4\rangle_S|0\rangle_A - \frac{1}{2}|2\rangle_S|2\rangle_A + \frac{\sqrt{6}}{4}|0\rangle_S|4\rangle_A\Big] \\ & + \frac{(\tanh\xi)^3}{\cosh\xi}\Big[\sqrt{\frac{5}{16}}|6\rangle_S|0\rangle_A - \sqrt{\frac{3}{16}}|4\rangle_S|2\rangle_A + \sqrt{\frac{3}{16}}|2\rangle_S|4\rangle_A - \sqrt{\frac{5}{16}}|0\rangle_S|6\rangle_A\Big].\end{aligned} \tag{3.19}$$

This result is equivalent to the product of two single-mode squeezed vacuum states

$$|\Psi\rangle_{SS-NOPO} = |\Psi\rangle_S|\Psi\rangle_A, \tag{3.20}$$

where

$$\begin{aligned}|\Psi\rangle_S &\approx \beta_0|0\rangle_S - \beta_2|2\rangle_S + \beta_4|4\rangle_S - \beta_6|6\rangle_S \\ |\Psi\rangle_A &\approx \beta_0|0\rangle_A + \beta_2|2\rangle_A + \beta_4|4\rangle_A + \beta_6|6\rangle_A,\end{aligned} \tag{3.21}$$

and β_{2n} is defined in equation 2.55. $|\Psi\rangle_S$ and $|\Psi\rangle_A$ are amplitude and phase-squeezed single-mode states in the symmetric and anti-symmetric modes, respectively, at a single FSR frequency, $\pm\omega_s$. We can transform our measurement operator, $\hat{X}_{\omega_s}(\theta,\phi)$, into this rotated basis:

$$\hat{X}_{\omega_s}(\theta,\phi) = \frac{1}{2}\Big[e^{-i(\theta+\phi)}(\hat{a}_S+\hat{a}_A)+e^{i(\theta+\phi)}(\hat{a}_S^\dagger+\hat{a}_A^\dagger)+e^{-i(\theta-\phi)}(\hat{a}_S-\hat{a}_A)+e^{i(\theta-\phi)}(\hat{a}_S^\dagger-\hat{a}_A^\dagger)\Big]. \tag{3.22}$$

We simplify equation 3.22 and define $\hat{X}_{S,A}(\theta,\phi)$ as the equivalent measurement operator of $\hat{X}_{\omega_s}(\theta,\phi)$ in this rotated basis:

$$\hat{X}_{S,A}(\theta,\phi) = \hat{X}_{\omega_s}(\theta,\phi) = \cos\phi\hat{X}_S(\theta) + \sin\phi\hat{X}_A(\theta+\pi/2), \tag{3.23}$$

where

$$\begin{aligned}\hat{X}_S(\theta) &= e^{-i\theta}\hat{a}_S + e^{i\theta}\hat{a}_S^\dagger \\ \hat{X}_A(\theta+\pi/2) &= -\,i(e^{-i\theta}\hat{a}_A - e^{i\theta}\hat{a}_A^\dagger).\end{aligned} \tag{3.24}$$

Therefore,

$$\begin{aligned}&{}_{SS-NOPO}\langle\Psi|\hat{X}_{\omega_s}(\theta,\phi)|\Psi\rangle_{SS-NOPO} \\ &\equiv {}_S\langle\Psi|\,{}_A\langle\Psi|\hat{X}_{S,A}(\theta,\phi)|\Psi\rangle_S|\Psi\rangle_A \\ &= {}_S\langle\Psi|\,{}_A\langle\Psi|\Big(\cos\phi\hat{X}_S(\theta) + \sin\phi\hat{X}_A(\theta+\pi/2)\Big)|\Psi\rangle_S|\Psi\rangle_A.\end{aligned} \tag{3.25}$$

Furthermore, we can access the k^{th}-order moments by

$$_{SS-NOPO}\langle\Psi|\Big(\hat{X}_{\omega_s}(\theta,\phi)\Big)^k|\Psi\rangle_{SS-NOPO} \equiv \ _S\langle\Psi|\ _A\langle\Psi|\Big(\hat{X}_{S,A}(\theta,\phi)\Big)^k|\Psi\rangle_S|\Psi\rangle_A. \quad (3.26)$$

We can see from equation 3.25 that measuring with a fixed demodulation phase, ϕ, will give a measurement result where the homodyne signal only depends on the state of the symmetric or anti-symmetric mode.
For $\phi = 0$,

$$\begin{aligned} &_S\langle\Psi|\ _A\langle\Psi|\Big(\hat{X}_{S,A}(\theta,\phi=0)\Big)^k|\Psi\rangle_S|\Psi\rangle_A \\ &= {}_S\langle\Psi|\Big(\hat{X}_S(\theta)\Big)^k|\Psi\rangle_S \\ &= {}_S\langle\Psi|\Big(\frac{1}{\sqrt{2}}\Big(\hat{X}_{+\omega_s}(\theta)+\hat{X}_{-\omega_s}(\theta)\Big)\Big)^k|\Psi\rangle_S, \end{aligned} \quad (3.27)$$

where

$$\hat{X}_{\pm\omega_s}(\theta) = \ e^{-i\theta}\hat{a}_{\pm\omega_s} + e^{i\theta}\hat{a}^\dagger_{\pm\omega_s}.$$

For $\phi = \pi/2$,

$$\begin{aligned} &_S\langle\Psi|\ _A\langle\Psi|\Big(\hat{X}_{S,A}(\theta,\phi=\pi/2)\Big)^k|\Psi\rangle_S|\Psi\rangle_A \\ &= {}_A\langle\Psi|\Big(\hat{X}_A(\theta+\pi/2)\Big)^k|\Psi\rangle_A \\ &= {}_A\langle\Psi|\Big(\frac{1}{\sqrt{2}}\Big(\hat{X}_{+\omega_s}(\theta+\pi/2)-\hat{X}_{-\omega_s}(\theta+\pi/2)\Big)\Big)^k|\Psi\rangle_A, \end{aligned} \quad (3.28)$$

where

$$\hat{X}_{\pm\omega_s}(\theta+\pi/2) = -i(e^{-i\theta}\hat{a}_{\pm\omega_s} - e^{i\theta}\hat{a}^\dagger_{\pm\omega_s}). \quad (3.29)$$

The equation 3.27 is an EPR measurement of the anti-correlations between the amplitude quadratures of the upper and lower side-bands, and equation 3.28 is an EPR measurement of the correlations between the phase quadratures of the upper and lower side-bands. Note that rotating the demodulation phase not only transitions between the symmetric and anti-symmetric modes but also has the effect of rotating the measurement quadrature. Therefore, for a fixed local oscillator phase of $\theta = 0$, for a demodulation phase of $\phi = 0$ ($\phi = \pi/2$) this will result in a measurement of the (anti)-correlations between the (phase) amplitude quadratures of the two modes. Both of these measurement results look the same because of the EPR entanglement that exists between the upper and lower side-bands.

A mix-down angle of $\phi = \pi/4$ results in a measurement that depends on the averaged sum of the symmetric and anti-symmetric modes.

For $\phi = \frac{\pi}{4}$,

$$
\begin{aligned}
&{}_S\langle\Psi|\,{}_A\langle\Psi|\Big(\hat{X}_{S,A}(\theta,\phi=\pi/4)\Big)^k|\Psi\rangle_S|\Psi\rangle_A \\
&= {}_S\langle\Psi|\,{}_A\langle\Psi|\bigg(\frac{1}{\sqrt{2}}\Big(\hat{X}_S(\theta)+\hat{X}_A(\theta+\pi/2)\Big)\bigg)^k|\Psi\rangle_S|\Psi\rangle_A \\
&= {}_S\langle\Psi|\,{}_A\langle\Psi|\bigg(\frac{1}{2}\Big(\hat{X}_{+\omega_s}(\theta)+\hat{X}_{-\omega_s}(\theta)+\hat{X}_{+\omega_s}(\theta+\pi/2)-\hat{X}_{-\omega_s}(\theta+\pi2)\Big)\bigg)^k|\Psi\rangle_S|\Psi\rangle_A.
\end{aligned}
\tag{3.30}
$$

Since the phase and amplitude quadratures of the upper or lower side-bands are uncorrelated, for a fixed local oscillator phase of $\theta = \pi/4$, this measurement results in a state that is statically equivalent to a thermal state. Interestingly, this demodulation phase produces a measurement result that is similar to probing the upper or lower side-band of the two-mode squeezed vacuum state described in equation 2.114. In chapter 5 we present experimental measurement results from applying this measurement operator to a two-mode squeezed vacuum state for these three special mix-down angles.

3.1.4 Side-band modes measured by spectrum analyser

We will now discuss a measurement technique that employs a random mix-down angle, such as a spectrum analyser. The first order moments of $\hat{X}_{S,A}(\theta,\phi)$ for phase-averaged demodulation are zero:

$$
\frac{1}{2\pi}\int_0^{2\pi}\hat{X}_{S,A}(\theta,\phi)d\phi = \frac{1}{2\pi}\int_0^{2\pi}\Big(\cos\phi\hat{X}_S(\theta)+\sin\phi\hat{X}_A(\theta+\pi/2)\Big)d\phi = 0. \tag{3.31}
$$

However, the second order moments are nonzero and instead results in a measurement of the average EPR variances of the symmetric and anti-symmetric modes

$$
\begin{aligned}
&\frac{1}{2\pi}\int_0^{2\pi}\Big(\hat{X}_{S,A}(\theta,\phi)\Big)^2 d\phi \\
&\quad= \frac{1}{2}\bigg[\Big(\hat{X}_S(\theta)\Big)^2+\Big(\hat{X}_S(\theta+\pi/2)\Big)^2\bigg] \\
&\quad= \frac{1}{4}\bigg[\Big(\hat{X}_{+\omega_s}(\theta)+\hat{X}_{-\omega_s}(\theta)\Big)^2+\Big(\hat{X}_{+\omega_s}(\theta+\pi/2)-\hat{X}_{-\omega_s}(\theta+\pi/2)\Big)^2\bigg].
\end{aligned}
\tag{3.32}
$$

The minimum variance of this measurement result is an average of the squeezing levels of the single-mode squeezed vacuum states in the symmetric and anti-symmetric modes. Therefore, a phase-averaged demodulation scheme is equivalent to the standard homodyne detection technique which returns a measurement result indistinguishable from a singe-mode squeezed vacuum state.

However, since the two single-mode states are indistinguishable, the ability to individually access them does not provide any more useful information about the state. Since a squeezed vacuum state is a Gaussian state, it can be fully characterised by its mean and standard deviation, which can be determined from these phase-averaged measurements. As we will show in the next section, the ability to use a fixed demodulation phase to access the symmetric *or* anti-symmetric side-band mode becomes useful when applied to an asymmetric two-mode state, such as a photon-subtracted two-mode squeezed vacuum state.

3.2 Two-mode projected state

The true nondegenerate properties of a SS-NOPO are demonstrated when frequency-resolved homodyne detection is applied to a photon-subtracted two-mode squeezed vacuum state. We will now show that the two single-mode states in the symmetric/anti-symmetric basis are no longer identical, and they can be individually characterised by this measurement technique that allows access to either the symmetric or anti-symmetric mode.

As we will discuss in chapters 4 and 6, it is experimentally possible to construct an optical projector that will subtract a photon from the symmetric side-band mode, and leave the anti-symmetric side-band mode untouched (or vice versa). The frequency side-band spectrum of the trigger mode can be shaped by a series of optical filtering cavities before detection by the APD. We will first present a simplified model where a single pair of FSR side-bands at $\pm\omega_s$ are isolated from the SS-NOPO spectrum. This model will then be extended to include mulitple FSR side-band pairs in the trigger mode, which represents the real trigger mode in our experiment.

3.2.1 Single frequency trigger mode

One ideal filter cavity system would be able to isolate an upper and lower side-band pair at a particular FSR frequency. If the frequency spacing between the side-bands is within the detection bandwidth of the APD, the projecting detector cannot distinguish from which side-band the annihilated photon originated. Therefore, this measurement result is equivalent to a superposition state of annihilation operators acting on the upper and lower side-bands, which is the projector

$$\hat{\Pi}_s = \hat{a}_{+\omega_s} + \hat{a}_{-\omega_s}. \tag{3.33}$$

The projected state can then be described by

$$\begin{aligned}|\Psi\rangle_{proj} &= \hat{\Pi}_s|\Psi\rangle_{SS-NOPO} \\ &= \Big[\hat{a}_{+\omega_s} + \hat{a}_{-\omega_s}\Big]\Big[\alpha_0|0\rangle_{+\omega_s}|0\rangle_{-\omega_s} + \alpha_2|1\rangle_{+\omega_s}|1\rangle_{-\omega_s} + \alpha_4|2\rangle_{+\omega_s}|2\rangle_{-\omega_s} \\ &+ \alpha_6|3\rangle_{+\omega_s}|3\rangle_{-\omega_s}\Big] \\ &= \alpha_2\Big[|0\rangle_{+\omega_s}|1\rangle_{-\omega_s} + |1\rangle_{+\omega_s}|0\rangle_{-\omega_s}\Big] + \alpha_4\sqrt{2}\Big[|1\rangle_{+\omega_s}|2\rangle_{-\omega_s} + |2\rangle_{+\omega_s}|1\rangle_{-\omega_s}\Big] \\ &+ \alpha_6\sqrt{3}\Big[|2\rangle_{+\omega_s}|3\rangle_{-\omega_s} + |3\rangle_{+\omega_s}|2\rangle_{-\omega_s}\Big].\end{aligned} \tag{3.34}$$

We can use the definitions from equation 3.16 to transform this equation into the symmetric/anti-symmetric basis:

$$\begin{aligned}|\Psi\rangle_{proj} &= \sqrt{2}\alpha_2|1\rangle_S|0\rangle_A + \alpha_4\Big[\sqrt{3}|3\rangle_S|0\rangle_A - |1\rangle_S|2\rangle_A\Big] \\ &+ \alpha_6\Bigg[\sqrt{\frac{15}{4}}|5\rangle_S|0\rangle_A - \sqrt{\frac{3}{2}}|3\rangle_S|2\rangle_A + \sqrt{\frac{3}{4}}|1\rangle_S|4\rangle_A\Bigg].\end{aligned} \tag{3.35}$$

Note that the odd- and even-photon number Fock states are now separated into the symmetric and anti-symmetric modes, respectively. Substituting the α-coefficients from equation 2.113 for two-mode squeezing gives

$$\begin{aligned}|\Psi\rangle_{proj} &= \frac{\sqrt{2}\tanh\xi}{\cosh\xi}|1\rangle_S|0\rangle_A + \frac{(\tanh\xi)^2}{\cosh\xi}\Big[\sqrt{3}|3\rangle_S|0\rangle_A - |1\rangle_S|2\rangle_A\Big] \\ &+ \frac{(\tanh\xi)^3}{\cosh\xi}\Bigg[\sqrt{\frac{15}{4}}|5\rangle_S|0\rangle_A - \sqrt{\frac{3}{2}}|3\rangle_S|2\rangle_A + \sqrt{\frac{3}{4}}|1\rangle_S|4\rangle_A\Bigg],\end{aligned} \tag{3.36}$$

which is equivalent to

$$\begin{aligned}|\Psi\rangle_{proj} &= \sqrt{2}\hat{a}_S|\Psi\rangle_S|\Psi\rangle_A \\ &= |\Phi\rangle_S|\Psi\rangle_A,\end{aligned} \tag{3.37}$$

where

$$|\Phi\rangle_S \approx -2\beta_2|1\rangle_S + 2\sqrt{2}\beta_4|3\rangle_S - 2\sqrt{3}\beta_6|5\rangle_S. \tag{3.38}$$

The state $|\Phi\rangle_S$ is a photon-subtracted squeezed vacuum state in the symmetric side-band mode at $\pm\omega_s$ FSR frequency for a truncated Fock space, and $|\Psi\rangle_A$ was previously defined in equation 3.21. The β-coefficients are the single-mode terms defined in equation 2.55. Therefore, a projector could be engineered that would subtract a single photon from the symmetric side-band mode and not the anti-symmetric mode, producing two independent and distinct quantum resource states in a *single* optical mode.

Applying our measurement operator to this projected state for a known demodulation phase allows us to access each quantum state separately. Thus, the k^{th}-order moments are accessible by

$$\begin{aligned}
{}_{proj}\langle\Psi|\Big(\hat{X}_{\omega_s}(\theta,\phi)\Big)^k|\Psi\rangle_{proj} &\equiv {}_S\langle\Phi|_A\langle\Psi|\Big(\hat{X}_{S,A}(\theta,\phi)\Big)^k|\Phi\rangle_S|\Psi\rangle_A \\
&= {}_S\langle\Phi|_A\langle\Psi|\Big(\cos\phi\hat{X}_S(\theta)+\sin\phi\hat{X}_A(\theta+\pi/2)\Big)^k|\Phi\rangle_S|\Psi\rangle_A.
\end{aligned} \tag{3.39}$$

For a demodulation phase $\phi = 0$,

$$ {}_S\langle\Phi|\ {}_A\langle\Psi|\Big(\hat{X}_{S,A}(\theta,\phi=0)\Big)^k|\Phi\rangle_S|\Psi\rangle_A = \ {}_S\langle\Phi|\Big(\hat{X}_S(\theta)\Big)^k|\Phi\rangle_S, \tag{3.40}$$

which results in the homodyne signal depending on only the photon-subtracted squeezed state in the symmetric side-band mode. And for a mix-down angle of $\phi = \pi/2$,

$$ {}_S\langle\Phi|\ {}_A\langle\Psi|\Big(\hat{X}_{S,A}(\theta,\phi=\pi/2)\Big)^k|\Phi\rangle_S|\Psi\rangle_A = \ {}_A\langle\Psi|\Big(\hat{X}_A(\theta+\pi/2)\Big)^k|\Psi\rangle_A, \tag{3.41}$$

which results in the homodyne signal depending on only the squeezed vacuum state in the anti-symmetric side-band mode.

3.2.2 Multi-frequency trigger mode

Our experimental implementation of this concept of applying a photon-subtraction operation to only the symmetric mode was a proof-of-principles experiment. As we shall see in chapter 6, we did not engineer an optical filtering system that isolated only a single frequency pair of upper and lower side-bands at $\pm\omega_s$, where ω_s is the FSR frequency of our SS-NOPO. Instead our cavity system transmits a small portion of two other FSR side-band pairs at $\pm 2\omega_s$ and $\pm 3\omega_s$. Therefore, it is necessary to extend our model to include multiple FSR frequencies in the projector. As we will discuss in chapter 6, due to the detection bandwidth of our APD and the transmission spectrum from the optical filter cavities, these three FSR pairs of upper and lower side-bands became entangled. While this is not ideal, it is interesting to note that such an entangled frequency spectrum is a required resource state for time-division-multiplexing (TDM).

First we define the two-mode squeezed vacuum state that consists of three FSR frequencies:

$$\begin{aligned}
|\Psi\rangle_{\pm T\omega_s} &= \alpha_0|0\rangle_{+T\omega_s}|0\rangle_{-T\omega_s} + \alpha_2\hat{a}^\dagger_{+T\omega_s}\hat{a}^\dagger_{-T\omega_s}|0\rangle_{+T\omega_s}|0\rangle_{-T\omega_s} \\
&\quad + \frac{\alpha_4}{2}\hat{a}^{\dagger 2}_{+T\omega_s}\hat{a}^{\dagger 2}_{-T\omega_s}|0\rangle_{+T\omega_s}|0\rangle_{-T\omega_s} + \frac{\alpha_6}{6}\hat{a}^{\dagger 3}_{+T\omega_s}\hat{a}^{\dagger 3}_{-T\omega_s}|0\rangle_{+T\omega_s}|0\rangle_{-T\omega_s},
\end{aligned} \tag{3.42}$$

where

$$
\begin{aligned}
|0\rangle_{\pm T\omega_s} &= |0\rangle_{\pm\omega_s} + |0\rangle_{\pm 2\omega_s} + |0\rangle_{\pm 3\omega_s} \\
\hat{a}^{\dagger}_{\pm T\omega_s} &= \gamma_1 \hat{a}^{\dagger}_{\pm\omega_s} + \gamma_2 \hat{a}^{\dagger}_{\pm 2\omega_s} + \gamma_3 \hat{a}^{\dagger}_{\pm 3\omega_s}
\end{aligned}
\tag{3.43}
$$

are the states and creation operators at $\pm\omega_s$, $\pm 2\omega_s$, and $\pm 3\omega_s$ FSR frequencies. The three FSR components in $\hat{a}^{\dagger}_{\pm T\omega_s}$ are given specific weightings (γ_1, γ_2, γ_3) that correspond to the measured transmission spectrum from our optical filtering system, normalised to $\gamma_1^2+\gamma_2^2+\gamma_3^2 = 1$. These weightings will be further discussed in chapters 4 and 5. We define the total symmetric and total anti-symmetric modes as

$$
\begin{aligned}
\hat{a}^{\dagger}_{TS} &= \frac{1}{\sqrt{2}}\Big[\gamma_1(\hat{a}^{\dagger}_{+\omega_s} + \hat{a}^{\dagger}_{-\omega_s}) + \gamma_2(\hat{a}^{\dagger}_{+2\omega_s} + \hat{a}^{\dagger}_{-2\omega_s}) + \gamma_3(\hat{a}^{\dagger}_{+3\omega_s} + \hat{a}^{\dagger}_{-3\omega_s})\Big] \\
\hat{a}^{\dagger}_{TA} &= \frac{1}{\sqrt{2}}\Big[\gamma_1(\hat{a}^{\dagger}_{+\omega_s} - \hat{a}^{\dagger}_{-\omega_s}) + \gamma_2(\hat{a}^{\dagger}_{+2\omega_s} - \hat{a}^{\dagger}_{-2\omega_s}) + \gamma_3(\hat{a}^{\dagger}_{+3\omega_s} - \hat{a}^{\dagger}_{-3\omega_s})\Big].
\end{aligned}
\tag{3.44}
$$

Using these definitions, we can transform equation 3.42 into the total symmetric and anti-symmetric basis to give

$$
|\Psi\rangle_{\pm T\omega_s} = |\Psi\rangle_{TS}|\Psi\rangle_{TA},
\tag{3.45}
$$

where

$$
\begin{aligned}
|\Psi\rangle_{TS} &= \frac{1}{\sqrt{2}}(\gamma_1|\Psi\rangle_S + \gamma_2|\Psi\rangle_{2S} + \gamma_3|\Psi\rangle_{3S}) \\
|\Psi\rangle_{TA} &= \frac{1}{\sqrt{2}}(\gamma_1|\Psi\rangle_A + \gamma_2|\Psi\rangle_{2A} + \gamma_3|\Psi\rangle_{3A}).
\end{aligned}
\tag{3.46}
$$

$|\Psi\rangle_S$ and $|\Psi\rangle_A$ are the single-mode squeezed vacuum states at $\pm\omega_s$ FSR frequency that were previously defined in equation 3.21. Similarly, $|\Psi\rangle_{2S}$ and $|\Psi\rangle_{2A}$ are single-mode squeezed states at $\pm 2\omega_s$ FSR frequency, and $|\Psi\rangle_{3S}$ and $|\Psi\rangle_{3A}$ are at $\pm 3\omega_s$ FSR frequency.

We can now define a multi-frequency projector as

$$
\hat{\Pi}_{T\omega_s} = \frac{1}{\sqrt{2}}\Big[\gamma_1(\hat{a}_{+\omega_s} + \hat{a}_{-\omega_s}) + \gamma_2(\hat{a}_{+2\omega_s} + \hat{a}_{-2\omega_s}) + \gamma_3(\hat{a}_{+3\omega_s} + \hat{a}_{-3\omega_s})\Big].
\tag{3.47}
$$

Acting this projector on the SS-NOPO squeezed vacuum spectrum results in

$$
\begin{aligned}
|\Psi\rangle_{TProj} &= \hat{\Pi}_{T\omega_s}|\Psi\rangle_{\pm T\omega_s} = \sqrt{2}\hat{a}_{TS}|\Psi\rangle_{TS}|\Psi\rangle_{TA} \\
&= |\Phi\rangle_{TS}|\Psi\rangle_{TA},
\end{aligned}
\tag{3.48}
$$

where

$$|\Phi\rangle_{TS} = \frac{1}{\sqrt{2}}\Big[\gamma_1|\Phi\rangle_S + \gamma_2|\Phi\rangle_{2S} + \gamma_3|\Phi\rangle_{3S}\Big]. \tag{3.49}$$

$|\Phi\rangle_S$ is a single-mode photon-subtracted squeezed vacuum state at $\pm\omega_s$ that was previously defined in equation 3.38. Similarly, $|\Phi\rangle_{2S}$ and $|\Phi\rangle_{3S}$ are single-mode photon-subtracted squeezed states at $\pm 2\omega_s$ and $\pm 3\omega_s$ FSR frequencies, respectively.

3.3 Summary

In this chapter we introduced new state generation theory pertaining to our experiments with two-mode squeezed vacuum and photon-subtracted two-mode squeezed vacuum. We defined a new basis consisting of the superpositions of the upper and lower side-bands ('symmetric' and 'anti-symmetric' modes) produced by a side-band-scale nondegenerate optical parametric oscillator (SS-NOPO). This introduced a novel way of interpreting the standard homodyne measurement in this symmetric/anti-symmetric basis.

We then mathematically derived what occurs when a frequency-resolved homodyne measurement is applied to a two-mode squeezed vacuum state produced by a SS-NOPO, which naturally preforms a measurement in the symmetric/anti-symmetric basis. This led to the theoretical prediction that a frequency-resolved measurement in this rotated side-band basis allows access to *both* the symmetric and anti-symmetric modes, which revealed two independent single-mode squeezed vacuum states with opposite squeezed-quadratures. By applying this measurement operator to a photon-subtracted two-mode squeezed vacuum state, we were able to mathematically demonstrate the power of this frequency-resolved technique, which gives access to either the symmetric or anti-symmetric mode. The model predicts an intriguing result that two distinct and independent quantum states will occur: a photon-subtracted squeezed vacuum state in the symmetric mode, and a squeezed vacuum state in the anti-symmetric mode. We then extended this model to include a multi-frequency projector that better represents our experimental projector which consists of three FSR side-band pairs at $\pm\omega_s, \pm 2\omega_s$, and $\pm 3\omega_s$.

Chapter 4

Experimental methods

Scientific discovery and scientific knowledge have been achieved only by those who have gone in pursuit of it without any practical purpose whatsoever in view.
Max Planck

In this chapter we discuss the details and characterisation of our quantum optics experiment that generates non-classical light. The experiment consists of the standard configuration necessary to generate a two-mode squeezed vacuum state from a side-band-scale nondegenerate optical parametric oscillator (SS-NOPO). In chapter 3 we demonstrated theoretically how projective measurements performed on this two-mode squeezed vacuum state could produce a photon-subtracted squeezed vacuum state in the symmetric mode and a squeezed vacuum state in the anti-symmetric mode. The experiment described in this chapter was designed as a proof-of-principles demonstration to test this prediction.

A series of optical filtering cavities are placed before the projecting detector (an APD). These cavities were engineered to have a symmetrical frequency transmission spectrum as described in §3.2.2, to send equal proportions of both the upper and lower frequency side-bands to the APD. There is a significant difference in how we implement our optical projector and measurement operator compared to previous work. As we shall show in the following chapters, utilising the nondegenerate side-bands produced by a SS-NOPO results in novel frequency side-band quantum states at multiple frequencies.

Firstly we will summarize the condition of the experiment when it was inherited from a previous group member. We will discuss the key components in the experiment and the various modifications that were made in the effort to improve the quality of quantum state generation. We will also introduce a novel technique for characterising the linewidth, free spectral range, and overall frequency transfer function of any optical cavity using only a standard power meter and an electro-optic intensity modulator.

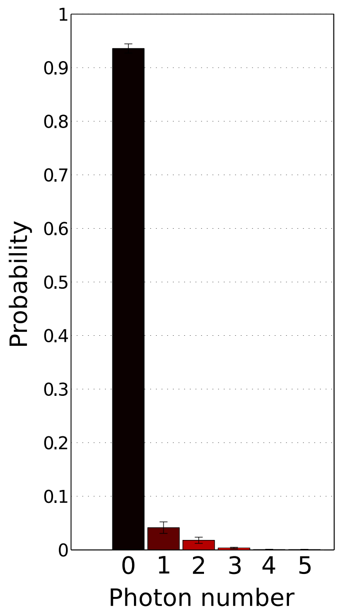

Figure 4.1: Experimental photon number distribution of photon-subtracted squeezed vacuum state produced by Generation I of experiment.

4.1 The experiment - Generation I

The first generation of this experiment included the optical infrastructure to generate a two-mode squeezed vacuum state, along with the optical filtering system necessary to spectrally filter the trigger photons for projected state generation. Preliminary characterisation of the quantum states generated by this experiment established that the optical system was functioning [298]. Figure 4.1 is a data set taken from Generation I of the experiment. The photon number distribution shown is from a quantum state tomographic reconstruction of the projected photon-subtracted squeezed vacuum state. These results were statistically-significantly different to the squeezed vacuum measurements. However, they had significant room for improvement. The vacuum probability is $\sim 94\%$ and the single-photon probability is $\sim 4\%$, which were typical results produced by Generation I of the experiment.

Possible reasons to explain the low single-photon probability have been subsequently thoroughly investigated. Various stability and alignment issues in Generation I (*GI*) of the experiment were identified and addressed. One of the most significant sources of instability in *GI* was a digital locking system that was used to phase-lock the OPO and two of the optical filtering cavities. The temperamental nature of the locking system meant it was often difficult and time-consuming to establish simultaneous lock of all three cavities. Once the cavities were locked, the system was unable to maintain lock for longer than a few minutes. It was also discovered that the *GI* locking system for the final and most vital filter cavity before the APD was malfunctioning. Therefore, this system lacked the locking stability and accuracy required during the long data collection times and needed to be replaced.

Increasing the APD gate rate from 100 kHz to 4 MHz and replacing the locking system led to a dramatic speed-up in the data acquisition time from ~ 13 hours to just ~ 2 hours. This time reduction significantly reduced the impact of experimental instability on the data. Due to the sensitive nature of projective state quantum optics experiments, prolonged collection times can expose the data to excess noise, and this contamination can ruin delicate quantum features. For example, features that were not statistically significant due to instability and noise in Generation I of the experiment became prominent in the data collected from Generation II (GII). In particular, GII data showed experimental evidence that a projected state produced from two-mode squeezed vacuum has *two* independent side-band modes with distinct quantum states.

This experiment utilises a 'chop-lock' technique during data collection, which will be further explained in the next section. GI used ultra-fast fibre optical switches instead of optical choppers (fan blades) to block the low-power 1550 nm beam during data collection. Due to the finite extinction ratio of these switches, it was discovered that 1550 nm photons were leaking through the switches during the 'off' setting, and corrupting the quality of the projected data. Also, the fibre in the switches was not polarisation maintaining, which caused further instability issues in the down-stream optics. These switches were replaced in GII with a new chop-lock system that utilises phase-locked free-space optical choppers.

Finally, there were some issues with the alignment techniques used to align the second harmonic generator (SHG) cavity, and with the beam alignment of the 775 nm 'pump' beam into the optical parametric oscillator (OPO) cavity. It is vital to have a well-aligned SHG cavity to maximise 775 nm power output. This 775 nm beam also needs to be well-aligned and mode-matched to the OPO cavity to ensure a sufficient amount of nonlinearity is generated. The previous alignment technique for the SHG cavity involved a detection path that was coupled through the OPO. Therefore, it was necessary to introduce a new detection path to extricate the SHG cavity alignment from the pump beam alignment into the OPO. Furthermore, a 775 nm *mode-matching cavity* was constructed that allows for more precise alignment of the pump beam into the OPO.

4.2 The experiment - Generation II

4.2.1 Overview

We will now describe the experiment in its current form after its numerous modifications and additions. First the main optical components will be briefly introduced.

Then we will summarise various stability issues that were addressed concerning the general infrastructure in the laboratory and experiment. Finally, we will systematically discuss the details of the experiment from the chop-lock technique and its main components to the various measurements made to characterise the experiment.

The experiment can be categorized into the following constituents:

1. The fundamental mode at 1550 nm is frequency up-converted by a second harmonic generator (SHG) to a 775 nm 'pump' beam.

2. The second harmonic pumps an optical parametric oscillator (OPO) to generate a two-mode squeezed vacuum state which has side-band-scale nondegeneracy.

3. A 775 nm mode-matching cavity is used to improve the alignment and mode-matching between the pump beam and the resonant cavity mode of the OPO.

4. The two-mode squeezed vacuum state is incident on a weakly-reflecting beam-splitter, which results in the reflection of a trigger field towards the projecting detector (APD), and the transmission of a signal field towards the homodyne detector for state characterisation.

5. The trigger field is frequency-filtered by several optical cavities before detection by the projecting detector (APD).

6. The final trigger beam is mode-matched into a 1550 nm optical fibre, which is connected to the APD used to detect photons subtracted from the squeezed vacuum state. These detection events herald a projected state at the characterising detector (homodyne detector), and initiate data collection of the homodyne signal for quantum state tomography of the projected state.

A frequency-offset temporal mode function is applied to the homodyne signal during post-processing to mode-match the signal field to the correlated trigger mode that initiated data collection. Figure 4.2 is a simplified schematic diagram of the Generation II experiment with numbered stars that correspond to the previously listed compartmental description of the experiment. All mode-matching optics and a large number of beam-steering mirrors have been removed from the schematic for visual clarity.

The experiment can be operated in two different modes: the *unprojected* state mode or the *projected* state mode. The unprojected state mode involves characterising the unprojected squeezed vacuum state by triggering data collection off dark counts from the APD. The projected state mode utilises the optical filter cavities shown in figure 4.2 to send photons at particular FSR frequencies to the APD. Data

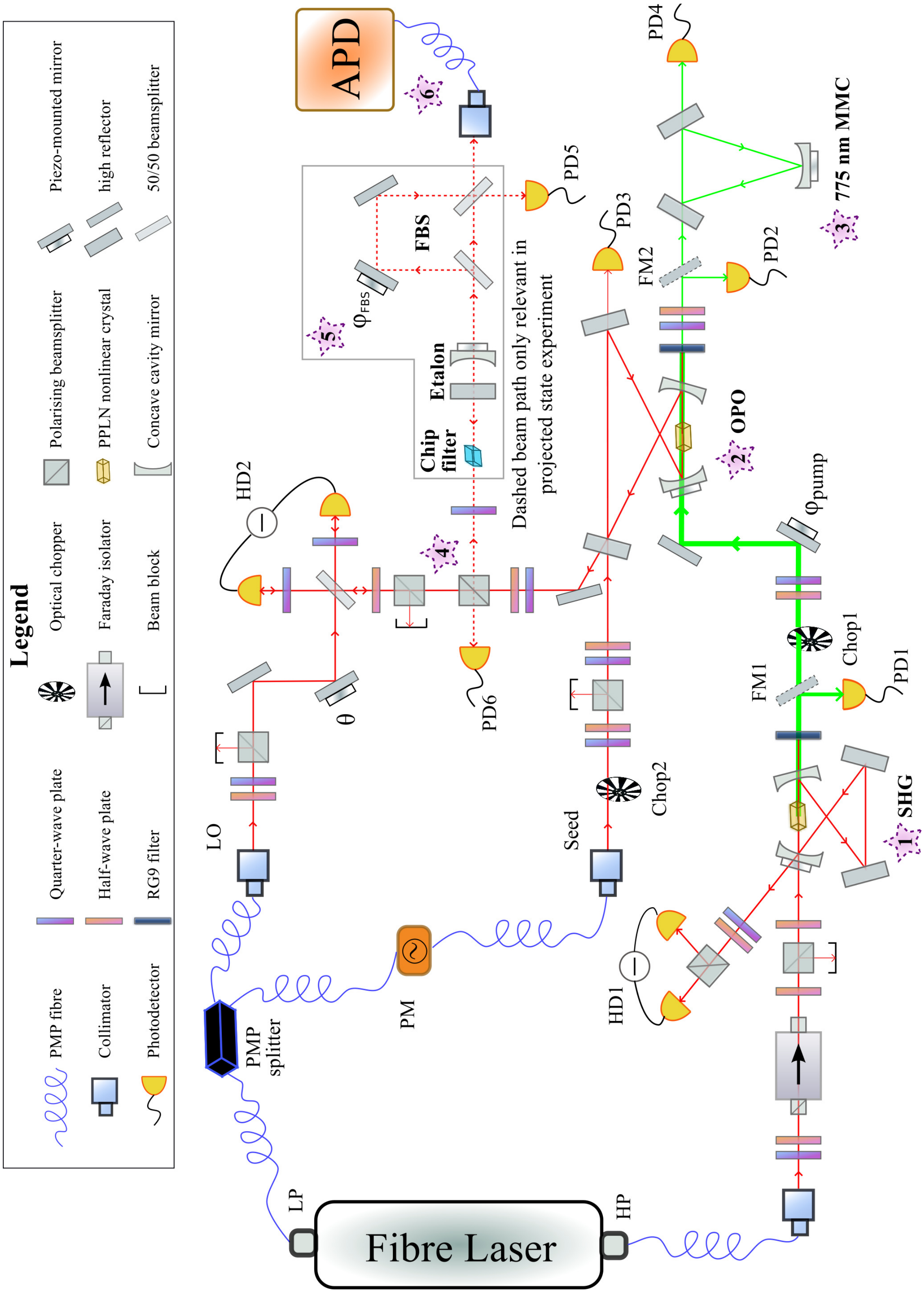

Figure 4.2: Simplified schematic diagram of Generation II experiment for unprojected and projected state generation. The optical systems labeled with numbered stars correspond to the numerical items in the compartmental description of the experiment. The illustrated legend applies to this and all subsequent schematics. Red beam: 1550 nm, green beam: 775 nm, HP: high power output, LP: low power output, PM: fibre phase modulator, FM: flipper mirror, PD: photodetector, HD: homodyne detector, LO: local oscillator, FBS: frequency beamsplitter.

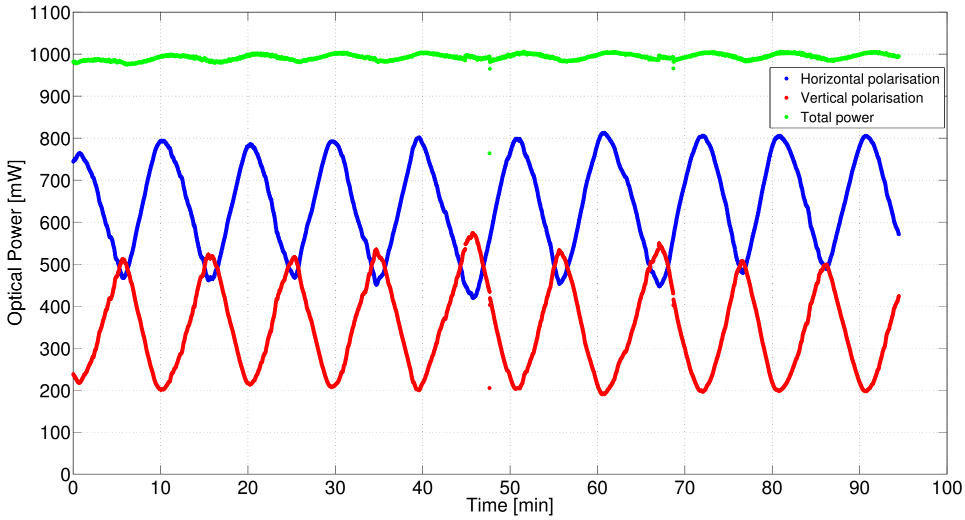

Figure 4.3: Polarisation stability measurement of laser and PMP fibre *before* fibre and laser shielding system was installed.

collection is then triggered off a mixture of real and false detection events. Ideally, a real photon detection event will correspond to a photon being subtracted from the two-mode squeezed vacuum state produced by the SS-NOPO, which projects this photon-subtracted squeezed vacuum state at the homodyne detector.

4.2.2 General stability

Quantum optics experiments are notoriously sensitive to disturbances, which can undermine the quality of the quantum state generated. Therefore, several efforts were made to isolate the optics table and laboratory from building vibrations and noise. We discovered that temperature fluctuations also had a detrimental effect on the stability of the optics, laser, optical fibre, and on the electronic equipment critical to running the experiment. Therefore, a new air conditioning system was installed in the laboratory capable of handling the heat load generated by the equipment. An intricate enclosure system was also installed over the entire optical table to minimise disturbances from air currents. We discovered that the SHG system was particularly sensitive to air currents so a separate smaller enclosure was installed over that optical system.

Our laser source had to be replaced during the various modifications to this experiment. The new laser is a continuous-wave high-power fibre laser at 1549.315 nm (NP Photonics, *The Rock*), which has a separate low power output of $\sim$ 20 mW and a high power output of $\sim$ 1 W (see figure 4.2). It was realised during characterisation and installation that the optical polarisation of the new laser and fibre optic system is extremely sensitive to temperature fluctuations and air currents.

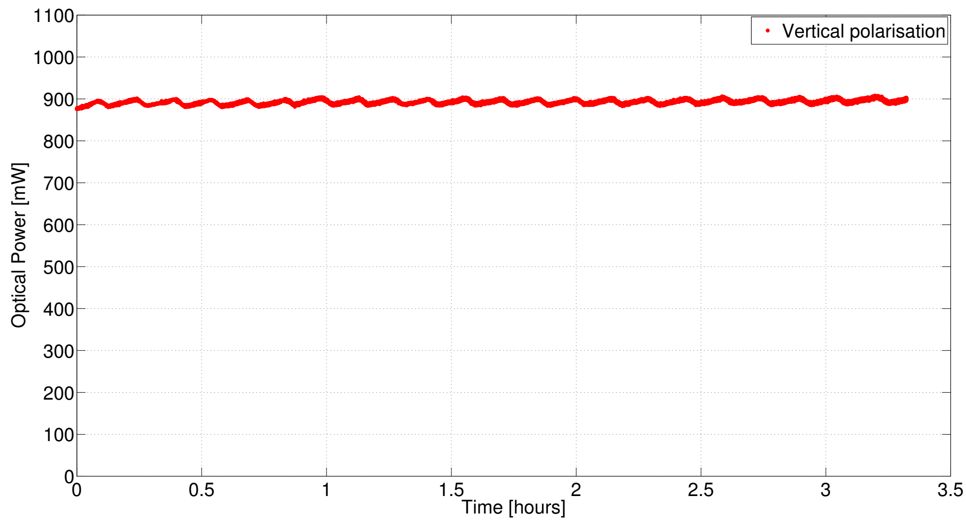

Figure 4.4: Polarisation stability measurement of laser and PMP fibre *after* fibre and laser shielding system was installed.

Polarisation-maintaining-panda (PMP) fibre optic cable is used to connect the fibre laser to the free-space collimators in the experiment. After installation of the laser and PMP fibre, the horizontal and vertical polarisation components of the high-power output displayed an oscillation of amplitude $\pm 30\%$ of the average power that repeated every ~ 10 minutes. A typical data set taken of these fluctuations before the fibre and laser were stabilised is shown in figure 4.3.

It was determined that these oscillations were correlated to the temperature cycling of the new air conditioning system. Since any polarisation drift will manifest as power and fringe visibility drift in the experiment, this level of fluctuation was unacceptable. Despite replacing any pre-existing fibre in the experiment with PMP fibre that had a 3 mm cable jacket, these large polarisation oscillations were still observed. The fibre shielding was insufficient to provide isolation from slight stresses on the fibre or room temperature fluctuations. Therefore, a fibre shielding system was designed and installed which held the PMP fibre in constant tension, and provided extra protection from the temperature fluctuations and air currents. Furthermore, a three-sided perspex box was constructed to shelter the laser and a curtain was installed to block air currents generated by the air conditioning system. These modifications significantly reduced the power fluctuations from $\pm 30\%$ to an acceptable level of $\pm 2\%$ of the average power, which is shown in figure 4.4.

4.2.3 Chop-lock technique

A low-power 1550 nm beam called the 'seed' is used to frequency-lock the OPO and optical filter cavities. In order to generate true two-mode squeezed vacuum, this

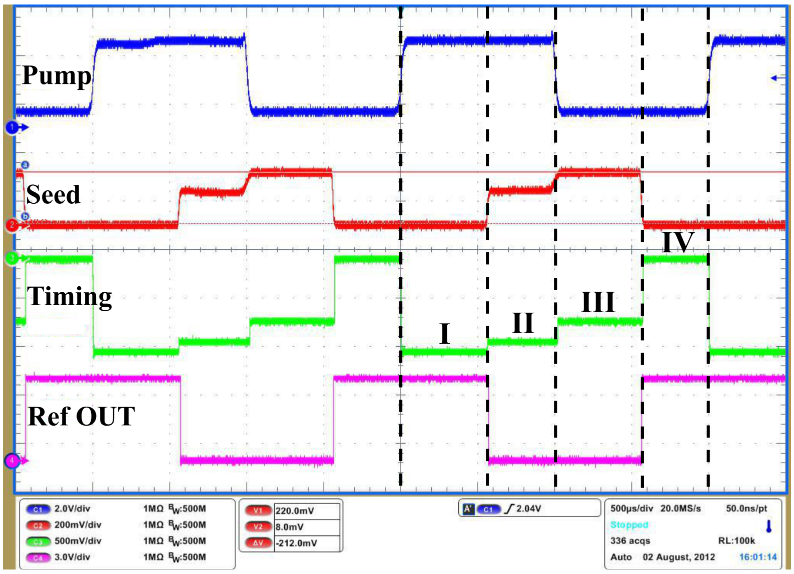

Figure 4.5: An oscilloscope trace of the 775 nm pump and 1550 nm seed beams being chopped, illustrating that the chopping periods of the optical choppers are phase-locked in quadrature. The timing signal generated by *QMATE* and the reference OUT signal from the seed optical chopper are also shown. There are four distinct measurement stages labelled I-IV; data collection occurs during stages I (pump 'on', seed 'off') and IV (pump and seed 'off').

beam must be blocked while the pump beam interacts with the OPO. Any photon leakage from the seed into the data collection stage can lead to APD detection events that do not correspond to a photon-subtraction event. Conversely, the pump beam must be blocked while the seed light is 'on' and used to lock the OPO. Therefore, specialised optical choppers were installed to completely block the pump and/or seed light during data collection. These two phase-locked optical choppers (Thorlabs MC2000, MC1F10 10-slot chopper blades) are used to periodically block these beams in quadrature. The chopper labelled 'Chop1' in figure 4.2 is in the pump beam and the 'Chop2' chopper is in the seed beam. This 'chop-lock' technique results in four distinct measurement stages (I-IV), as shown in figure 4.5 where the pump and seed alternate being 'off' and 'on.'

A home-built analogue electronics system called *QMATE* (Quantum Measurement And Timing Electronics) was designed and constructed by Shane Brandon of our electronics workshop team. *QMATE* produces two signals that are used in post-processing to analysis the data. Its design was based on the previous digital system from *GI* (circuit diagram for *QMATE* is shown in appendix 7.2, figure 1). *QMATE* produces a periodic signal of constant voltage levels that is used as a timing signal to separate the collected data into their respective measurement stages. This timing signal is phase-locked to the leading edge of the chopped pump signal, which is measured by *PD2* shown in figure 4.2. This system also generates a real-time signal that is proportional to the level of parametric gain from the OPO, which is used to estimate the pump/seed phase. Data capture is triggered while the reference OUT signal from the seed chopper is high, which corresponds to the seed beam being 'off'. Four signals are captured during data collection: the high-frequency homodyne signal, low-frequency homodyne signal, and the *QMATE* timing and parametric gain signals. The purpose of each measurement stage and the signals collected therein will now be discussed.

Stages I and IV

Data collection of the four signals occurs during stages I and IV of the timing signal from *QMATE*. In stage I, the pump beam is 'on' and the seed beam is 'off', resulting in the homodyne data capture of either squeezed vacuum or photon-subtracted squeezed vacuum data, depending on which configuration the experiment is operating. Homodyne quantum noise measurements of the vacuum are performed during stage IV while both beams are blocked. The timing signal is used to separate the acquired homodyne data into these two stages. Due to limitations of the phase-lock system, there is a small phase drift between the two optical choppers, which can lead to the pump beam being accidentally 'on' during a vacuum measurement. In order to avoid contamination of the measurement stages from this drift, stage I of the timing signal tracks the leading edge of the pump chopper.

Another advantage of this tracking feature is realised when operating the experiment in photon-subtraction mode, as it maximises the chances of capturing a real photon-subtracted event during stage I. The low APD detection efficiency and high dark count probability leads to an overall low count rate of real photon-subtracted events. This leads to longer data acquisition times as a large number of quadrature measurements must be performed for accurate reconstruction of the quantum state. As with any complex quantum optics experiment, long data collection times can lead to instability issues, which can degrade the quality of the projected state. The best way to avoid these problems is to minimise the data collection time by maximising the chances of capturing a real photon-subtracted event.

Stage II

Attempts to experimentally phase-lock the pump beam relative to the seed were unsuccessful due to an unknown phase drift. Therefore, the pump phase wanders during data acquisition and must be tracked for successful reconstruction of the quantum state during post-processing. The optical phase relationship between the parametric down-converted pump photons and the seed field can be calculated from the level of parametric gain produced by the OPO. Careful attention was paid to ensure that the optical phase drift of this signal was on a time scale larger than 2

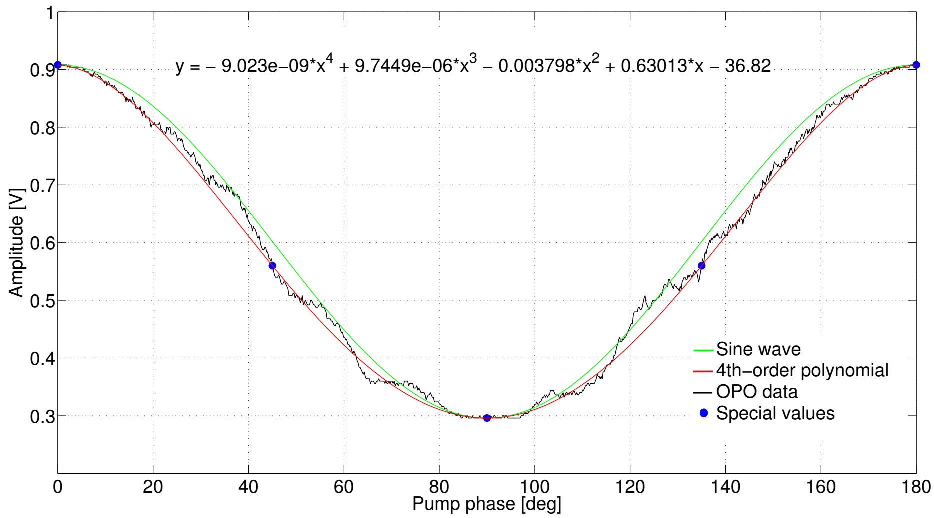

Figure 4.6: Parametric gain data from our OPO as a function of pump phase. The special values marked with blue dots correspond to maximum parametric gain at $\phi_{pump} = 0°$, $G = 1$ at $\phi_{pump} = 45°$ and minimum parametric gain at $\phi_{pump} = 90°$. The sine function described by equation 4.1 is shown in green. A better fit to the experimental OPO data (black) is provided by the 4th-order polynomial equation shown in the figure (red).

ms (one full chopping period of all stages I-IV) to maintain correlation between this phase information and the captured high-frequency homodyne signal.

It has been shown that a pump phase angle of $\phi_{pump} = 0$ ($\phi_{pump} = \pi/2$) corresponds to parametric amplification (attenuation) of the seed, and phase (amplitude) quadrature squeezing [146,147]. Therefore, the pump phase angle can be determined by monitoring the level of classical parametric gain from the OPO, and fitting this data with the appropriate equation. The actual values of the gain measurement are just arbitrary numbers and only used to estimate the pump phase.

The InGaAs photodetector *PD3* shown in figure 4.2 is used to quantify the parametric gain levels of the OPO as the pump phase wanders. Figure 4.5 shows the seed undergoing parametric attenuation as seen by the voltage level in stage II, $\mathcal{U}_{II}$, being below that of stage III, $\mathcal{U}_{III}$. Therefore, the amount of classical gain is quantified as $G = \mathcal{U}_{II}/\mathcal{U}_{III}$. The voltage level from *PD3* is sampled twice by *QMATE* over a full chop cycle (once during stage II and once during stage III), and the ratio of these values is recorded during data acquisition.

A typical data set of parametric gain measurements from our OPO is shown in figure 4.6. We tried fitting this curve with an equation based on a sine wave, defined as

$$\mathcal{U}_{pump} = \frac{1}{2}\left[(\mathcal{U}_{max,p} - \mathcal{U}_{min,p}) \sin\left(2\phi_{pump} + \frac{\pi}{2}\right) + \mathcal{U}_{max,p} + \mathcal{U}_{min,p}\right] \tag{4.1}$$

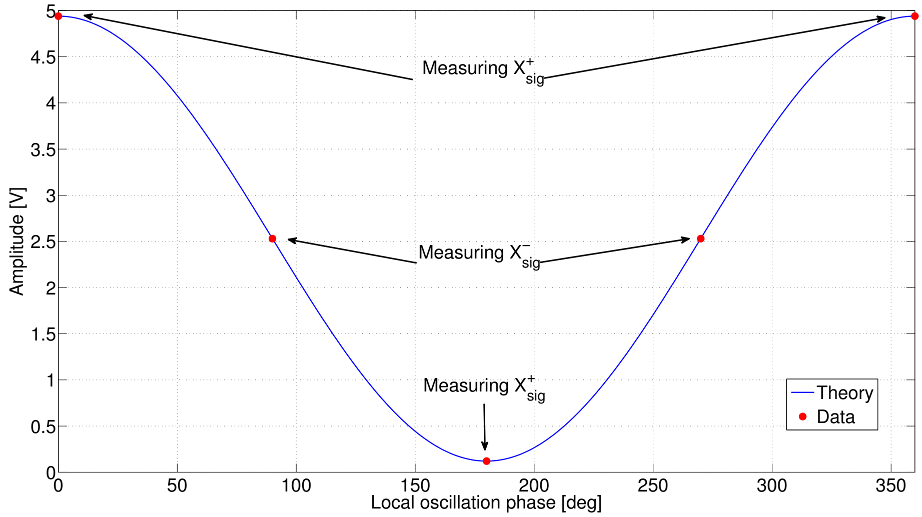

Figure 4.7: Classical interference curve from homodyne detector between LO and signal fields as a function of local oscillator phase. Experimental measurements of arbitrary voltage values at the special angles of $\theta = 0°, 90°, 180°$ are shown and fitted with a theory curve describe by equation 4.2. Maximum and minimum points on the interference curve correspond to a homodyne measurement of the amplitude quadrature of the signal field, and the halfway point corresponds to measuring the phase quadrature.

where $\mathcal{U}_{max,p}$ ($\mathcal{U}_{min,p}$) corresponds to the overall maximum (minimum) voltage of the parametric gain signal, respectively. However, this equation does not provide the desired level of fit to the data due to the asymmetry of the parametric gain curve. We found that fitting a 4th-order polynomial to the arbitrary voltage values at the special angles $\phi_{pump} = 0$, $\phi_{pump} = \pi/4$, and $\phi_{pump} = \pi/2$ provided a better fit to the overall gain curve. An example of such a 4th-order polynomial equation and fit is shown in figure 4.6. Therefore, this technique was used in post-processing to derive the pump phase from the parametric gain signal using *PD3* and *QMATE*.

Stage III

Tomography of the state is performed by varying the local oscillator (LO) phase for a series of homodyne measurements. Therefore, the LO phase must be tracked so a measurement angle can be assigned to the quadrature data, as described in §2.8.2. This is done by capturing the low-frequency homodyne detector signal during stage III when the pump is 'off' and the seed is 'on'. There is a known phase relationship between the classical interference of the LO and signal fields to which quadrature of the signal field is being measured. This relationship can be seen in equation 2.103, which describes the subtracted output from a homodyne detector. The classical interference signal is at a maximum when the LO phase is $\theta = 0$. This angle corre-

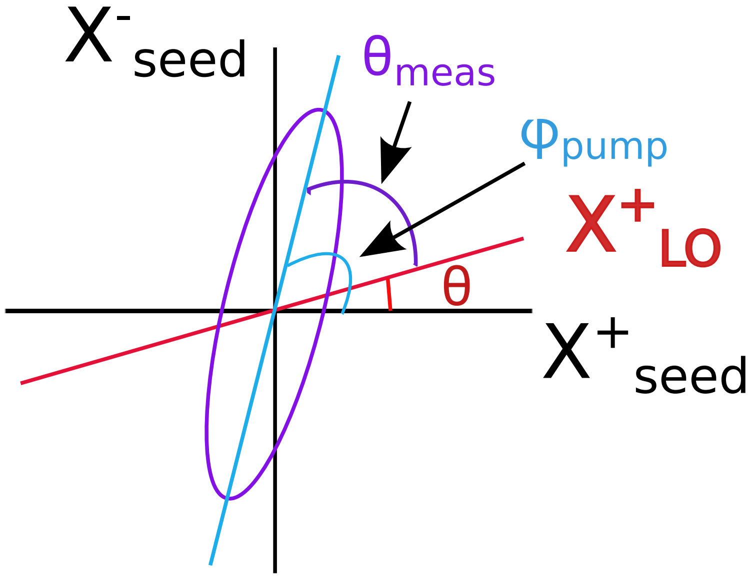

Figure 4.8: Optical phase relationships between seed, pump, and local oscillator. The angle labelled between the amplitude quadratures of the LO (red) and seed (black) fields is the LO phase, θ. The angle between the major axis (light blue) of the squeezing ellipse and the amplitude quadrature of the seed field is the pump phase, ϕ_{pump}. The overall measurement angle, θ_{meas}, is located between the LO axis and major axis of the squeezing ellipse.

sponds to measuring the amplitude quadrature of the signal field, $\hat{X}^+_{sig}$. Similarly, halfway between maximum and minimum interference ($\theta = \pi/2$) corresponds to measuring the phase quadrature of the signal field, $\hat{X}^-_{sig}$. This relationship between the classical interference and LO measurement angle are illustrated in figure 4.7. Thus, the LO phase can be determined by data capturing this interference signal, and modelling it by

$$\mathcal{U}_{LO} = \frac{1}{2}\left[(\mathcal{U}_{max,LO} - \mathcal{U}_{min,LO}) \sin\left(\theta + \frac{\pi}{2}\right) + \mathcal{U}_{max,LO} + \mathcal{U}_{min,LO}\right] \tag{4.2}$$

where $\mathcal{U}_{max,LO}$ ($\mathcal{U}_{min,LO}$) corresponds to the overall maximum (minimum) voltage of the low-frequency homodyne detector signal, which measures of the classical interference between the LO and seed. A sample-and-hold circuit was used to sample the photodetector signal from *HD2* (labelled in the experimental schematic, figure 4.2) during stage III while the seed and LO are interfering, and hold the level until the next full chop cycle. The circuit diagram for the LO phase sample-and-hold circuit is shown in appendix 7.2 (figure 2). As with the parametric gain signal, any time delays due to electronic circuits were minimised to ensure the information derived from these signals pertained to the quadrature data captured from the high-frequency homodyne signal during the same chop cycle.

As discussed in §2.8.2, an overall measurement angle has to be assigned to the

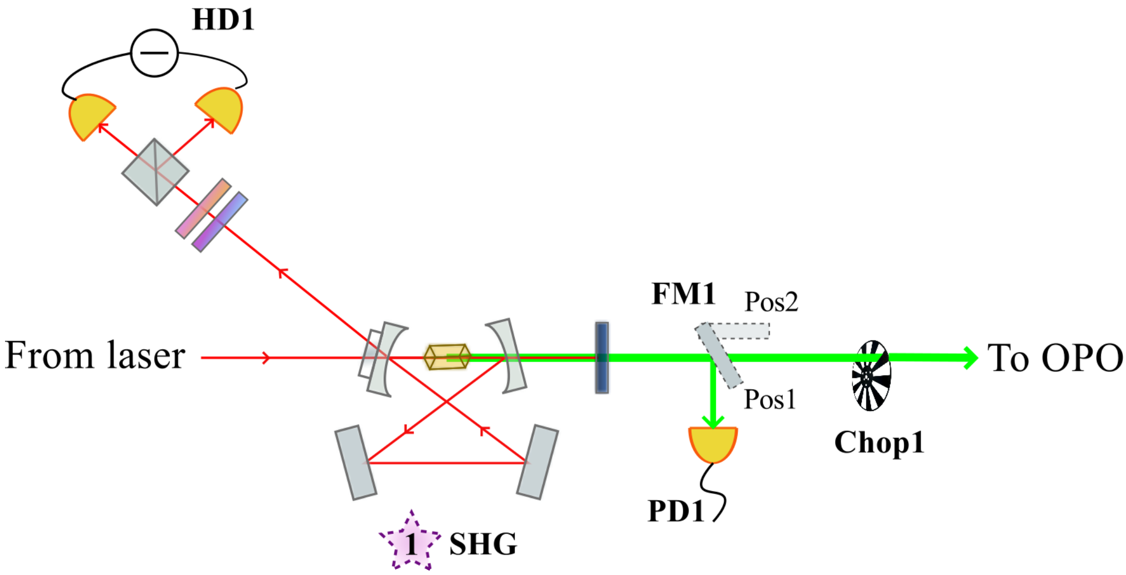

Figure 4.9: Schematic diagram of the second harmonic generator (SHG) in Generation II experiment. A 'flipper mirror'(*FM1*) is used in the transmitted path which can be set in one of two positions as illustrated (*Pos1* or *Pos2*). Red beam: 1550 nm, green beam: 775 nm, PD1: silicon photodetector, HD1: 1550 nm homodyne detector.

quadrature data for use in the maximum-likelihood reconstruction algorithm. For an accurate reconstruction of the quantum state, this measurement phase, θ_{meas}, must depend on the optical phase relationships between the pump, seed and local oscillator. Figure 4.8 is a phase-space diagram which illustrates the phase conventions used to calculate θ_{meas}. The LO phase, θ, is defined as the angle between the amplitude quadratures of the local oscillator and seed fields. We define the pump phase, ϕ_{pump}, as the angle between the semi-major axis of the squeezing ellipse and the amplitude quadrature of the seed field. Conceptually, the pump phase rotates the squeezing ellipse relative to the seed quadratures, while the LO phase rotates the measurement axis. The overall phase assigned to the quadrature data used in the MaxLik quantum state tomographic reconstruction is therefore defined as

$$\theta_{meas} = \theta - \phi_{pump} + \frac{\pi}{2}. \tag{4.3}$$

4.2.4 Second harmonic generator

It is important in these types of quantum experiments that all laser beams originate from the same laser source so that a common phase relationship is established. Therefore, the first step to generating the squeezed vacuum state is to convert the high-power 1550 nm laser output to the second harmonic at 775 nm. This is done by using an optical cavity called a second harmonic generator (SHG) which has a nonlinear crystal inside.

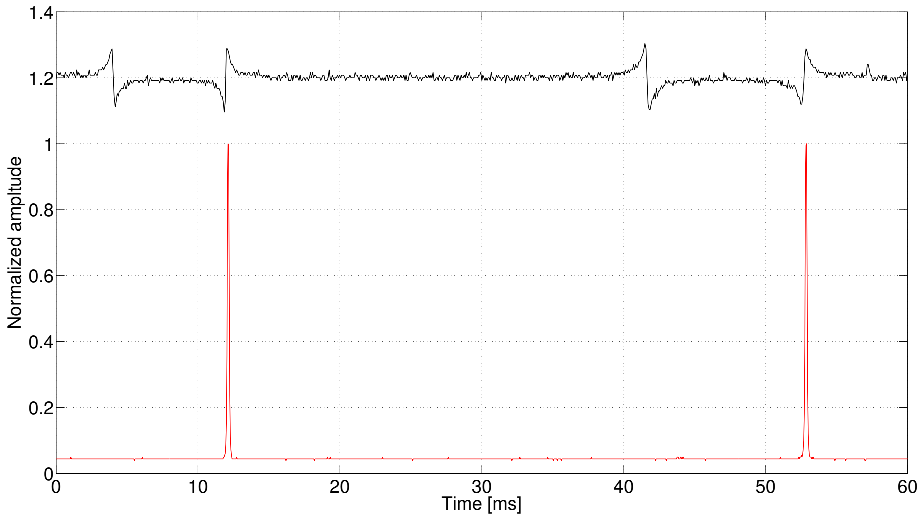

Figure 4.10: SHG cavity modes (red) and corresponding bipolar error signal (black) from homodyne locking technique used to frequency lock the SHG to the TEM00 mode.

Our SHG cavity in a standard bow-tie configuration (see figure 4.9) with the parameters listed in table 4.1. A type I periodically-poled lithium niobate (PPLN) nonlinear crystal is placed between the two curved mirrors in the cavity at the location of the smallest beam waist to maximise the nonlinear process. As shown in figure 4.9, a Schott RG9 filter is used at the output of the cavity to filter any residual high-power 1550 nm light. A 'flipper mirror' (*FM1*) is used in the transmitted path which can be set in one of two positions. Position 1 sends the 775 nm to a silicon photodetector, *PD1*, which is used to monitor the SHG cavity modes during realignment. Position 2 allows the 775 nm light to pass onto a beam path which leads through an optical chopper, $Chop1$, and eventually into the OPO.

length	FSR	poling period	measured E_{nl}	crystal temperature
412 mm	728 MHz	18.92 μm	2.6 x 10^{-3} W^{-1}	158°C

Table 4.1: Cavity parameters of SHG in Generation II experiment.

It is vital to frequency lock the SHG cavity to the driving laser to maintain a stable 775 nm output. Therefore, a bipolar error signal must be generated that is correlated to any frequency detuning which may occur between these systems. The SHG is locked using a technique called 'homodyne locking' [299]. In this technique, a homodyne detector (*HD1*) is used to monitor the phase quadrature of the reflected light from the cavity input coupler, which has been shown to be related to the frequency detuning between the input field and the circulating cavity field [300].

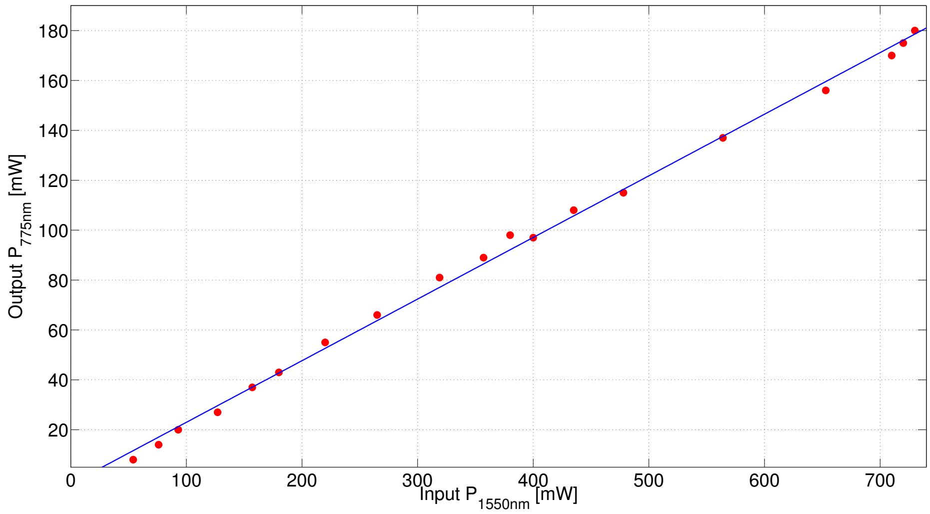

Figure 4.11: Characterisation of second harmonic generation from a phase-locked SHG cavity for various input 1550 nm powers.

Two error signals are generated in which one corresponds to the light field rejected by the cavity, and the other corresponds to the cavity mode of interest. We use the latter signal to frequency lock the SHG on resonance with the TEM00 mode, as shown in figure 4.10. It has been shown that utilising this locking technique on a cavity which generates squeezed vacuum allows for homodyne measurements of the squeezed field while locking the cavity [299]. However, as the SHG does not produce squeezed vacuum, this ability to perform homodyne measurements on a squeezed field while phase-locking the cavity was not exploited.

The conversion efficiency for a phase-locked SHG cavity is measured before any measurements are taken to quantify the nonlinear behaviour of the OPO for a particular input 775 nm power. Figure 4.11 illustrates the second harmonic power conversion relationship from the phase-locked SHG cavity. It is important to characterise this curve to determine appropriate input powers of 1550 nm light for operating this cavity in an unsaturated conversion region. The conversion relationship is considered to be saturated when increasing the incident fundamental optical power does not correspond to a proportional increase in the generated second harmonic optical power. As evident from the trend shown in figure 4.11, the conversion efficiency remains almost linear for the highest input power of 1550 nm light that our fibre laser can produce. Ideally, the second harmonic power would increase quadratically with respect to the incident fundamental power, as predicted by simple mathematical modelling of an SHG [242]. However, due to the characteristics of our SHG cavity, such as large optical losses, large beam waist at the crystal location, and low effective nonlinearity of the PPLN crystal, the frequency doubling of this optical cavity

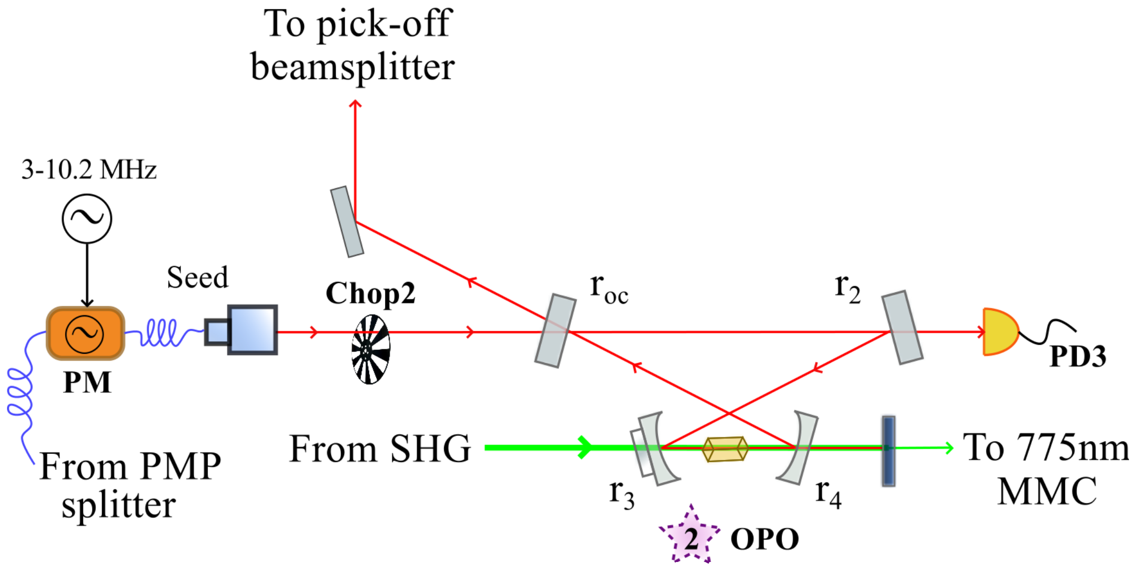

Figure 4.12: Schematic diagram of the optical parametric oscillator (OPO) in Generation II experiment. Red beam: 1550 nm, green beam: 775 nm, PM: fibre phase modulator, PD3: fast InGaAs photodetector, MMC: mode-matching cavity.

follows a more linear relationship [298]. Furthermore, there are clearly competing nonlinearities in this cavity as the *third* harmonic at 387.5 nm has been observed exiting the cavity. This concept of competing nonlinearities in an optical cavity will be further explained in §4.2.6. Despite these imperfections, the SHG cavity can produce a final maximum 775 nm power of 180 mW from 736 mW of input 1550 nm light, which is sufficient for the subsequent experiments.

4.2.5 Sub-threshold optical parametric oscillator

As previously discussed in §2.5.3, a two-mode squeezed vacuum state is produced by the nonlinear interaction of the 775 nm 'pump' beam with a second nonlinear optical cavity called an optical parametric oscillator (OPO). The pump photons undergo parametric down-conversion in the nonlinear crystal, which results in pairs of entangled photons at 1550 nm. These down-converted photons are generated at symmetrically correlated frequencies evenly spaced about the carrier within the down-conversion bandwidth of the nonlinear crystal. Surrounding the crystal with an optical cavity suppresses the generation of photons at frequencies outside the cavity resonances. Therefore, a frequency-shaped spectrum of entangled upper and lower side-bands, called an entangled frequency comb, are emitted by the OPO at $\Omega_0 \pm n\omega_s$, where Ω_0 is the optical carrier angular frequency, ω_s is the FSR angular frequency, and $n = 1, 2, 3, \ldots$ is the FSR number. The two-mode squeezed vacuum state produced by a side-band-scale nondegenerate OPO (SS-NOPO) consists of these upper and lower side-band pairs of entangled photons.

Description	Symbol	Value
Total cavity path length	p	582.5 mm
Measured free spectral range	ω_s	$2\pi \times 515$ MHz
Measured linewidth (FWHM)	γ_{FWHM}	$2\pi \times 8.76$ MHz
Finesse	$\mathcal{F}$	~ 59
OPO decay rate (HWHM)	β	$2\pi \times 4.07$ MHz
Measured output coupler 1550 nm reflectivity	r_{oc}	0.916
Cavity mirror 1550 nm reflectivity	r_2	0.9995
Cavity mirror 1550 nm reflectivity	r_3	0.9999
Cavity mirror 1550 nm reflectivity	r_4	0.9999
OPO escape efficiency	η_{esc}	0.848
Total cavity loss	L	0.015
Measured single-pass nonlinear conversion efficiency	E_{nl}	7.2×10^{-3} W^{-1}
Quasi-phase matching temperature of crystal (PPLN)	T_c	156.6°C
Pump threshold power	P_{Th}	340 mW

Table 4.2: Cavity parameters of OPO in Generation II experiment.

A simplified schematic of our OPO is illustrated in figure 4.12, and its various parameters are listed in table 4.2. These values were used in our data analysis code to reconstruct the measured quantum state using quantum state tomography and the MaxLik technique. Three of these parameters, β, η_{esc}, and P_{Th}, are related to r_{oc}, L, and E_{nl}, and were mathematically defined in §2.7.1. The OPO has a type I PPLN nonlinear crystal of similar poling period to the SHG crystal and a higher nonlinear conversion efficiency. We operated the OPO in the sub-threshold regime for the purposes of generating squeezed vacuum. This is accomplished by maintaining the power of the 775 nm pump beam well-below the pump threshold power, P_{Th}.

The finesse, $\mathcal{F}$, of an optical cavity can be defined in terms of the magnitude of the round trip gain, g_{rt}, where $g_{rt} \equiv |\tilde{g}_{rt}(\omega)|$, and [301]

$$\tilde{g}_{rt}(\omega) \equiv R_{oc}R_2R_3R_4 \exp\Big[- Lp - \frac{i\omega p}{c}\Big]. \tag{4.4}$$

R_{oc}, R_2, R_3, R_4 are the complex amplitude reflectance coefficients associated with each cavity mirror illustrated in figure 4.12 ($|R_{oc}|^2 = r_{oc}$), L is the overall cavity loss, p is the total path length, and ω is the optical angular frequency. Therefore the finesse is

$$\mathcal{F} = \frac{\pi\sqrt{g_{rt}}}{1 - g_{rt}}, \tag{4.5}$$

where

$$g_{rt} \equiv |\tilde{g}_{rt}(\omega)| = R_{oc}R_2R_3R_4e^{-Lp}, \tag{4.6}$$

The finesse of a cavity can also be calculated from its FSR and linewidth as

$$\mathcal{F} = \frac{\omega_s}{\gamma_{_{FWHM}}}. \tag{4.7}$$

We use a modified version of the Pound-Drever-Hall modulation-based technique to frequency-lock the OPO to the laser [302, 303]. This technique usually involves phase modulation at frequencies outside the cavity linewidth. If the carrier is near resonance and the phase side-bands are at a high enough frequency then they will be completely reflected. The conventional approach involves measuring the reflected light with a photodetector and mixing-down the signal with the original modulation. This leads to a bipolar error signal that is related to the frequency detuning between the input field and the cavity mode of interest. Instead of using phase modulation at very high frequencies (compared to the cavity linewidth), we use modulation at a frequency *within* the linewidth of our OPO. This way the modulated signal on the light is transmitted through the cavity and we can phase-lock the OPO using a photodetector on the *transmitted port* instead of in the reflected beam (which goes to the rest of the experiment). A fibre broadband low-loss $LiNbO_3$ electro-optic phase modulator (EOspace, PM-0K5-10-PFA-PFA-UL) is used to place $3 - 10.2$ MHz phase modulation on the carrier (see *PM* in figure 4.12). Since this frequency is within the linewidth of our OPO, the modulation is transmitted through the mirror labelled r_2 and is detected by a fast photodetector (*PD3*) on the transmitted port. Multiplying the voltage signal from *PD3* with the original high-frequency modulation and low-pass filtering the result generates the necessary bipolar error signal to frequency-lock the input field to the cavity mode of interest.

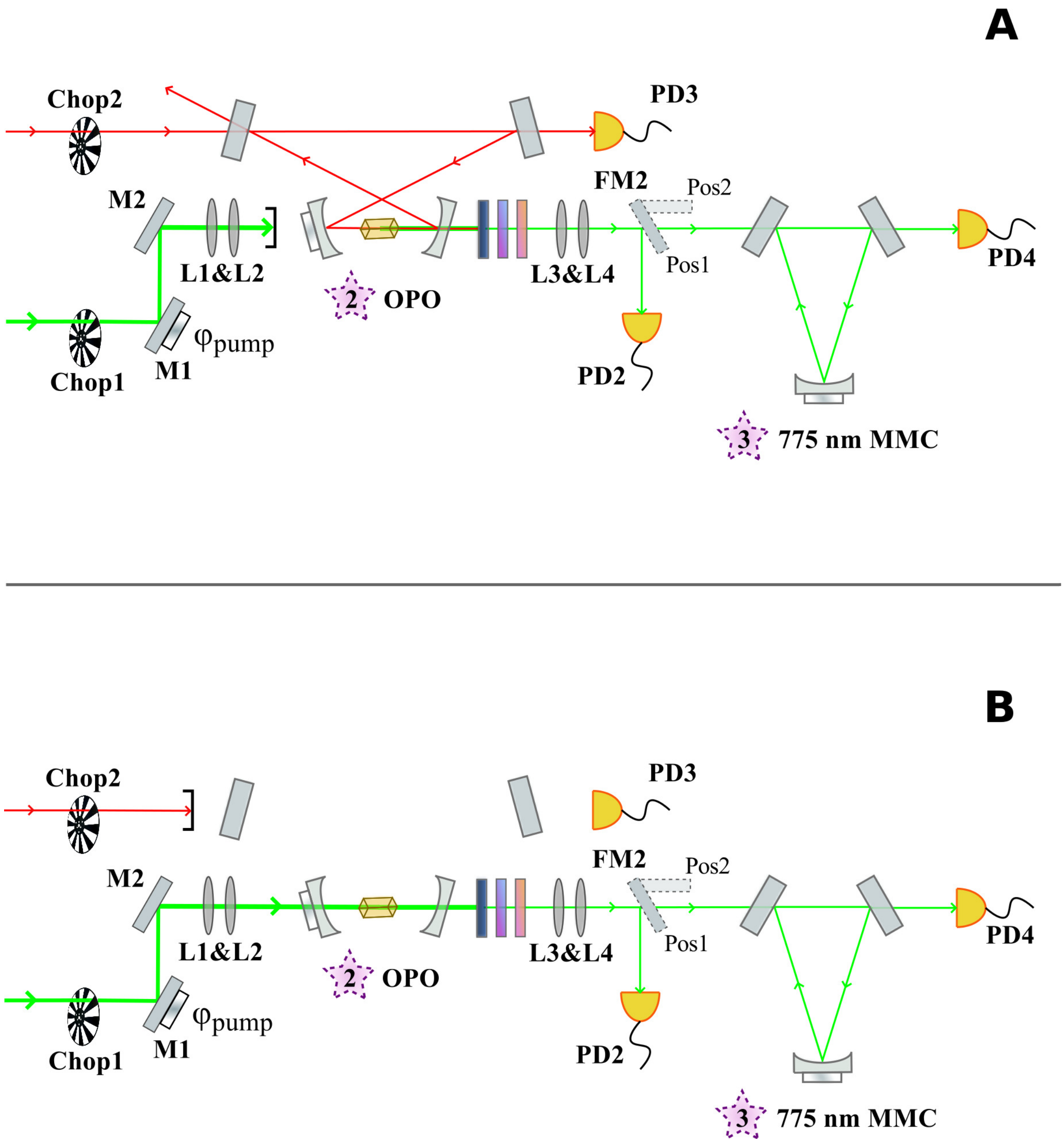

Figure 4.13: Schematic diagram of 775 nm mode-matching cavity (MMC) used to improve pump alignment and mode-matching into the OPO. A 'flipper mirror'(*FM2*) can be set in one of two positions as illustrated (*Pos1* or *Pos2*); *Pos2* sends the 775 nm light towards the MMC. A) Optical configuration used to construct, align, and mode-match the MMC to the seed-generated 775 nm beam which is transmitted by the OPO. B) Optical configuration used to align and mode-match the pump beam into the MMC. Red beam: 1550 nm, green beam: 775 nm, M1 & M2: pump beam-steering mirrors, L1 & L2: mode-matching optics for pump beam into OPO, L3 & L4: mode-matching optics for MMC, PD2 & PD4: silicon photondetectors, PD3: fast InGaAs photodetector.

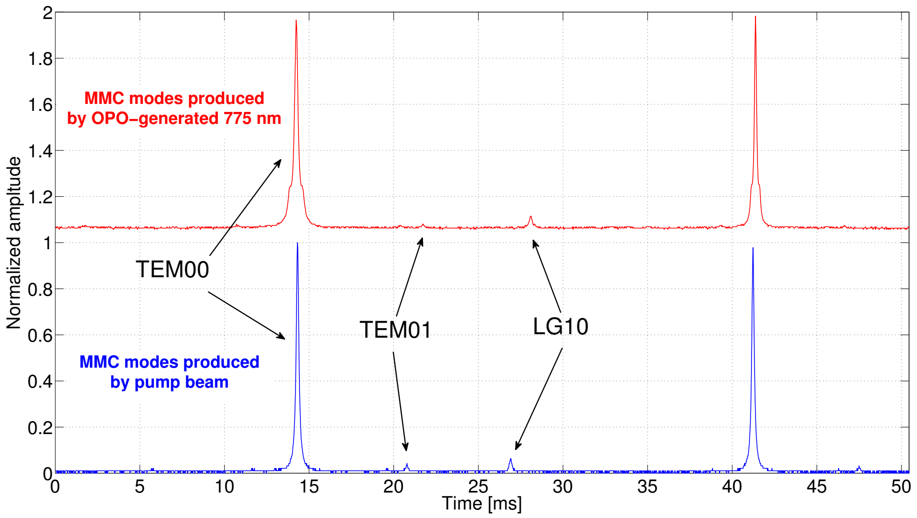

Figure 4.14: Transmission spectrum from the 775 nm mode-matching cavity for different input fields as the path length is varied with a piezoelectric transducer. The top red trace corresponds to the mode structure from the OPO-generated 775 nm beam as the input field, whereas the bottom blue trace corresponds to the pump beam as the input field.

4.2.6 775 nm mode-matching cavity

The importance of high-quality alignment and mode-matching of the 775 nm pump beam to the OPO was briefly mentioned in the beginning of this chapter. Nonlinear behaviour is dependent on a strong interaction between the down-converted pump field and the OPO cavity mode of interest. Coarse alignment of the pump beam into the OPO can be performed by maximising the parametric gain signal from the cavity. However, this technique does not provide sufficient information concerning the quality of mode-matching between the pump beam and the OPO. Therefore, a 775 nm 'mode-matching cavity' (MMC) was constructed to allow for mode-mismatch to be quantified, and to provide a more sensitive response to pump misalignment. Low mode-mismatch and good pump alignment is heralded when a similar mode structure of the mode-matching cavity is observed whether the circulating field originated from the pump beam or from the OPO-generated 775 nm light.

Figure 4.13 is a simplified schematic of the construction and use of our three-mirror 775 nm MMC. The schematic depicts the alignment procedure for first constructing the MMC, and then using it to improve and quantify the alignment and mode-mismatch of the pump beam into the OPO. The first step in constructing a 775 nm mode-matching cavity is to generate the second harmonic from the OPO (figure 4.13A). This is achieved by increasing the intensity of the 1550 nm input field until a detectable amount of 775 nm is produced. For this system, 380μW of 775 nm is produced by our phase-locked OPO for an input 1550 nm power of 15.6 mW. The high-power pump beam is blocked from entering the OPO during this procedure, as illustrated in figure 4.13A. Therefore, the 775 nm light entering the MMC is generated by the bright 1550 nm beam undergoing parametric up-conversion in the OPO (which is temporarily acting as an SHG). The MMC is then mode-matched and aligned to this OPO-generated 775 nm field. The optics used to mode-match the 775 nm light into the MMC are labelled *L3* & *L4* in figure 4.13A.

The top oscilloscope trace in figure 4.14 shows the final mode-structure after the MMC was aligned to the OPO-generated 775 nm field. The ultimate goal when constructing a single-mode optical cavity is to achieve a completely single-mode structure (e.g. have only the fundamental transverse electromagnetic (TEM) mode (TEM00) present). However, this was not a requirement for the MMC's structure as this cavity will only serve as a means of *comparison* between the pump and the OPO fields. We will compare the MMC's mode structures produced by the OPO-generated 775 nm to that produced by the pump beam. Therefore, the presence of small higher-order modes, such as a Laguerre-Gaussian mode, LG10, (which indicates slight mode-mismatch between the OPO field and the MMC) and TEM01 (a misalignment mode), will not affect the final outcome as the *ratios* of these higher-order modes to the fundamental TEM00 mode will be compared for the different input fields.

Once the MMC has been aligned and mode-matched to the OPO-generated 775 nm field, the MMC can be used to improve and quantify the pump alignment and mode-mismatch to the OPO-generated mode. First the 1550 nm seed beam is blocked from entering the OPO, and the pump beam is allowed to pass through the OPO and into the MMC (figure 4.13B). There are two beam-steering mirrors in the pump path before the OPO, *M1* and *M2*, which allow for adjustments to the beam alignment into the OPO. There are also optics in the beam path before the OPO which are used to mode-match the pump beam into the OPO, and are labelled *L1* & *L2* in figure 4.13B. Adjusting these mirrors and lenses has a cascading affect on the alignment and mode-matching of the pump beam into the MMC. Thus, the alignment of the pump beam can be adjusted using this set of optics until the mode-structure of the MMC generated by the pump beam is similar to that generated by the OPO field.

The bottom oscilloscope trace in figure 4.14 shows the final mode-structure produced by the pump beam after it was realigned to the cavity mode dictated by the MMC (and hence by the OPO). The mode ratios for the OPO-generated 775 nm field compared to that generated by the pump beam are listed for comparison in table 4.3. Comparing these mode ratios illustrates the high quality of both alignment and mode-matching between the pump beam and the OPO cavity field.

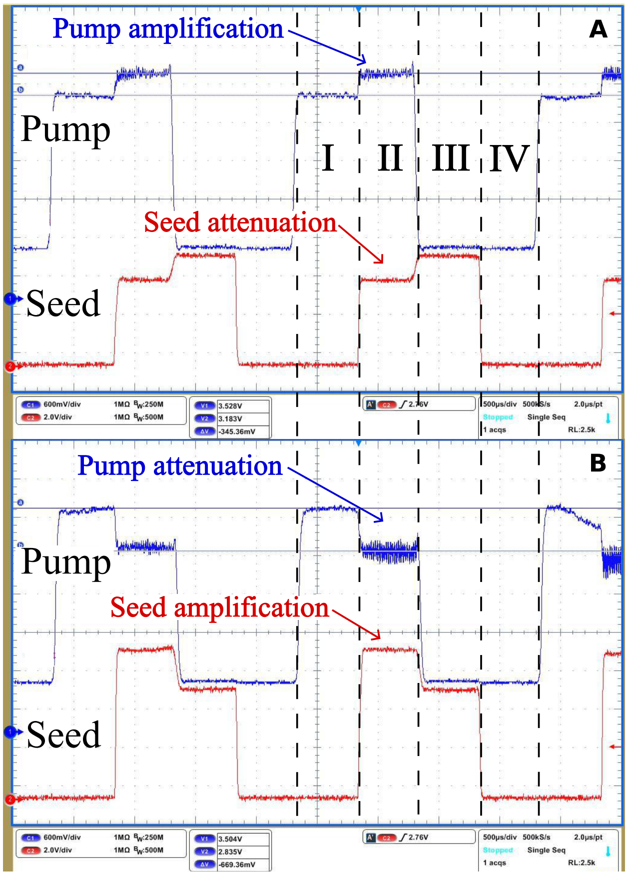

Figure 4.15: Observation of competing nonlinearities in the OPO between the pump beam (top blue) and a strong 1550 nm seed beam (bottom red) in stage II of the optical chopping period.

775 nm Source	$\frac{\text{LG10}}{\text{TEM00}}$	$\frac{\text{TEM01}}{\text{TEM00}}$
OPO	5.0%	1.7%
SHG	4.5%	1.7%

Table 4.3: Typical set of measurements to quantify the mode-mismatch and alignment quality of the pump beam into the OPO. The mode structure of the 775 nm mode-matching cavity is compared for the two different 775 nm input fields.

The presence of competing nonlinearies between the pump and the OPO field is further indication of the high-quality of pump mode-matching and alignment to the OPO. Parametric amplification and attenuation of the *pump* field was observed in the OPO for a bright 1550 nm input field (figure 4.15). As the optical phase of the pump beam is swept (ϕ_{pump} on *M1* in figure 4.13), parametric behaviour is observed in stage II of the four measurement stages which are bought about while operating the experiment in 'chop-lock mode' as described earlier in §4.2.3. Figure 4.15A is an oscilloscope trace of the fundamental field undergoing parametric attenuation ('seed attenuation') due to nonlinear interactions with the down-converted pump field. At the same time the *pump* field experiences amplification ('pump amplification') from interactions with the OPO-generated second harmonic field. As evident in figures 4.15A and 4.15B, these two processes have an orthogonal phase relationship: as the pump undergoes attenuation, the seed undergoes amplification, and vice versa. The observation of competing nonlinearies is also an indication that the assumption made in the simplified cavity model that the pump can be treated as a static field is not applicable [242]. Therefore, the 1550 nm input field power was decreased until this interaction was no longer observed so that the simplified cavity model of nonlinear behaviour would be applicable.

4.2.7 Tap-off beamsplitter reflectivity

The ideal reflectivity of the tap-off beamsplitter in a projected state experiment (shown in figure 4.16) depends on several experimental parameters. These parameters have been thoroughly investigated for photon-subtracted squeezed vacuum state experiments at various wavelengths [227, 265, 304]. The tap-off beamsplitter reflectivity, r_2, must be optimized to obtain a high-quality quantum non-Gaussian state with the minimum possible value of the Wigner function at the origin, W(0,0). The quality of a quantum non-Gaussian state can also be quantified by the 'quantum non-Gaussian character witness,' which was introduced by Filip and Mišta Jr. as a novel measurement of non-classicality for Gaussian and non-Gaussian states with positive Wigner functions [305]. Maximising this quantity corresponds to maximis-

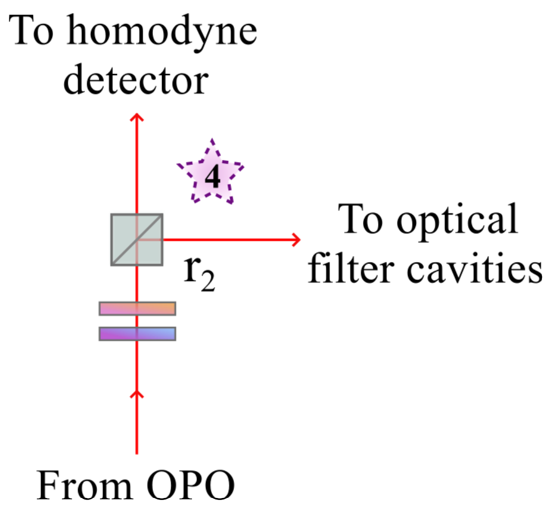

Figure 4.16: Schematic diagram of tap-off beamsplitter in projected state experiment.

ing the non-Gaussian qualities of the measured state. This non-classicality measure will be explained in more detail in §6.1.

The projecting detector in experiments at $\sim$ 860 nm tend to be silicon (Si) single-photon detectors, whereas experiments conducted at $\sim$ 1550 nm typically use indium gallium arsenide (InGaAs) detectors. Standard InGaAs single-photon detectors (APDs) have significantly lower quantum efficiencies and higher dark count probabilities compared to Si-APDs. Dark counts are false detection events that occur in the single-photon detector that do not correspond to a photon-subtraction event from the squeezed vacuum state. It has been shown that a high dark count probability and low detection efficiency can have a negative influence on the quality of the projected state [227,265,304]. These effects can be compensated for somewhat by increasing r_2, and therefore ensuring the count rate from real photon-subtraction events is higher than the dark count rate.

However, there is a limit to increasing r_2 as too high of a reflectivity begins to degrade the quality of the projected state, as illustrated in figure 4.17. A variety of single-photon detector types were numerically investigated for both the Si and InGaAs wavelengths using the theoretical model outlined in §2.6. These types included a perfect photon-number-resolving detector, a perfect non-photon-number-resolving detector, an imperfect photon-number-resolving detector, and an imperfect non-photon-number-resolving detector. As shown in figure 4.17, the optimal value of r_2 for a Schrödinger kitten state prepared with a Si-APD ($r_2 = 0.01$) is notably smaller than for state preparation with an InGaAs-APD ($r_2 = 0.09$) [304]. These calculations were based on experimental parameters similar to our experiment [304].

Under the circumstances of a Si-APD, the smaller r_2 results in a better character witness value and a deeper W(0,0). However, if r_2 is too small, then it is easy to

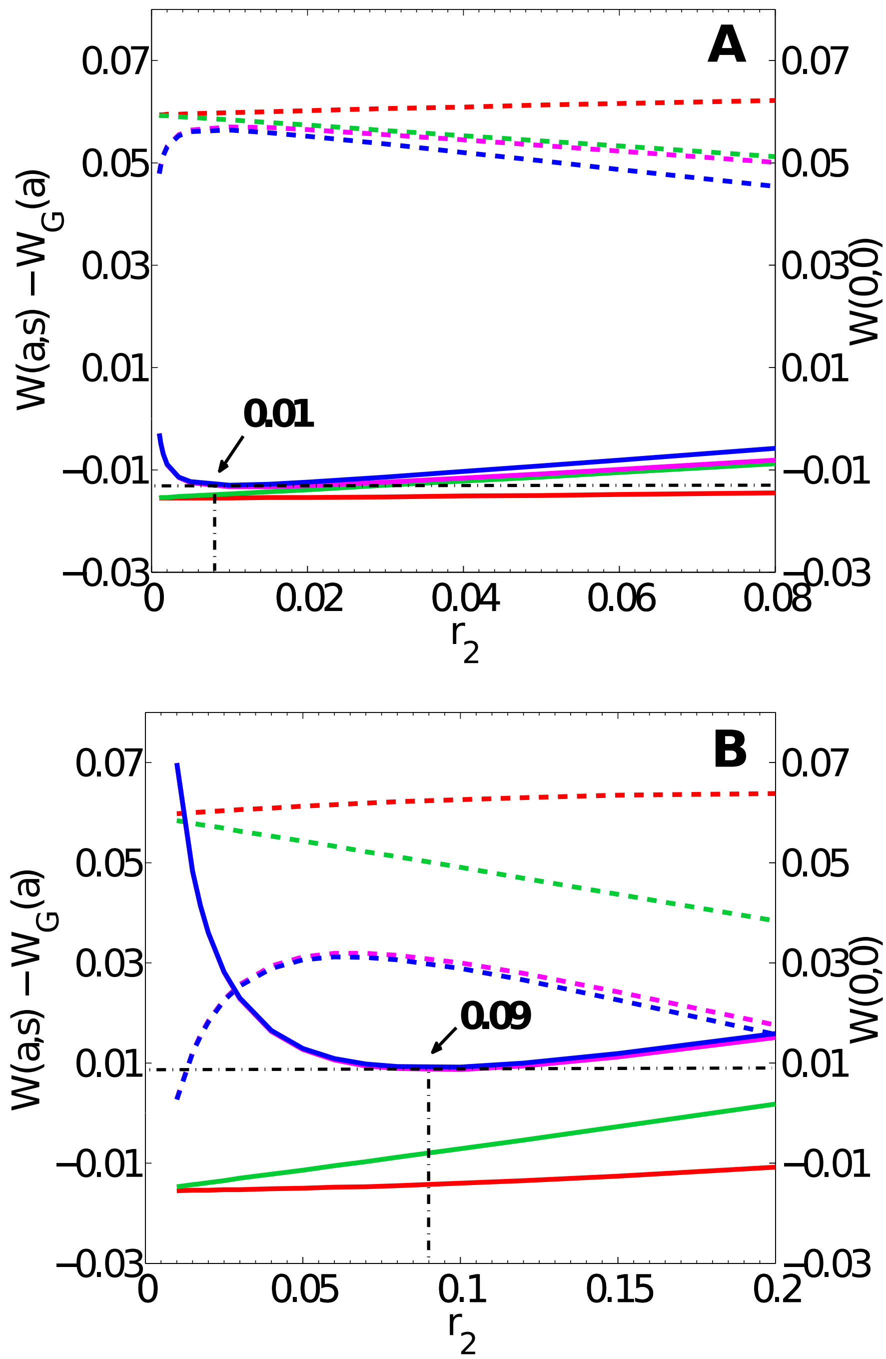

Figure 4.17: Quantum non-Gaussian character witness and $W(0,0)$ as a function of tap-off beamsplitter reflectivity, r_2 for A) a Si-APD and B) an InGaAs-APD. Dash lines and solid lines represent $W(a,s) - W_G(a)$ on left vertical axis and $W(0,0)$ on right vertical axis, respectively. Red: perfect photon-number-resolving detector, green: perfect non-photon-number-resolving detector, pink: imperfect photon-number-resolving detector, blue: imperfect non-photon-number-resolving detector.

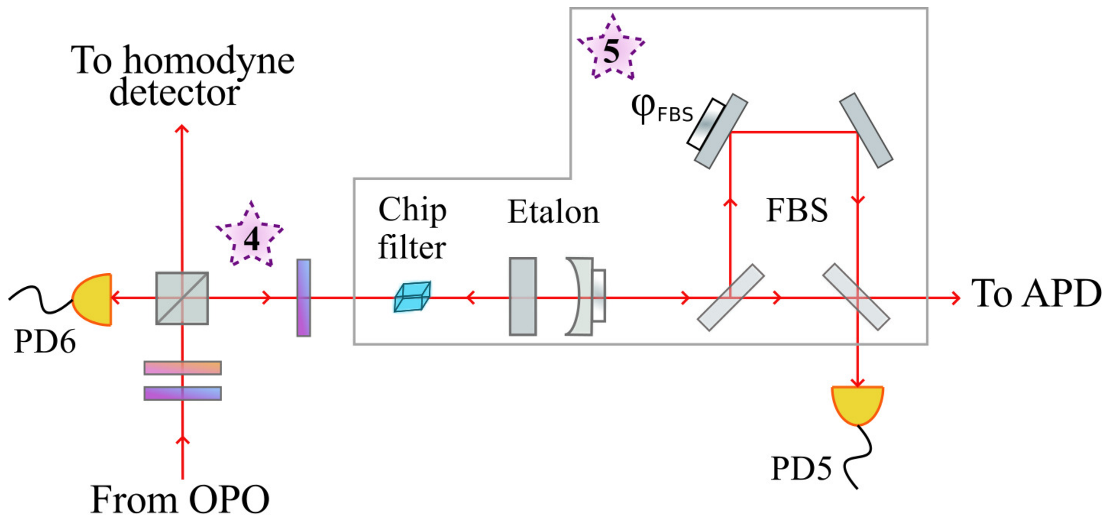

Figure 4.18: Schematic diagram of the optical filter cavities used in the projected state experiment.

induce false clicks since the number of real APD counts, which are proportional to r_2, will be lower than the amount of dark counts. Therefore, it is necessary to compromise a small r_2 that is still high enough to ensure the count rate is larger than the dark count rate. This has been validated by the results reported in most kitten state generation experiments using Si-APDs [216,217,221,227]. The measured value for the tap-off reflectivity in our experiment is $r_2 = 8\%$, which was close to optimum for our system.

4.2.8 Optical filter cavities

The interaction of the squeezed vacuum field with the tap-off beamsplitter results in the separation of the trigger field from the signal field. The trigger field is sent to the APD and used to herald photon-subtracted squeezed vacuum states at the homodyne detector. However, as a SS-NOPO generates a frequency comb of entangled side-band pairs, it is important to isolate particular pairs of side-bands in this trigger field so as to generate projected states in the desired frequency modes. Therefore, the spectrum of the trigger field is filtered by a series of optical cavities, as shown in figure 4.18. These cavities were engineered with the intention to isolate a particular frequency side-band pair at ±515 MHz from the entangled comb produced by the SS-NOPO. However, as we discussed in §3.2.2, the overall frequency transmission function of these cavities includes a small portion of ±1030 MHz and ±1545 MHz side-bands. We will now introduce the three filter elements and describe their purpose in shaping the trigger spectrum. Their optical properties and locking parameters are summarized in table 4.4.

4.2.8.1 Chip filter

The first element in the filtering system is a 'chip filter' (Bookham, part number TF100-1549315-0783). This device is a thin-film narrowband interference filter with a transmission passband centred on 1549.315 nm (the laser wavelength). The purpose of this 'top-hat' filter is to restrict the SS-NOPO frequency comb from ~ 2 THz to ~ 100 GHz. Frequency locking this filter is not required as it is a bulk optical device.

Filter element	Type	Linewidth (FWHM)	FSR or Measured ω_m	Dither locking frequency
Chip filter	Top-hat filter	3.7 GHz	1000 GHz	—
Etalon	Linear empty cavity	1.3 GHz	338 GHz	26.1 kHz
FBS	Unbalanced Mach-Zehnder interferometer	—	509 MHz	31.14 kHz

Table 4.4: Summary of properties and locking parameters of the elements which compose the optical filtering system. ω_m is the actual FBS frequency; this was designed to be $\omega_m = \omega_s = 515$ MHz; the constructed FBS has $\omega_m = 509$ MHz.

4.2.8.2 Etalon

The second element is a free-space Fabry-Perot empty cavity called an etalon, as shown in figure 4.18. The purpose of this cavity is to maximise the transmission of ± 515 MHz side-bands to the FBS while minimising the transmission of other FSR side-bands. A compromise had to be made when designing its ideal linewidth due to the Lorentzian-shape of the transmission function. The FSR of the etalon also needed to be well outside the bandwidth of the chip filter to suppress side-bands at undesirable frequencies within the top-hat transmission function.

The cavity was frequency-locked to the laser using a dither locking technique [303]. A modulation signal at 26.1 kHz was sent to the piezo to modulate a cavity mirror. This modulation frequency was purposely chosen close to a resonance frequency of the piezo to maximise the modulation depth. The reflected light from the etalon was measured by photodetector *PD6* (see figure 4.18). This photodetector signal was mixed-down with the original modulation signal, and the result was low-pass filtered to give a bipolar error signal. This locking system was extremely robust to any disturbances and could stay locked for hours.

4.2.8.3 Frequency beamsplitter

The final filtering cavity is an unbalanced Mach-Zehnder interferometer which acts as a frequency beamsplitter (FBS) to spatially separate frequency side-bands. The physics of how this interferometer works was described in §2.3.3 and a schematic of the FBS is shown in figure 4.18. The interferometer first separates the input beam on a 50/50 beamsplitter. The output beams follow different path lengths before recombining on a second 50/50 beamsplitter. It has been experimentally demonstrated that the path-length difference can be purposely engineered to provide a particular phase-shift to side-bands at specific frequencies, which spatially separates them at the outputs [101].

Our FBS has a design frequency of $\omega_s = 515$ MHz and a path length difference which spatially separates the $\pm\omega_s$, $\pm 3\omega_s$, $\pm 5\omega_s$, … side-bands from the optical carrier and $\pm 2\omega_s, \pm 4\omega_s, \ldots$ side-bands. The path-length difference, $p_{_{FBS}}$, required to achieve this spatial separation is defined as

$$p_{_{FBS}} = \frac{c\pi}{\omega_s} = \sim 29\text{cm}. \tag{4.8}$$

Therefore, an FBS with this path length difference will send light at $\pm\omega_s$, $\pm 3\omega_s$, $\pm 5\omega_s$, … frequencies towards the APD in our experiment, while the light at Ω_0, $\pm 2\omega_s$, $\pm 4\omega_s$, … frequencies are sent towards the photodetector, *PD5* (see figure 4.18). We referred to an FBS with this path length configuration as 'configuration *A*' in §2.3.3.

The signal from *PD5* is used to frequency lock the optical-scale phase shift due to the piezo-mounted mirror labelled $\phi_{_{FBS}}$ in figure 4.18. A dither-locking technique similar to the etalon locking system (but using a different modulation frequency of 31.14 kHz) is used to lock $\phi_{_{FBS}} = 0$. This optical phase reflects the optical carrier and $\pm 2\omega_s$, $\pm 4\omega_s$, … frequencies away from the APD, and sends the $\pm\omega_s$, $\pm 3\omega_s$, $\pm 5\omega_s$, … frequencies towards the APD. An optical phase of $\phi_{_{FBS}} = \pi$ would do the opposite and transmit the Ω_0, $\pm 2\omega_s$, $\pm 4\omega_s$, … frequencies to APD.

The quality of interference depends on the mode-matching and alignment of the beams in the interferometer, and can be quantified by measuring the interference visibility, $\zeta_{_{FBS}}$. In the case of an FBS in configuration *A*, an ideal visibility of $\zeta_{_{FBS}} = 1$ corresponds to the perfect spatial separation of the Ω_0, $\pm 2\omega_s$, $\pm 4\omega_s$, … frequencies from the $\pm\omega_s$, $\pm 3\omega_s$, $\pm 5\omega_s$, … frequencies. Therefore, the interference visibility can quantify the spatial separation efficiency of frequency side-bands by this filter element.

The interference visibility is measured by sweeping the optical phase $\phi_{_{FBS}}$ to move between $\phi_{FBS} = 0$ and $\phi_{FBS} = \pi$, and calculating

$$\zeta_{FBS} = \frac{\mathcal{U}_{max} - \mathcal{U}_{min}}{\mathcal{U}_{max} + \mathcal{U}_{min} - 2\mathcal{U}_{dark}}, \tag{4.9}$$

where $\mathcal{U}_{max}$ corresponds to the maximum voltage of the interference sine wave (which occurs when $\phi_{FBS} = 0$), $\mathcal{U}_{min}$ corresponds to the minimum voltage (which occurs when $\phi_{FBS} = \pi$), and $\mathcal{U}_{dark}$ is the electronic noise floor of the photodetector, *PD5*. The measured fringe visibility of our FBS was 92%, which meant $\sim$ 8% of the undesired frequencies (Ω_0, $\pm 2\omega_s$, $\pm 4\omega_s$, $\ldots$) were accidentally sent to the APD when the FBS was phase-locked to $\phi_{FBS} = 0$.

4.2.9 APD fibre coupling efficiency, η_f

The final stage of the experiment is to couple the free-space light transmitted by the FBS into the fibre optic cable connected to the APD (Id Quantique, id-200). It is crucial to capture as much light from the trigger field as possible. Any loss reduces the number of real photons that could be detected by the APD. Decreasing this count rate relative to the already high dark count rate can diminish the quality of the projected state. Each data collection event triggered by a non-photon-subtracting event results in the homodyne detector measuring an unprojected two-mode squeezed vacuum state instead of a projected photon-subtracted two-mode squeezed vacuum state. Since a Gaussian state has a completely positive Wigner function, adding this quantum state to the non-Gaussian quantum state greatly reduces the negativity near the origin in phase space.

A possible source of APD events triggered by non-photon-subtracting events is the leakage of local oscillator photons into the APD fibre. This beam does not pass through an optical chopper, and must be constantly 'on' during data collection for the purposes of quantum state tomography of the projected state. Due to the sensitive nature of single-photon experiments, any detection of an LO photon by the APD corrupts the quality of the projected quantum non-Gaussian state. While monitoring the APD count rate during realignments of the experiment, it was discovered that the count rate rose dramatically when the LO was unblocked and allowed to enter the homodyne detection set-up. It was inferred from this observation that LO photons were reflecting off the photodetectors in the experiment and travelling down the optical filter system into the APD fibre. The possible path these reflected LO photons could be taking to reach the APD fibre is illustrated in figure 4.19A.

An optical circulator was placed within the homodyne detection set-up to minimise these reflected photons from reaching the APD. The circulator consists of two quarter-wave plates, a half-wave plate and a polarising beamsplitter, as shown in

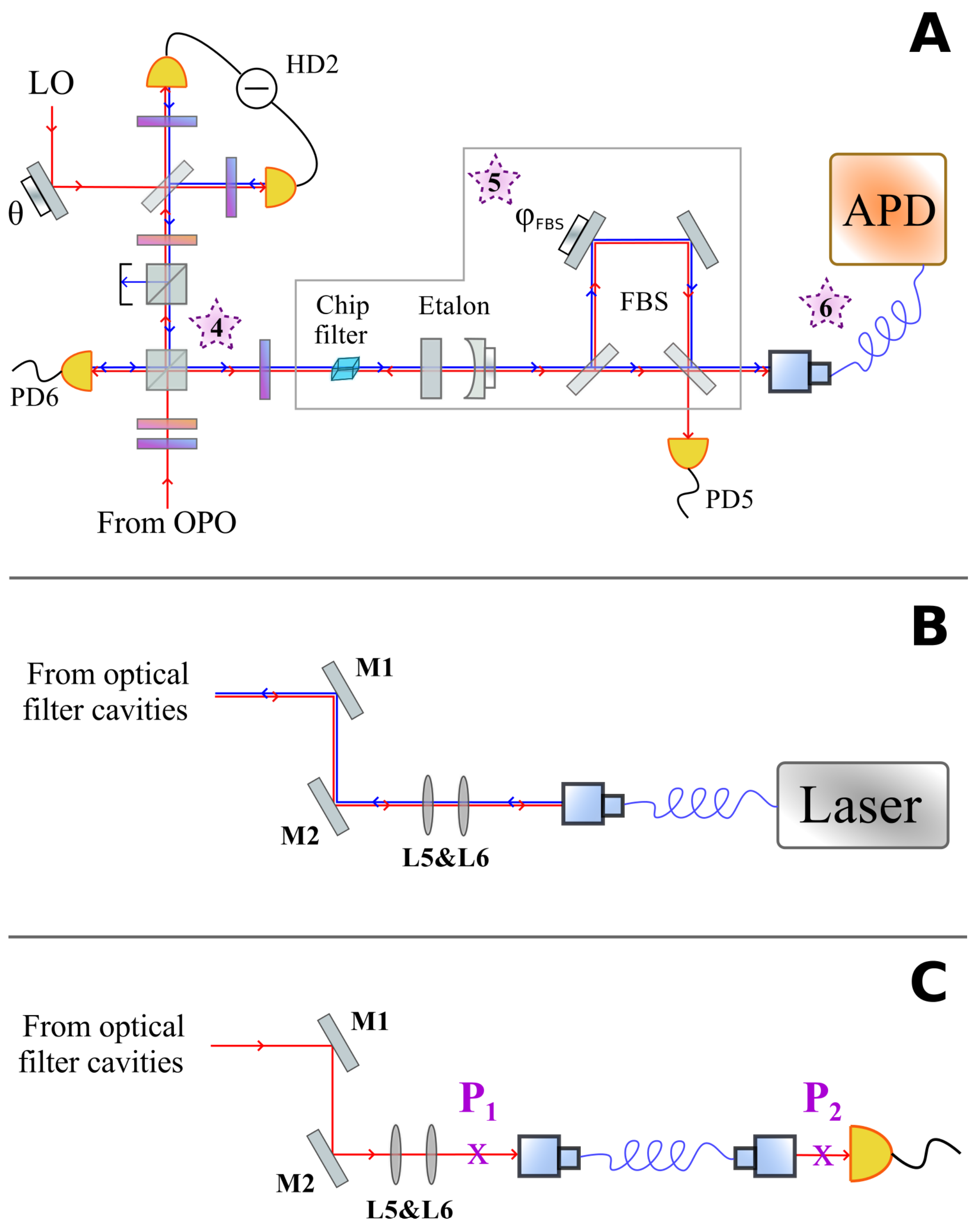

Figure 4.19: Schematic diagrams of coupling light transmitted by the optical filter cavities into the APD fibre optic cable. A) Schematic illustrating potential pathways light may reflect off photodetectors and travel to the APD fibre; blue: reflected beams off photodetectors. B) Procedure for aligning light from optical filters into the APD fibre; blue: direction of light travelling from laser. C) Procedure for measuring the fibre coupling efficiency, $\eta_f = P_2/P_1$.

figure 4.19A. Fortunately, most of the LO photons are blocked from the APD by the FBS when it is phase-locked to $\phi_{FBS} = 0$ (i.e. pass the carrier to *PD5*). However, the wave plates in the circulator must be tuned to minimise the amount of reflected photons from *reaching* the FBS. Therefore, our alignment technique involves phase-locking the FBS to pass the carrier to the APD, which maximises the APD count rate caused by leaking LO photons. Despite the low detection efficiency of our APD ($\eta_{APD} = \sim 8\%$), locking the FBS phase to pass the LO photons to the APD allows us to see a real time reaction in the count rate as we tune the circulator wave plates. The wave plates are tuned until the APD count rate is lowered to dark count levels (~ 10 counts/sec). We cannot tune the wave plates with any further precision due to the APD's poor detection efficiency and high dark count rate.

In order to achieve a high fibre coupling efficiency, the light from the experiment needs to be aligned to the same spatial mode and alignment plane as projected by light leaving the fibre. Therefore, a common alignment technique is to send light *through* the fibre you wish to couple into, and spatially overlap this beam with the light from your experiment. This procedure is illustrated in figure 4.19B by the blue beam emanating from the fibre ('fibre beam') and the red beam coming from the optical filter cavities. This alignment procedure again involved phase-locking the etalon and FBS to pass the carrier to the APD, which provided a bright enough beam from the experiment to see on an IR card. Then light from the laser was connected to the APD fibre, and a beam profiler was used to measure the fibre beam's waist position and size. The light from the FBS was then mode-matched to the beam profile of the fibre beam using lenses *L5* & *L6* in figure 4.19B.

The spatial alignment of the FBS beam onto the plane of the fibre beam was done using two beam-steering mirrors labelled *M1* & *M2* in figure 4.19B, and the X-Y-Z mount of the APD fibre coupler. First coarse alignment of the two beams was achieved via beam-walking. Then fine-tuning of this alignment was accomplished by utilising various reflections caused by the fibre beam entering the optical filter system 'backwards.' Thus the mode-structure of the etalon cavity was used like a mode-matching cavity to fine-tune the alignment of the two beams. Light from the fibre would interact with the etalon and reflect back to *PD5*. Since the etalon was already well-aligned to the beam from the experiment, it was reasonable to assume that achieving a similar mode-structure (i.e. single-mode) with the fibre beam would improve the coupling efficiency. This was accomplished by blocking the light from the experiment from entering the etalon, sweeping the cavity, and adjusting the X-Y-Z mount of the fibre coupler to beam-steer the light into the etalon until a single-mode structure is observed via $PD5$.

Finally, the fibre coupling efficiency was quantified by disconnecting the laser to the APD fibre, phase-locking the etalon and FBS to pass the carrier to the APD, and measuring the APD fibre *output* with a power meter (figure 4.19C). The coupling efficiency from free-space to fibre is determined by comparing the optical power just before the coupling collimator, P_1, to the optical power inside the fibre. However, it can be difficult to do an accurate 'in-fibre' power measurement. Therefore, we use a second collimator to transmit the coupled light back into free-space and measured the light with a standard power meter, P_2. The loss from the second collimator is minimal and therefore can be ignored. We measured the free-space to fibre coupling efficiency to be $\eta_f = P_2/P_1 = 0.73$.

4.3 Characterising classical parameters of optical cavities

The properties of a quantum state produced by an optical cavity rely on classical parameters of that cavity, such as its linewidth and FSR. Therefore these parameters need to be accurately measured. Furthermore, knowing the frequency transmission function of the optical filter system in our projected state experiment becomes important when applying temporal mode-matching to the captured homodyne signal. Since we are interested in quantum states at particular side-bands frequencies, post-processing the homodyne data from our experiment requires a *frequency-offset* temporal mode-matching function (or 'spectral mode-function'). This spectral mode-function is designed to select the part of the homodyne signal which is correlated with the detected trigger mode. Since the filter cavities shape the trigger mode spectrum, it is important to know the frequency transfer function of this filter system. Therefore, two techniques were investigated to measure the linewidth and FSR frequencies of the optical cavities using an intensity modulator.

4.3.1 Calibrating the horizontal axis of oscilloscope

The linewidth and FSR of the OPO and filter cavities that were summarised in tables 4.2 and 4.4 were measured using two basic techniques involving amplitude modulation side-bands. The first technique is well-known and involves placing amplitude modulation on the carrier to calibrate a frequency scale to an oscilloscope's horizontal axis as the transmission spectrum from a cavity is measured. A basic photodetector is used to measure the transmitted light from the cavity as the path length is varied by sweeping a mirror with a piezoelectric transducer. The cavity is used as an 'optical spectrum analyser' to display the frequency of the amplitude side-bands relative to the carrier [306]. A fibre broadband low-loss $LiNbO_3$ electro-optic intensity modulator (EOspace, AZ-0K5-10-PFA-PFA-UL) was used to

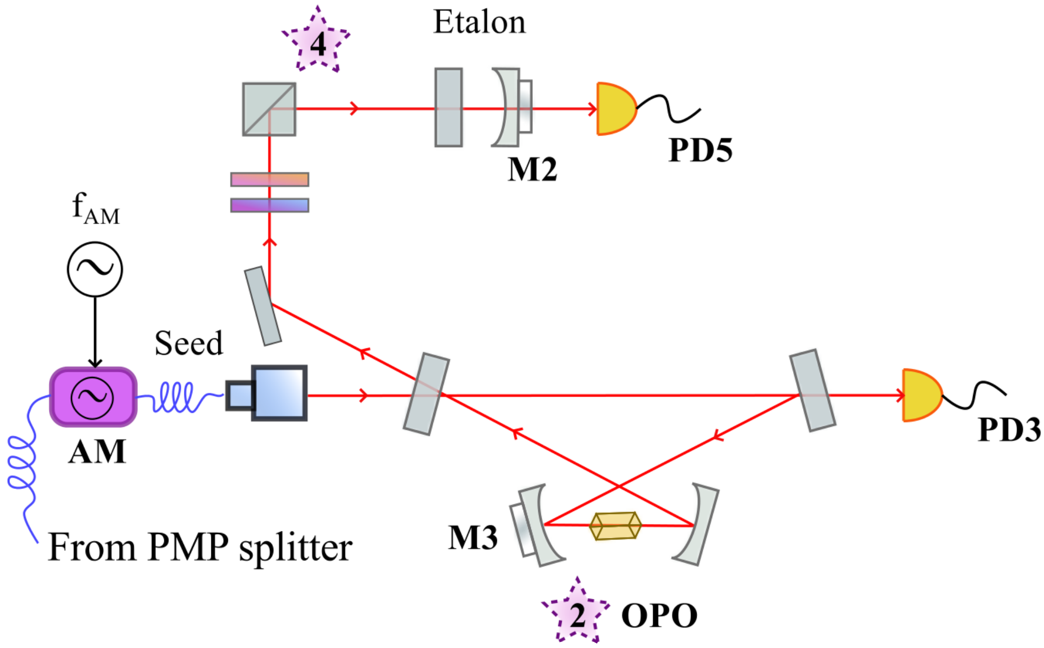

Figure 4.20: Schematic diagram of measurement technique used to measure the linewidth and FSR of the OPO and etalon. Amplitude modulation at f_{AM} is placed on the carrier and used to calibrate a frequency scale to the horizontal axis of an oscilloscope trace. AM: fibre amplitude modulator

generate amplitude modulation side-bands at a range of frequencies, f_{AM}. These side-bands were then used to calibrate the horizontal axis of an oscilloscope trace to a frequency scale. A schematic of this experimental technique is shown in figure 4.20.

Figure 4.21 shows oscilloscope traces of this side-band method being applied on the OPO (figure 4.21A) and etalon (figure 4.21B). By placing amplitude modulation side-bands at known frequencies, the horizontal axis of the scope was calibrated to a frequency scale, so that the FSR and linewidth could be determined. Figure 4.21A shows the OPO transmission spectrum measured by *PD3* as *M3* is swept at a frequency of 4 Hz (see figure 4.20). The 80 MHz side-bands are clearly visible symmetrically about the fundamental cavity mode (TEM00). Using this technique led to the estimation that the OPO linewidth is 8.767 ± 0.1 MHz (FWHM) and the FSR is 516.6 ± 0.33 MHz.

Due to the much larger linewidth and FSR of the etalon, measurements of its linewidth and FSR required the highest modulation frequency produced by our signal generator, which is 3 GHz. Figure 4.21B shows the etalon transmission spectrum measured by *PD5* as *M2* is swept at a frequency of 8 Hz (see figure 4.20). Again these 3 GHz side-bands were used to calibrate the horizontal axis of the oscilloscope and the linewidth was estimated to be 1.23 ± 0.03 GHz (FWHM) and the FSR to be 337.6 ± 0.83 GHz.

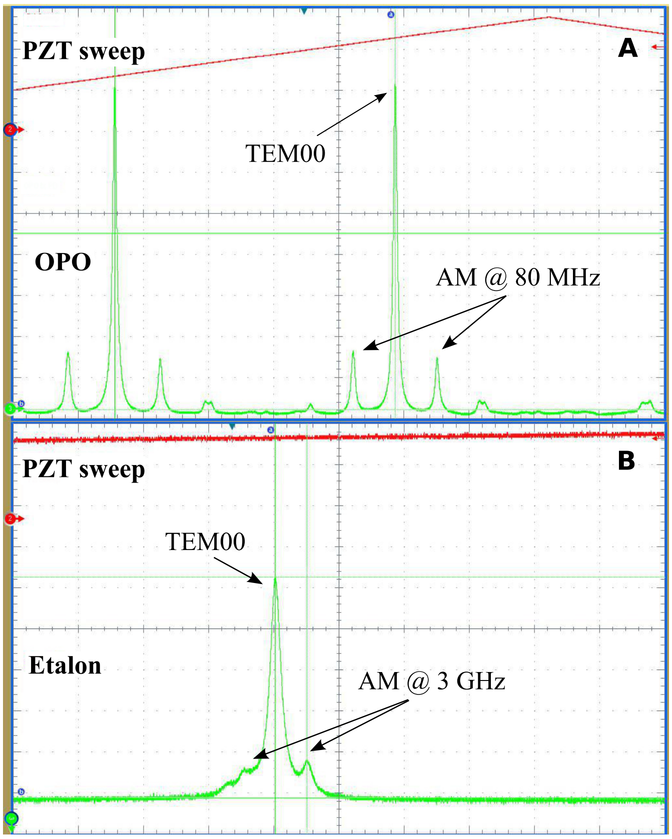

Figure 4.21: Oscilloscope screenshot of the OPO and etalon transmission spectrums with amplitude modulation (AM) side-bands placed on the carrier (green trace). Both cavities are aligned such that the TEM00 mode is the dominant mode. A) OPO transmission spectrum with 80 MHz AM as the cavity is swept at a frequency of 4 Hz (red trace). B) Etalon transmission spectrum with 3 GHz AM as the cavity is swept at a frequency of 8 Hz (red trace).

4.3.2 Measuring a frequency transfer function of an optical system

While characterising the experiment before undertaking a projected state data run, we discovered a novel way to measure the frequency transfer function of the optical filtering system and OPO *without* the need for a fast photodetector. A fibre amplitude modulator is used to place intensity side-bands on the light (see figure 4.22). This modulated light is sent to a cavity and the resulting transmitted (or reflected) power from this cavity is then recorded as a function of modulation frequency, f_{AM}. These low-frequency (DC) power measurements map the cavity linewidth and FSR.

We first used this technique on the OPO by phase-locking the cavity on resonance, and mapping the reflected power with a power meter (Newport, 918D-IR-OD3, S/N 10316) as a function of modulation frequency (see schematic in figure 4.22A). The etalon and FBS were phase-locked to pass the carrier to the power meter during these measurements. Since the OPO was locked on resonance to the carrier, the reflected power drops as the modulation frequency approaches the OPO linewidth centred on the first FSR (515 MHz). The results from these power measurements are shown in figure 4.23, where the minimum of the reflected power spectrum is centred on 515 MHz. Using this technique we were able to estimate the linewidth of the OPO to be 8.75 ± 0.1 MHz, which is within error of the estimated value found using the calibrated oscilloscope technique previously described. Table 4.6 shows a complete comparison between all measured values found using either technique.

For the next set of measurements, the circulating field in the OPO was 'blocked' to remove the influence of its reflected spectrum from the characterisation of the optical filter cavities (see figure 4.22B). The transmitted light from the filter cavities was measured as a function of amplitude modulation frequencies for two measurement configurations. In this first configuration, the etalon was frequency-locked to the carrier while the FBS optical phase ϕ_{FBS} was swept. As mentioned in §4.2.8.3, when only the optical carrier frequency is sent to the FBS (i.e. no side-bands are present), sweeping the FBS phase from $\phi_{FBS} = 0$ to $\phi_{FBS} = \pi$ sweeps the interference curve from maximum (i.e. sending the carrier towards *PD5*) to minimum (i.e. sending the carrier away from *PD5*). Therefore the FBS visibility, ζ_{FBS}, could be redefined as

$$\zeta_{FBS} \propto \frac{\left|P(\phi_{FBS} = 0) - P(\phi_{FBS} = \pi)\right|}{\left|P(\phi_{FBS} = 0) + P(\phi_{FBS} = \pi)\right|}, \tag{4.10}$$

where $P(\phi_{FBS} = 0)$ is the optical power sent to *PD5* when $\phi_{FBS} = 0$, and $P(\phi_{FBS} = \pi)$ is the optical power sent to *PD5* when $\phi_{FBS} = \pi$.

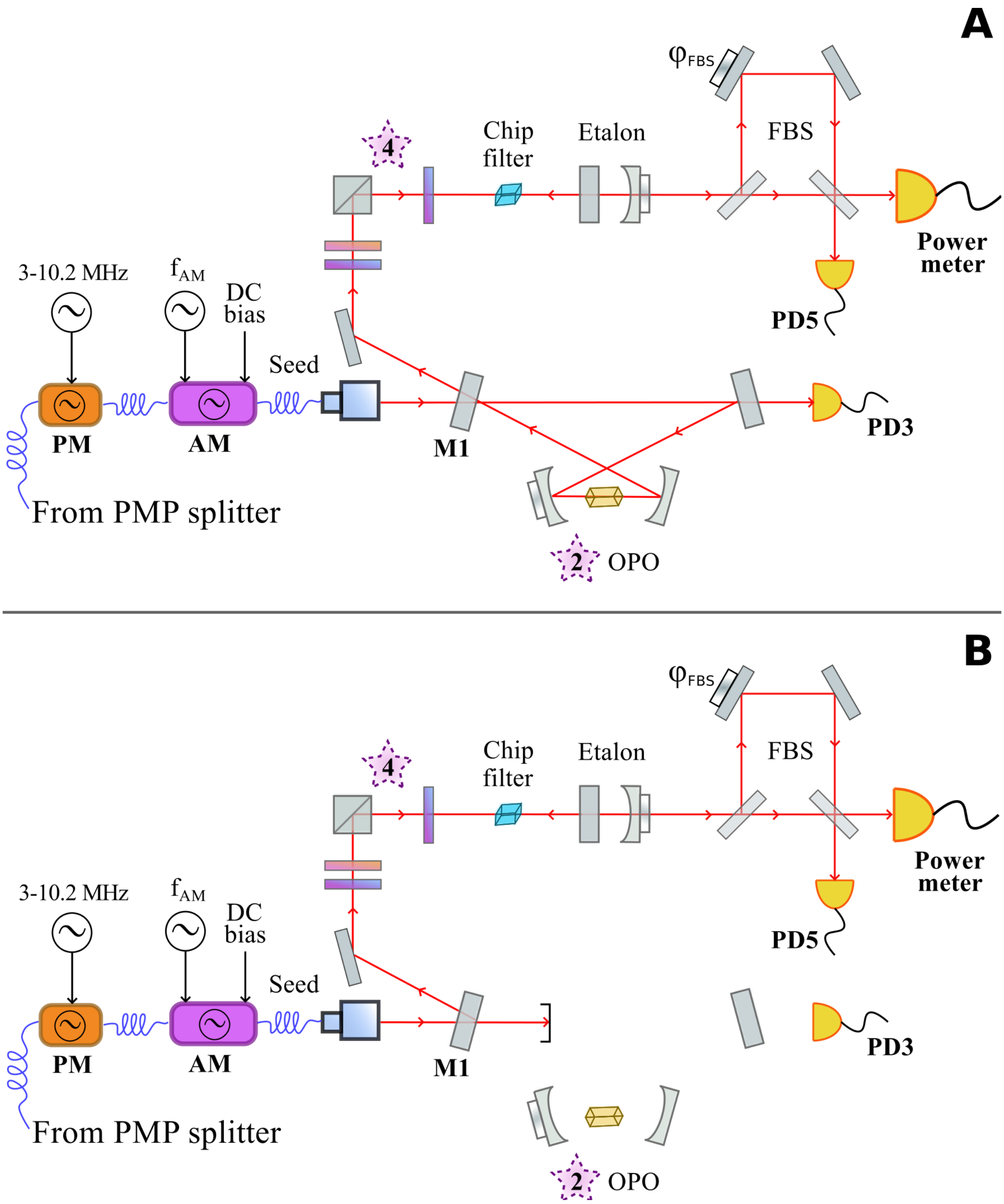

Figure 4.22: Schematic diagram of measurement technique used to characterise frequency transfer function of OPO and optical filter system. Amplitude modulation at f_{AM} is placed on the carrier and used to map the transmitted or reflected power as a function of modulation frequency. A) Schematic of how the linewidth and FSR of the OPO was characterised. B) Schematic of how the OPO was 'blocked' and the frequency transfer function of just the filter cavities was characterised. PM: fibre phase modulator, AM: fibre amplitude modulator.

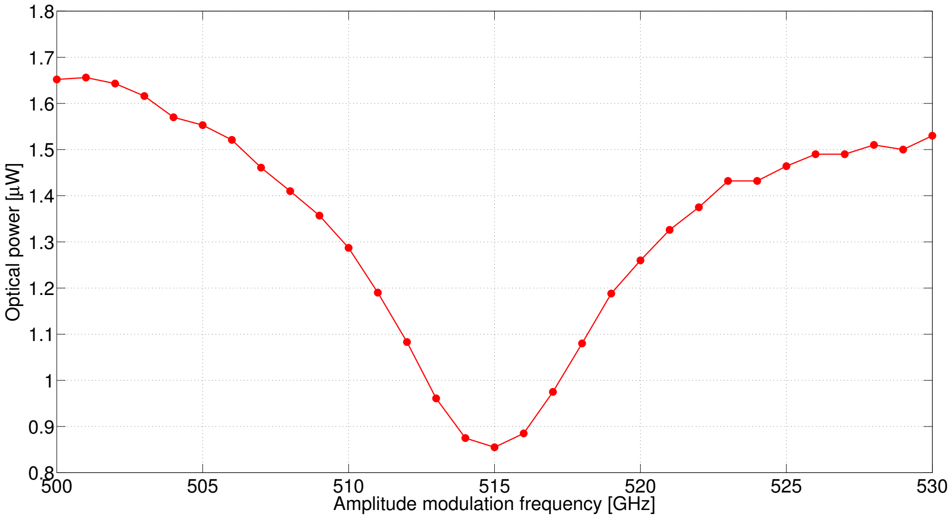

Figure 4.23: Characterisation of the OPO linewidth and FSR by intensity modulating the light at several frequencies and measuring the reflected optical power. The FWHM measurement from the experimental data shown gives a linewidth of 8.75 ± 0.1 MHz. The minimum of the spectrum occurs at the FSR of the cavity, which is measured to be 515 ± 0.2 MHz.

Take the scenario that the etalon and chip filter have been removed from the optical set-up, leaving only an ideal FBS in the filter chain. Amplitude modulation side-bands are placed on the carrier at exactly $\pm\omega_s$ (FBS design frequency), and the modulator is adjusted such that the sum of the side-bands' optical powers *equals* the optical power of the carrier, $P_c = P_{+\omega_s} + P_{-\omega_s}$. When the FBS phase is $\phi_{FBS} = 0$, the photodetector *PD5* outputs a voltage proportional to P_c. When the FBS phase is $\phi_{FBS} = \pi$, the photodetector *PD5* outputs a voltage proportional to $P_{+\omega_s} + P_{-\omega_s}$. Therefore, according to equation 4.10 the measured visibility becomes $\zeta_{FBS} = 0$ as $P(\phi_{FBS} = 0) = P(\phi_{FBS} = \pi)$. This measurement result does not mean the FBS has poor interference but simply that placing AM side-bands on the light affects the measurement. Therefore the measured FBS visibility will change as a function of modulation frequency. This effect can be exploited to experimentally determine the actual FBS frequency, ω_m, by measuring the visibility as a function of modulation frequency.

However, the etalon and chip filter are in the path way before the FBS in the actual experiment, which influences the power ratios between the amplitude side-bands and carrier before the spectrum reaches the FBS. Fortunately, this does not cause a problem as we are interested in the *overall* frequency transfer function, and not the individual functions of each filter element. The amplitude modulator has a DC bias input that can be used to adjust the optical power ratio between the side-bands relative to the optical carrier. The OPO can be used as an optical

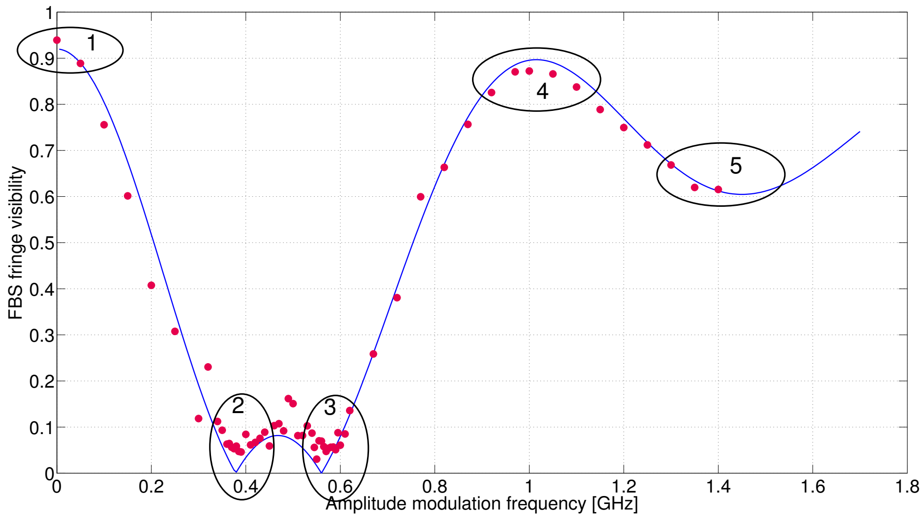

Figure 4.24: Characterisation of optical filter system with amplitude modulation for a sweeping FBS phase. The experimental data (red dots) is fitted with a theory curve (blue line) that modelled the three optical elements in the filtering system. Model parameters used are listed in table 4.5.

spectrum analyser (before it is 'broken') to set a consistent power ratio between the AM side-bands and carrier before each measurement of the filter system. The FBS visibility was measured with *PD5* as a function of modulation frequency, and the measurement results are shown in figure 4.24.

A theory model of the transmission spectrum of the optical filter system was then developed based on the theoretical spectral transmission response of the Fabry-Perot resonator defined as [307]

$$\mathcal{T}_{cav}(\omega) = \frac{1}{1 + \left[\left(\frac{2\mathcal{F}}{\pi}\right)\sin\left(\frac{\pi\omega}{\omega_{fsr}}\right)\right]^2} \tag{4.11}$$

where $\mathcal{F}$ and ω_{fsr} are the finesse and FSR of the cavity under investigation, respectively. The transmission function of the FBS was modelled after the response of an interferometer with the peak of the transmission curve centred on the FBS frequency, ω_m [242]

$$\mathcal{T}_{_{FBS}}(\omega) = \zeta_{_{FBS}} \sin^2(g_1\omega - g_2) + \left(\frac{1-\zeta_{_{FBS}}}{2}\right), \tag{4.12}$$

where $\zeta_{_{FBS}}$ is the FBS visibility measured without AM side-bands on the light ($\zeta_{_{FBS}} = 0.92$), g_1 is a factor that controls the frequency of the sine wave and was numerically found to be related to ω_m (actual FBS frequency), and g_2 is a factor that controls the phase shift of the sine wave. This factor was numerically found to be related to the lock-point of the FBS optical phase, ϕ_{FBS}. Ideally the FBS would be locked perfectly to a specific phase (e.g. $\phi_{FBS} = 0$) but experimentally this is not possible due to phase drifts in the experiment and finite reaction times of the locking system. Therefore, the overall transmission function of the optical filter cavities is modelled by,

$$\begin{aligned}\mathcal{T}_{tot}(\omega) &= \mathcal{T}_{chip}(\omega)\mathcal{T}_{etalon}(\omega)\mathcal{T}_{FBS}(\omega) \\ &= \frac{1}{1+\left[\left(\frac{2\mathcal{F}_{chip}}{\pi}\right)\sin\left(\frac{\pi\omega}{\omega_{chip}}\right)\right]^2} \\ &\times \frac{1}{1+\left[\left(\frac{2\mathcal{F}_{etalon}}{\pi}\right)\sin\left(\frac{\pi\omega}{\omega_{etalon}}\right)\right]^2} \\ &\times \left[\zeta_{FBS}\sin^2(g_1\omega - g_2) + \left(\frac{1-\zeta_{FBS}}{2}\right)\right],\end{aligned} \tag{4.13}$$

where $\mathcal{F}_{chip}$ (ω_{chip}) is the finesse (FSR) of the chip filter, and $\mathcal{F}_{etalon}$ (ω_{etalon}) is the finesse (FSR) of the etalon cavity. A summary of the parameters used in the model to fit the experimental data is given in table 4.5.

There were some restrictions on the parameter values chosen for the theoretical model. The etalon's linewidth and FSR had been experimentally measured using the calibrated oscilloscope method, and the FBS path length difference was known to be $\sim$ 29 cm, which corresponds to $\omega_m \approx$ 515 MHz. However, since the *exact* values are unknown, various combinations were tried until a unique solution was found that agreed with the experimental data shown in figure 4.24.

There are five identifiable regions in figure 4.24 that each correspond to particular parameters of the filter cavities. *Region 1* corresponds to the FBS visibility in equation 4.13, and is determined by the measured visibility when there are no AM side-bands ($\zeta_{FBS} = 0.92$). *Regions 2 & 3* of the theory curve predicts two minima in the FBS visibility at $f_1 \approx 380$ MHz and $f_2 \approx 560$ MHz. These minima in the FBS visibility were observed during the experimental measurements. The interference curve amplitude decreased as the amplitude modulation frequency approached these special values, and then a phase-flip occurred in the interference curve after the side-band frequency passed f_1 or f_2. A set of measurements illustrating this phase-flip behaviour in the FBS interference curve for AM frequencies between $350-400$ MHz is shown in figure 4.25.

The values of the minimum visibility frequencies were experimentally determined to be $f_1 \approx 385$ MHz and $f_2 \approx 565$ MHz. The frequency locations of these minima in

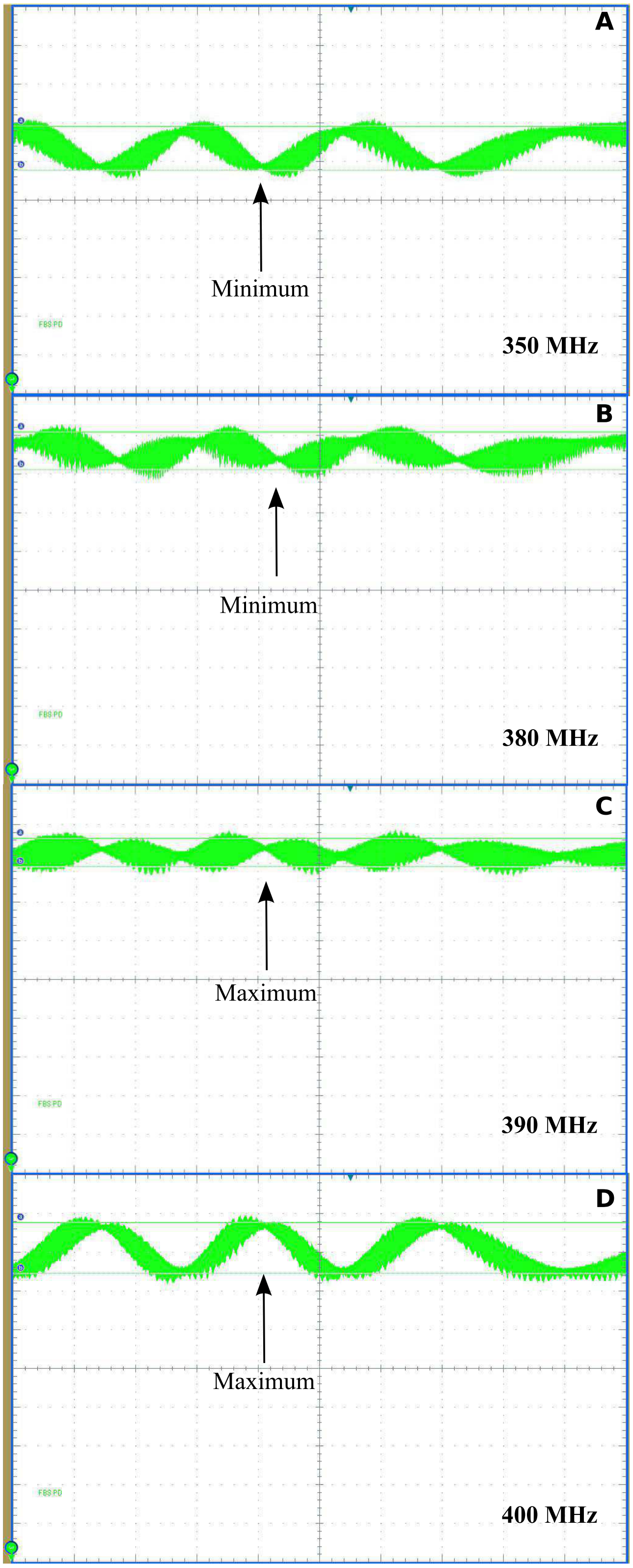

Figure 4.25: A set of measurements illustrating the phase-flip behaviour in the FBS interference curve for AM frequencies between $350-400$ MHz. A) The FBS visibility is reduced for AM at 350 MHz. B) The FBS visibility is at a minimum for AM at 380 MHz. C) The FBS visibility curve has phase-flipped for AM at 390 MHz. D) The FBS visibility curve begins to increase in amplitude for AM at 400 MHz.

Model parameter	Symbol	Value
Frequency range	ω	-$2\pi \times 5.15$ GHz to $2\pi \times 5.15$ GHz
Chip filter linewidth (FWHM)	γ_{chip}	$2\pi \times 3.7$ GHz
Chip filter FSR	ω_{chip}	$2\pi \times 1000$ GHz
Chip filter finesse	$\mathcal{F}_{chip} = \dfrac{\omega_{chip}}{\gamma_{chip}}$	~ 270
Etalon linewidth (FWHM)	γ_{etalon}	$2\pi \times 1.3$ GHz
Etalon FSR	ω_{etalon}	$2\pi \times 338$ GHz
Etalon finesse	$\mathcal{F}_{etalon} = \dfrac{\omega_{etalon}}{\gamma_{etalon}}$	~ 260
FBS visibility	ζ_{FBS}	0.92
FBS factor related to ω_m	$g1$	$\dfrac{1.55}{2\pi}$
FBS factor related to lock point	$g2$	2.6781 rads

Table 4.5: Parameters used in optical filter model described by equation 4.13.

the theory curve were found to be dependent on the etalon linewidth and the FBS factor g_1. A unique solution was found that produced a theory curve (shown in figure 4.24) which agreed with the experimentally measured frequencies. The solution gave the etalon linewidth to be 1.3 GHz (FWHM) and to have an FSR of 338 GHz. The FBS path length was designed with the intention that $\omega_m = \omega_s = 515$ MHz. However, these characterisation measurements determined that the FBS frequency is in fact $\omega_m = 509$ MHz. These parameter values are reasonable and within error of the previously measured values of the etalon, which were found by calibrating scope (see table 4.6 for comparison).

An equation to model the chip filter like a cavity ($\mathcal{T}_{chip}(\omega)$) had to be included in the model in order for the theory curve to agree with the experimental data in *regions 4 & 5*. Originally, the frequency response of the chip filter was thought to be constant over its bandwidth (100 GHz), and therefore was not included in the theoretical model. However, by not including the chip filter in the model, the theory curve would overshoot the experimental data in *region 4* and undershoot the data in *region 5*. Adjusting the etalon and FBS parameters had little to no affect

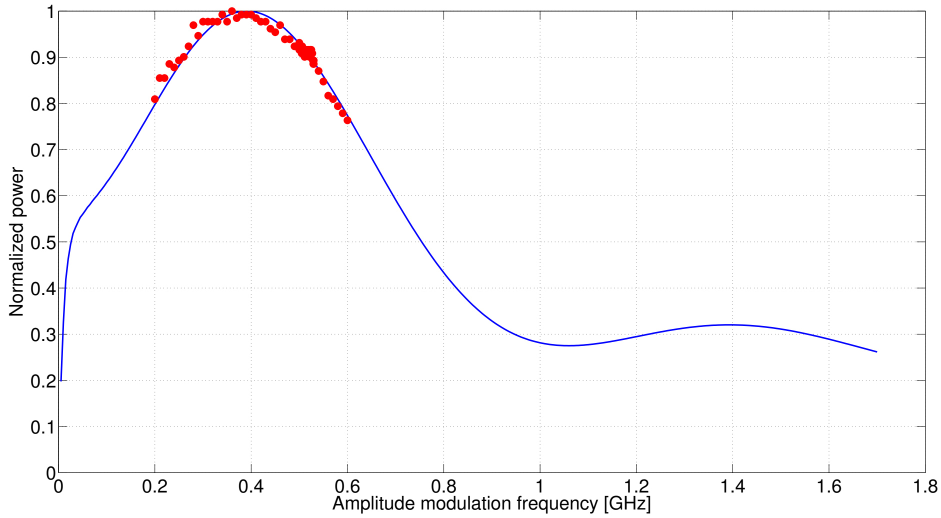

Figure 4.26: Characterisation of optical filter system with amplitude modulation for a locked FBS phase. The experimental data (red dots) was fitted with a theory curve (blue line) that modelled the three optical elements in the filtering system. The model parameters used are listed in table 4.5.

on the theory curve in this frequency region above $\sim$ 800 MHz. Adding a third equation to the model to represent the chip filter ($\mathcal{T}_{chip}(\omega)$) was the only solution found that allowed the model to agree with the experimental data in *regions 4* & *5*. This solution gave the chip filter linewidth to be 3.7 GHz (FWHM) and to have an FSR of 1000 GHz.

Filter element	Measurement technique	Linewidth (FWHM)	FSR or Measured ω_m
OPO	Calibrated scope	8.767 ± 0.1 MHz	516.6 ± 0.33 MHz
Etalon	Calibrated scope	1.23 ± 0.03 GHz	337.6 ± 0.83 GHz
OPO	AM + power meter	8.75 ± 0.1 MHz	515 ± 0.2 MHz
Chip filter	AM + power meter	3.7 GHz*	1000 GHz*
Etalon	AM + power meter	1.3 GHz*	338 GHz*
FBS	AM + power meter	—	509 MHz*

Table 4.6: Summary of cavity linewidth and FSR measurements performed using two different techniques. * refers to values determine by the theoretical model described by equation 4.13

In the second set of characterisation measurements, the OPO was still 'broken' and the etalon remained locked to the optical carrier. However, the FBS optical phase was now phase-locked (instead of being swept) to the phase $\phi_{FBS} = 0$, which

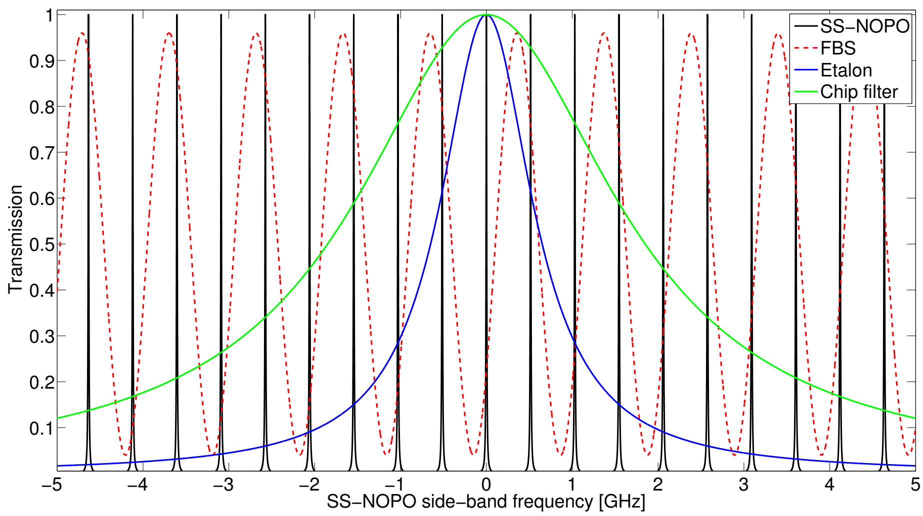

Figure 4.27: Theoretical transmission spectrum of the SS-NOPO and optical filter system generated using model parameters listed in table 4.5. Black: SS-NOPO, red: frequency beamsplitter, blue: etalon, green: chip filter.

sent the carrier to *PD5* (away from the power meter in the APD path). These are the phase-locked conditions for the etalon and FBS during a projected state data run. The optical power transmitted by the optical filtering system in this locked configuration was recorded as a function of amplitude modulation frequency. Figure 4.26 shows the experimental measurements and corresponding theory curve given by equation 4.13 and the parameters listed in table 4.5. This curve was generated by the same model and parameters previously determined by the FBS visibility measurements. The one parameter that could not be determined by the FBS visibility measurements was the FBS factor g_2, which is related to the FBS phase-lock point. This factor could not be previously determined as the FBS phase was being *swept* during the FBS visibility measurements, and therefore g_2 had no physical meaning. This factor was adjusted until the model was in agreement with the experimental data *without* adjusting the other parameters previously identified by the FBS visibility measurements. The final theoretical transmission functions for each filter element (along with the OPO transmission function) based on the parameters listed in table 4.6 for the 'AM + power meter' measurement technique are shown in figure 4.27.

An important realisation concerning this second set of characterisation measurements is that both the APD and the power meter are 'color blind' to these frequency side-bands. As we discussed in §2.5.3, a SS-NOPO produces entangled side-bands shifted in frequency away from the carrier by MHz-GHz. This frequency shift results in side-bands that differ by fractions of a nanometre in wavelength, and therefore look the same colour to an APD or power meter. Thus, the transmission spectrum measured by the power meter for this range of AM frequencies should be similar to the spectrum seen by the APD. Neither detector can distinguish between the photons generated at the first (515 MHz), second (1030 MHz), or third (1545 MHz) FSRs of our SS-NOPO.

Therefore, this second set of measurements performed with a phase-locked FBS is actually a *prediction* of the trigger mode spectrum that would be measured by the APD during a projected state data run. One way to test this idea would be to use the theory curve shown in figure 4.26 to generate a spectral mode function that would weight each FSR component in a multi-frequency temporal mode-matching equation. The concept of such a multi-frequency weighted projector being related to the trigger mode spectrum was discussed in §3.2.2. This hypothesis would be confirmed if the quality of the projected state improved when the weightings predicted by this measurement set were used in the frequency-offset temporal mode-function. This technique of optimising the mode-function to match the trigger field is a well-known practice, and usually leads to an improvement in the quality of the projected state [275]. We will further discuss and apply such a multi-frequency temporal mode-function based on these measured results in chapters 5 and 6.

4.4 Summary

We introduced the main concepts involved in a projective experiment that generates photon-subtracted squeezed vacuum states. In doing so we have discussed details of the experiment, and listed significant modifications that were made to said experiment which culminated into 'Generation II.' Various characterisation methods of classical parameters of cavities were presented, and important results on the frequency transfer function of the optical filtering system were discussed. Finally, a novel technique was introduced that allows for the characterisation of the frequency transfer function of an optical cavity up to a gigahertz frequency range without requiring a wide-bandwidth photodetector.

Chapter 5

Two-mode squeezed vacuum results

In science one tries to tell people, in such a way as to be understood by everyone, something that no one ever knew before. But in the case of poetry, it's the exact opposite!
Paul Dirac

In this chapter we will first introduce our data acquisition technique used to characterise both the *unprojected* and *projected* quantum states. The details of our post-processing technique will be discussed, which involves applying a *frequency-offset* temporal mode-matching function to the homodyne signal. This mode function is designed to select the part of the homodyne signal that is correlated with the detected trigger mode. In the case of the *unprojected* squeezed vacuum state, data acquisition is initiated by APD dark counts. Therefore the quantum state is uncorrelated with the (non-existent) trigger mode. Instead this mode function serves to combine temporal mode-matching with phase-locked frequency demodulation, which allows full reconstruction of the two single-mode squeezed vacuum states that exist in the symmetric and anti-symmetric side-band modes of the two-mode squeezed vacuum state. This concept of a symmetric/anti-symmetric side-band basis was defined in §3.1.3, and here we present experimental results of quantum state tomography of both the symmetric and anti-symmetric modes. Having access to the demodulation phase also allows full reconstruction of a state with statistics similar to a thermal state from the same homodyne data set (something not possible with conventional homodyne tomography). This chapter will also introduce the concept of a 'pump phase lock,' which is implemented during data post-processing. This lock was found to be necessary to improve the quality of the reconstructed quantum states.

In the case of two-mode squeezed vacuum, the symmetric and anti-symmetric modes are both single-mode squeezed vacuum states and therefore indistinguishable.

We will see in chapter 6 that these modes become distinguishable when photon-subtraction is applied to the two-mode squeezed vacuum state in a hybrid discrete-continuous variable experiment.

5.1 Data acquisition & post-processing

5.1.1 Data sampling

We used an Agilent *Acqiris* 10-bit digitizer (DC282, U1065A) to digitally-sample the analogue signals. A trigger NIM pulse from the APD was used to initiate data collection with the *Acqiris* during stages I and IV. The chop-lock technique and the resultant four measurement stages (I-IV) were discussed in §4.2.3. A fast homodyne detector with a 2 GHz analogue bandwidth was used to characterise the quantum states at particular FSR frequencies (515 MHz, 1030 MHz, and 1545 MHz) [298]. Due to limitations in the available sampling frequencies of the *Acqiris*, we were unable to avoid aliasing the high-frequency homodyne signal. According to the Shannon-Nyquist theorem, the signal must be sampled at twice the highest frequency component to avoid data aliasing [308]. We were limited to a sampling frequency of 2 Gsamples/sec (GS/s). In order to avoid data aliases, we would have had to digitally sample our 2 GHz bandwidth homodyne signal at *4 GS/s*. As this was not possible due to the processing restrictions of the *Acqiris*, the homodyne signal was undersampled, which caused data aliasing. However, the data at the frequencies of interest were still recoverable as the FSR frequencies are not multiples of the sampling frequency. Thus, this undersampling did not overlap the FSRs but instead aliased them to separate frequencies which did not destroy the information. Table 5.1 summarises the FSR frequencies and their aliases.

However, the FSR data was corrupted by the aliasing effects as the 1030 MHz and 1545 MHz signals were aliased down in frequency and therefore corrupted by unaliased noise at those lower frequencies. Aliasing had the effect of raising the electronic noise floor of the measurement. The data at 515 MHz is not aliased but is instead affected by aliased noise from 1485 MHz. In §2.7.2 we discussed how a raised electronic noise floor can be modelled as poor quantum efficiency, $\eta_e(f)$. The aliased noise has an equivalent effect of raising the electronic noise floor, and as a result decreases the effective homodyne detection efficiencies at the FSR frequencies.

In order to characterise this effect, the noise profiles of the homodyne detector and *Acqiris* digitizer were measured, and are shown in figure 5.1. Since the noise/gain profile of the detector decreases rapidly after 2 GHz, the contributions from aliased frequencies above 2 GHz can be ignored. Therefore the effect from the aliased noise can be quantified by defining a frequency-dependent homodyne

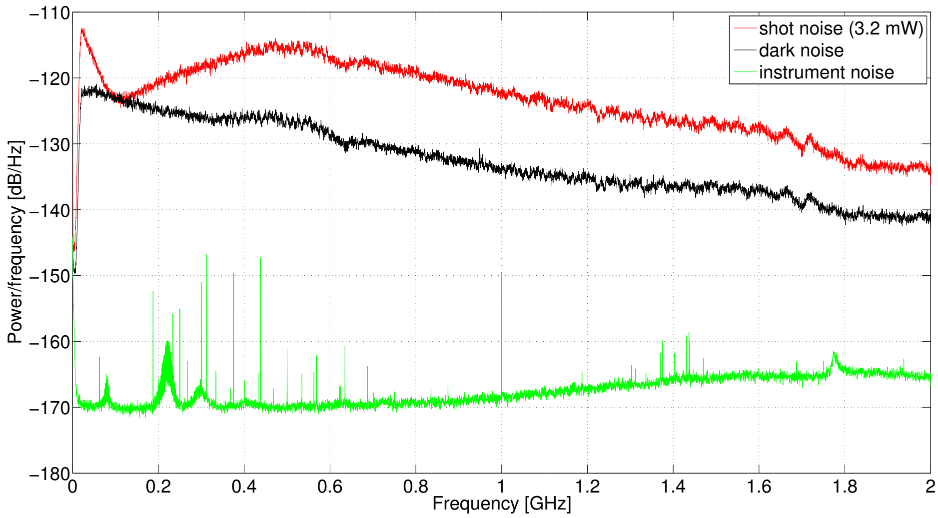

Figure 5.1: Characterisation of shot noise for a local oscillator optical power of 3.2 mW (red) and dark noise (black) of the 2 GHz homodyne detector. The noise floor of the Agilent *Acqiris* 10-bit digitizer used for data acquisition is shown in green.

detection efficiency,

$$\begin{aligned}\eta_e(f) &= 1 - \frac{P_{dark}(f)}{P_{shot}(f)} \\ &= 1 - \frac{P_{shot}(f_B) + P_{dark}(f_A)}{P_{shot}(f_B) + P_{shot}(f_A)}\end{aligned} \tag{5.1}$$

where $P_{shot}(f_A)$ ($P_{dark}(f_A)$) is the power spectral density of shot (dark) noise within the OPO bandwidth centred on an FSR frequency, f_A, respectively. $P_{shot}(f_B)$ is the power spectral density of shot noise within the OPO bandwidth centred on the corresponding aliased frequency, f_B. This results in frequency-dependent effective homodyne detection efficiencies due to undersampling the homodyne data. The detection efficiencies at the FSR frequencies are summarised in table 5.1.

Original frequency, f_A	Aliased frequency, f_B	$\eta_e(f_A)$
515 MHz	1485 MHz*	0.86
1030 MHz	970 MHz	0.424
1545 MHz	455 MHz	0.055

Table 5.1: Summary of the aliased frequencies and resultant detection efficiencies, $\eta_e(f_A)$, for three FSR frequencies. * the 515 MHz signal is not aliased; noise at 1485 MHz is aliased onto the 515 MHz FSR signal, corrupting the detection efficiency at 515 MHz.

5.1.2 Extracting quadrature data of side-band modes

As previously discussed, the detection of a trigger photon by the APD heralds the projection of a photon-subtracted state at the homodyne detector. The continuous variable quadrature data captured by the homodyne detector must be processed to select that portion of the signal which is correlated with the temporal and spectral qualities of the detected trigger mode. As the detection of a trigger photon occurs at a distinct moment in time, a temporal mode function must be applied to the homodyne data. The most common temporal mode function is a double-sided exponentially decaying correlation function of the OPO output [216,221,230,231,309,310]

$$\Gamma(\tau, t) = \exp\Big[-\beta|t+\tau|\Big], \tag{5.2}$$

where β is the half width at half maximum (HWHM) of the OPO decay function in angular frequency (for our experiment, $\beta = 2\pi \times 4.07$ MHz), and τ is the temporal offset between the APD click time and collection time of the homodyne data. The nature of our time-and-frequency-resolved homodyne measurement operator implemented in our experiment means that we have an additional frequency demodulation stage in our post-processing. This allows us to reconstruct quantum states at specific FSR frequencies within the bandwidth of our OPO. Therefore, we implement a frequency filter to demodulate the homodyne data at a particular frequency, ω_s,

$$\Upsilon(\omega_s, \phi, t) = \cos(\omega_s t + \phi), \tag{5.3}$$

where ϕ is the demodulation phase offset.

In equation 3.14 we defined the continuous-time equation of the measurement operator, $\hat{X}_{\omega_s}(\theta, \phi)$, designed to isolate a signal at a particular frequency, ω_s, from the homodyne data. Since the homodyne data is digitally sampled at 10 000 samples/APD event, a frequency-offset temporal mode function is applied to the homodyne data in discrete time and then numerically summed to give a single quadrature value:

$$\begin{aligned}\hat{X}(\omega_s, \theta, \phi, \tau) &= \sum_{i=1}^{i=10000} \Gamma\Big(\tau, t(i)\Big)\Upsilon\Big(\omega_s, \phi, t(i)\Big)\hat{X}\Big(\theta, t(i)\Big) \\ &= \sum_{i=1}^{i=10000} \exp\Big[-\beta|t(i)+\tau|\Big]\cos\Big(\omega_s t(i) + \phi\Big)\hat{X}\Big(\theta, t(i)\Big),\end{aligned} \tag{5.4}$$

where $\hat{X}\Big(\theta, t(i)\Big)$ is the digitally sampled homodyne data measurement. The homodyne data is captured over a 5 μs data window for a particular local oscillator phase, θ. Implementing the demodulation stage numerically in post-processing gives us the ability to choose which frequency components of the generated state to investigate. Furthermore, we can choose which side-band mode(s) to reconstruct by adjusting the demodulation phase, ϕ and temporal offset, τ, of the mode function. These offsets interact to produce an overall demodulation phase, ϑ, which reveals either the symmetric or anti-symmetric modes defined in §3.1.3.

The actual time delay due to electronics between the APD 'click' and the captured homodyne data is difficult to measure. Therefore, it is common practice to reconstruct the quantum state for a variety of temporal offsets, and use the temporal mode function that best reconstructs the quantum state that shares maximal entanglement with the trigger mode [275]. For our experiments, maximal entanglement is quantified by the largest possible single-photon probability, minimum value in the Wigner function, and best quantum non-Gaussian character witness for the photon-subtracted squeezed vacuum state (which will be further discussed in §6.1).

In our demodulation scheme, the real time delay is integrated into the overall phase rotation, ϑ. Thus, the optimum τ and ϕ values that show maximum entanglement vary for different demodulation frequencies. For example, the frequency-offset temporal mode function applied to the homodyne data to reconstruct the quantum state in the symmetric side-band mode at the first FSR frequency is done at specific τ and ϕ values,

$$\hat{X}(\omega_s, \theta, \phi_1, \tau_1) = \sum_{i=1}^{i=10000} \exp\Big[-\beta|t(i)+\tau_1|\Big] \cos\Big(\omega_s t(i) + \phi_1\Big) \hat{X}\Big(\theta, t(i)\Big), \tag{5.5}$$

where τ_1 and ϕ_1 interact to produce a unique demodulation phase that reveals the symmetric side-band mode at the first FSR frequency, $\omega_s = 515$ MHz. Reconstruction of the same side-band mode at the second FSR frequency, $2\omega_s$, requires a different set of parameters, τ_2 and ϕ_2. Similarly, reconstruction at the third FSR frequency, $3\omega_s$, again requires another set of parameters, τ_3 and ϕ_3. An example of three FSR mode functions corresponding to three different temporal offsets are shown in figure 5.2.

As we will show in chapter 6, due to the multiple FSR spectral quality of the optical filter cavities in our the projected state experiment, we actually created a state that was entangled between the FSRs. Therefore, the optimal mode function for reconstruction of these states is a combination of the temporal mode function with a multi-frequency demodulation function and a particular set of τ_m and ϕ_m values, as well as phase and temporal offsets related to the individual FSR parameters (τ_1,

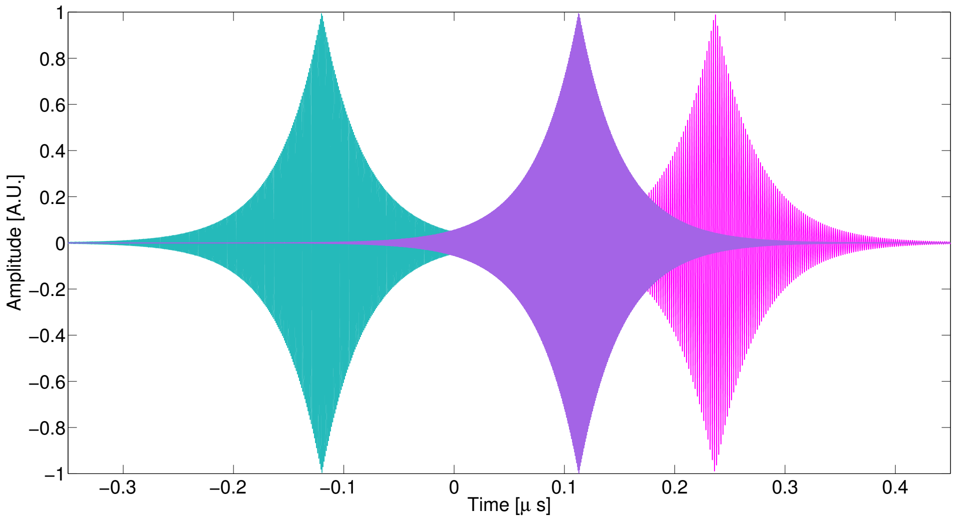

Figure 5.2: Three sets of temporal mode functions corresponding to different temporal offsets (τ).

ϕ_1, τ_2, ϕ_2, τ_3, ϕ_3):

$$\hat{X}(\omega_s, \theta, \phi_m, \tau_m) = \sum_{i=1}^{i=10000} \Big[\gamma_1 \Xi_1 + \gamma_2 \Xi_2 + \gamma_3 \Xi_3\Big] \hat{X}\Big(\theta, t(i)\Big), \tag{5.6}$$

where

$$\begin{aligned} \Xi_1 &= \Gamma\Big(\tau_m, t(i)\Big) \times \Upsilon\Big(\omega_s, \phi_m, t(i)\Big) \qquad (5.7)\\ &= \exp\Big[-\beta\Big|t(i) + \tau_m\Big|\Big] \sin\Big(\omega_s t(i) + \phi_m\Big) \\ \Xi_2 &= \Gamma\Big(\tau_m, \Delta\tau_2, t(i)\Big) \times \Upsilon\Big(2\omega_s, \phi_m, \Delta\phi_2, t(i)\Big) \qquad (5.8)\\ &= \exp\Big[-\beta\Big|t(i) + \tau_m + \Delta\tau_2\Big|\Big] \sin\Big(2\omega_s t(i) + \phi_m + \Delta\phi_2\Big) \\ \Xi_3 &= \Gamma\Big(\tau_m, \Delta\tau_3, t(i)\Big) \times \Upsilon\Big(3\omega_s, \phi_m, \Delta\phi_3, t(i)\Big) \qquad (5.9)\\ &= \exp\Big[-\beta\Big|t(i) + \tau_m + \Delta\tau_3\Big|\Big] \sin\Big(3\omega_s t(i) + \phi_m + \Delta\phi_3\Big), \end{aligned}$$

and

$$\begin{aligned} \gamma_1 &= \sqrt{\frac{P(\omega_s)\eta_e(\omega_s)}{\mathcal{N}}} \qquad (5.10)\\ \gamma_2 &= \sqrt{\frac{P(2\omega_s)\eta_e(2\omega_s)}{\mathcal{N}}} \\ \gamma_3 &= \sqrt{\frac{P(3\omega_s)\eta_e(3\omega_s)}{\mathcal{N}}}, \end{aligned}$$

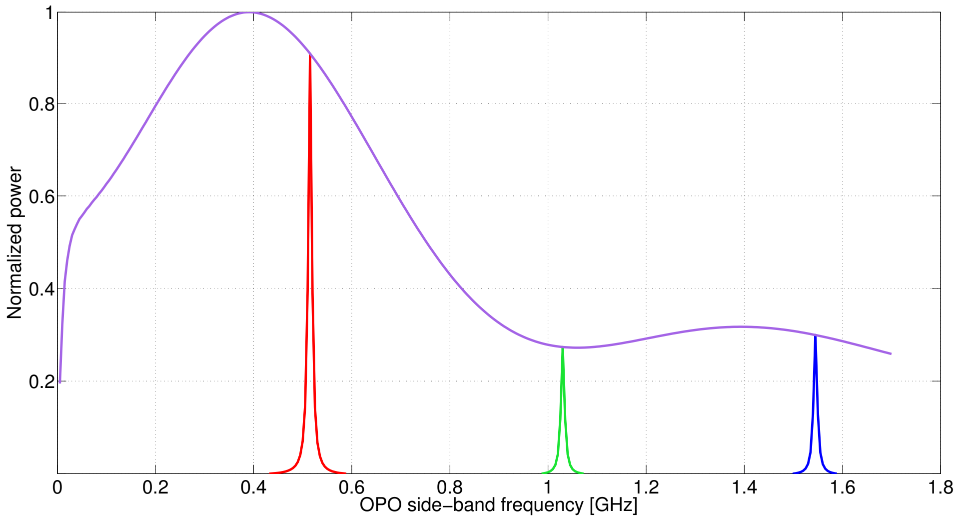

Figure 5.3: Overall spectral mode function from the optical filtering system (purple), and transmitted SS-NOPO FSR side-bands frequencies at first FSR (red), second FSR (green) and third FSR (blue) to the APD.

where

$$\mathcal{N} = P(\omega_s)\eta_e(\omega_s) + P(2\omega_s)\eta_e(2\omega_s) + P(3\omega_s)\eta_e(3\omega_s). \tag{5.11}$$

$P(\omega_s)$, $P(2\omega_s)$, and $P(3\omega_s)$ are the normalized transmissions from the frequency characterisation curve of the optical filters (shown in figure 5.3) at the first, second, and third FSR, respectively. $\eta_e(\omega_s)$, $\eta_e(2\omega_s)$, and $\eta_e(3\omega_s)$ are the effective homodyne detection efficiencies listed in table 5.1 as they arise from aliasing effects. Figure 5.4 illustrates the mode function weightings as a function of side-band frequency which results in the γ-coefficients used in the three FSR frequency-offset temporal mode function. Note that the specific phase relationships between the FSRs for a particular side-band mode must be upheld in equation 5.6 in order to reveal the correlations. These phase relationships are defined as

$$\begin{aligned}
\Delta\tau_2 &= \tau_2 - \tau_1 \\
\Delta\tau_3 &= \tau_3 - \tau_1 \\
\Delta\phi_2 &= \phi_2 - \phi_1 \\
\Delta\phi_3 &= \phi_3 - \phi_1,
\end{aligned} \tag{5.12}$$

where these temporal and phase offsets come from the τ and ϕ values used to reveal a particular side-band mode at each individual FSR frequency (τ_1,ϕ_1 are for the 515 MHz side-band mode, τ_2,ϕ_2 are for the 1030 MHz side-band mode, and τ_3,ϕ_3 are for the 1545 MHz side-band mode).

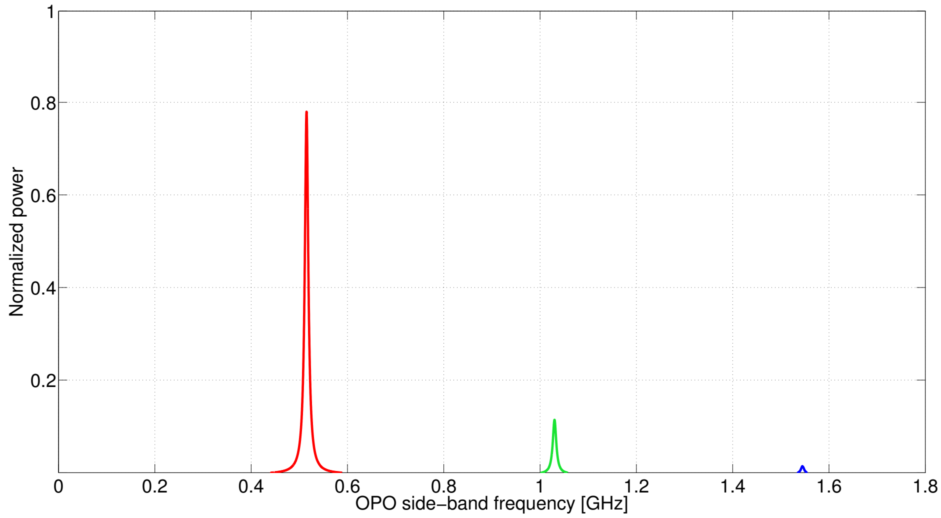

Figure 5.4: Final weightings of the FSR components in the multi-frequency temporal mode function used in projected state reconstruction.

5.1.3 Locking the pump phase

It was determined that an as-yet unknown phase drift in the experiment was manifesting in the pump phase, ϕ_{pump}, and affecting the quality of reconstructed quantum state. This first manifested itself in measurements of the classical phase difference between the pump and seed phases. Attempts to experimentally lock the pump phase were unsuccessful due to that technical issue. Therefore, the pump phase was 'locked' during post-processing of the tomography data. Recall from §4.2.3 where we discussed the chop-lock method used to lock the experiment during data acquisition. This method involves two optical choppers (one in the pump beam, the other in the seed beam before the OPO) which are phase-locked in quadrature. This creates four measurements stages (I-IV) in which the pump and seed go through combinations of being 'on' and 'off.' The pump phase is allowed to wander randomly during data acquisition, and must be estimated so an overall phase can be assigned to the quadrature data (used in MaxLik reconstruction). Therefore, the pump phase is estimated by measuring the parametric gain in the OPO during stage II at the moment of data collection (triggered by an APD event, whether dark or real). The pump phase is then calculated during post-processing using the recorded parametric gain level and equation 4.1.

The pump phase 'lock' is initiated in the data analysis by selecting to keep homodyne data that was taken while the pump phase was within a certain 'pump phase window.' A histogram of the pump phase data was made in order to determine the phase phase window size and on what phase it should be centred. Since the pump phase ranges from -90° to 0°, we chose a histogram bin size of 6° to give 15

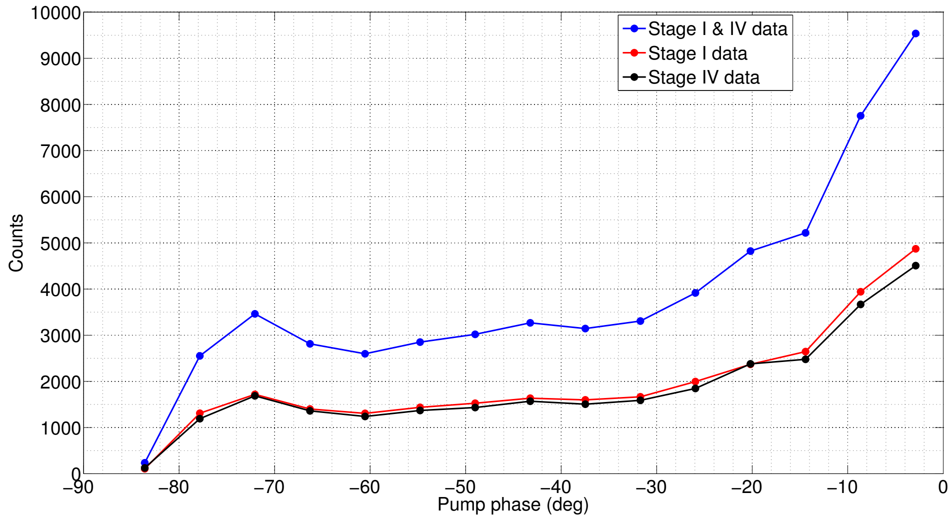

Figure 5.5: Histogram of the pump phase data from unprojected state data set. Blue: all data from stages I & IV; red: data from stage I (pump 'on', seed 'off'); black: data from stage IV (vacuum).

histogram bins. The resulting histogram is shown in figure 5.5. As the homodyne data is sorted into stage I (pump 'on', seed 'off') and stage IV (pump 'off', seed 'off') during post-processing, we can compare the histogram count rate (i.e. number of pump phase measurements that fit in a particular bin) for each of these stages. Since the *unprojected* squeezed vacuum state data collection is initiated by APD dark counts, the count rates between stage I and IV should be approximately the same (which they are).

Note that there is a clear bias in the pump phase drift towards $\phi_{pump} = 0$ (parametric amplification). We used this bias to our advantage to maximise the amount of quadrature kept for a smaller pump phase window. Having a smaller pump phase window (i.e. 2.5°) minimises the pump phase drift in the reconstructed quantum state, and as we shall show in §5.3, significantly improves the quality of the quantum state.

5.2 Data presentation — Unlocked pump phase

As it was not possible to experimentally lock the pump phase due to technical issues, we will first present a complete set of classical parametric gain measurements, spectrum analyser measurements, and reconstructed quantum states for both the symmetric and anti-symmetric modes for an unlocked pump phase (i.e. the pump phase window was *not* applied during post-processing).

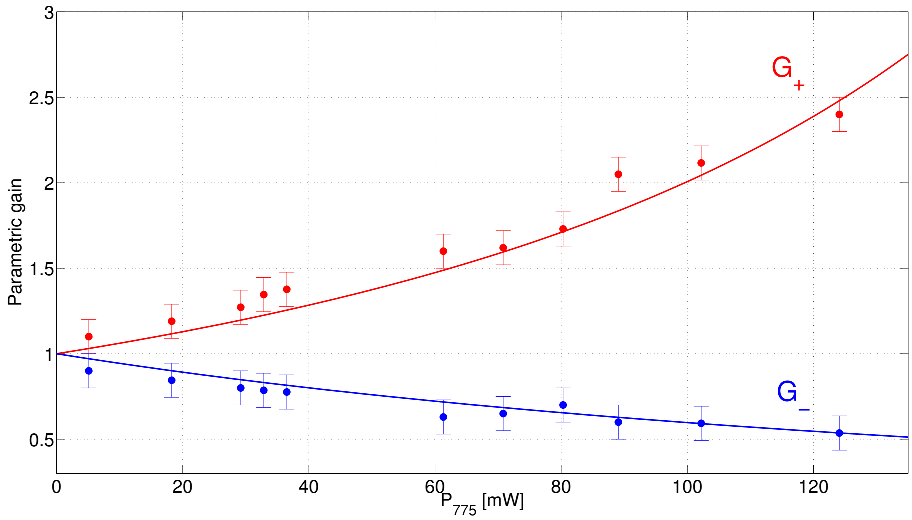

Figure 5.6: Characterisation of the parametric gain profile of the OPO was quantified for a *wandering* pump phase as a function of 775 nm pump power. Red: parametric amplification, G_+, for theory (line) and experimental data (dots); blue: parametric attenuation, G_-, for theory (line) and experimental data (dots). The theory curves are defined by equation 2.144.

5.2.1 Classical parametric gain measurements

As we discussed in §2.7.1 there is a relationship between the amount of classical parametric gain (and loss) in a system, and the amount of observed squeezing and anti-squeezing. Therefore, before discussing the levels of squeezing observed from our system, we will first present experimental data characterising the amount of parametric gain observed for a range of input pump beam optical powers.

Parametric amplification of the fundamental 1550 nm field occurs when the optical phase between the down-converted pump photons and the input 1550 nm field is $\phi_{pump} = 0$. At this phase the optical power of the 1550 nm field is amplified relative to the intensity of the original input field. Similarly, parametric attenuation (or 'de-amplification') of the fundamental field occurs when the optical phase between the down-converted pump photons and the input 1550 nm field is $\phi_{pump} = \pi/2$. Thus reducing the optical power below the level of the input field.

Classical parametric amplification and attenuation of the low-power 1550 nm input field was observed while the OPO was phase-locked on resonance. The theoretical amount of gain that could be observed is defined by equation 2.144, and depends on parameters such as the pump threshold, P_{Th} and the input pump power, P_{775}. Characterisation of the parametric gain profile of the OPO was quantified for a *wandering* pump phase, and is shown in figure 5.6 as a function of input pump power. The maximum observed gain levels are $G_+ = 2.4$ and $G_- = 0.536$ for an input pump power of $P_{pump} = 124$ mW. A comparison of these quantities to the values predicted by equation 2.144, as well as a summary of the experimental conditions these measurements were taken are summarised in table 5.2.

5.2.2 Spectrum analyser measurements at 515 MHz

As detailed in chapter 4, the experiment can be operated in two configurations: *unprojected* state mode or *projected* state mode. When operating in unprojected mode, the experiment generates a two-mode squeezed vacuum state. Measuring this state with our fast homodyne detector and spectrum analyser is equivalent to applying our time-and-frequency-resolved measurement operator to the two-mode state for a *random* demodulation phase. As discussed in chapter 3, this results in an averaged variance measurement of the symmetric and anti-symmetric modes, and can only return a non-zero result for the 2nd-order moment of the measurement operator, $\hat{X}_{\omega_s}(\theta, t)$. For the unprojected state, both of these side-band modes are single-mode squeezed vacuum states, arising in the spectrum analyser measurement to always be of a single-mode squeezed vacuum state.

The unprojected squeezed vacuum state was characterised with a high-frequency spectrum analyser for a *wandering* pump phase. The squeezing and anti-squeezing levels of the system were measured at the FSR frequency of 515 MHz. We used a fast spectrum analyser to perform a zero-span measurement centred on 515 MHz (with a resolution bandwidth of 500kHz) with the experiment operating in 'chop-lock' mode. Performing this measurement during chop-lock mode allows for real-time comparisons between the squeezed vacuum state and vacuum quantum noise (see figure 5.7). The best squeezing level observed was -2.35 $\pm$ 0.5 dB, which had a corresponding anti-squeezing level of 3.9 $\pm$ 0.5 dB for an input pump power of 124 mW. Table 5.2 summarises relevant cavity parameters needed to calculate the theoretical squeezing levels ($V^{\pm}$) and parametric gain ($G_{\pm}$) from equations 2.139 and 2.144, and the measurement conditions of the experimental data.

5.2.3 Quantum state tomography — 515 MHz modes

Implementing a time-and-frequency-resolved homodyne measurement with a fixed demodulation phase allows for the symmetric and anti-symmetric modes to be distinguished and probed individually. This measurement technique also allows for all statistical moments of either mode to be measured. Performing tomography of the unprojected state with a frequency-offset temporal mode function in post-processing, as described by equation 5.5, implements such a measurement.

Data acquisition for quantum state tomography of the unprojected state is trig-

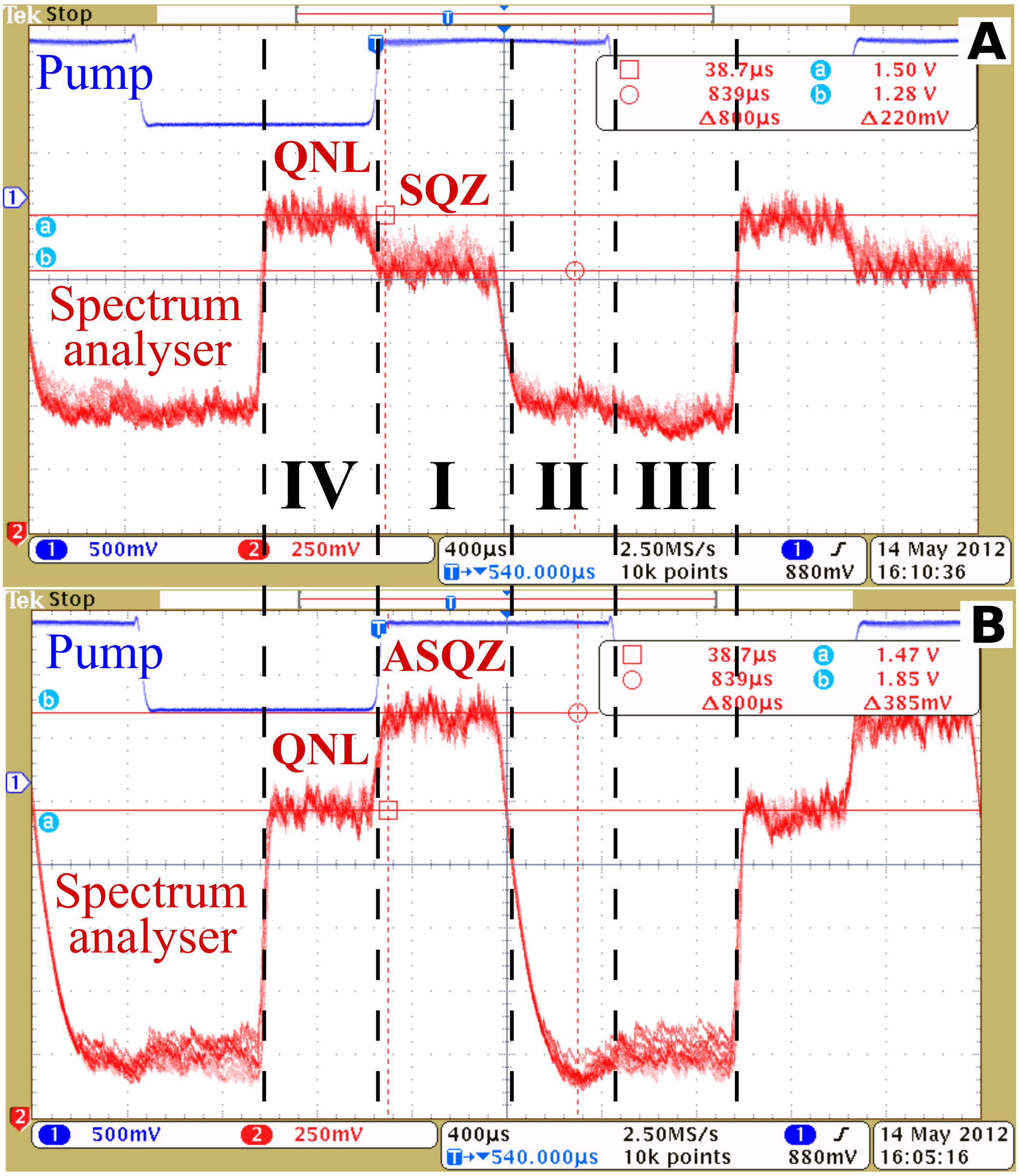

Figure 5.7: Zero-span spectrum analyser measurements of the squeezed vacuum state from our OPO while in chop-lock mode for a *wandering* pump phase (resolution bandwidth (RBW) = 500 kHz, zero-span set to 515 MHz, LO power = 3.2 mW, 100 mV = 1 dB). A) Captured screenshot of squeezing measurement (-2.2 dB). B) Captured screenshot of anti-squeezing measurement (3.85 dB). Red: spectrum analyser trace, blue: chopped pump beam, QNL = quantum noise limit, SQZ = squeezing, ASQZ = anti-squeezing.

Description	Symbol	Value
Quantum efficiency of homodyne detector	η_{QE}	0.9
Propagation efficiency	η_t	0.88
Homodyne detector interference visibility	ζ	0.924
Homodyne detection efficiency	$\eta_{HD} = \eta_{QE}\eta_t\zeta^2$	0.676
OPO escape efficiency	η_{esc}	0.848
Total cavity loss	L	0.015
Pump threshold power	P_{Th}	340* mW
Pump power	P_{775}	124 mW
Theoretical amplification gain	G_+	2.477
Theoretical attenuation gain	G_-	0.537
Measured amplification gain	—	2.4
Measured attenuation gain	—	0.536
Theoretical anti-squeezing level	V^+	4.876 dB
Theoretical squeezing level	V^-	-2.591 dB
Measured anti-squeezing level (spectrum analyser)	—	3.9 ± 0.5 dB**
Measured squeezing level (spectrum analyser)	—	-2.35 ± 0.5 dB**

Table 5.2: OPO cavity parameters and measurement conditions for parametric gain and spectrum analyser measurements for a *wandering* pump phase. * P_{Th} was calculated using equation 2.143; ** best observed squeezing level and corresponding anti-squeezing level.

gered by false detection events (dark counts) of the APD. The trigger photons in the experiment are treated as propagation loss, η_t, and are not used to trigger data collection. The filtering parameters, τ and ϕ, interact to produce an overall constant demodulation phase which allows access to particular side-band modes.

We will now present quantum state tomography results for an unlocked pump phase. There are three categories of results which will be discussed:

1. Data *uncorrected* for imperfect homodyne detection efficiency
2. Data *corrected* for imperfect *optical* homodyne detection efficiency (η_{HD})
3. Data *corrected* for both η_{HD} and $\eta_e(f)$, where $\eta_e(f)$ is the detection efficiency at each FSR frequency, f, due to a raised electronic noise floor caused by data aliasing (previously discussed in §5.1.1)

Table 5.3 is a summary of the experimental and reconstruction parameters that were used to collect and analysis all data presented in this chapter.

Parameter	Value
Pump power	124 mW
LO power	3.2 mW
η_{HD}	0.676
η_e(515 MHz)	0.86
$\eta_{HD}\eta_e$(515 MHz)	0.5814
η_e(1030 MHz)	0.424
$\eta_{HD}\eta_e$(1030 MHz)	0.2866
Data sampling rate	2 GS/s
Homodyne data length	5 μs

Table 5.3: Summary of experimental and reconstruction parameters that were used to collect and analysis all unprojected data presented in this chapter.

5.2.3.1 Without detection efficiency correction

We were able to access the symmetric and anti-symmetric side-band modes of the two-mode squeezed vacuum state for an unlocked pump phase by changing the parameters τ and ϕ. We were able to reconstruct the states at the first FSR frequency of our SS-NOPO by choosing a demodulation frequency of 515 MHz. Table 5.4 is a

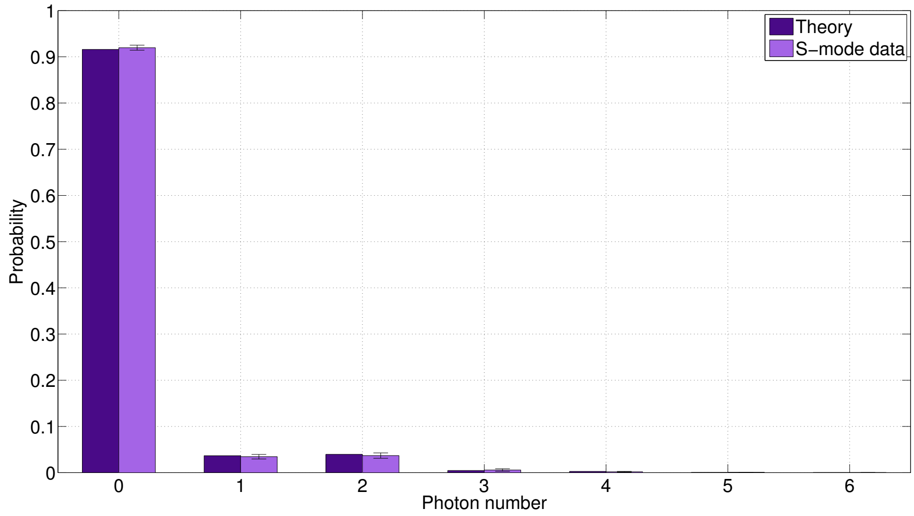

Figure 5.8: Comparison of uncorrected experimental and theoretical photon number distributions of the 515 MHz *unprojected* symmetric side-band mode (S-mode) for an *unlocked* pump phase. The reconstruction parameters are listed in tables 5.3 & 5.4, and the model parameters are listed in table 5.5.

summary of the parameters used during post-processing to reconstruct three quantum states from the *unprojected* state data: symmetric side-band mode (single-mode squeezed vacuum state), anti-symmetric side-band mode (single-mode squeezed vacuum state), and a 'thermal state' (reconstructed state that looks like a thermal state). In §3.1.1 we discussed how measuring one-half of a two-mode squeezed state produces a result that is statistically equivalent to a thermal state [135,251,293–295]. Since our measurement technique gives us access to the symmetric/anti-symmetric modes, we can also access a mixture of these modes (see equation 3.30). As we shall show in the following data presentations, this type of measurement results in a state statistically equivalent to a thermal state.

Side-band mode	Demodulation frequency	τ	ϕ
Symmetric mode	515 MHz	-238.3 ns	60°
Anti-symmetric mode	515 MHz	-184.8 ns	175.4°
'Thermal' mode	515 MHz	-148 ns	107.5°

Table 5.4: Summary of parameters that were used to reconstruct unprojected states for an *unlocked* pump phase at the first FSR (515 MHz).

Figure 5.8 shows the uncorrected experimental photon number distribution (PND) of the unprojected symmetric side-band mode (S-mode) at 515 MHz. This PND was

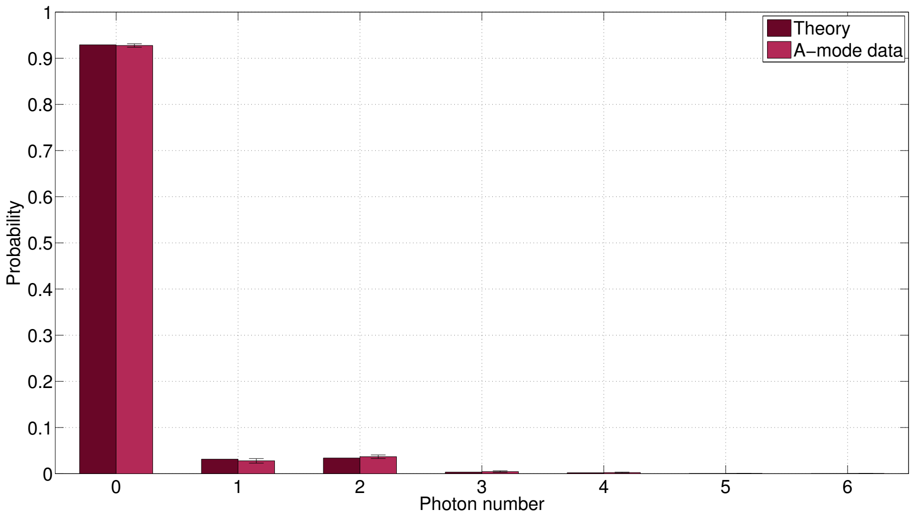

Figure 5.9: Comparison of uncorrected experimental and theoretical photon number distributions of the 515 MHz *unprojected* anti-symmetric side-band mode (A-mode) for an *unlocked* pump phase. The reconstruction parameters are listed in tables 5.3 & 5.4, and the model parameters are listed in table 5.5.

reconstructed from homodyne tomography data of the unprojected state using the parameters listed in tables 5.3 & 5.4, and the MaxLik technique explained in §2.8. Figure 5.8 also shows the theoretical PND of an impure single-mode squeezed vacuum mathematically simulated using the impure squeezed vacuum model outline in §2.6.1. The model parameters used to generate this theoretical PND are listed in table 5.5. The model and experimental PNDs shown in figure 5.8 agree within error.

Side-band mode	Pure squeezing level	Loss, r_1	η_{HD}
515 MHz symmetric mode	-3.909 dB	0.004916	0.676
515 MHz anti-symmetric mode	-3.561 dB	0.004916	0.676

Table 5.5: Summary of model parameters used to simulated impure squeezed vacuum states for unprojected state results with *unlocked* pump phase at the first FSR (515 MHz).

Figure 5.9 shows the uncorrected experimental PND of the unprojected anti-symmetric side-band mode (A-mode) at 515 MHz reconstructed using the parameters listed in tables 5.3 & 5.4. The theoretical PND of an impure single-mode squeezed vacuum is also shown, which was mathematically simulated using the model parameters listed in table 5.5. As with the symmetric mode data, the anti-symmetric mode data and model shown in figure 5.9 are in agreement within error.

In §2.2.3 we discussed how the PND of a thermal state can be related to a

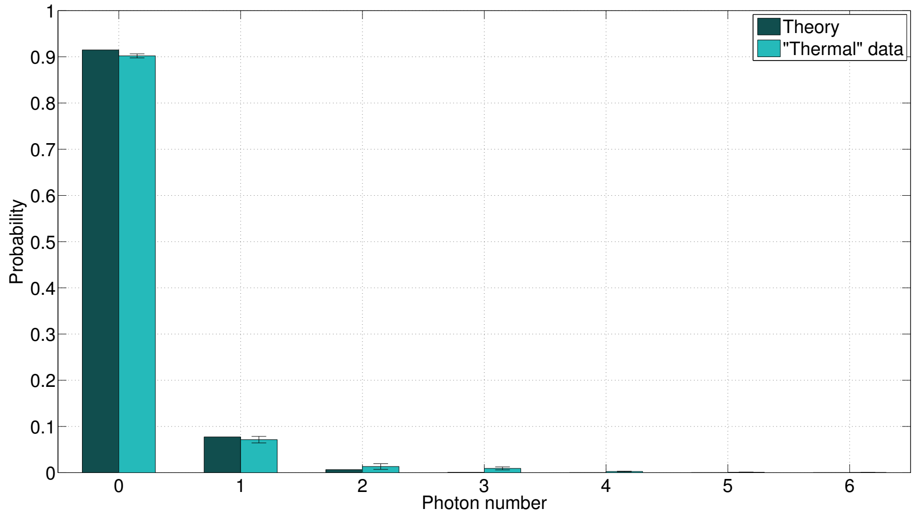

Figure 5.10: Comparison of uncorrected experimental and theoretical photon number distributions of a 'thermal' mode at 515 MHz for an *unlocked* pump phase. The theoretical thermal state PND was calculated using equation 2.49 and corresponds to -2.6 dB of squeezing. The reconstruction parameters are listed in tables 5.3 & 5.4.

certain level of squeezing, which can be modelled by equation 2.49. By choosing the appropriate filtering parameters we were able to reconstruct a state from the unprojected data which has the statistics of a 'thermal' state. Figure 5.10 shows the uncorrected experimental PND of this state that appears to be a 'thermal' mode at 515 MHz. This PND was reconstructed from the same homodyne data set as the previous S-mode and A-mode PNDs, and was reconstructed using the parameters listed in tables 5.3 & 5.4.

Because of the known relationship between the PND of a thermal state and the squeezing level, we can estimate the squeezing level from the uncorrected experimental PND, and compare this with the value previously measured using the spectrum analyser. Table 5.6 compares the theoretically predicted squeezing levels by equation 2.139, and experimentally measured values for the squeezed vacuum results with an *unlocked* pump phase.

In §2.1.4 we summarised how a state's density matrix in the Fock basis can be calculated from its Wigner function and vice versa. This method was used to reconstruct the experimental Wigner functions based on the reconstructed density matrices. Figure 5.11 shows the Wigner functions for the squeezed vacuum symmetric mode (figure 5.11A) and the 'thermal' mode (figure 5.11B). Due to the low level of squeezing these experimental Wigner functions look similar. We will see them become more noticeably different as the data is corrected for imperfect homodyne detection in the next section.

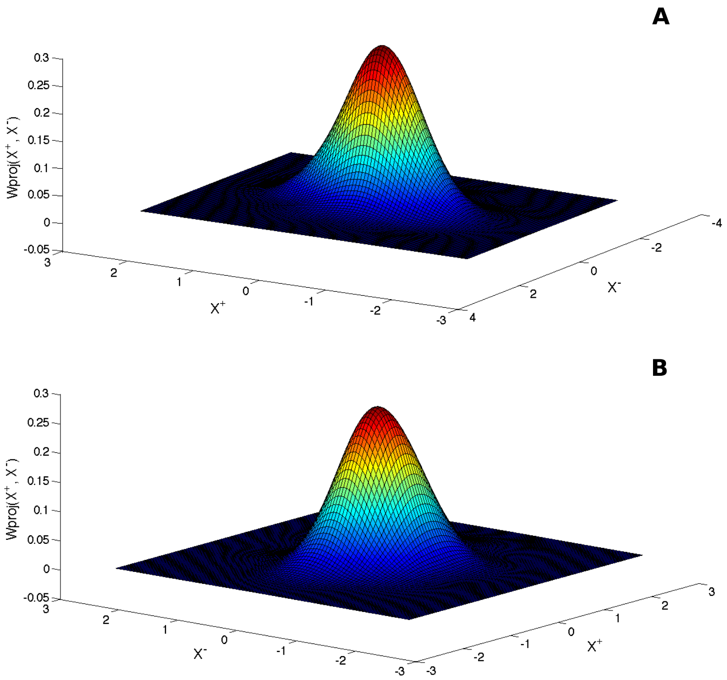

Figure 5.11: Experimental uncorrected Wigner functions reconstructed from *unprojected* data at 515 MHz for an *unlocked* pump phase. A) Squeezed vacuum (symmetric mode), and B) 'thermal' mode. The reconstruction parameters are listed in tables 5.3 & 5.4.

5.2.3.2 Corrected for η_{HD}

It was discussed in §2.8.3 that imperfect homodyne detection efficiency can be explicitly included in the maximum likelihood algorithm [245, 280]. We used this method to corrected for homodyne detection inefficiency. First we will present results from only correcting for the imperfect detection efficiency due to *optical* characteristics of the experiment, which is defined as $\eta_{HD} = \eta_{QE}\eta_t\zeta^2$. The experimental values for these parameters are defined in table 5.2, and give $\eta_{HD} = 0.676$ for the unprojected state measurements.

Figure 5.12 shows the PNDs for the unprojected symmetric, anti-symmetric, and 'thermal' modes at 515 MHz corrected for $\eta_{HD} = 0.676$ and with an unlocked pump phase. These PNDs were reconstructed using the parameters listed in tables 5.3 & 5.4. Correcting for η_{HD} in the reconstruction code does *not* correct for $\eta_e(f)$, which is the poor detection efficiency caused by data aliasing effects described in §5.1.1.

Figure 5.13 shows the Wigner functions for the unprojected squeezed vacuum symmetric mode (figure 5.13A) and the 'thermal' mode (figure 5.13B). Note that correcting for imperfect homodyne detection, η_{HD}, increases the level of squeezing in the state and results in the Wigner functions becoming more noticeably different.

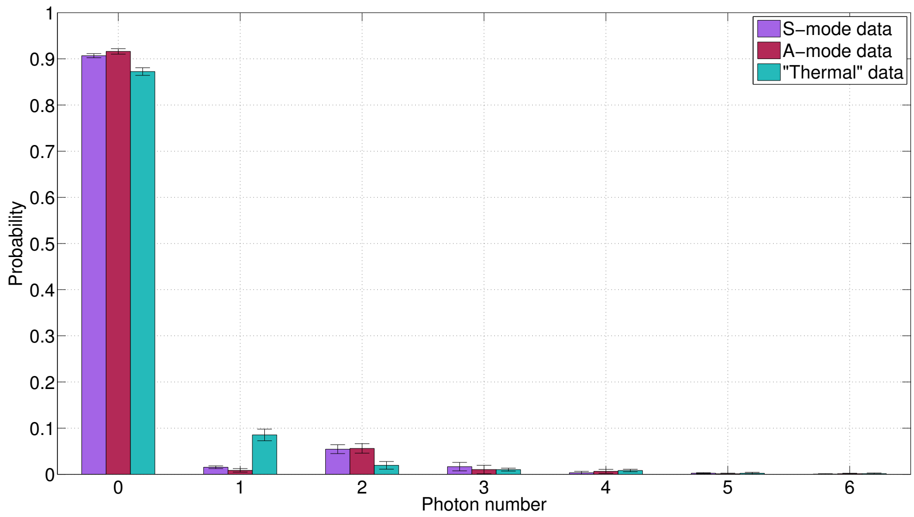

Figure 5.12: Comparison of experimental photon number distributions corrected for $\eta_{HD} = 0.676$ for the *unprojected* symmetric (S-mode), anti-symmetric (A-mode), and 'thermal' modes at 515 MHz for an *unlocked* pump phase. The reconstruction parameters are listed in tables 5.3 & 5.4.

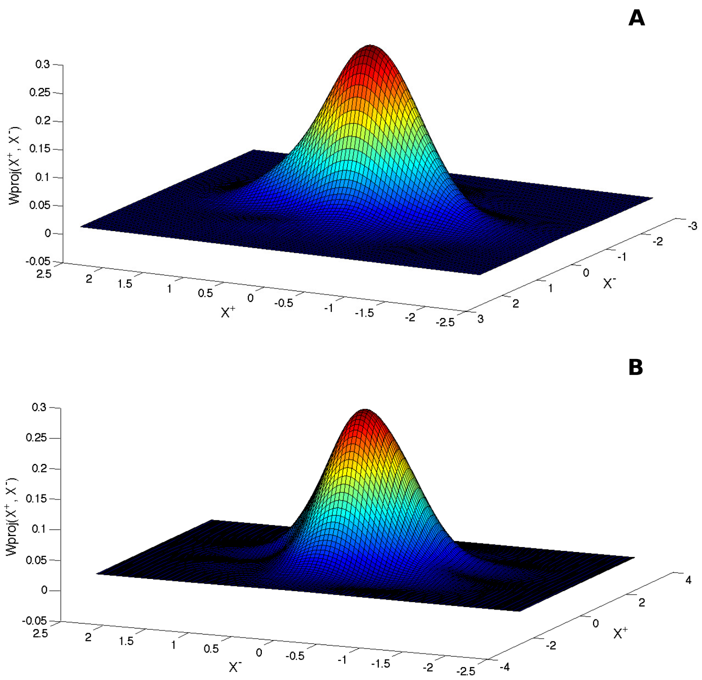

Figure 5.13: Experimental Wigner functions corrected for $\eta_{HD} = 0.676$ reconstructed from *unprojected* data at 515 MHz for an *unlocked* pump phase. A) Squeezed vacuum (symmetric mode), and B) 'thermal' mode. The reconstruction parameters are listed in tables 5.3 & 5.4.

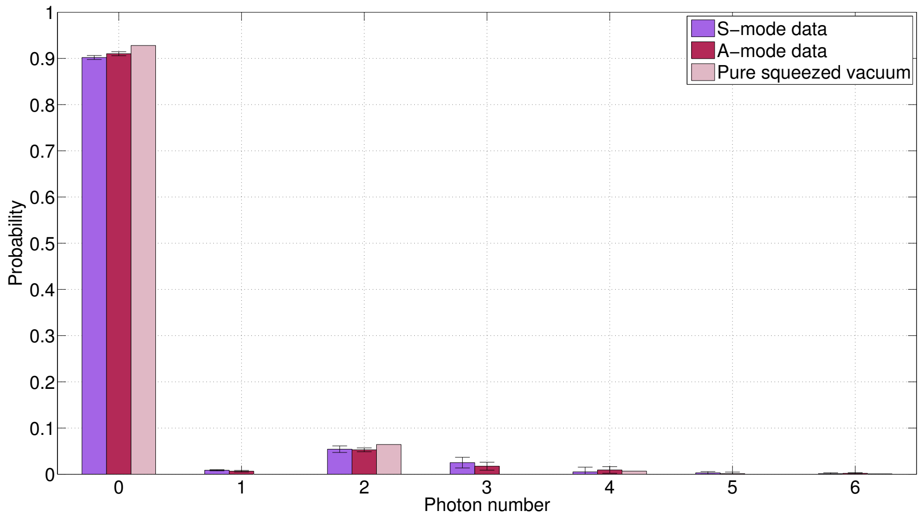

Figure 5.14: Comparison of experimental photon number distributions corrected for $\eta_{HD}\eta_e(515\,\text{MHz}) = 0.5814$ for the *unprojected* symmetric (S-mode) and anti-symmetric (A-mode) modes at 515 MHz for an *unlocked* pump phase to a pure squeezed vacuum state with -3.4 dB of squeezing. The reconstruction parameters are listed in tables 5.3 & 5.4, and the pure squeezed vacuum PND was calculated using equation 2.54.

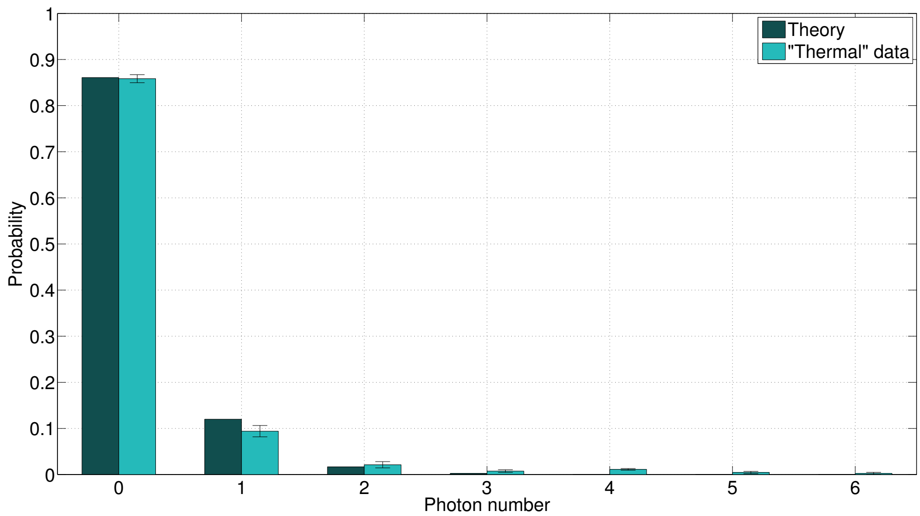

Figure 5.15: Comparison of experimental photon number distributions corrected for $\eta_{HD}\eta_e(515\,\text{MHz}) = 0.5814$ for the 'thermal' mode at 515 MHz for an *unlocked* pump phase to a theoretical thermal state corresponding to -3.4 dB of squeezing. The reconstruction parameters are listed in tables 5.3 & 5.4, and the theoretical thermal state PND was calculated using equation 2.49.

Measurement technique or theoretical prediction	Squeezing level	Anti-squeezing level
Predicted by eqn 2.139	-2.591 dB	4.876 dB
Spectrum analyser measurement	-2.35 $\pm$ 0.5 dB	3.9 $\pm$ 0.5 dB
Estimated from 'thermal' reconstructed PND	-2.6 dB	—

Table 5.6: Summary of the theoretically predicted squeezing levels by equation 2.139 and the experimentally measured values for the squeezed vacuum results with an *unlocked* pump phase.

5.2.3.3 Corrected for $\eta_{HD}\eta_e(f)$

Finally we present experimental results corrected for both η_{HD} *and* $\eta_e(f)$, where $\eta_e(f)$ models a loss in frequency-dependent detection efficiency caused by data aliasing effects. By correcting for both of these detection inefficiencies, the experimental results of the unprojected symmetric and anti-symmetric modes shown in figure 5.14 closely resemble a pure squeezed vacuum state. These PNDs were reconstructed using $\eta_{HD}\eta_e(515\text{ MHz}) = 0.5814$, as well as the parameters listed in tables 5.3 & 5.4.

The pure squeezed vacuum state PND shown was calculated using equation 2.54 for a squeezing level of -3.4 dB. Figure 5.15 shows the PND for the 'thermal' mode corrected for $\eta_{HD}\eta_e(515\text{ MHz}) = 0.5814$, and reconstructed using the parameters listed in tables 5.3 & 5.4. The theoretical PND of a thermal state shown corresponds to -3.4 dB of squeezing. Note that this squeezing level of -3.4 dB is similar to the pure squeezing levels used in the theoretical model to calculate PNDs for the impure uncorrected symmetric and anti-symmetric mode experimental data (see table 5.5).

5.3 Quantum state tomography — Locked pump phase

We will now present the data results of the unprojected states with the pump phase 'locked.' Figure 5.16 illustrates how the quality of the unprojected symmetric mode squeezed vacuum state demodulated at 515 MHz is considerably improved by implementing a pump phase lock with a smaller and smaller window. The amount of uncorrected squeezing is shown to increase (i.e. lower variance) as the pump

Pump phase window	Demodulation frequency	τ	ϕ
-90° – 0°	515 MHz	-238.3 ns	60°
-70° – 0°	515 MHz	-208.5 ns	18°
-50° – 0°	515 MHz	-250 ns	59.5°
-30° – 0°	515 MHz	-280 ns	81°
-10° – 0°	515 MHz	-281 ns	84°
-5° – 0°	515 MHz	-282 ns	59°
-3.5° – 0°	515 MHz	-284 ns	80.5°
-2.5° – 0°	515 MHz	-296 ns	81.6°

Table 5.7: Summary of parameters that were used to reconstruct *unprojected* states for various pump phase windows at the first FSR (515 MHz).

phase window is narrowed from $\Delta 90°$ to $\Delta 2.5°$. The amount of squeezing shown for a $\Delta 90°$ pump phase window corresponds to the data results presented in §5.2.3 for an *unlocked* pump phase. The optimal pump phase window was found to be $\phi_{pump} = -2.5°$ to $0°$, which kept enough quadrature data for the results to be statistically significant and reliable. Rejecting large amounts of data affects the size of the errorbars, as illustrated in figure 5.16 (errorbar sizes increase as the pump phase window is lowered). Lowering this window further rejects too much data and the results become unreliable. The reconstruction parameters associated with each data point in figure 5.16 are listed in tables 5.3 & 5.7.

A probable explanation for why 'locking' the pump phase improves the quality of the quantum state is that an unknown phase drift in the experiment is affecting the pump phase, causing erratic phase jitter in the squeezing angle, ϕ_{pump}. This jitter may be difficult to accurately track by the parametric gain measurement used to estimate the pump phase. However, keeping only the data corresponding to a pump phase that falls within a small phase range around $\phi_{pump} = -1.25°$ removes the phase jitter effect. Therefore, the remaining data results presented in this chapter and in chapter 6 are with a $\Delta 2.5°$ pump phase window centred on $\phi_{pump} = -1.25°$ applied to the data.

5.3.1 515 MHz unprojected modes

Since the combination of τ and ϕ results in an effective phase rotation, there are multiple combinations of these values that can demodulate the data to expose the various side-band modes. Figure 5.17 illustrates the several sets of unprojected squeezed vacuum and thermal states that were found as the overall demodulation

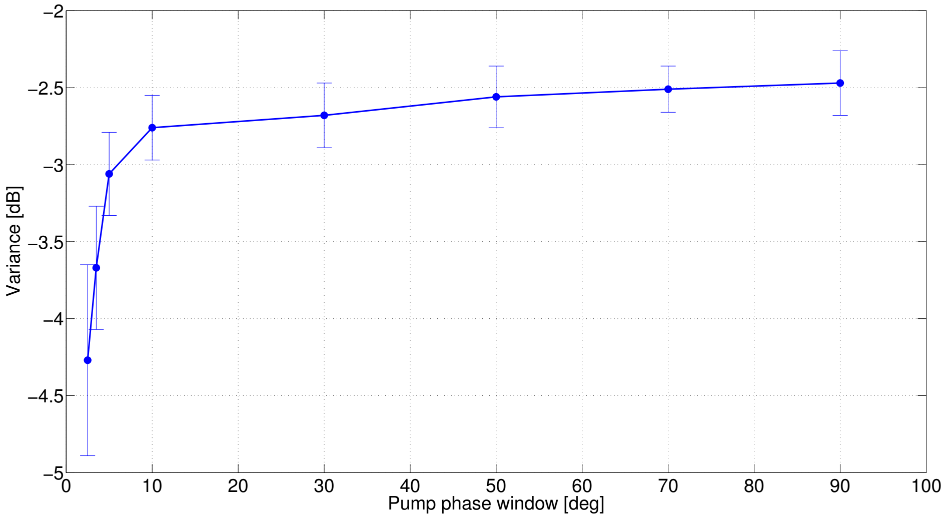

Figure 5.16: Uncorrected minimum variance of *unprojected* symmetric mode squeezed vacuum states demodulated at 515 MHz for various pump phase window sizes. The reconstruction parameters are listed in tables 5.3 & 5.7.

phase, ϑ, was rotated. We defined this overall demodulation phase as

$$\vartheta = -\omega_s \tau + \phi, \tag{5.13}$$

where ω_s is the demodulation angular frequency at an FSR frequency. However, there is only one unique set of τ and ϕ values that result in the best quality state for each mode. For the unprojected states, the 'best quality' is defined as the highest two-photon probability in the reconstructed symmetric and anti-symmetric mode squeezed vacuum states, and as the highest one-photon probability in the reconstructed 'thermal' mode. We will now present the PNDs of the unprojected symmetric and anti-symmetric modes demodulated at 515 MHz for a *locked* pump phase.

5.3.1.1 Without detection efficiency correction

Figure 5.18 shows the uncorrected experimental photon number distribution (PND) of the unprojected symmetric side-band mode (S-mode) at 515 MHz for a *locked* pump phase. This PND was reconstructed from homodyne tomography data of the unprojected state using the parameters listed in tables 5.3 & 5.8. Figure 5.18 also shows the theoretical PND of an impure single-mode squeezed vacuum mathematically simulated using the impure squeezed vacuum model outline in §2.6.1. The model parameters used to generate this theoretical PND of an impure squeezed vacuum state are listed in table 5.9. The model and experimental PNDs shown in figure 5.18 agree within error. Since the unprojected symmetric and anti-symmetric

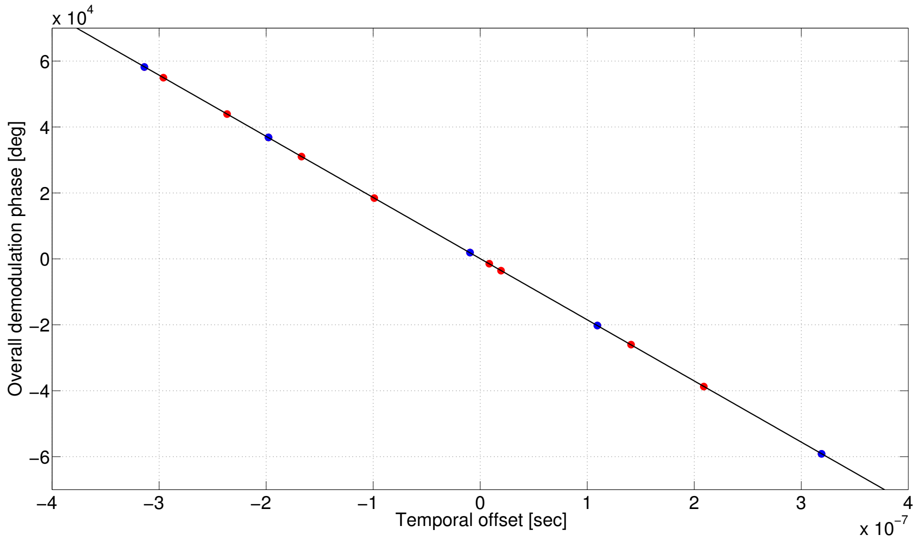

Figure 5.17: Multiple *unprojected* symmetric, anti-symmetric, and 'thermal' side-band modes at 515 MHz for several sets of τ and ϕ values for a *locked* pump phase. The overall demodulation phase is plotted as a function of the temporal offset, τ. Red dot: squeezed vacuum state, blue dot: 'thermal' state, black line: linear best fit.

modes are indistinguishable squeezed vacuum states, we will only present the PNDs and Wigner functions for the S-mode states for the rest of this chapter.

Side-band mode	Demodulation frequency	pump phase window	τ_1	ϕ_1
Symmetric mode	515 MHz	-2.5° – 0°	-296 ns	81.6°
'Thermal' mode	515 MHz	-2.5° – 0°	319 ns	4°

Table 5.8: Summary of parameters that were used to reconstruct unprojected states for a *locked* pump phase at the first FSR (515 MHz).

Figure 5.19 shows the uncorrected experimental PND of a state that appears to be a 'thermal' mode at 515 MHz. This PND was reconstructed from the same homodyne data set as the previous S-mode and A-mode PNDs, and was reconstructed using the parameters listed in tables 5.3 & 5.8.

Figure 5.20 shows the uncorrected Wigner functions for the unprojected squeezed vacuum symmetric mode (figure 5.20A) and the 'thermal' mode (figure 5.20B). The application of a pump phase window has made these Wigner functions become more noticeably different, even for *uncorrected* data.

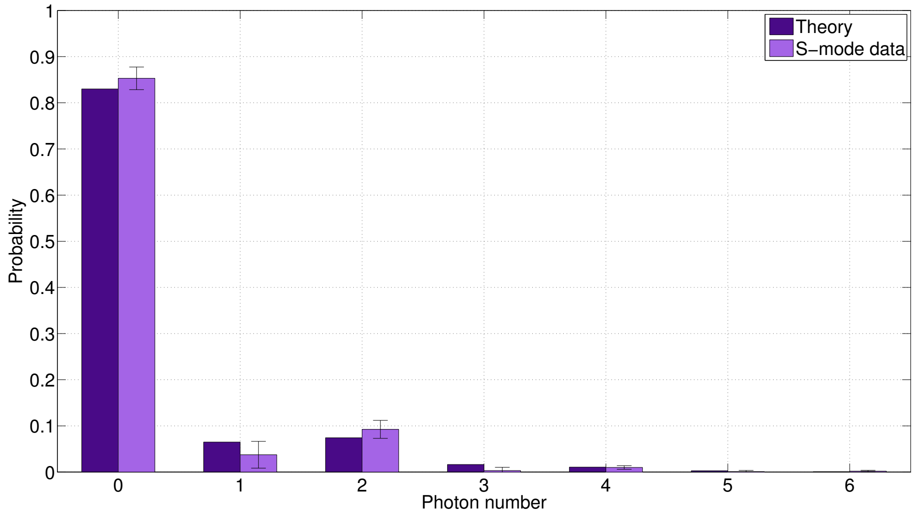

Figure 5.18: Comparison of uncorrected experimental and theoretical photon number distributions of the 515 MHz *unprojected* symmetric side-band mode (S-mode) for a *locked* pump phase. The reconstruction parameters are listed in tables 5.3 & 5.8, and the model parameters are listed in table 5.9.

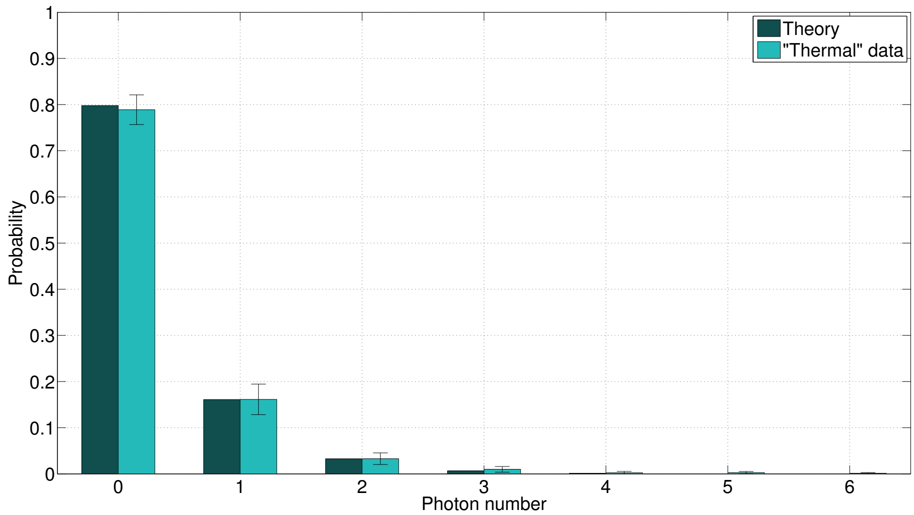

Figure 5.19: Comparison of uncorrected experimental and theoretical photon number distributions of a 'thermal' mode at 515 MHz for a *locked* pump phase. The theoretical thermal state PND was calculated using equation 2.49 and corresponds to -4.21 dB of squeezing. The reconstruction parameters are listed in tables 5.3 & 5.8.

Side-band mode	Pure squeezing level	Loss, r_1	η_{HD}
515 MHz S-mode	-5.82 dB	0.004916	0.676
1030 MHz S-mode	-3.474 dB	0.004916	0.676
1545 MHz S-mode	-3.301 dB	0.004916	0.676

Table 5.9: Summary of model parameters used to simulated impure squeezed vacuum states for unprojected state results with *locked* pump phase at 515 MHz, 1030 MHz, and 1545 MHz.

5.3.1.2 Corrected for η_{HD}

Figure 5.21 shows the PNDs for the unprojected symmetric and 'thermal' modes at 515 MHz corrected for $\eta_{HD} = 0.676$ and with a locked pump phase. These PNDs were reconstructed using the parameters listed in tables 5.3 & 5.8. Correcting for η_{HD} in the reconstruction code does *not* correct for $\eta_e(f)$, which is the poor detection efficiency caused by data aliasing effects described in §5.1.1.

Figure 5.22 shows the Wigner functions for the unprojected squeezed vacuum symmetric mode (figure 5.22A) and the 'thermal' mode (figure 5.22B). Note that correcting for imperfect homodyne detection, η_{HD}, increases the level of squeezing in the state and results in the Wigner functions becoming even more different to each other as compared to figure 5.20.

5.3.1.3 Corrected for $\eta_{HD}\eta_e(f)$

Finally we present experimental results corrected for both η_{HD} *and* $\eta_e(f)$, where $\eta_e(f)$ models a loss in detection efficiency caused by data aliasing effects. By correcting for both of these detection inefficiencies, the experimental results of the unprojected symmetric mode shown in figure 5.23 closely resemble a pure squeezed vacuum state corresponding to -5.82 dB of squeezing. These PNDs were reconstructed using $\eta_{HD}\eta_e(515\,\text{MHz}) = 0.5814$, as well as the parameters listed in tables 5.3 & 5.8.

The pure squeezed vacuum state PND shown was calculated using equation 2.54 for a squeezing level of -5.82 dB. Figure 5.24 shows the PND for the 'thermal' mode corrected for $\eta_{HD}\eta_e(515\text{ MHz}) = 0.5814$, and reconstructed using the parameters listed in tables 5.3 & 5.8. The theoretical PND of a thermal state shown corresponds to -5.82 dB of squeezing. Note that this squeezing level *is* the pure squeezing level used in the theoretical model to calculate the PND for the impure uncorrected symmetric mode at 515 MHz (see table 5.9).

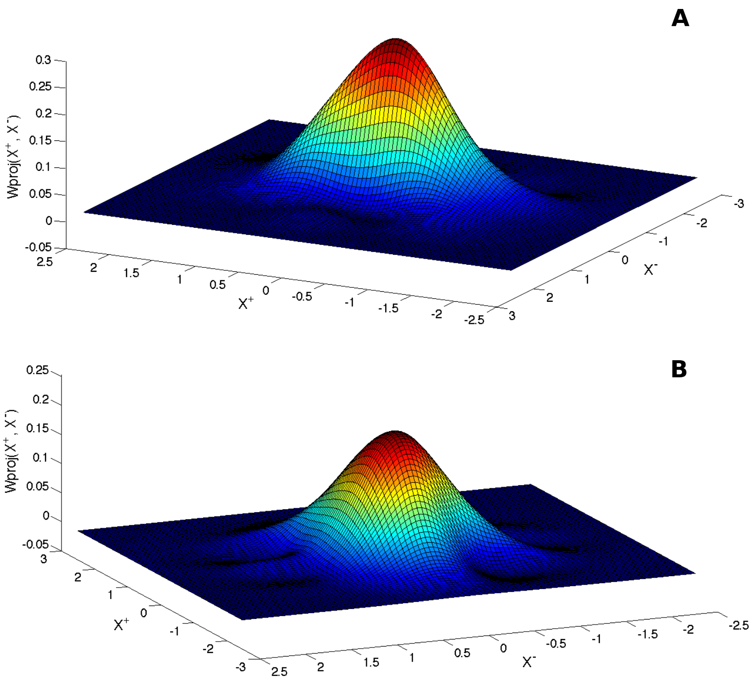

Figure 5.20: Experimental uncorrected Wigner functions reconstructed from *unprojected* data at 515 MHz for a *locked* pump phase. A) Squeezed vacuum (symmetric mode), and B) 'thermal' mode. The reconstruction parameters are listed in tables 5.3 & 5.8.

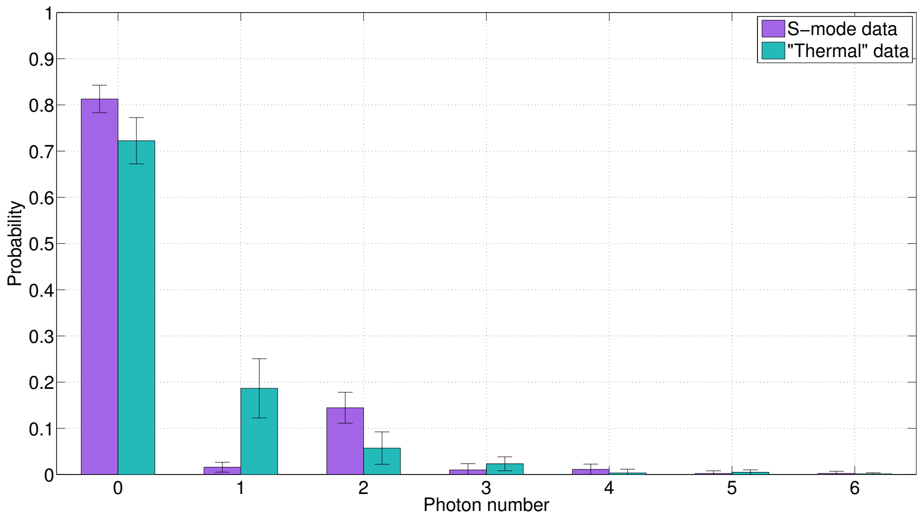

Figure 5.21: Comparison of experimental photon number distributions corrected for $\eta_{HD} = 0.676$ for *unprojected* symmetric (S-mode) and 'thermal' modes at 515 MHz for a *locked* pump phase. The reconstruction parameters are listed in tables 5.3 & 5.8.

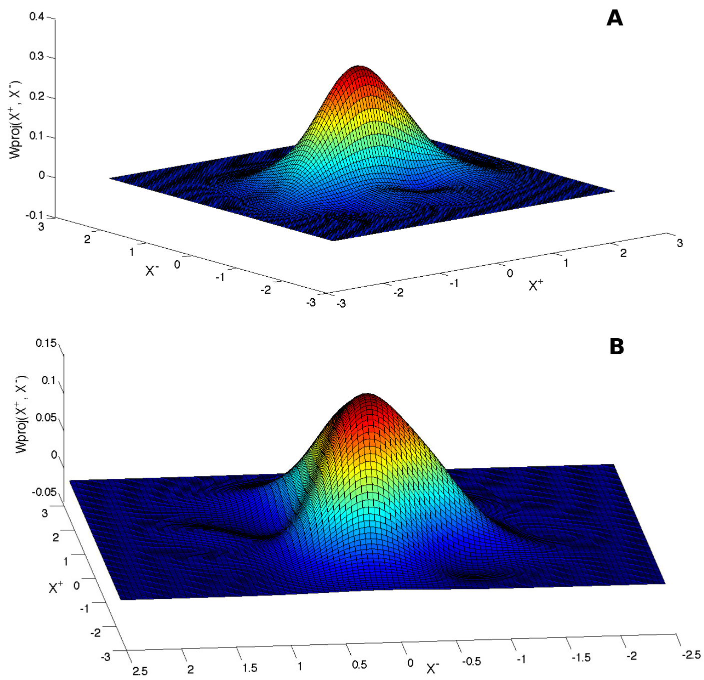

Figure 5.22: Experimental Wigner functions corrected for $\eta_{HD} = 0.676$ reconstructed from *unprojected* data at 515 MHz for a *locked* pump phase. A) Squeezed vacuum (symmetric mode), and B) 'thermal' mode. The reconstruction parameters are listed in tables 5.3 & 5.8.

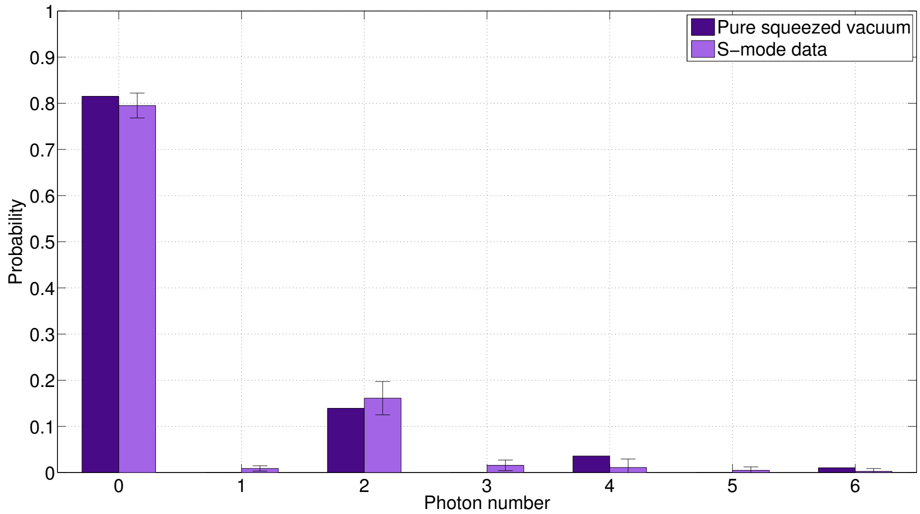

Figure 5.23: Comparison of experimental photon number distributions corrected for $\eta_{HD}\eta_e(515\text{ MHz}) = 0.5814$ for the *unprojected* symmetric (S-mode) mode at 515 MHz for a *locked* pump phase to a pure squeezed vacuum state with -5.82 dB of squeezing. The reconstruction parameters are listed in tables 5.3 & 5.8, and the pure squeezed vacuum PND was calculated using equation 2.54.

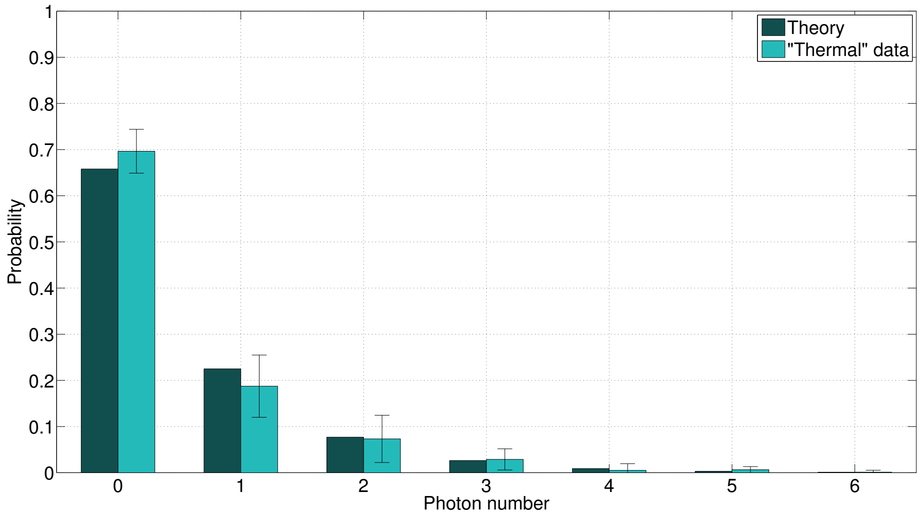

Figure 5.24: Comparison of experimental photon number distributions corrected for $\eta_{HD}\eta_e(515\text{ MHz}) = 0.5814$ for the 'thermal' mode at 515 MHz for a *locked* pump phase to a theoretical thermal state corresponding to -5.82 dB of squeezing. The reconstruction parameters are listed in tables 5.3 & 5.8, and the theoretical thermal state PND was calculated using equation 2.49.

5.3.2 1030 MHz unprojected modes

As discussed previously, a SS-NOPO generates squeezed vacuum states at every FSR frequency within the down-conversion bandwidth of the nonlinear crystal. We have access to the FSR states within the 2 GHz detection bandwidth of our homodyne detector. In the case of the unprojected states, each of the FSR states are *independent* squeezed states. Thus, we can probe the quantum states at the second FSR by choosing to demodulate at 1030 MHz. Theoretically the squeezed vacuum state at this frequency should be of a similar quality to the first FSR squeezed vacuum state. However, the data aliasing effect decreased the detection efficiency at the second FSR ($\eta_e(1030\text{ MHz}) = 0.424$) compared to at the first FSR ($\eta_e(1030\text{ MHz}) = 0.86$). We will show that the uncorrected unprojected symmetric mode data at 1030 MHz corresponds to a theoretical PND with a lower pure squeezing level than used to model the 515 MHz unprojected symmetric mode (see table 5.9). If the 1030 MHz data is only corrected for *optical* detection efficiency, η_{HD}, then the reconstructed PND still does not correspond to the same squeezing level as the 515 MHz data. It is only when both the optical detection efficiency and the aliasing effects are corrected for does the squeezing level of the reconstructed unprojected squeezed vacuum state at 1030 MHz look similar (to within less than 0.5 dB) to the 515 MHz states.

5.3.2.1 Without detection efficiency correction

Figure 5.25 shows the uncorrected experimental photon number distribution (PND) of the unprojected symmetric side-band mode (S-mode) at 1030 MHz for a *locked* pump phase. This PND was reconstructed from homodyne tomography data of the unprojected state using the parameters listed in tables 5.3 & 5.10. Figure 5.25 also shows the theoretical PND of an impure single-mode squeezed vacuum mathematically simulated using the impure squeezed vacuum model outline in §2.6.1. The model parameters used to generate this theoretical PND are listed in table 5.9. The model and experimental PNDs shown in figure 5.25 agree within error. Note that a lower pure squeezing level had to be used to model the data from 1030 MHz. We will show later in this section that this can be explained by the corruption of the quality of the squeezed vacuum state (i.e. lowered two-photon probability) due to the data aliasing effects.

Side-band mode	Demodulation frequency	pump phase window	τ_2	ϕ_2
Symmetric mode	1030 MHz	-2.5° – 0°	120 ns	48°
'Thermal' mode	1030 MHz	-2.5° – 0°	66.5 ns	129°

Table 5.10: Summary of parameters that were used to reconstruct unprojected states for a *locked* pump phase at the second FSR (1030 MHz).

Figure 5.26 shows the uncorrected experimental PND of a state that appears to be a 'thermal' mode at 1030 MHz. This PND was reconstructed from the same homodyne data set as the previous S-mode PND, and was reconstructed using the parameters listed in tables 5.3 & 5.10. Figure 5.27 shows the uncorrected Wigner functions for the unprojected squeezed vacuum symmetric mode (figure 5.27A) and the 'thermal' mode (figure 5.27B).

5.3.2.2 Corrected for η_{HD}

Figure 5.28 shows the PNDs for the unprojected symmetric and 'thermal' modes at 1030 MHz corrected for $\eta_{HD} = 0.676$ and with a locked pump phase. These PNDs were reconstructed using the parameters listed in tables 5.3 & 5.10.

Figure 5.29 shows the Wigner functions for the unprojected squeezed vacuum symmetric mode (figure 5.29A) and the 'thermal' mode (figure 5.29B). Note that correcting for imperfect homodyne detection, η_{HD}, increases the level of squeezing in the state. However, the PND and Wigner function for these corrected modes corresponds to a lower squeezing level (i.e. lower two-photon probability in the

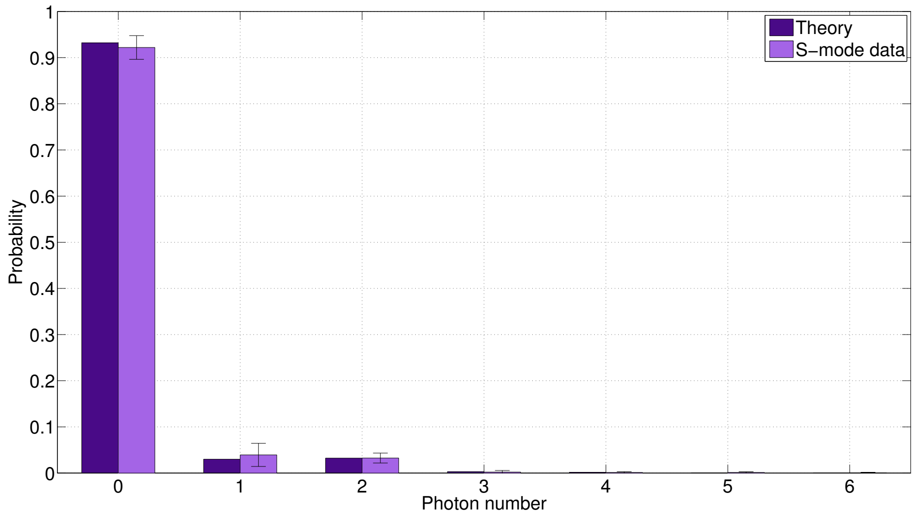

Figure 5.25: Comparison of uncorrected experimental and theoretical photon number distributions of the 1030 MHz *unprojected* symmetric side-band mode (S-mode) for a *locked* pump phase. The reconstruction parameters are listed in tables 5.3 & 5.10, and the model parameters are listed in table 5.9.

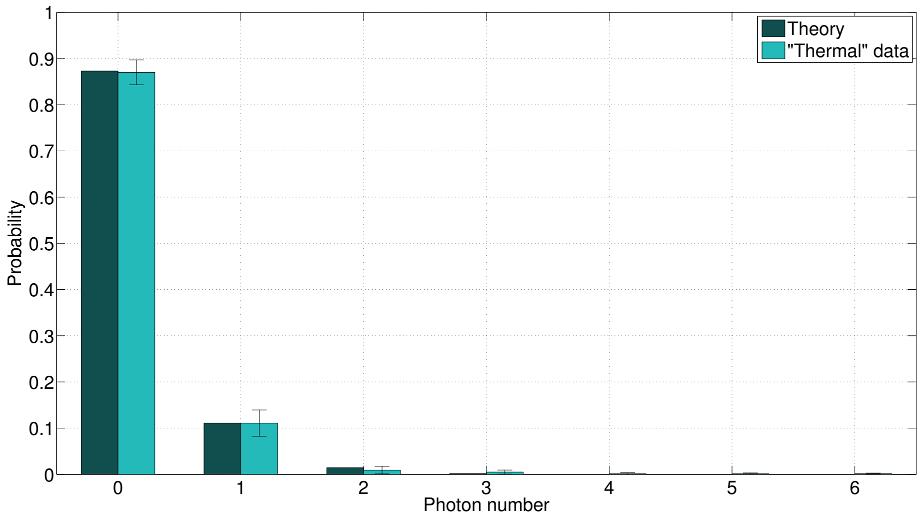

Figure 5.26: Comparison of uncorrected experimental and theoretical photon number distributions of a 'thermal' mode at 1030 MHz for a *locked* pump phase. The theoretical thermal state PND was calculated using equation 2.49 and corresponds to -3.24 dB of squeezing. The reconstruction parameters are listed in tables 5.3 & 5.10.

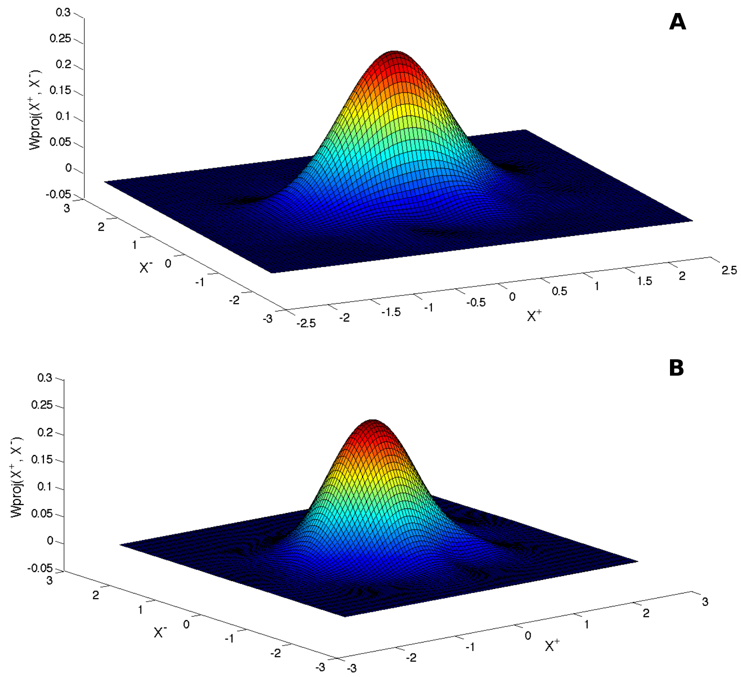

Figure 5.27: Experimental uncorrected Wigner functions reconstructed from *unprojected* data at 1030 MHz for a *locked* pump phase. A) Squeezed vacuum (symmetric mode), and B) 'thermal' mode. The reconstruction parameters are listed in tables 5.3 & 5.10.

squeezed vacuum state and lower one-photon probability in the 'thermal' state) compared to the 515 MHz modes corrected for η_{HD}. In the next section we will show what happens when we correct the 1030 MHz modes for both η_{HD} *and* $\eta_e(f)$.

5.3.2.3 Corrected for $\eta_{HD}\eta_e(f)$

Now we present experimental results corrected for both η_{HD} *and* $\eta_e(f)$, where $\eta_e(f)$ models a loss in detection efficiency caused by data aliasing effects. By correcting for both of these detection inefficiencies, the experimental results of the unprojected symmetric mode shown in figure 5.30 closely resemble a pure squeezed vacuum state corresponding to -5.4 dB of squeezing. This is only 0.42 dB less squeezing than the 515 MHz unprojected symmetric mode when corrected for $\eta_{HD}\eta_e(f)$. These PNDs were reconstructed using $\eta_{HD}\eta_e(1030 \text{ MHz}) = 0.2866$, as well as the parameters listed in tables 5.3 & 5.10.

The pure squeezed vacuum state PND shown was calculated using equation 2.54 for a squeezing level of -5.4 dB. Figure 5.31 shows the PND for the 'thermal' mode corrected for $\eta_{HD}\eta_e(1030 \text{ MHz}) = 0.2866$, and reconstructed using the parameters listed in tables 5.3 & 5.10. The theoretical PND of a thermal state shown corresponds to -5.4 dB of squeezing. Note that by correcting for the data aliasing effects, the reconstructed states at 1030 MHz are quite similar to the states previously pre-

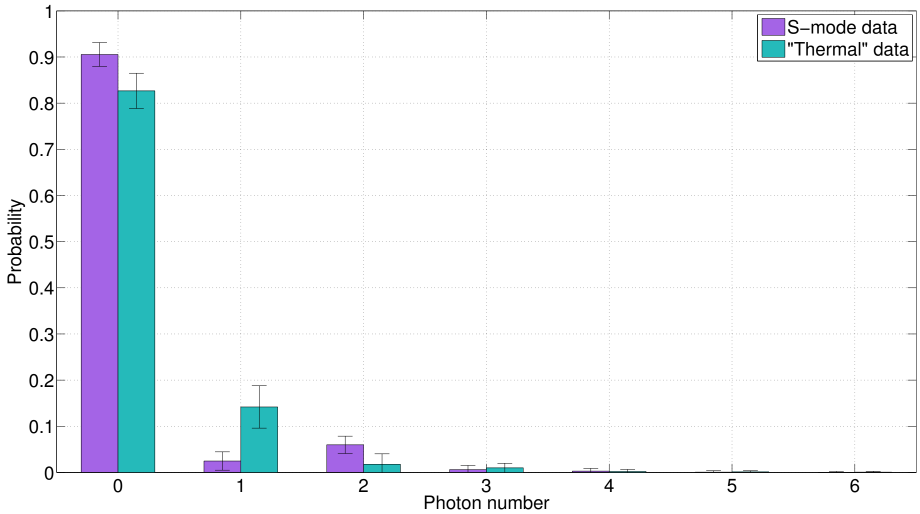

Figure 5.28: Comparison of experimental photon number distributions corrected for $\eta_{HD} = 0.676$ for the *unprojected* symmetric (S-mode) and 'thermal' modes at 1030 MHz for a *locked* pump phase. The reconstruction parameters are listed in tables 5.3 & 5.10.

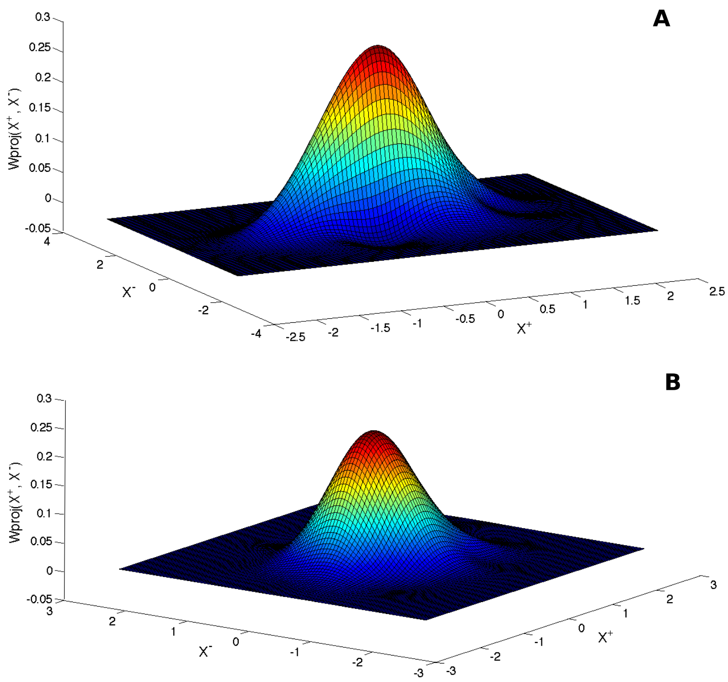

Figure 5.29: Experimental Wigner functions corrected for $\eta_{HD} = 0.676$ reconstructed from *unprojected* data at 1030 MHz for a *locked* pump phase. A) Squeezed vacuum (symmetric mode), and B) 'thermal' mode. The reconstruction parameters are listed in tables 5.3 & 5.10.

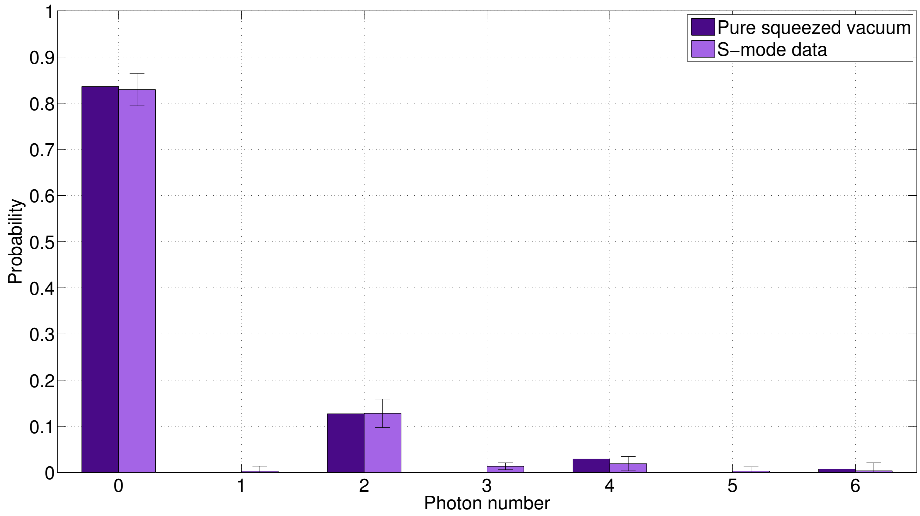

Figure 5.30: Comparison of experimental photon number distributions corrected for $\eta_{HD}\eta_e(1030\,\text{MHz}) = 0.2866$ for the *unprojected* symmetric (S-mode) mode at 1030 MHz for a *locked* pump phase to a pure squeezed vacuum state with -5.4 dB of squeezing.

sented for 515 MHz. Since the detection efficiency $\eta_e(f)$ at 1030 MHz is considerably lower than that at 515 MHz, it can be argued that this lowered quantum efficiency explains the lower squeezing levels for the uncorrected PNDs.

5.3.3 1545 MHz unprojected modes

5.3.3.1 Without detection efficiency correction

The quantum states at the third FSR can be reconstructed by demodulating at 1545 MHz. As with the second FSR measurement, data aliasing effects have decreased the detection efficiency at the third FSR significantly. Figure 5.32 shows the uncorrected experimental photon number distribution (PND) of the unprojected symmetric side-band mode (S-mode) at 1545 MHz for a *locked* pump phase. This PND was reconstructed from homodyne tomography data of the unprojected state using the parameters listed in tables 5.3 & 5.11. Figure 5.32 also shows the theoretical PND of an impure single-mode squeezed vacuum mathematically simulated using the impure squeezed vacuum model outline in §2.6.1. The model parameters used to generate this theoretical PND are listed in table 5.9. The model and experimental PNDs shown in figure 5.32 agree within error.

Figure 5.33 shows the uncorrected experimental PND of a state that appears to be a ‘thermal’ mode at 1545 MHz. This PND was reconstructed from the same homodyne data set as the previous S-mode PND, and was reconstructed using the parameters listed in tables 5.3 & 5.11. Figure 5.34 shows the uncorrected Wigner

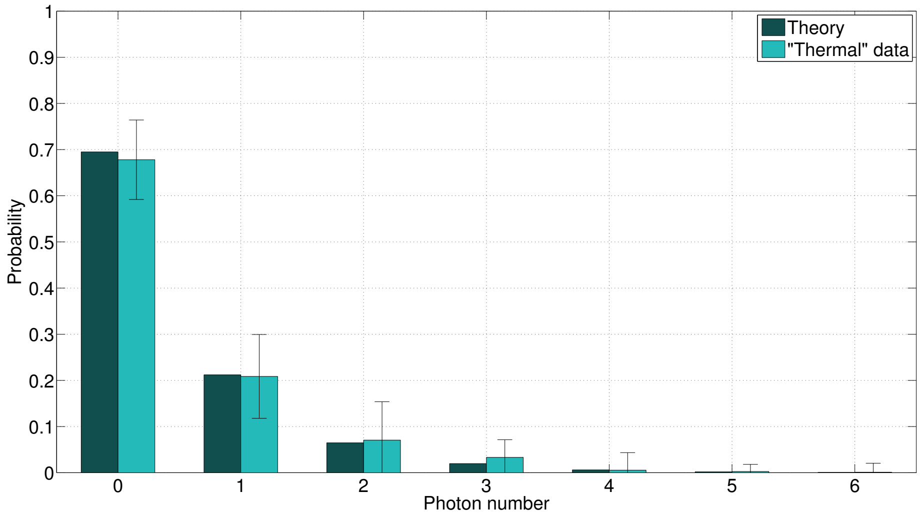

Figure 5.31: Comparison of experimental photon number distributions corrected for $\eta_{HD}\eta_e(1030\,\text{MHz}) = 0.2866$ for the 'thermal' mode at 1030 MHz for a *locked* pump phase to a theoretical thermal state corresponding to -5.4 dB of squeezing.

Side-band mode	Demodulation frequency	pump phase window	τ_3	ϕ_3
Symmetric mode	1545 MHz	-2.5° – 0°	-113 ns	26.5°
'Thermal' mode	1545 MHz	-2.5° – 0°	-141.5 ns	10.5°

Table 5.11: Summary of parameters that were used to reconstruct unprojected states for a *locked* pump phase at the third FSR (1545 MHz).

functions for the unprojected squeezed vacuum symmetric mode (figure 5.34A) and the 'thermal' mode (figure 5.34B).

5.3.3.2 Corrected for η_{HD}

Figure 5.35 shows the PNDs for the unprojected symmetric and 'thermal' modes at 1545 MHz corrected for $\eta_{HD} = 0.676$ and with a locked pump phase. These PNDs were reconstructed using the parameters listed in tables 5.3 & 5.11.

Figure 5.36 shows the Wigner functions for the unprojected squeezed vacuum symmetric mode (figure 5.36A) and the 'thermal' mode (figure 5.36B). Note that correcting for imperfect homodyne detection, η_{HD}, increases the level of squeezing in the state. However, the PND and Wigner function for these corrected modes still corresponds to a lower squeezing level (i.e. lower two-photon probability in the squeezed vacuum state and lower one-photon probability in the 'thermal' state) compared to the 515 MHz and 1030 MHz modes corrected for η_{HD}. We tried cor-

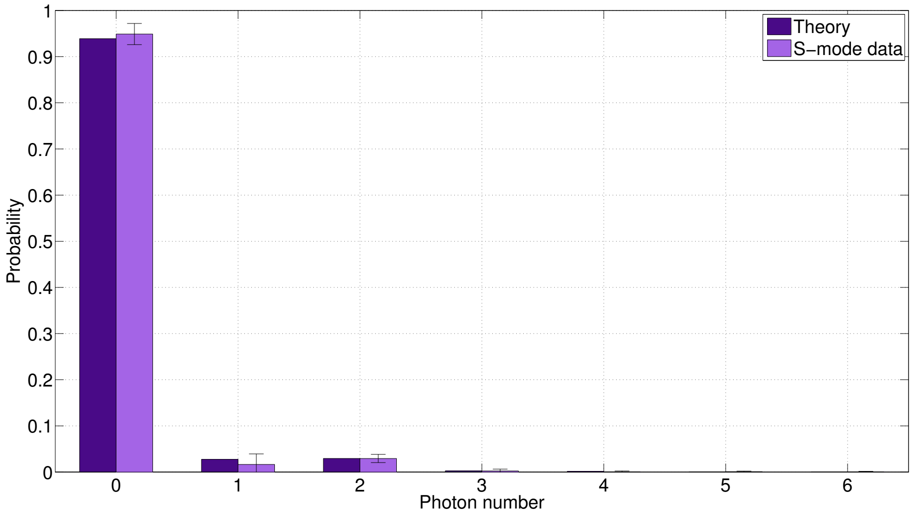

Figure 5.32: Comparison of uncorrected experimental and theoretical photon number distributions of the 1545 MHz *unprojected* symmetric side-band mode (S-mode) for a *locked* pump phase. The reconstruction parameters are listed in tables 5.3 & 5.11, and the model parameters are listed in table 5.9.

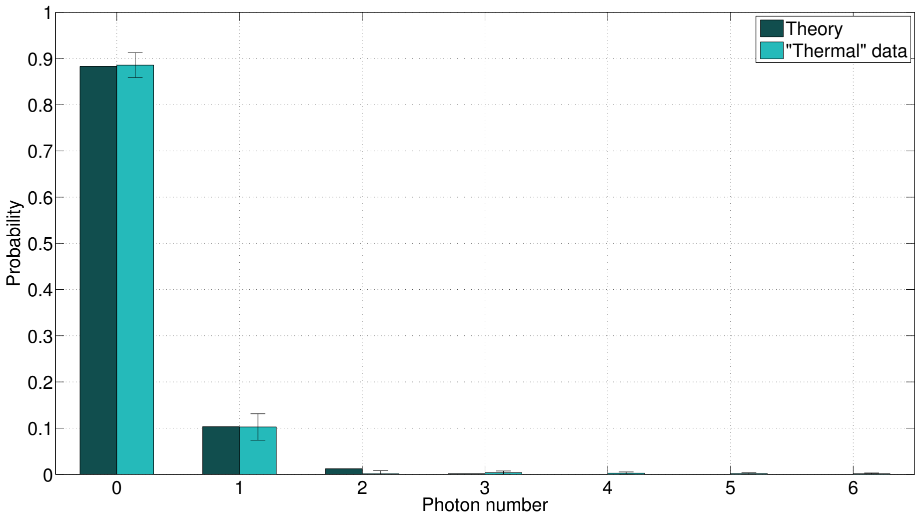

Figure 5.33: Comparison of uncorrected experimental and theoretical photon number distributions of a 'thermal' mode at 1545 MHz for a *locked* pump phase. The theoretical thermal state PND was calculated using equation 2.49 and corresponds to -3.09 dB of squeezing. The reconstruction parameters are listed in tables 5.3 & 5.11.

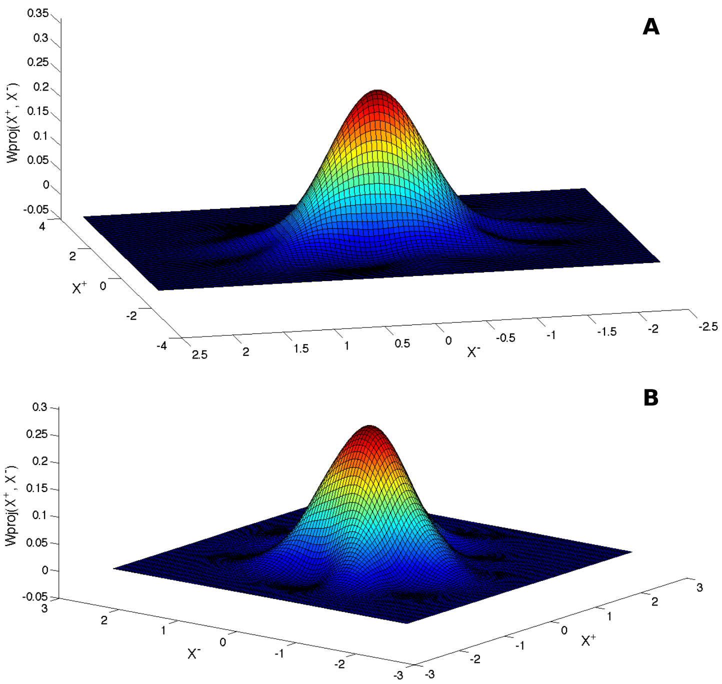

Figure 5.34: Experimental uncorrected Wigner functions reconstructed from *unprojected* data at 1545 MHz for a *locked* pump phase. A) Squeezed vacuum (symmetric mode), and B) 'thermal' mode. The reconstruction parameters are listed in tables 5.3 & 5.11.

recting the 1545 MHz data for both η_{HD} and $\eta_e(1545\,\text{MHz}) = 0.055$ but this led to unphysical results ($p_1 > 0.3$ & $p_2 > 0.4$). This is not surprising given the extremely small value of $\eta_e(f)$ at this frequency. However, as we shall show in chapter 6, there are real quantum states captured from this FSR that make a significant contribution to the quality of the reconstructed *projected* states. The unphysical results found by correcting the unprojected data for both η_{HD} and $\eta_e(f)$ are not an indication of unphysical results in chapter 6 as the $\eta_e(f)$ correction was not applied to the projected data. Rather $\eta_e(1545\,\text{MHz})$ was only used to calculate the magnitude of the third FSR contribution to the multi-FSR temporal mode function described by equation 5.6.

Table 5.12 summarises the estimated squeezing levels from the uncorrected 'thermal' mode experimental data and corrected ($\eta_{HD}\eta_e(f)$) squeezed vacuum mode experimental data at the three FSRs.

5.3.4 Multi-frequency mode function

Finally, as the data acquisition of the unprojected state was triggered by APD dark counts, there should be no correlations between the states generated at each FSR. We can demonstrate that each FSR behaves as an independent squeezed vacuum mode by observing the effects from demodulation with the multi-frequency mode

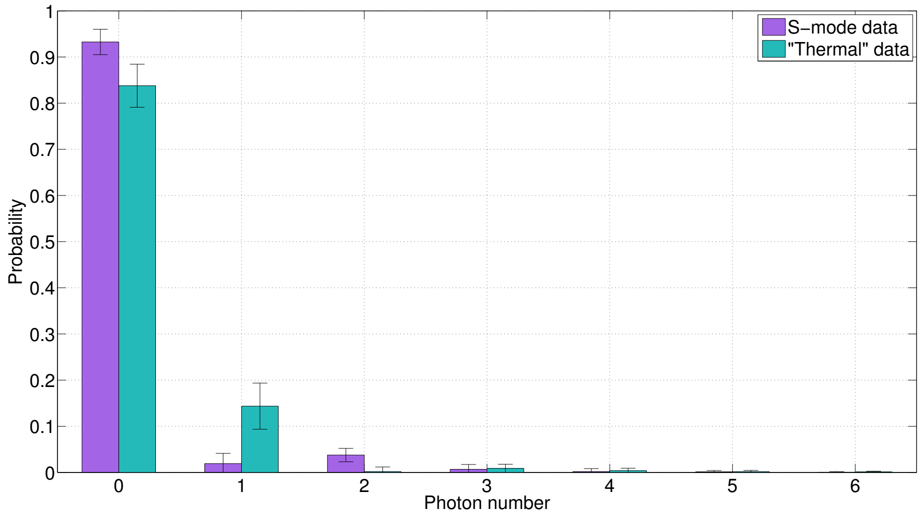

Figure 5.35: Comparison of experimental photon number distributions corrected for $\eta_{HD} = 0.676$ for the *unprojected* symmetric (S-mode) and 'thermal' modes at 1545 MHz for a *locked* pump phase. The reconstruction parameters are listed in tables 5.3 & 5.11.

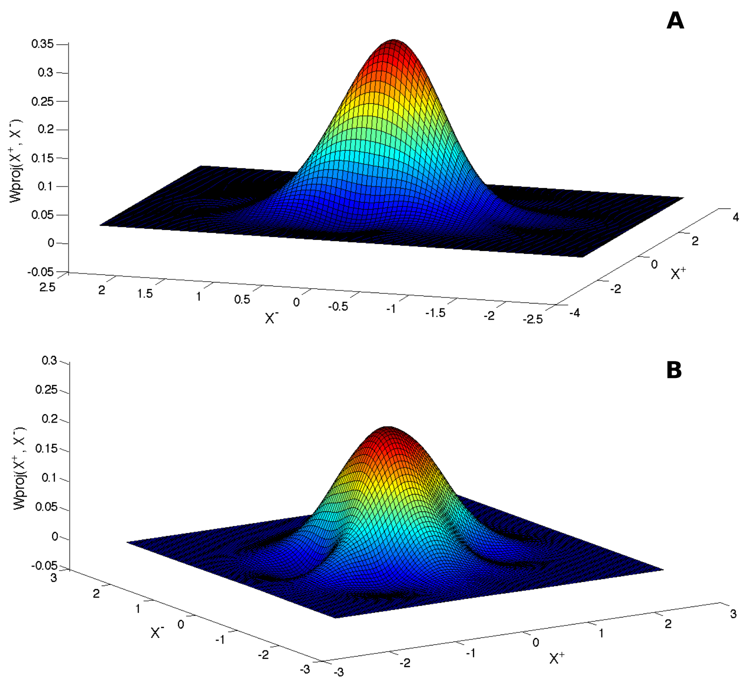

Figure 5.36: Experimental Wigner functions corrected for $\eta_{HD} = 0.676$ reconstructed from *unprojected* data at 1545 MHz for a *locked* pump phase. A) Squeezed vacuum (symmetric mode), and B) 'thermal' mode. The reconstruction parameters are listed in tables 5.3 & 5.11.

FSR frequency	Estimated V^- from 'thermal' mode uncorrected	Estimated V^- from S-mode corrected $\eta_{HD}\eta_e(f)$
515 MHz	-4.21 dB	-5.82 dB
1030 MHz	-3.24 dB	-5.4 dB
1545 MHz	-3.09 dB	—

Table 5.12: Summary of the estimated squeezing levels from the uncorrected 'thermal' mode experimental data and corrected $(\eta_{HD}\eta_e(f))$ squeezed vacuum mode experimental data at the three FSRs.

function described by equation 5.6. This mode function was specifically formulated to reveal the possible correlations that may exist between the FSRs in the projected state caused by the multi-FSR spectrum of the trigger mode. Therefore, if the unprojected FSR states are indeed independent squeezed vacuum states, then using this multi-FSR demodulation function in the post-processing should result in a weighted average of the three FSR squeezed vacuum states. That is

$$\mathrm{diag}(\hat{\rho}_{Ave}) = \gamma_1^2 \times \mathrm{diag}(\hat{\rho}_{515}) + \gamma_2^2 \times \mathrm{diag}(\hat{\rho}_{1030}) + \gamma_3^2 \times \mathrm{diag}(\hat{\rho}_{1545}), \tag{5.14}$$

where $\mathrm{diag}(\rho_f)$ are the experimental PNDs of the unprojected symmetric modes at each of the FSR frequencies, and the coefficients γ_1, γ_2, γ_3 are calculated via equation 5.10. Considering the lower qualities of the uncorrected squeezed vacuum states at 1030 MHz and 1545 MHz compared to at 515 MHz, if no correlations exist between these states then using a multi-FSR temporal mode function would be like taking a weighted average of these three states. Such a reconstructed state should be of lesser quality (i.e. lower two-photon probability) then compared to the 'best' squeezed vacuum reconstructed state, which was the unprojected symmetric mode at 515 MHz.

5.3.4.1 Without detection efficiency correction

Figure 5.37 shows the uncorrected experimental photon number distributions (PND) of the unprojected symmetric side-band mode (S-mode) reconstructed using the multi-FSR temporal mode function described by equation 5.6 for a *locked* pump phase. This PND was reconstructed from homodyne tomography data of the unprojected state using the parameters listed in tables 5.3 & 5.13. As discussed in §5.1.2, the parameters used in the multi-frequency temporal mode function are related to the demodulation frequencies, temporal offsets, and demodulation phase offsets of the unprojected symmetric modes at 515 MHz, 1030 MHz and 1545 MHz.

The parameters $\Delta\tau_2$ and $\Delta\phi_2$ come from the relationships between the values listed in table 5.10 for the 1030 MHz unprojected symmetric mode, and the values listed in table 5.8 for the 515 MHz unprojected symmetric mode as defined by equation 5.12. While the parameters $\Delta\tau_3$ and $\Delta\phi_3$ come from the relationships between the values listed in table 5.11 for the 1545 MHz unprojected symmetric mode, and the values listed in table 5.8 for the 515 MHz unprojected symmetric mode. For clarity the values of these various offsets that were used to reconstruct the quantum state using the multi-frequency temporal mode function are summarised in table 5.13.

ω_s	τ_m	ϕ_m	$\Delta\tau_2$	$\Delta\phi_2$	$\Delta\tau_3$	$\Delta\phi_3$
$2\pi \times 515$ MHz	-237.5 ns	71.2°	416 ns	-33.6°	183 ns	-55.1°

Table 5.13: Summary of parameters that were used to reconstruct the unprojected symmetric mode state for a *locked* pump phase ($\Delta\phi_{pump} = 2.5°$) using the multi-FSR temporal mode function described by equation 5.6.

Figure 5.37 also shows the uncorrected experimental photon number distribution (PND) of the unprojected symmetric side-band mode (S-mode) at 515 MHz for a *locked* pump phase. This PND was reconstructed using the parameters listed in tables 5.3 & 5.8, and is the FSR state with the highest two-photon probability. Comparing these two PNDs of the reconstructed unprojected symmetric mode shows that our prediction was correct: demodulating the unprojected data with this multi-FSR temporal mode function results in a worse squeezed vacuum (i.e. lower two-photon probability), indicating that correlations between the FSR states do not exist. We can further show that the multi-FSR state is in fact closer to a weighted-average calculated using equation 5.14 of the three individual FSR unprojected symmetric mode states. This calculated PND of the weighted average is shown in figure 5.37.

5.3.4.2 Corrected for η_{HD}

Figure 5.38 shows the PNDs for the unprojected symmetric modes for the multi-FSR temoral mode function and for demodulation at only 515 MHz with both corrected for $\eta_{HD} = 0.676$ (and with a locked pump phase). The multi-FSR PND was reconstructed using the parameters listed in tables 5.3 & 5.13, whereas the 515 MHz unprojected symmetric mode was reconstructed using the parameters listed in table 5.8. Note that even after the data has been corrected for homodyne efficiency the two-photon probability of the multi-FSR state is lower than the 515 MHz state.

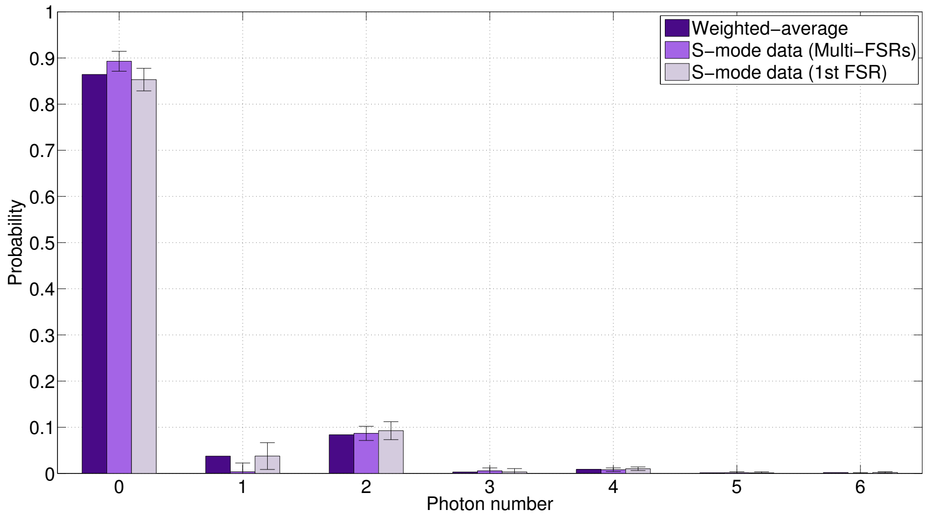

Figure 5.37: Comparison of uncorrected experimental photon number distributions of the multi-FSR *unprojected* symmetric side-band mode (S-mode Multi-FSRs) and the 515 MHz *unprojected* symmetric mode (S-mode 1st FSR) for a *locked* pump phase to a calculated weighted average of the three individual FSR *unprojected* symmetric mode states. The reconstruction parameters are listed in tables 5.3, 5.8 & 5.13. The weighted average was calculated via equation 5.14.

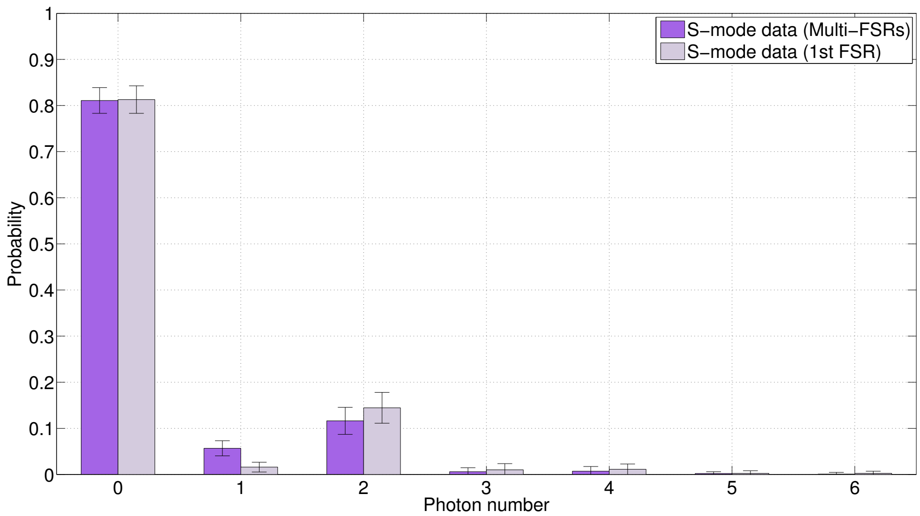

Figure 5.38: Comparison of experimental photon number distributions corrected for $\eta_{HD} = 0.676$ of the multi-FSR *unprojected* symmetric mode and the 515 MHz *unprojected* symmetric mode for a *locked* pump phase. The reconstruction parameters are listed in tables 5.3, 5.8 & 5.13.

5.4 Summary

We first summarized our data acquisition technique and discussed the effect undersampling the homodyne signal had on the effective detection efficiencies at the various FSR frequencies. Then we introduced the frequency-offset temporal mode functions that were applied to the homodyne data to extract quadrature data. An innovative measurement technique was experimentally applied to a two-mode squeezed vacuum state generated by a SS-NOPO. Quantum tomography of the single-mode squeezed vacuum states in the symmetric/anti-symmetric side-band modes were reconstructed at multiple FSR frequencies via phase-locked time-and-frequency-resolved measurements. Since data collection of the unprojected two-mode squeezed vacuum state was initiated by APD dark counts, the unprojected squeezed vacuum states at the multiple FSRs were uncorrelated. Therefore, applying the multi-frequency demodulation function resulted in a weighted-average of the quantum states at the three FSRs, and failed to improve the quality of the squeezed vacuum state.

In the next chapter we shall turn our attention to *projected* state data, where we will show that the properties of Gaussianity, equivalence between the symmetric and anti-symmetric modes, and independent states at each FSR will all be changed.

Chapter 6

Two-mode photon-subtracted squeezed vacuum results

What we observe is not nature itself, but nature exposed to our method of questioning.
Werner Heisenberg

In this chapter we present the data results from our projected state experiment where the detection of filtered trigger photons heralded simultaneous generation of a photon-subtracted squeezed vacuum state and a single-mode squeezed vacuum state in orthogonal side-band modes. We will present the tomographic state reconstruction of these quantum states in different side-band modes for the first three FSRs of our side-band-scale nondegenerate optical parametric oscillator (SS-NOPO). We then apply a multi-FSR temporal mode function to the projected data that demodulates at multiple FSR frequencies. Applying this mode function reveals entanglement between the FSR side-band states due to the transmission spectrum of our optical filter cavities. A recently introduced quantum non-Gaussian character witness is discussed and applied to our photon-subtracted squeezed state. The result demonstrates that despite its positive Wigner function, the photon-subtracted squeezed vacuum state in the symmetric mode can be classified as a quantum non-Gaussian state. Finally, we discuss some numerical simulation results that investigated the effects a high APD dark count rate and low detection efficiencies have on the quality of a projected state.

6.1 Quantum non-Gaussian character witness

First we will discuss a measure of non-classicality which will be used to classify our photon-subtracted squeezed vacuum state as a quantum non-Gaussian state. A common method used to determine the non-classicality of a state was to test for negativity in the Wigner function [311]. However, for some non-classical quantum states, such as squeezed vacuum states, this criterion does not work because they possess positive Wigner functions. In addition, some heralded quantum states have positive Wigner functions that could not be prepared from Gaussian states and linear optical devices. The Wigner function is also extremely sensitive to various experimental imperfections that are present in projective state experiments, especially those conducted at telecommunication wavelengths, and any negativity can easily degrade in the Wigner function [304]. Therefore, Filip and Mišta Jr. recently proposed a new character witness that shows how some states with positive Wigner functions cannot be constructed with Gaussian states and linear optical devices [305]. States beyond a convex set of stochastic mixture of coherent states are defined as non-classical states. Similarly, quantum non-Gaussian states are referred to as states beyond a convex set of stochastic mixture of quantum Gaussian states [312, 313].

The quantum non-Gaussian character witness can be written in the Fock state basis, and is introduced as a linear combination of zero photon probability, p_0, and one photon probability, p_1, in the Fock state basis density matrix [312, 313],

$$W(a) = ap_0 + p_1 \tag{6.1}$$

where

$$p_0 = \frac{\exp[-e^r \sinh r]}{\cosh r} \tag{6.2}$$

$$p_1 = \frac{\exp[4r] - 1}{4} \frac{\exp[-e^r \sinh r]}{\cosh^3 r}. \tag{6.3}$$

$a \in [0, 1]$ is a dimensionless number and $r \in [0, \infty)$ is the squeezing parameter. A quantum Gaussian boundary, $W_G(a)$, is defined as the maximum value of $W(a)$ over a and r. The quantum non-Gaussian character witness value is defined as $W(a) - W_G(a)$. If this witness value is larger than 0, then the state is a quantum non-Gaussian state.

For quantum states related to squeezed states, such as squeezed single photon states or Schrödinger kitten states from photon-subtracted squeezed states, the quantum non-Gaussian character witness is generalized by an anti-squeezing operation [313],

$$W(a, s) = ap_0(s) + p_1(s) \tag{6.4}$$

where

$$p_n(s) = \langle n|\hat{S}^\dagger(s)\hat{\rho}\hat{S}(s)|n\rangle. \tag{6.5}$$

$\hat{S}^\dagger(s)$ and $\hat{S}(s)$ are the anti-squeezing and squeezing operators as a function of the anti-squeezing parameter, s, respectively, and $\hat{\rho}$ corresponds to the density matrix of the state in the Fock basis. The quantum non-Gaussian character witness value for these quantum states is defined as $W(a,s) - W_G(a)$. Again, if this witness value is larger than 0, then the state can be classified as a quantum non-Gaussian state. Equivalently, a classical boundary is defined as the maximum value of

$$W_{cl}(a) = ap_0 + p_1 \tag{6.6}$$

over a, where

$$\begin{aligned} p_0 &= \exp[-\bar{n}] \\ p_1 &= \bar{n}\exp[-\bar{n}], \end{aligned} \tag{6.7}$$

and $\bar{n} \in [0, \infty]$ is the mean photon number. Therefore, it is easy to identify the quantum non-Gaussian or non-classical characteristic of a state via its density matrix.

6.2 Two-mode projected states at individual FSRs

A photon-subtracted squeezed vacuum state is traditionally generated by degenerate PDC where the correlated photons are indistinguishable. Single-photon states are generally projected from nondegenerate PDC where the photons are distinguishable in either spatial or polarisation modes. Recently, a SS-NOPO was used to generate a single-photon state. The correlated upper ($+\omega_s$) and lower ($-\omega_s$) frequency side-bands of the SS-NOPO were first spatially separated (ω_s is the FSR angular frequency of the SS-NOPO). Then the detection of a photon in the lower side-band via an APD heralded the presence of a single photon in the upper side-band [218]. However, generation of a photon-subtracted squeezed vacuum state from a SS-NOPO at distinguishable side-band frequencies is yet to be experimentally realised. We will show in this chapter that exploiting the side-band scale naturally produced by a SS-NOPO leads to powerful resource states that could be used in various quantum communication and computation applications.

As we showed mathematically in chapter 3, applying an optical projector to a two-mode squeezed vacuum state that subtracts a photon in a superposition state of the upper and lower side-bands has the added advantage of producing *two* separate and *distinguishable* quantum states. The symmetric side-band mode is affected by the photon-subtraction event (producing a photon-subtracted squeezed vacuum state), whereas the anti-symmetric side-band mode remains a squeezed vacuum state. These states are independent and travelling in the same optical mode, making this projected state an attractive new quantum resource state for various quantum technologies.

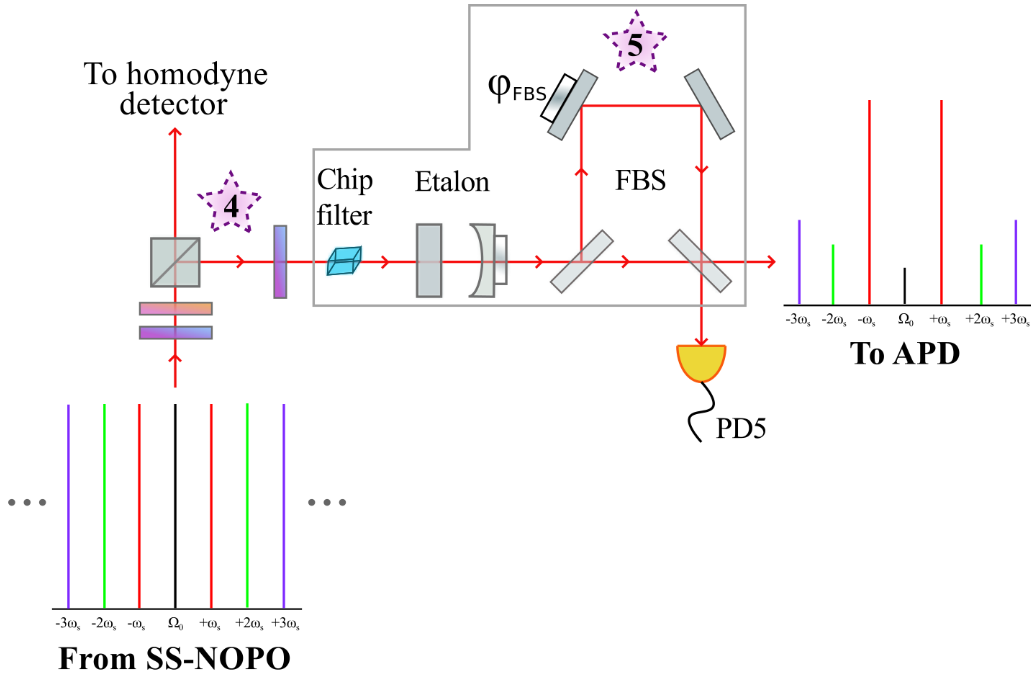

Figure 6.1: Schematic diagram of our optical filtering system and the resulting optical trigger mode spectrum sent to the APD.

It was also shown in chapter 3 that applying a phase-locked-frequency-resolved homodyne measurement operator to such a projected state allows full characterisation of both the symmetric and anti-symmetric side-band modes. The use of such a measurement is necessary as standard homodyne measurement techniques cannot individually access either the symmetric or anti-symmetric mode.

These concurrent quantum resource states can be experimentally generated if a superposition state between the upper and lower side-bands is maintained during the projective and homodyne measurements of the state. It is crucial that neither detector can distinguish between $+\omega_s$ and $-\omega_s$ side-bands during the experiment in order for the superposition state to be maintained. Therefore, the optical filtering applied to the trigger mode in our experiment resulted in a projective measurement that could not distinguish from which side-band the measured photon originated. Figure 6.1 shows a schematic of our filtering system used to isolate particular *pairs* of frequency side-bands produced by a SS-NOPO. The full spectrum from the SS-NOPO is sent to the tap-off beamsplitter, where a small portion ($\sim 8\%$) is reflected towards the optical filter cavities. The majority of the light from the SS-NOPO is transmitted to the homodyne detector for characterisation. The optical filter system shapes the spectrum, which results in the trigger mode spectrum illustrated in figure 6.1 to be sent to the APD for projective state measurements. If we wanted to reproduce the trigger spectrum used in [218] (i.e. sent only $-\omega_s$ to the APD), we would have to change the FBS configuration to 'configuration B' as previously described in §2.3.3 ($\phi_{FBS} = \pi/2$ and phase shift from the path length difference of $\varsigma_{FBS} = \pi/2$).

Homodyne detection coupled with frequency demodulation results in our measurement modes to be in the rotated side-band basis, previously defined as the symmetric and anti-symmetric modes, $+\omega_s + -\omega_s$ and $+\omega_s - -\omega_s$, respectively. The way that we subtract a single photon from the two-mode squeezed vacuum state generated by our SS-NOPO makes it equivalent to subtracting a photon from the single-mode squeezed vacuum state in the symmetric mode without affecting the single-mode squeezed vacuum state in the anti-symmetric mode. Therefore, a photon-subtracted squeezed state is projected in the symmetric side-band mode, and a squeezed vacuum state remains in the orthogonal mode.

The temporal and spectral mode-matching discussed in §5.1.2 was applied to the captured homodyne data during quantum state reconstruction. The details of our measurement conditions and data acquisition parameters are summarised in table 6.1.

Data acquisition of the projected state was initiated by the detection of a trigger photon by the APD. The filter cavities before the APD were designed to isolate the upper and lower side-bands at the first FSR frequency of 515 MHz from the rest of the down-conversion spectrum. Due to the optical limitations of the filter chain, a small portion of the second and third FSR side-band pairs were also transmitted to the APD, as illustrated in figure 6.1. However, the majority of the spectrum was concentrated at the first FSR.

We will now present quantum state tomography results for the projected states demodulated at a single FSR frequency for a 'locked' pump phase. There are two categories of results which will be discussed:

1. Data *uncorrected* for imperfect homodyne detection efficiency

2. Data *corrected* for imperfect *optical* homodyne detection efficiency (η_{HD})

Unlike the results presented in chapter 5, we will not correct the projected states for both η_{HD} and $\eta_e(f)$. The data aliasing effects previously described in chapter 5 influences how best to *reconstruct* the projected state by using a frequency-offset temporal mode function which incorporates the data aliasing effects into the *weightings* of the various frequency components (see equation 5.6). We used such a multi-FSR weighted temporal mode function on the unprojected data in chapter 5, which resulted in a 'worse' unprojected squeezed vacuum state as each FSR state was acting as an independent state. We will see that using the same multi-FSR function (but with the appropriate τ and ϕ offsets) will result in 'better' projected states as the FSR states are now *entangled* due to the multi-frequency spectrum of the trigger mode.

Parameter	Symbol	Value
Pump power	P_{775}	124 mW
LO power	—	3.2 mW
Quantum efficiency of homodyne detector	η_{QE}	0.9
Propagation efficiency	η_t	0.959*
Homodyne detector interference visibility	ζ	0.924
Homodyne detection efficiency	$\eta_{HD} = \eta_{QE}\eta_t\zeta^2$	0.7368
Detection efficiency (515 MHz) due to data aliasing	$\eta_e(515\,\text{MHz})$	0.86
Detection efficiency (1030 MHz) due to data aliasing	$\eta_e(1030\,\text{MHz})$	0.424
Detection efficiency (1545 MHz) due to data aliasing	$\eta_e(1545\,\text{MHz})$	0.055
Data sampling rate	—	2 GS/s
Homodyne data length	—	5 μs

Table 6.1: Summary of experimental and reconstruction parameters that were used to collect and analysis all *projected* data presented in this chapter. * the tap-off reflectivity, r_2, is not included in the propagation efficiency for the projected state data (as it was in the *unprojected* state data).

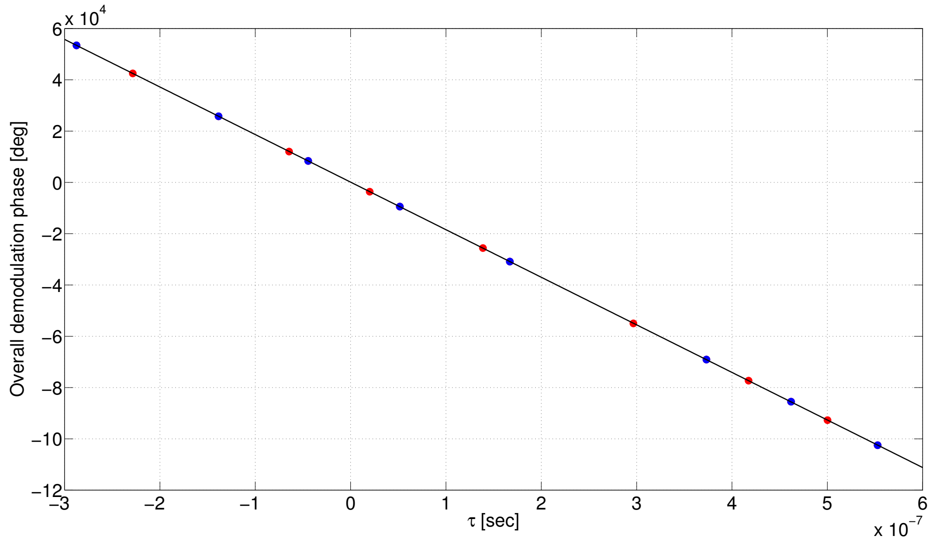

Figure 6.2: Multiple *projected* symmetric and anti-symmetric side-band mode states at 515 MHz for several sets of τ and ϕ values. The overall demodulation phase is plotted as a function of the temporal offset, τ. Red dot: projected squeezed vacuum state, blue dot: photon-subtracted squeezed vacuum state, black line: linear best fit.

6.2.1 515 MHz projected modes

Since the demodulation stage is implemented during post-processing, we can choose to reconstruct the quantum states at individual FSR frequencies by numerically implementing equation 5.5. We showed in the previous chapter that the temporal and demodulation offsets interact to produce an overall rotation (defined by equation 5.13) through the symmetric and anti-symmetric modes. A similar effect occurred when analysing the projected data where multiple photon-subtracted and squeezed vacuum states were found for various combinations of τ and ϕ. The various projected side-band states found at the first FSR of 515 MHz for a *locked* pump phase are shown in figure 6.2.

6.2.1.1 Without detection efficiency correction

Figure 6.3 shows the uncorrected experimental photon number distribution (PND) of the *projected* symmetric side-band mode (S-mode) at 515 MHz for a *locked* pump phase. This PND was reconstructed from homodyne tomography data of the projected state using the parameters listed in tables 6.1 & 6.2. Figure 6.3 also shows the theoretical PND of photon-subtracted squeezed vacuum state mathematically simulated using the model outlined in §2.6. The model parameters used to generate the theoretical PND of the *projected* symmetric mode at 515 MHz are listed in table 6.3. The model and experimental PNDs shown in figure 6.3 agree within error.

Side-band mode	Demodulation frequency	pump phase window	τ_1	ϕ_1
Symmetric mode	515 MHz	-2.5° – 0°	51.6 ns	154.3°
Anti-symmetric mode	515 MHz	-2.5° – 0°	20 ns	78°

Table 6.2: Summary of parameters that were used to reconstruct *projected* states for a *locked* pump phase at the first FSR (515 MHz).

Side-band mode	Pure squeezing level	Loss r_1	Tap-off r_2	η_{HD}	η_{APD}	P_{dc}
515 MHz S-mode	-3.474 dB	0.005	0.008	0.7368	0.08	0.00175
515 MHz A-mode	-5.646 dB	0.005	0	0.7368	—	—

Table 6.3: Summary of model parameters used to simulated *projected* symmetric mode (S-mode) and anti-symmetric mode (A-mode) states at 515 MHz with *locked* pump phase.

Figure 6.4 shows the uncorrected experimental photon number distribution (PND) of the *projected* anti-symmetric side-band mode (A-mode) at 515 MHz for a *locked* pump phase. This PND was reconstructed from the homodyne tomography data using the parameters listed in tables 6.1 & 6.2. Figure 6.4 also shows the theoretical PND of the impure squeezed vacuum state mathematically simulated using the model outlined in §2.6. The model parameters used to generate the theoretical PND of the *projected* anti-symmetric mode at 515 MHz are listed in table 6.3. The model and experimental PNDs shown in figure 6.4 agree within error.

In §2.1.4 we summarised how a state's density matrix in the Fock basis can be calculated from its Wigner function and vice versa. This method was used to reconstruct the experimental Wigner functions based on the reconstructed density matrices. Figure 6.5 shows the uncorrected Wigner functions for the projected photon-subtracted squeezed vacuum state in the symmetric mode (figure 6.5A) and the squeezed vacuum state in the anti-symmetric mode (figure 6.5B) at 515 MHz for a *locked* pump phase. These quantum states possess experimental Wigner functions that are clearly different, with the projected symmetric mode Wigner function becoming non-Gaussian. We will see these modes become even more obviously different as the data is corrected for imperfect homodyne detection in the next section.

In §6.1 we reviewed a recently introduced measure for classifying states as quantum Gaussian or quantum non-Gaussian based on the zero-photon probability, p_0,

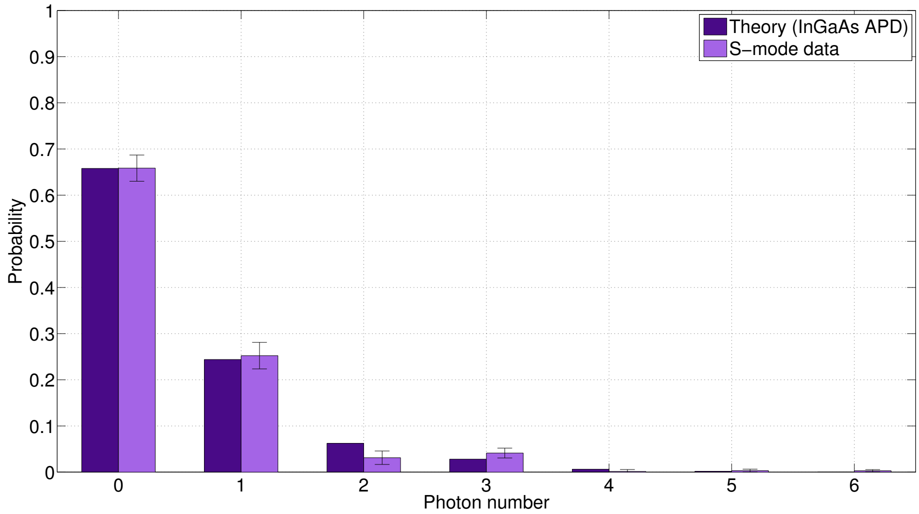

Figure 6.3: Comparison of uncorrected experimental and theoretical photon number distributions of the 515 MHz *projected* symmetric side-band mode (S-mode) for a *locked* pump phase. The reconstruction parameters are listed in tables 6.1 & 6.2, and the model parameters are listed in table 6.3.

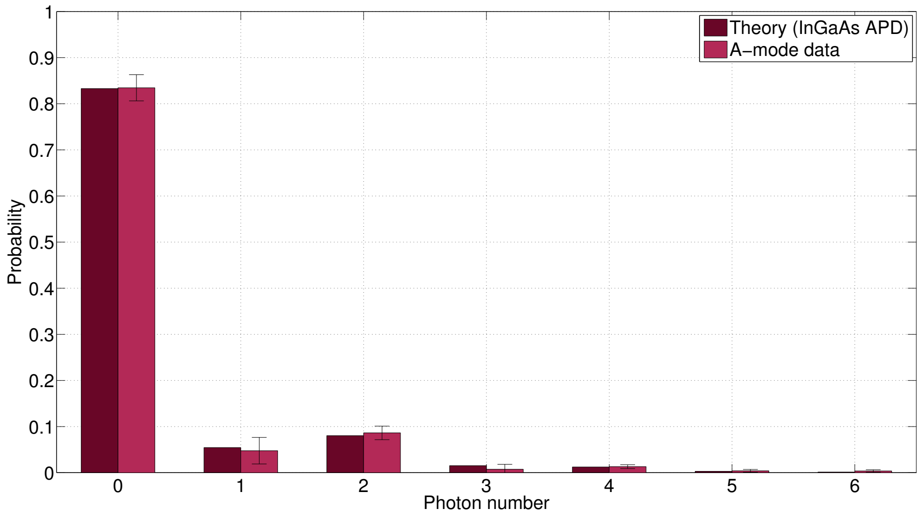

Figure 6.4: Comparison of uncorrected experimental and theoretical photon number distributions of the 515 MHz *projected* anti-symmetric (A-mode) side-band mode for a *locked* pump phase. The reconstruction parameters are listed in tables 6.1 & 6.2, and the model parameters are listed in table 6.3.

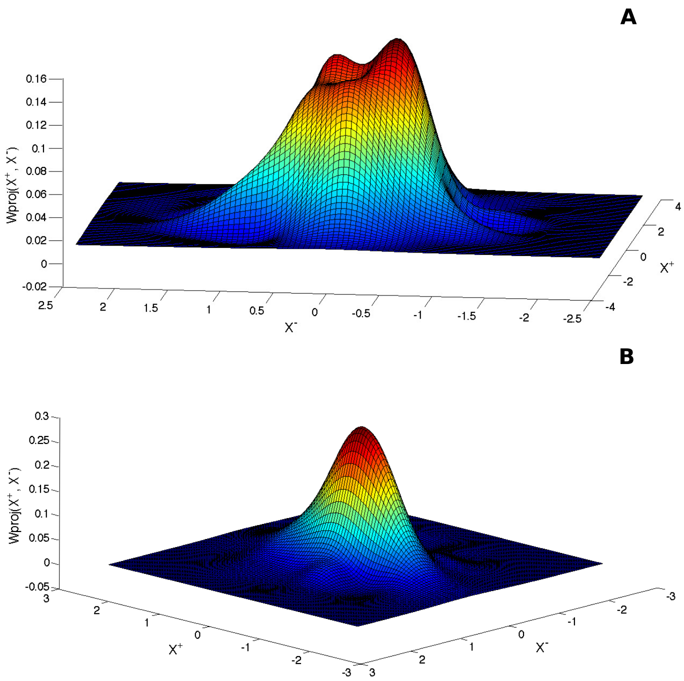

Figure 6.5: Experimental uncorrected Wigner functions reconstructed from *projected* data at 515 MHz for a *locked* pump phase. A) Photon-subtracted squeezed vacuum state (symmetric mode), and B) squeezed vacuum state (anti-symmetric mode). The reconstruction parameters are listed in tables 6.1 & 6.2.

and single-photon probability, p_1. We applied this quantum non-Gaussian character witness to our projected state data via equation 6.5 by applying the anti-squeezing operation to our experimental density matrix. This allowed us to calculate the (p_0, p_1) trajectory of our experimental data. If this trajectory crosses both the classical boundary (defined by equation 6.6) and the quantum Gaussian boundary (defined as $W_G(a)$ in §6.1), then the state can be classified as a *quantum non-Gaussian state*.

Figure 6.6 shows the uncorrected (p_0, p_1) trajectory of the photon-subtracted squeezed vacuum state (symmetric mode) at 515 MHz for a *locked* pump phase and using the reconstruction parameters listed in table 6.2. Note that the uncorrected (p_0, p_1) trajectory crosses the classical boundary but does not cross the Gaussian boundary by a statistically-significant margin. Therefore this experimental state can be statistically classified as a quantum Gaussian state but not as a quantum non-Gaussian state.

The quantum non-Gaussian character witness is defined in §6.1 as $W(a, s) - W_G(a)$. If this witness value is larger than 0, then the state is a quantum non-Gaussian state. Therefore, we can obtain the optimal witness $W(a_{opt}, s) - W_G(a_{opt})$ as a function of the anti-squeezing parameter, s, for our reconstructed density matrix. Figure 6.7 shows this optimal witness as a function of s for uncorrected exper-

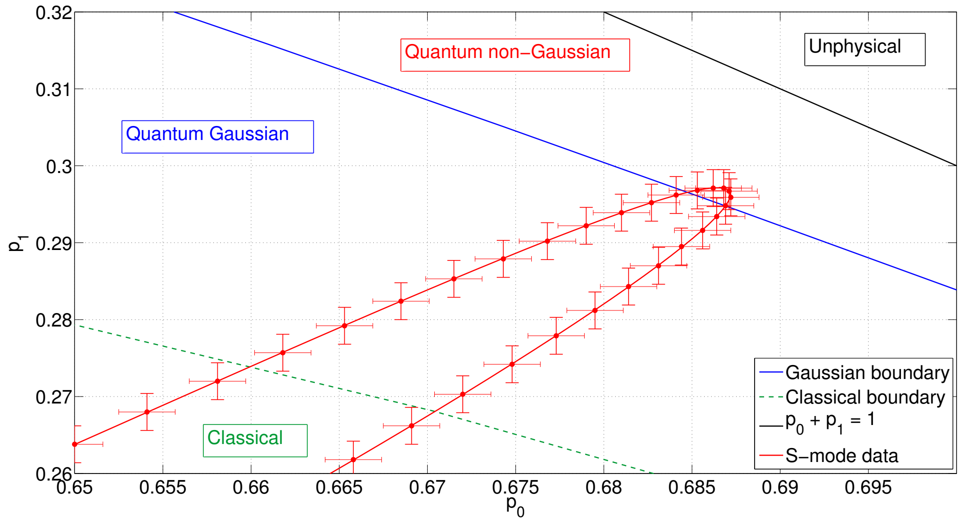

Figure 6.6: *Projected* symmetric mode (p_0, p_1) trajectory of our uncorrected experimental data at 515 MHz for a *locked* pump phase. The uncorrected trajectory crosses the classical boundary by a statistically-significant margin but does not statistically cross the Gaussian boundary, which means this experimental state cannot be statistically classified as a quantum non-Gaussian state.

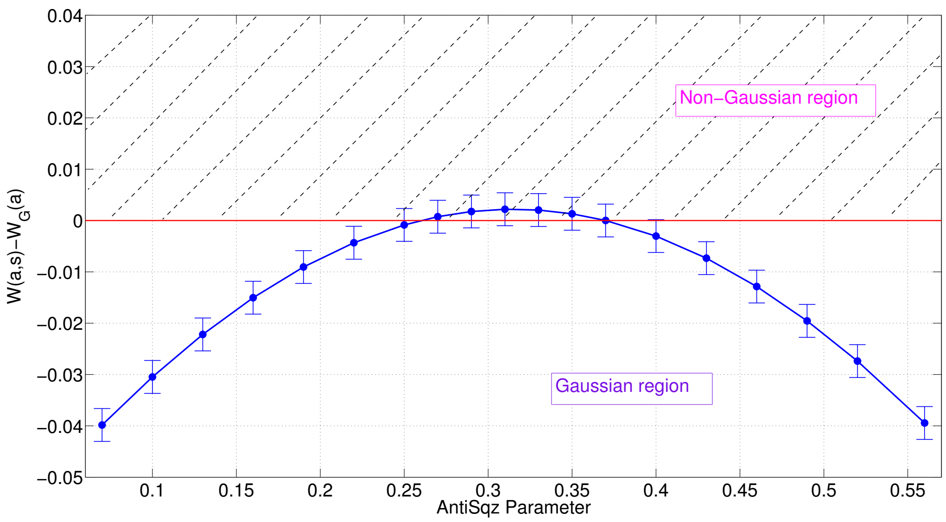

Figure 6.7: Quantum non-Gaussian character witness of our uncorrected *projected* symmetric mode state at 515 MHz for a *locked* pump phase. As the peak of this uncorrected curve does not cross the $W(a, s) - W_G(a) = 0$ boundary by a statistically-significant margin, this state cannot be classified as a quantum non-Gaussian state.

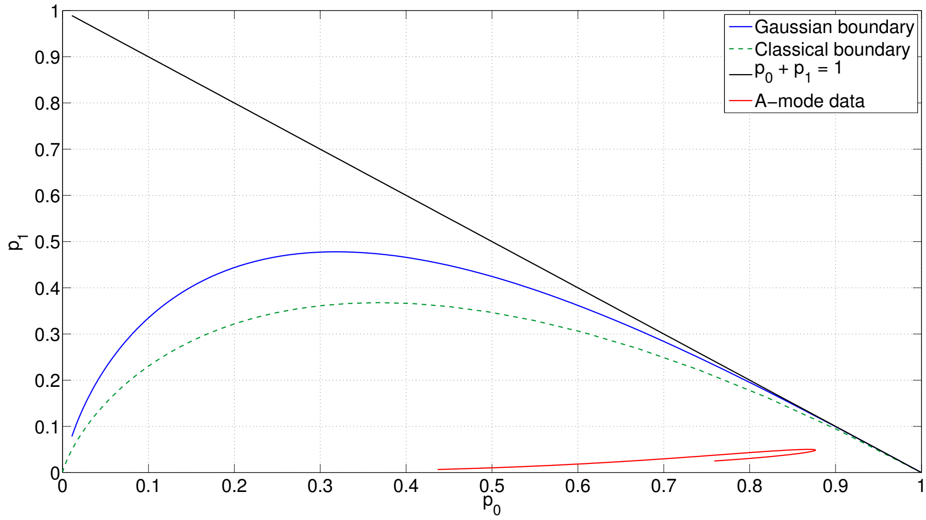

Figure 6.8: *Projected* anti-symmetric mode (p_0, p_1) trajectory of our uncorrected experimental data at 515 MHz for a *locked* pump phase. The uncorrected trajectory does not cross either the classical boundary or the Gaussian boundary due to the low single-photon probability of the squeezed vacuum state.

imental data of the state in the projected symmetric side-band mode at 515 MHz for a *locked* pump phase.

We also applied this non-Gaussian character witness to the uncorrected *projected* anti-symmetric side-band state at 515 MHz for a *locked* pump phase. A squeezed vacuum state is a quantum Gaussian state, and therefore we would expect the (p_0, p_1) trajectory of our uncorrected experimental data to cross the classical boundary and not the Gaussian boundary. Figure 6.8 shows the uncorrected (p_0, p_1) trajectory of the projected squeezed vacuum state (anti-symmetric mode) at 515 MHz for a *locked* pump phase. This trajectory was obtained by applying the anti-squeezing operation to our uncorrected experimental density matrix obtained using the reconstruction parameters listed in table 6.2. Anti-squeezing the experimental data results in a (p_0, p_1) trajectory which does not cross either boundary. The PND of the uncorrected projected squeezed vacuum state at 515 MHz does not have a high enough single-photon probability to be classified as a quantum Gaussian state using this character witness. It is possible that because this character witness is based on the p_0 and p_1 properties of the state and not the two-photon probability, it cannot be used to characterise squeezed vacuum states. Therefore, we propose that a new character witness could be defined that applies to the p_0 and p_2 properties of a reconstructed state. This could be further investigated in future work.

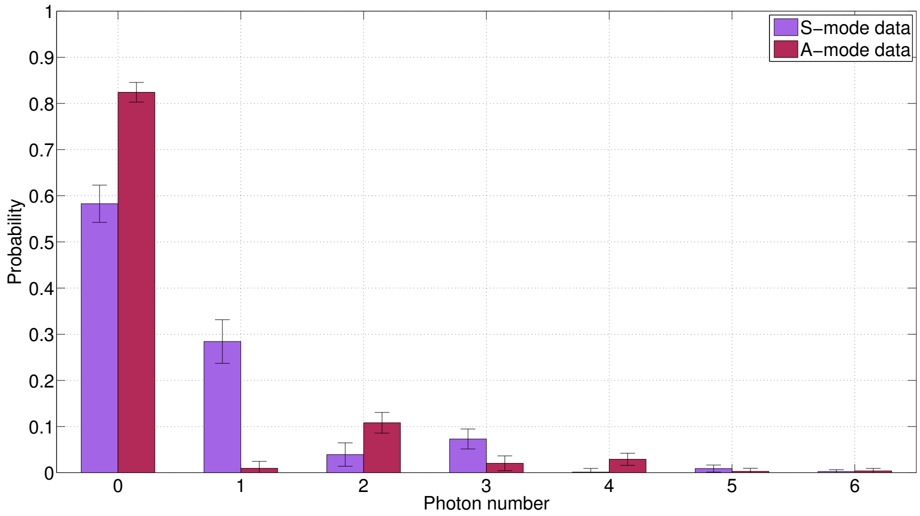

Figure 6.9: Comparison of experimental photon number distributions corrected for $\eta_{HD} = 0.7368$ for the *projected* symmetric (S-mode) and anti-symmetric (A-mode) side-band modes at 515 MHz for a *locked* pump phase. The reconstruction parameters are listed in tables 6.1 & 6.2.

6.2.1.2 Corrected for η_{HD}

It was discussed in §2.8.3 that the optical homodyne detection efficiency can be explicitly included in the maximum likelihood algorithm [245, 280]. Now we will present tomographic reconstruction results from only correcting for the imperfect detection efficiency due to *optical* characteristics of the experiment, which is given as $\eta_{HD} = \eta_{QE}\eta_t\zeta^2$. The experimental values for these parameters are defined in table 6.1, and give $\eta_{HD} = 0.7368$ for the projected state measurements. Note that this detection efficiency is higher than the values used to the correct the unprojected states (which was $\eta_{HD} = 0.676$). This is because the tap-off reflectivity, $r_2 \approx 0.08$, is not included in the propagation efficiency, η_t, for the projected state data as it was in the unprojected state analysis.

Figure 6.9 shows the PNDs for the projected symmetric and anti-symmetric side-band modes at 515 MHz corrected for $\eta_{HD} = 0.7368$ and with a *locked* pump phase. These PNDs were reconstructed using the parameters listed in tables 6.1 & 6.2. Correcting for η_{HD} in the reconstruction code does *not* correct for $\eta_e(f)$, which is the poor detection efficiency caused by data aliasing effects described in §5.1.1.

Figure 6.10 shows the Wigner functions for the photon-subtracted squeezed vacuum state in the symmetric mode (figure 6.10A) and the squeezed vacuum state in the anti-symmetric mode (figure 6.10B) at 515 MHz corrected for $\eta_{HD} = 0.7368$ and with a *locked* pump phase. These quantum states clearly possess distinctive experimental Wigner functions, with the projected symmetric mode Wigner function

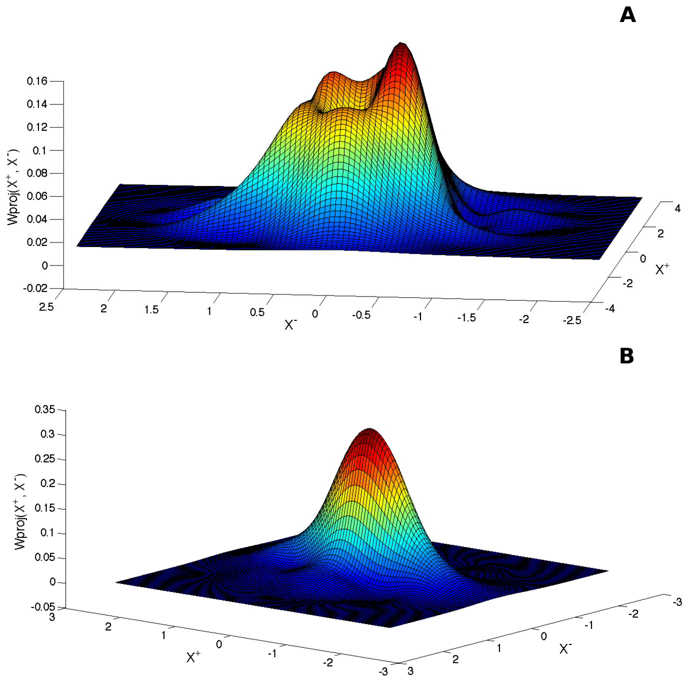

Figure 6.10: Experimental Wigner functions corrected for $\eta_{HD} = 0.7368$ reconstructed from *projected* data at 515 MHz for a *locked* pump phase. A) Photon-subtracted squeezed vacuum state (symmetric mode), and B) squeezed vacuum state (anti-symmetric mode). The reconstruction parameters are listed in tables 6.1 & 6.2.

becoming even more non-Gaussian after the data has been corrected for η_{HD}.

Figure 6.11 shows the (p_0, p_1) trajectory of the photon-subtracted squeezed vacuum state (symmetric mode) at 515 MHz corrected for $\eta_{HD} = 0.7368$ and with a *locked* pump phase. This trajectory was obtained by applying the anti-squeezing operation to our corrected experimental density matrix obtained using the reconstruction parameters listed in table 6.2. Note that the efficiency-corrected (p_0, p_1) trajectory crosses both the classical and Gaussian boundaries by a statistically-significant margin. Therefore the state in the projected symmetric side-band mode at 515 MHz corrected for $\eta_{HD} = 0.7368$ can be classified as a quantum non-Gaussian state.

Figure 6.12 shows the optimal witness $(W(a_{opt}, s) - W_G(a_{opt}))$ as a function of the anti-squeezing parameter, s, for experimental data corrected for $\eta_{HD} = 0.7368$ of the state in the projected symmetric side-band mode at 515 MHz for a *locked* pump phase. As the peak of this curve crosses the $W(a, s) - W_G(a) = 0$ boundary by a statistically-significant margin, this state can be classified as a quantum non-Gaussian state. Therefore, despite the positive Wigner function shown in figure 6.10A, this character witness identifies our state as a quantum non-Gaussian state by a statistically-significant margin. This indicates that this state cannot be prepared by merely mixing Gaussian states.

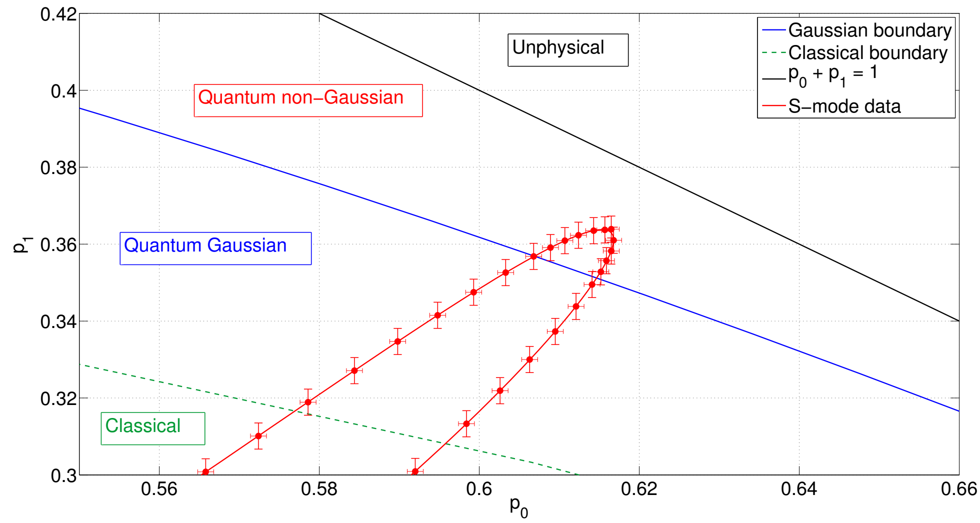

Figure 6.11: *Projected* symmetric mode (p_0, p_1) trajectory of our experimental data corrected for $\eta_{HD} = 0.7368$ at 515 MHz for a *locked* pump phase. The efficiency-corrected trajectory crosses both the classical and Gaussian boundaries by a statistically-significant margin, which means this experimental state can be classified as a quantum non-Gaussian state.

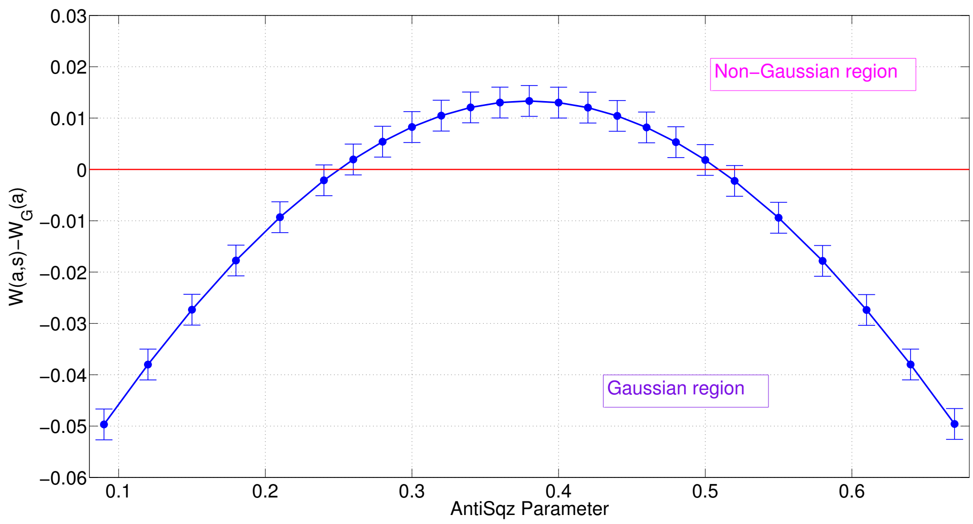

Figure 6.12: Quantum non-Gaussian character witness of our *projected* symmetric mode state corrected for $\eta_{HD} = 0.7368$ at 515 MHz for a *locked* pump phase. As the peak of this efficiency-corrected curve crosses the $W(a, s) - W_G(a) = 0$ boundary by a statistically-significant margin, this state can be classified as a quantum non-Gaussian state.

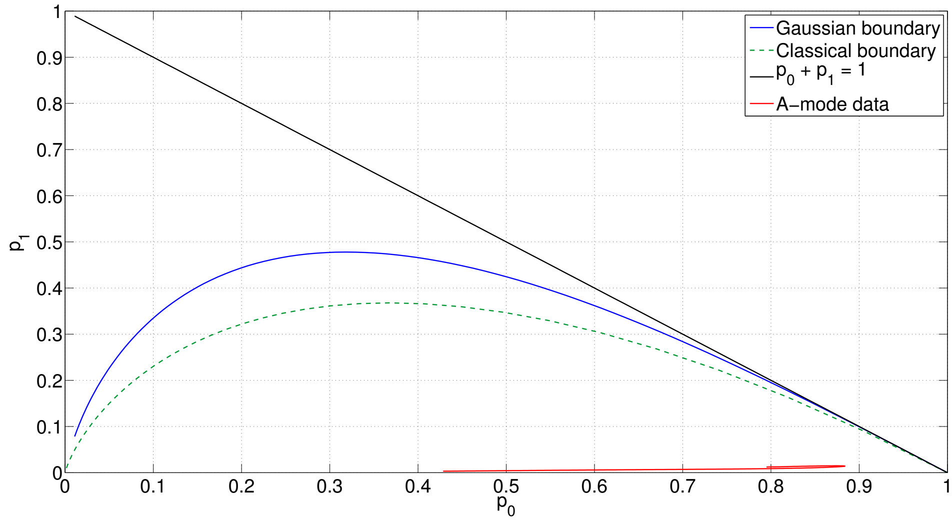

Figure 6.13: *Projected* anti-symmetric mode (p_0, p_1) trajectory of our experimental data corrected for $\eta_{HD} = 0.7368$ at 515 MHz for a *locked* pump phase. The efficiency-corrected trajectory does not cross either the classical boundary or the Gaussian boundary due to the low single-photon probability of the squeezed vacuum state.

Finally, we applied this non-Gaussian character witness to the corrected projected anti-symmetric side-band state at 515 MHz. Figure 6.13 shows the efficiency-corrected (p_0, p_1) trajectory of the squeezed vacuum state (anti-symmetric mode) at 515 MHz for a *locked* pump phase using the reconstruction parameters listed in table 6.2. Anti-squeezing the experimental data results in a (p_0, p_1) trajectory which again does not cross either boundary. In fact the trajectory is even further away from the classical boundary compared to figure 6.8 due to the much lower single-photon probability after the experimental data was corrected for η_{HD}. Therefore, the PND of the corrected projected squeezed vacuum state at 515 MHz does not have a high enough single-photon probability to be classified as a quantum Gaussian state using this character witness. We will only present witness data for the projected symmetric side-band modes of remaining states in this chapter.

6.2.2 1030 MHz and 1545 MHz projected modes

Since a smaller portion of the 1030 MHz and 1545 MHz side-band pairs are transmitted by the optical filtering system compared to the 515 MHz side-band pair, there is a smaller probability that a photon detected by the APD originated from the second or third FSR. As we shall see, this caused the single-photon probabilities of the states in the projected symmetric side-band modes at 1030 MHz and 1545 MHz to be lower than the single-photon probability of the 515 MHz projected symmetric mode state. A trend will be shown where a reduction in observed squeezing at these frequencies will have a detrimental effect on the non-classicality and non-Gaussianity of the projected states.

6.2.2.1 Without detection efficiency correction

Figure 6.14 shows the uncorrected experimental PNDs of the *projected* symmetric side-band modes (S-mode) at 1030 MHz and 1545 MHz for a *locked* pump phase. The experimental PND shown in figure 6.14A was reconstructed from homodyne tomography data of the projected state using the parameters listed in tables 6.1 & 6.4. This figure also shows the theoretical PND of a photon-subtracted squeezed vacuum state mathematically simulated using the model outlined in §2.6. The model parameters used to generate this theoretical PND of the symmetric mode at 1030 MHz are listed in table 6.6. The model and experimental PNDs shown in figure 6.14A agree within error. The experimental PND shown in figure 6.14B was reconstructed using the parameters listed in tables 6.1 & 6.5. The theoretical PND shown is of a photon-subtracted squeezed vacuum state mathematically simulated using the parameters listed in table 6.6. The model and experimental PNDs shown in figure 6.14B also agree within error.

Figure 6.15 shows the uncorrected experimental PNDs of the *projected* anti-symmetric side-band modes (A-mode) at 1030 MHz and 1545 MHz for a *locked* pump phase. The experimental PND shown in figure 6.15A was reconstructed from homodyne tomography data of the projected state using the parameters listed in tables 6.1 & 6.4. Figure 6.15A also shows the theoretical PND of the impure squeezed vacuum state mathematically simulated using the model outlined in §2.6. The model parameters used to generate the theoretical PND of the projected anti-symmetric mode at 1030 MHz are listed in table 6.6. The model and experimental PNDs shown in figure 6.15A agree within error. The experimental PND shown in figure 6.15B was reconstructed using the parameters listed in tables 6.1 & 6.5. The theoretical PND shown was mathematically simulated using the parameters listed in table 6.6. The model and experimental PNDs shown in figure 6.15B also agree within error.

Note that the reduction in observed squeezing at 1030 MHz and 1545 MHz directly leads to a different prediction for the projected PNDs at 1030 MHz and 1545 MHz compared to the projected PND at 515 MHz. A smaller η_{HD} was needed to model the projected PNDs at the second and third FSRs due to the reduced observed squeezing level, and the lower probability of photon-subtraction events corresponding to photons at these frequencies.

Figure 6.16 shows the uncorrected Wigner functions for the 1030 MHz and 1545 MHz projected states. The uncorrected Wigner functions for the photon-subtracted squeezed vacuum state in the symmetric mode and the squeezed vacuum state in

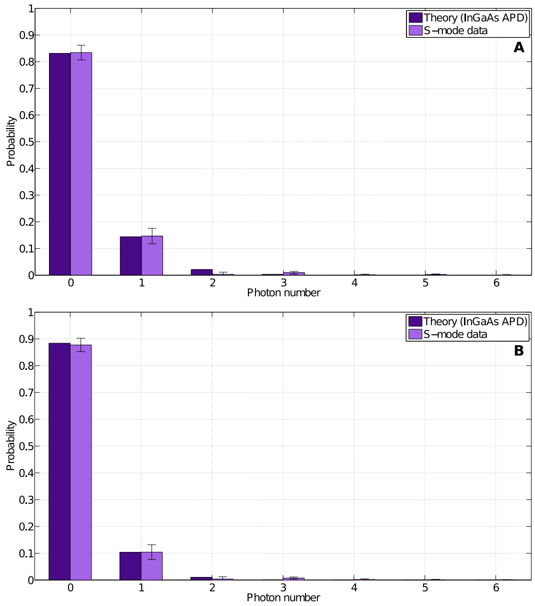

Figure 6.14: Comparison of uncorrected experimental and theoretical photon number distributions of the *projected* 1030 MHz and 1545 MHz symmetric side-band modes (S-mode) for a *locked* pump phase. A) 1030 MHz S-mode state reconstructed using the parameters listed in tables 6.1 & 6.4, and the model parameters are listed in table 6.6. B) 1545 MHz S-mode state reconstructed using the parameters listed in tables 6.1 & 6.5, and the model parameters are listed in table 6.6.

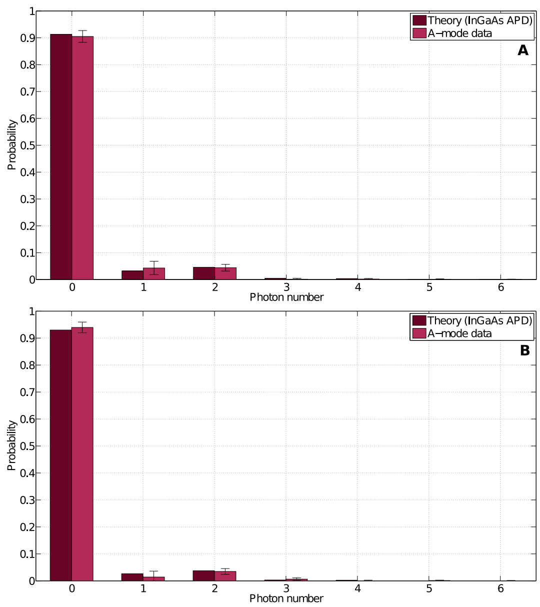

Figure 6.15: Comparison of uncorrected experimental and theoretical photon number distributions of the *projected* 1030 MHz and 1545 MHz anti-symmetric (A-mode) side-band modes for a *locked* pump phase. A) 1030 MHz A-mode state reconstructed using the parameters listed in tables 6.1 & 6.4, and the model parameters are listed in table 6.6. B) 1545 MHz A-mode state reconstructed using the parameters listed in tables 6.1 & 6.5, and the model parameters are listed in table 6.6.

Side-band mode	Demodulation frequency	pump phase window	τ_2	ϕ_2
Symmetric mode	1030 MHz	-2.5° – 0°	-153.3 ns	71.8°
Anti-symmetric mode	1030 MHz	-2.5° – 0°	-160 ns	124°

Table 6.4: Summary of parameters that were used to reconstruct projected states for a *locked* pump phase at the second FSR (1030 MHz).

Side-band mode	Demodulation frequency	Pump phase window	τ_3	ϕ_3
Symmetric mode	1545 MHz	-2.5° – 0°	-162.9 ns	22.6°
Anti-symmetric mode	1545 MHz	-2.5° – 0°	-140.5 ns	173°

Table 6.5: Summary of parameters that were used to reconstruct projected states for a *locked* pump phase at the third FSR (1545 MHz).

the anti-symmetric mode at 1030 MHz for a *locked* pump phase are shown in figures 6.16A and 6.16B, respectively. Whereas the uncorrected Wigner functions for the photon-subtracted squeezed vacuum state in the symmetric mode and the squeezed vacuum state in the anti-symmetric mode at 1545 MHz for a *locked* pump phase are shown in figures 6.16C and 6.16D, respectively.

These pairs of Wigner functions at each FSR are less obviously different to each other when compared to the states at 515 MHz. However, the Wigner functions of the projected symmetric mode states at 1030 MHz and 1545 MHz have a less Gaussian shape compared to the Wigner functions of the projected anti-symmetric states as evident by their flattened tops. We will see these states become more noticeably different after the data has been corrected for imperfect homodyne detection in the next section.

Figure 6.17 shows the uncorrected (p_0, p_1) trajectories of the photon-subtracted squeezed vacuum state (symmetric mode) at 1030 MHz and 1545 MHz for a *locked* pump phase. The trajectory shown in figure 6.17A is for the 1030 MHz state and was obtained by applying the anti-squeezing operation to our uncorrected experimental density matrix reconstructed using the parameters listed in table 6.4. Whereas the trajectory shown in figure 6.17B is for the 1545 MHz state and was obtained by applying the anti-squeezing operation to our uncorrected experimental density matrix reconstructed using the parameters listed in table 6.5. Note that the uncorrected (p_0, p_1) trajectory for the 1030 MHz projected state only crosses the classical bound-

Side-band mode	Pure squeezing level	Loss r_1	Tap-off r_2	η_{HD}	η_{APD}	P_{dc}
1030 MHz S-mode	-3.474 dB	0.005	0.008	0.3	0.08	0.00175
1030 MHz A-mode	-3.909 dB	0.005	0	0.7368	—	—
1545 MHz S-mode	-3.474 dB	0.005	0.008	0.195	0.08	0.00175
1545 MHz A-mode	-3.474 dB	0.005	0	0.7368	—	—

Table 6.6: Summary of model parameters used to simulated symmetric mode (S-mode) and anti-symmetric mode (A-mode) for the 1030 MHz and 1545 MHz states from the projected data results with *locked* pump phase.

ary by a statistically-significant margin and does not cross the Gaussian boundary at all. The uncorrected (p_0, p_1) trajectory for the 1545 MHz projected state does not cross either the classical or Gaussian boundaries. Therefore the projected symmetric mode state at 1030 MHz can be classified as a quantum Gaussian state but not as a quantum non-Gaussian state, and the projected symmetric mode state at 1545 MHz is classified as a classical state.

Figure 6.18 shows the optimal witness $W(a_{opt}, s) - W_G(a_{opt})$ as a function of the anti-squeezing parameter, s, for uncorrected experimental data of the states in the projected symmetric side-band modes at 1030 MHz (figure 6.18A) and 1545 MHz (figure 6.18B) for a *locked* pump phase. Both of these graphs illustrate that since the peak of the curves do not cross the $W(a, s) - W_G(a) = 0$ boundary, these states cannot be classified as quantum non-Gaussian states.

6.2.2.2 Corrected for η_{HD}

Figure 6.19 shows the PNDs for the projected symmetric and anti-symmetric side-band modes at 1030 MHz and 1545 MHz corrected for $\eta_{HD} = 0.7368$ and with a *locked* pump phase. The PNDs shown in figure 6.19A were reconstructed using the parameters listed in tables 6.1 & 6.4. Correcting for η_{HD} in the reconstruction code does *not* correct for $\eta_e(\mathrm{f})$, which is the poor detection efficiency caused by data aliasing effects described in §5.1.1. The PNDs shown in figure 6.19B were reconstructed using the parameters listed in tables 6.1 & 6.5. Figures 6.20A and 6.20B shows the corresponding Wigner functions for the modes at 1030 MHz, whereas figures 6.20C and 6.20D shows the corresponding Wigner functions for the modes at 1545 MHz. The pairs of Wigner functions have become more noticeably different between the projected symmetric and anti-symmetric modes after the data has been corrected for η_{HD}. A small dip is starting to appear in the Wigner function of the 1030 MHz

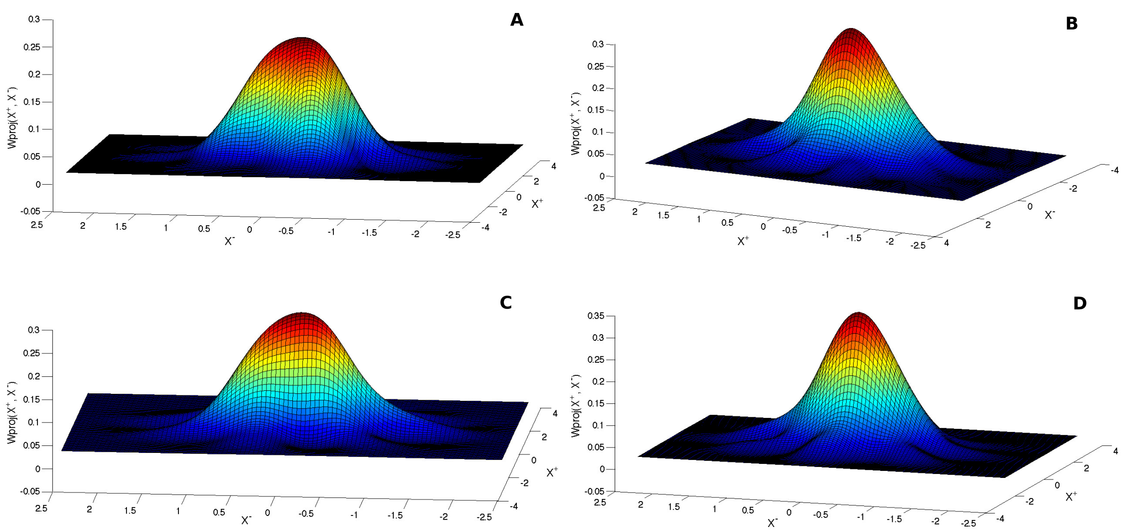

Figure 6.16: Experimental uncorrected Wigner functions reconstructed from *projected* data at 1030 MHz and 1545 MHz for a *locked* pump phase. A) 1030 MHz photon-subtracted squeezed vacuum state (symmetric mode), B) 1030 MHz squeezed vacuum state (anti-symmetric mode), C) 1545 MHz photon-subtracted squeezed vacuum state (symmetric mode), and D) 1545 MHz squeezed vacuum state (anti-symmetric mode). The reconstruction parameters are listed in tables 6.1, 6.4 & 6.5.

projected symmetric mode state.

Figure 6.21 shows the efficiency-corrected (p_0, p_1) trajectories of the photon-subtracted squeezed vacuum states (symmetric mode) at 1030 MHz (figure 6.21A) and 1545 MHz (figure 6.21B) corrected for $\eta_{HD} = 0.7368$ and with a *locked* pump phase. Figures 6.22A and 6.22B shows the corresponding optimal witnesses for the 1030 MHz and 1545 MHz states, respectively. Note that the efficiency-corrected (p_0, p_1) trajectory of the 1030 MHz state crosses the classical boundary by a statistically-significant margin but still does not cross the Gaussian boundary. Whereas the trajectory for the 1545 MHz state does not cross either boundary. Therefore the 1030 MHz projected symmetric side-band mode state corrected for $\eta_{HD} = 0.7368$ is still classified as a quantum Gaussian state despite the improvements made to the state by correcting for η_{HD}, and the 1545 MHz projected symmetric mode state is still classified as a classical state.

6.2.3 Comparing projected A-mode with unprojected S-mode

We now will briefly discuss a ‘sanity check’ by comparing the *projected* squeezed vacuum state in the anti-symmetric mode at 515 MHz to the *unprojected* squeezed vacuum state in the symmetric mode at 515 MHz, which was previously shown in chapter 5. Figure 6.23 shows the uncorrected experimental PND of the *projected* anti-symmetric side-band mode and of the *unprojected* symmetric mode at

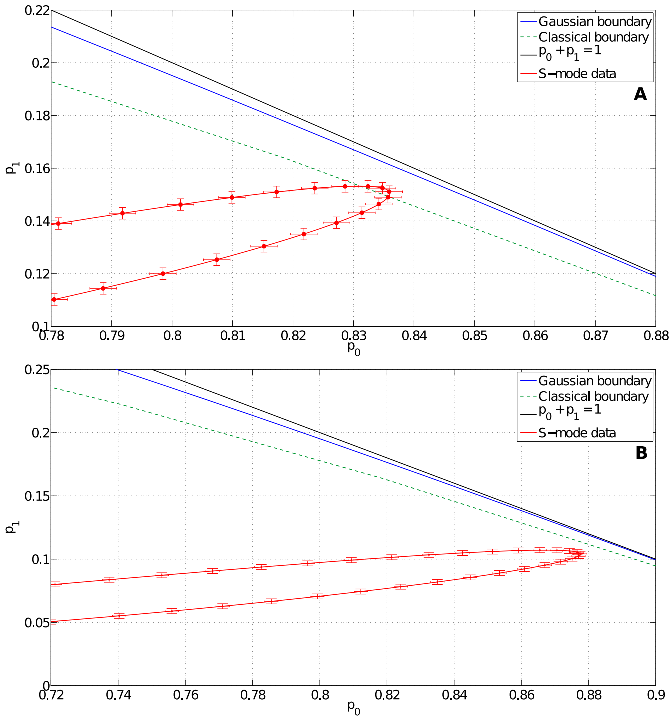

Figure 6.17: *Projected* symmetric mode (p_0, p_1) trajectories of our uncorrected experimental data at 1030 MHz and 1545 MHz for a *locked* pump phase. A) Uncorrected trajectory for the 1030 MHz S-mode state; it crosses the classical boundary by a statistically-significant margin but does not cross the Gaussian boundary at all, which means this experimental state cannot be classified as a quantum non-Gaussian state. B) Uncorrected trajectory for the 1545 MHz S-mode state; it does not cross either boundary and is therefore classified as a classical state.

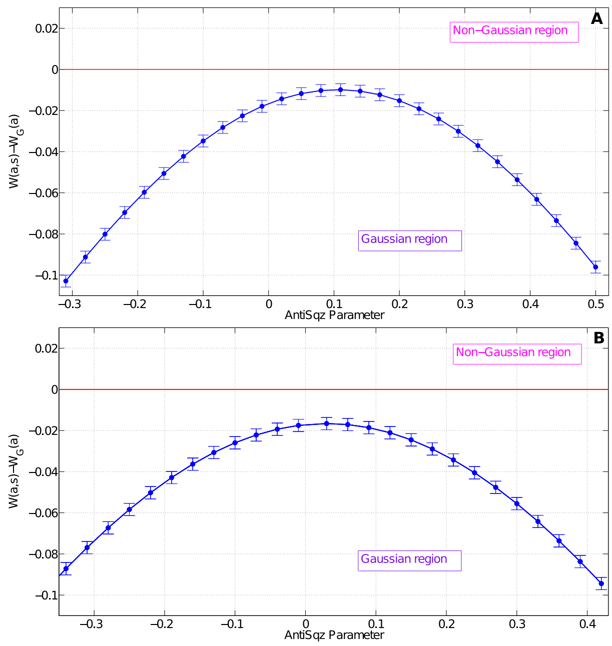

Figure 6.18: Quantum non-Gaussian character witness of our uncorrected *projected* symmetric mode states at 1030 MHz and 1545 MHz for a *locked* pump phase. A) Character witness for the 1030 MHz S-mode state, and B) Character witness for the 1545 MHz S-mode state. As neither peak of these uncorrected curves crosses the $W(a,s) - W_G(a) = 0$ boundary, neither state can be classified as a quantum non-Gaussian state.

515 MHz for a *locked* pump phase. The *projected* anti-symmetric mode PND was reconstructed from the homodyne tomography data using the parameters listed in tables 6.1 & 6.2. Whereas the *unprojected* symmetric PND was previously shown in chapter 5 and was reconstructed using the parameters listed in tables 5.3 & 5.8. Theoretically these states should be the same as both experimental data runs had the same amount of input pump power and squeezing from the OPO. Note that these PNDs agree within error.

6.3 Frequency-entangled projected states

The multi-frequency spectral nature of the transmission function from the filter cavities caused the trigger mode to consist of multiple FSR side-band pairs. This is demonstrated by our ability to reconstruct side-band modes at multiple FSR frequencies instead of only at the first FSR. Since the APD cannot distinguish between these frequencies, this projective measurement results in an *entangled* state between the multiple FSR states. Isolating a single FSR pair by demodulating at an individual frequency destroys any possible correlations that may exist between the FSRs.

In chapter 4 we made the hypothesis that the quality of the projected state may

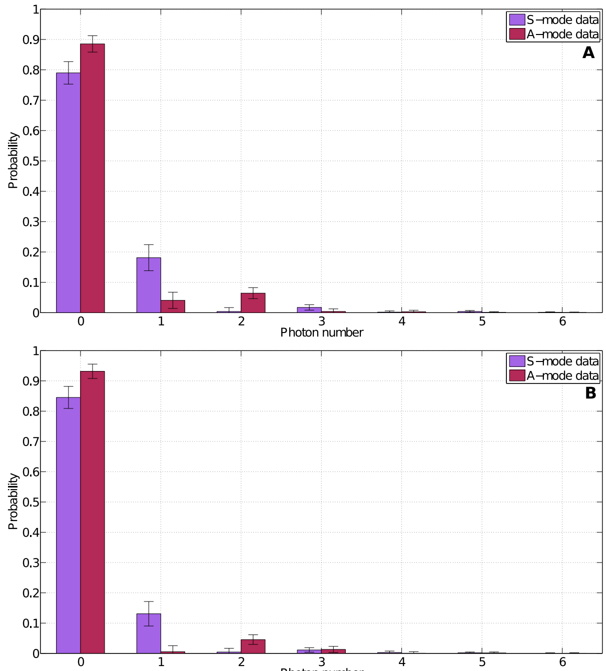

Figure 6.19: Comparison of experimental photon number distributions corrected for $\eta_{HD} = 0.7368$ for the *projected* symmetric (S-mode) and anti-symmetric (A-mode) side-band modes at 1030 MHz and 1545 MHz for a *locked* pump phase. A) 1030 MHz S- and A-mode states reconstructed using the parameters listed in tables 6.1 & 6.4. B) 1545 MHz S- and A-mode states reconstructed using the parameters listed in tables 6.1 & 6.5.

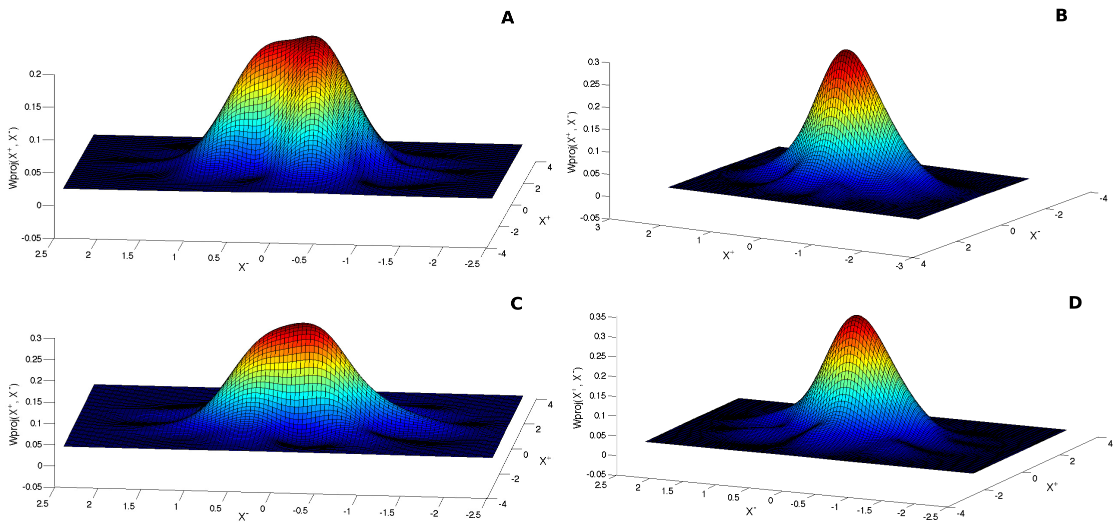

Figure 6.20: Experimental Wigner functions corrected for $\eta_{HD} = 0.7368$ reconstructed from *projected* data at 1030 MHz and 1545 MHz for a *locked* pump phase. A) 1030 MHz photon-subtracted squeezed vacuum state (symmetric mode), B) 1030 MHz squeezed vacuum state (anti-symmetric mode), C) 1545 MHz photon-subtracted squeezed vacuum state (symmetric mode), and D) 1545 MHz squeezed vacuum state (anti-symmetric mode). The reconstruction parameters are listed in tables 6.1, 6.4, & 6.5.

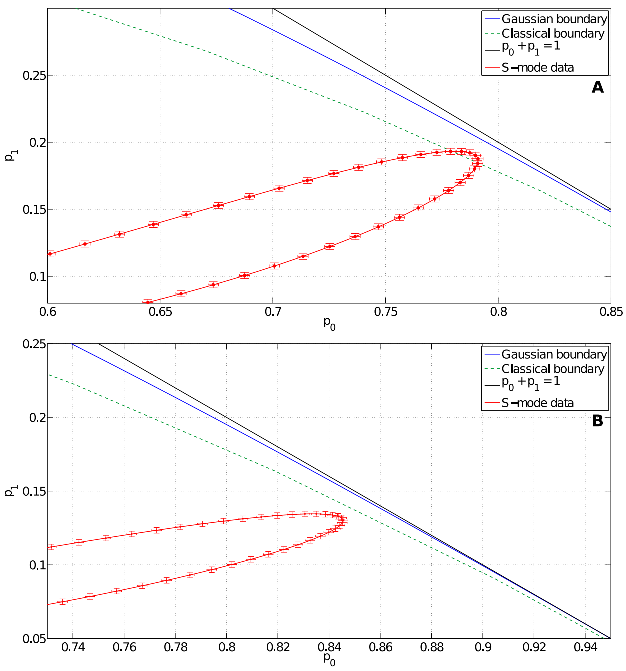

Figure 6.21: *Projected* symmetric mode (p_0, p_1) trajectory of our experimental data corrected for $\eta_{HD} = 0.7368$ at 1030 MHz and 1545 MHz for a *locked* pump phase. A) Efficiency-corrected trajectory for the 1030 MHz S-mode state; it crosses the classical boundary by a statistically-significant margin but does not cross the Gaussian boundary, which means this experimental state cannot be statistically classified as a quantum non-Gaussian state. B) Efficiency-corrected trajectory for the 1545 MHz S-mode state; it does not cross either boundary and is therefore classified as a classical state.

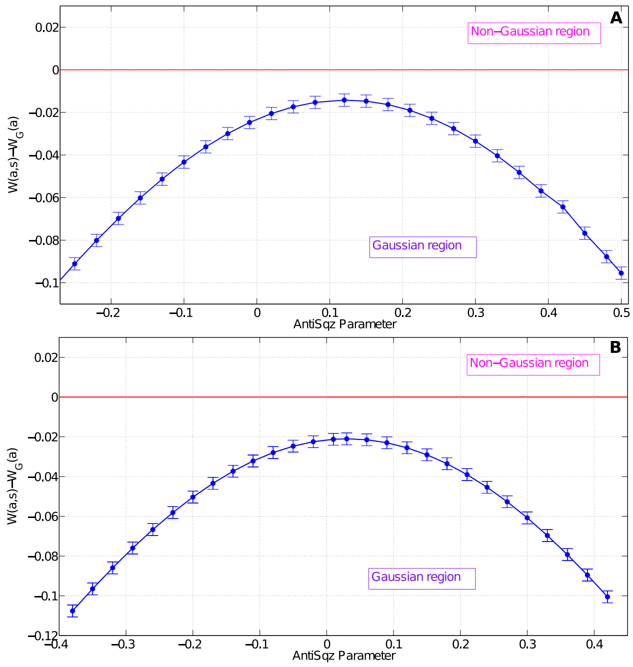

Figure 6.22: Quantum non-Gaussian character witness of our *projected* symmetric mode states corrected for $\eta_{HD} = 0.7368$ at 1030 MHz and 1545 MHz for a *locked* pump phase. A) Efficiency-corrected character witness for the 1030 MHz S-mode state, and B) Efficiency-corrected character witness for the 1545 MHz S-mode state. As neither peak of these corrected curves crosses the $W(a,s) - W_G(a) = 0$ boundary, neither state can be classified as a quantum non-Gaussian state.

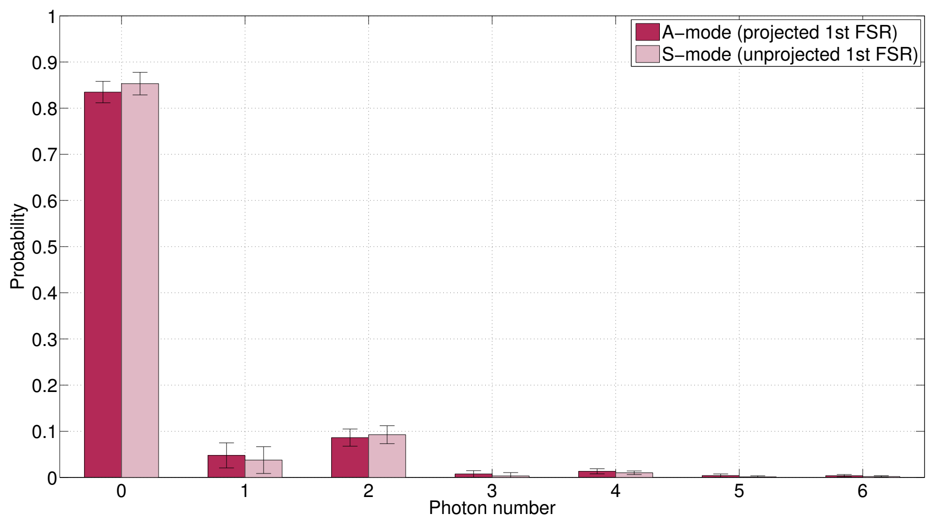

Figure 6.23: Comparison of uncorrected experimental and theoretical photon number distributions of the *projected* 515 MHz anti-symmetric (A-mode projected) side-band mode to the uncorrected experimental photon number distribution of the *unprojected* 515 MHz symmetric (S-mode unprojected) side-band mode for a *locked* pump phase. The reconstruction parameters for the A-mode projected state are listed in tables 6.1 & 6.2, and for the S-mode unprojected state are listed in tables 5.3 & 5.8.

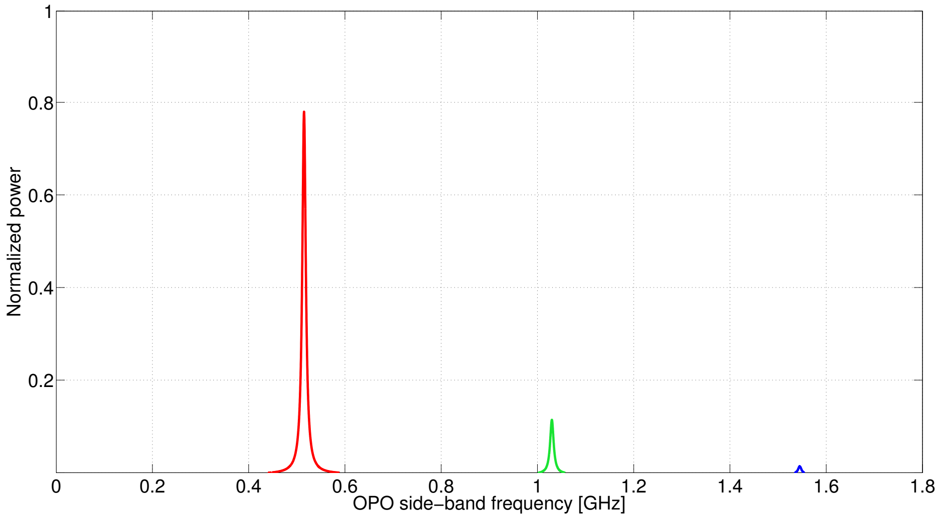

Figure 6.24: Final weightings of the FSR components in the multi-frequency temporal mode function used in projected state reconstruction.

improve if we applied a frequency-offset temporal mode function which best matched the trigger spectrum. However, due to the presence of data aliasing, the ideal temporal mode function needs to incorporate both the FSR weightings predicted by the measured optical trigger spectrum (presented in §4.3.2) *and* the detection efficiency ratios at each FSR frequency determined in §5.1.1. We will show later in this section that adjusting the detection efficiency ratios away from the experimentally determined values decreases the single-photon probability and increases the zero-photon probability of the photon-subtracted squeezed vacuum state (i.e. makes the state 'worse').

Therefore, we applied a multi-frequency temporal mode function (as described by equation 5.6) with the weightings of the FSR components determined by the measured optical trigger mode spectrum multiplied by $\eta_e(f)$ for each frequency - see equation 5.10. Figure 6.24 shows the final weightings of each FSR component used in the multi-frequency temporal mode function. The temporal and phase offsets used in the function follow the relationships described by equation 5.12, and are summarised in table 6.7.

We showed in §5.3.4 that the quality of the reconstructed *unprojected* squeezed vacuum state was worse when this multi-frequency temporal mode function was used. We argued that this occurred because the individual FSR states in the unprojected data were *independent*. Therefore using the multi-FSR function resulted in a weighted average, which combined 'worse' unprojected squeezed vacuum states from the second and third FSRs with the 'better' state at the first FSR in a weighted fashion. However, if the FSR states were *entangled* then using this type of function may uncover the hidden correlations and improve the quality of the reconstructed state. Due to the multi-FSR spectrum of our trigger mode, it is probable that we created an entangled state between the first three FSR states generated by our SS-NOPO. We will now present data that supports this claim.

6.3.1 Without detection efficiency correction

Figure 6.25 shows the uncorrected experimental PND of the *projected* symmetric side-band mode (S-mode) reconstructed using the multi-frequency temporal mode function described by equation 5.6 for a *locked* pump phase. This PND was reconstructed from homodyne tomography data of the projected state using the parameters listed in tables 6.1 & 6.7. Figure 6.25 also shows the uncorrected experimental PND of the *projected* symmetric side-band mode (S-mode) at 515 MHz reconstructed using the parameters listed in tables 6.1 & 6.2. These PNDs are shown together to illustrate the increase in the single-photon probability and decrease in zero-photon and two-photon probabilities of the multi-FSR S-mode state compared to that of the 515 MHz S-mode state. To reiterate, this multi-frequency temporal mode function incorporates the quantum states from *all* three FSRs. In spite of the poorer qualities of the individual 1030 MHz and 1545 MHz projected S-mode states compared to the 515 MHz projected S-mode state, the multi-FSR state is somewhat improved compared to the 515 MHz state alone. This is in all likelihood due to the entanglement between the FSRs, and utilising the more complex temporal mode function reveals those hidden correlations. Applying this same function to the unprojected data (shown in §5.3.4) resulted in a 'worse' (weighted average) squeezed vacuum state because entanglement did not exist between the FSR states. Thus, combining 'worse' data due to data aliasing effects with 'better' data (i.e. 515 MHz state) gave an overall 'worse' state (i.e. a weighted average). To strengthen this argument, we show a third PND in figure 6.25 which was calculated from a weighted average of the three individual *projected* symmetric mode FSR states via,

$$\mathrm{diag}(\hat{\rho}_{Ave}) = \gamma_1^2 \times \mathrm{diag}(\hat{\rho}_{515}) + \gamma_2^2 \times \mathrm{diag}(\hat{\rho}_{1030}) + \gamma_3^2 \times \mathrm{diag}(\hat{\rho}_{1545}), \tag{6.8}$$

where $\mathrm{diag}(\rho_f)$ are the experimental PNDs of the projected symmetric modes at each of the FSR frequencies, and the coefficients γ_1, γ_2, γ_3 are calculated via equation 5.10. As expected, the weighted average is of worse quality (i.e. lower single-photon probability and higher zero-photon probability) compared to both of the other PNDs shown in figure 6.25.

Figure 6.26 shows the uncorrected experimental PND of the *projected* anti-symmetric side-band mode (A-mode) reconstructed using the multi-frequency tem-

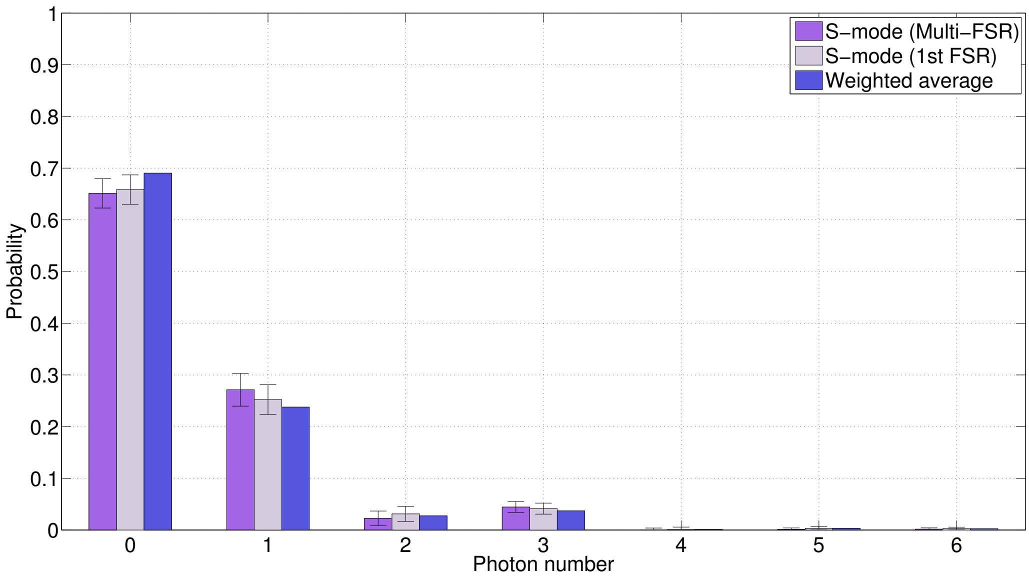

Figure 6.25: Comparison of uncorrected experimental photon number distributions of the state in the *projected* symmetric side-band mode reconstructed using the multi-frequency temporal mode function (S-mode Multi-FSR) to the uncorrected experimental photon number distribution of the state in the *projected* symmetric side-band mode at 515 MHz (S-mode 1st FSR) for a *locked* pump phase, along with the PND of the weighted average of all three *projected* S-mode FSR states (weighted average). The reconstruction parameters for the S-mode multi-FSR state are listed in tables 6.1 & 6.7, and for the S-mode 1st FSR state are listed in tables 6.1 & 6.2. The weighted average was calculated via equation 6.8.

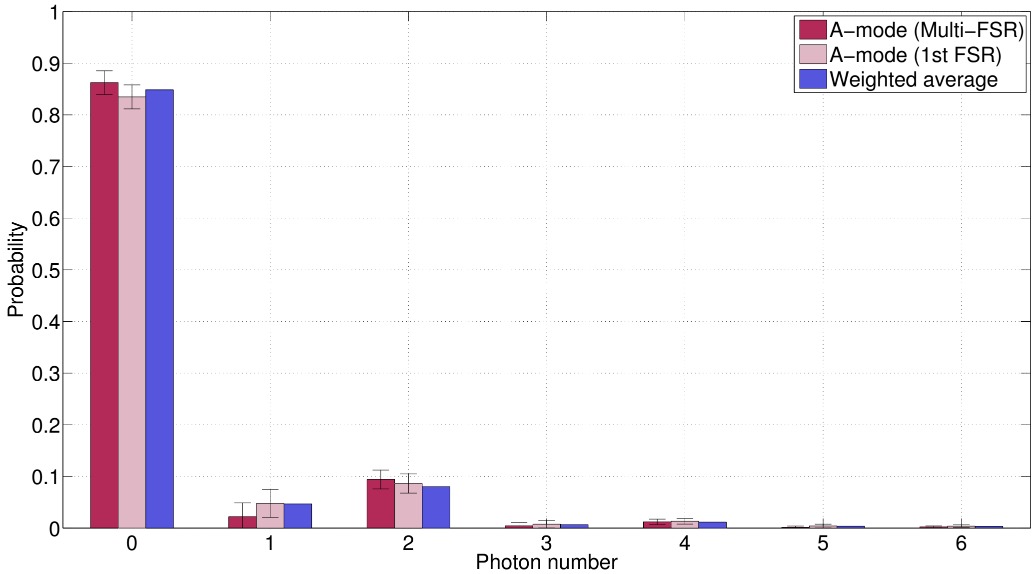

Figure 6.26: Comparison of uncorrected experimental photon number distributions of the *projected* anti-symmetric side-band mode state (A-mode Multi-FSR) reconstructed using the multi-frequency temporal mode function to the uncorrected experimental PND of the *projected* anti-symmetric side-band mode state at 515 MHz (A-mode 1st FSR) for a *locked* pump phase, along with the PND of the weighted average of all three *projected* A-mode FSR states (weighted average). The reconstruction parameters for the *projected* A-mode multi-FSR state are listed in tables 6.1 & 6.7, and the reconstruction parameters for the *projected* A-mode 1st FSR state are listed in tables 6.1 & 6.2. The weighted average was calculated via equation 6.8.

Side-band mode	τ_m	ϕ_m	$\Delta\tau_2$	$\Delta\phi_2$	$\Delta\tau_3$	$\Delta\phi_3$
S-mode	52.6 ns	148.4°	-204.9 ns	-82.5°	-214.5 ns	-131.7°
A-mode	22.3 ns	70.6°	-180 ns	46°	-160.5 ns	95°

Table 6.7: Summary of parameters that were used to reconstruct the projected states for a *locked* pump phase ($\Delta\phi_{pump} = 2.5°$, $\omega_s = 2\pi \times 515$ MHz) using the multi-FSR temporal mode function described by equation 5.6.

poral mode function described by equation 5.6 for a *locked* pump phase. This PND was reconstructed from homodyne tomography data of the projected state using the parameters listed in tables 6.1 & 6.7. Figure 6.26 also shows the uncorrected experimental PND of the *projected* anti-symmetric side-band mode at 515 MHz reconstructed using the parameters listed in tables 6.1 & 6.2. These PNDs are shown together to illustrate the increase in the two-photon probability and decrease in one-photon probability of the multi-FSR A-mode state compared to that of the 515 MHz A-mode state. In spite of the poorer qualities of the individual 1030 MHz and 1545 MHz projected A-mode states compared to the 515 MHz projected A-mode state, the multi-FSR state is somewhat improved compared to the 515 MHz state alone. The two-photon probability of the multi-FSR state is now larger than the one-photon probability by a statistically-significant margin. This is in all likelihood due to the entanglement between the FSRs, and utilising the more complex temporal mode function reveals those hidden correlations. To strengthen this argument, we show a third PND in figure 6.26 which was calculated from a weighted average of the three individual *projected* anti-symmetric mode FSR states via equation 6.8. As expected, the weighted average is of worse quality (i.e. lower two-photon probability and higher one-photon probability) compared to the multi-FSR PND.

Figure 6.27 shows the uncorrected Wigner functions for the multi-FSR photon-subtracted squeezed vacuum state in the symmetric mode (figure 6.27A) and the squeezed vacuum state in the anti-symmetric mode (figure 6.27B) reconstructed using the multi-frequency temporal mode function described by equation 5.6 for a *locked* pump phase. These Wigner functions are more obviously different than compared to the states at 515 MHz (figure 6.5). The Wigner function of the projected symmetric mode state has a clear dip near $W(0, 0)$ *without correction for inefficient detection*, and has a distinct non-Gaussian shape compared to the Wigner function of the projected anti-symmetric mode state. We will see these modes become even more different after the data has been corrected for imperfect homodyne detection in the next section.

Figure 6.28 shows the uncorrected (p_0, p_1) trajectory of the multi-FSR photon-

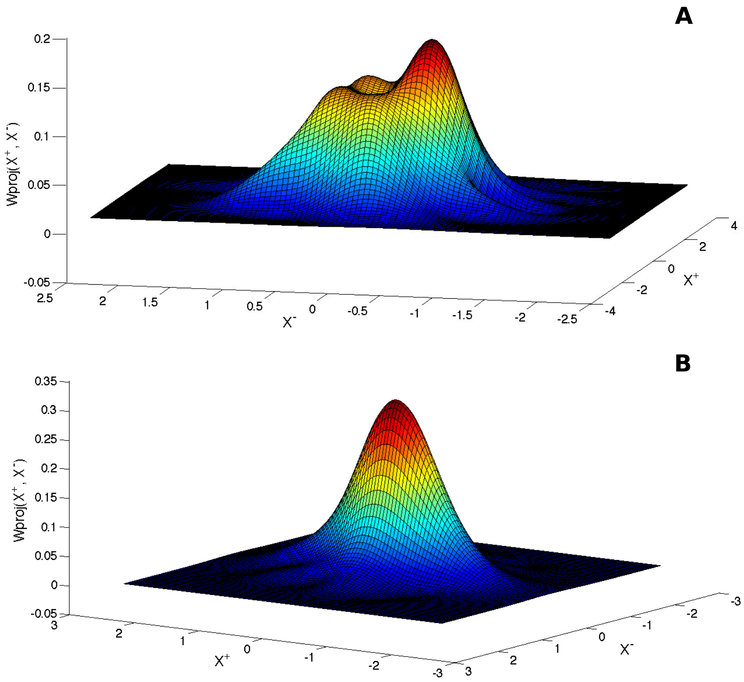

Figure 6.27: Experimental uncorrected Wigner functions reconstructed from *projected* data using the multi-frequency temporal mode function described by equation 5.6 for a *locked* pump phase. A) Photon-subtracted squeezed vacuum state (symmetric mode), and B) squeezed vacuum state (anti-symmetric mode). The reconstruction parameters are listed in tables 6.1 & 6.7.

subtracted squeezed vacuum state (symmetric mode) reconstructed using the multi-frequency temporal mode function described by equation 5.6 for a *locked* pump phase. This trajectory was obtained by applying the anti-squeezing operation to our uncorrected experimental density matrix obtained using the reconstruction parameters listed in table 6.7. Note that unlike the uncorrected (p_0, p_1) trajectory of the projected symmetric mode state at 515 MHz, the uncorrected (p_0, p_1) trajectory of this multi-FSR state crosses both the classical boundary *and* the Gaussian boundary by a statistically-significant margin. Therefore, unlike the 515 MHz state, this multi-FSR experimental state can be statistically classified as a quantum *non-*Gaussian state.

Figure 6.29 shows the corresponding optimal quantum non-Gaussian character witness, $W(a_{opt}, s) - W_G(a_{opt})$, as a function of the anti-squeezing parameter, s. As the peak of this curve crosses the $W(a, s) - W_G(a) = 0$ boundary by a statistically-significant margin, this state can be classified as a quantum non-Gaussian state.

Experimental characterisation of the frequency transfer function of the optical filter cavities was presented in chapter 4. The γ-factors in the multi-FSR temporal mode function used in the state reconstructions presented in this section are weightings derived from these filter measurements combined with the effective homodyne detection efficiencies, $\eta_e(f)$, due to data aliasing. The FSR proportions used in the

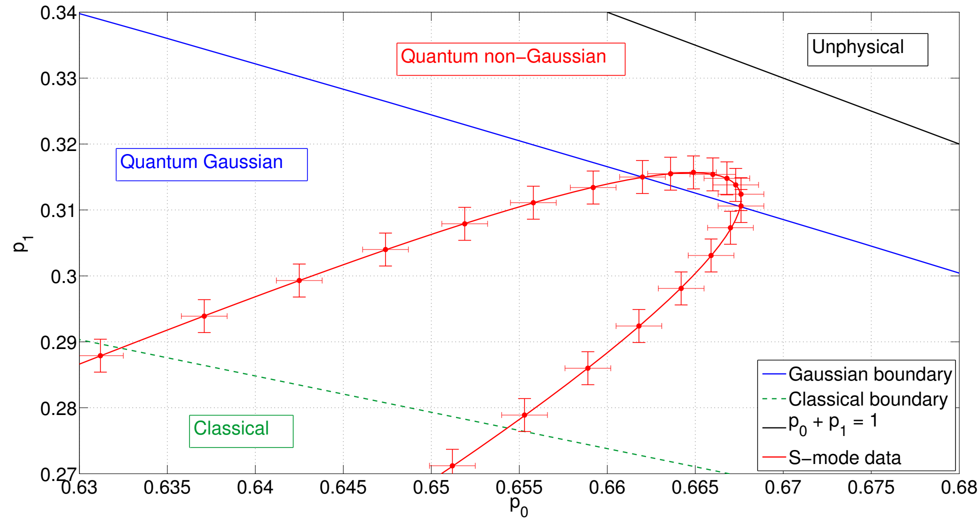

Figure 6.28: *Projected* symmetric mode (p_0, p_1) trajectory of our uncorrected experimental data reconstructed using the multi-frequency temporal mode function described by equation 5.6 for a *locked* pump phase. The uncorrected trajectory crosses both the classical boundary *and* the Gaussian boundary by a statistically-significant margin, which means this experimental state can be statistically classified as a quantum *non*-Gaussian state.

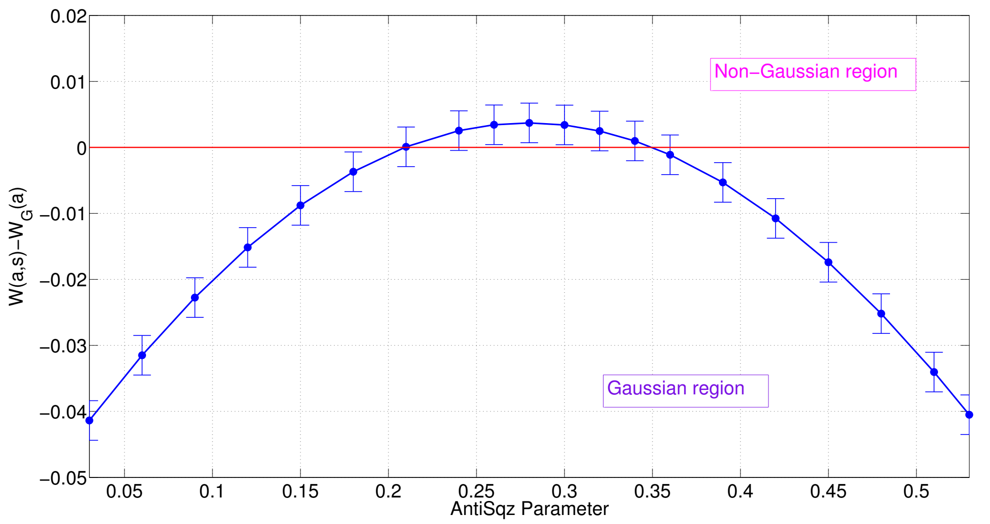

Figure 6.29: Quantum non-Gaussian character witness of our uncorrected *projected* symmetric mode state reconstructed using the multi-frequency temporal mode function described by equation 5.6 for a *locked* pump phase. As the peak of this uncorrected curve crosses the $W(a, s)$ - $W_G(a) = 0$ boundary by a statistically-significant margin, this state can be classified as a quantum non-Gaussian state.

final mode function is depicted in figure 6.24. It is important to verify whether the mode function derived from these measurements is in fact the ideal function. As we have already justified the filter parameters derived from the various measurements (see §4.3.2), we will now concentrate on testing whether the effective homodyne detection efficiencies, $\eta_e(f)$, previously discussed are the optimal values for shaping the ratios of the FSR components in the temporal mode function.

The relationship between adjusting the effective homodyne detection efficiencies used in the mode function, and the zero-photon and single-photon probabilities of the reconstructed photon-subtracted squeezed vacuum state was investigated. As discussed in §5.1.1, undersampling the homodyne signal led to data aliasing effects, which lowered the effective homodyne detection efficiencies at the FSR frequencies. This effect was quantified by the $\eta_e(f)$ parameter (equation 5.1), which affected the final FSR ratios in the mode function (equation 5.10). We found that the most influential quantity of these efficiencies on the mode function was the detection efficiency ratio between the second and third FSRs,

$$\mathrm{DetRatio} = \frac{\eta_e(1030\,\mathrm{MHz})}{\eta_e(1545\,\mathrm{MHz})} \tag{6.9}$$

Experimental characterisation of the data aliasing effects determined this ratio to be ~ 7.663 from table 6.1. Hypothetically, we could treat that ratio as a free parameter in the tomographic reconstruction of the experimental data and explore how the results change as a consequence. Adjustments to $\eta_e(1030\,\mathrm{MHz})/\eta_e(1545\,\mathrm{MHz})$ away from the measured quantity led to a statistically-significant decrease in the single-photon probability of the photon-subtracted squeezed vacuum state, which is shown in figure 6.30. There is also a statistically-significant increase in the zero-photon probability. Therefore, the spectral mode function based on the measured cavity parameters and measured homodyne detection efficiencies resulted in the optimum reconstruction of the quantum states.

6.3.2 Corrected for η_{HD}

Figure 6.31 shows the PNDs for the *projected* symmetric side-band mode (S-mode Multi-FSR) reconstructed using the multi-frequency temporal mode function described by equation 5.6 corrected for $\eta_{HD} = 0.7368$ and with a *locked* pump phase. This PND was reconstructed from homodyne tomography data of the projected state using the parameters listed in tables 6.1 & 6.7. Figure 6.31 also shows the PND of the symmetric side-band mode (S-mode 1st FSR) at 515 MHz corrected for $\eta_{HD} = 0.7368$ and reconstructed using the parameters listed in tables 6.1 & 6.2. These PNDs are shown together to illustrate the increase in the single-photon prob-

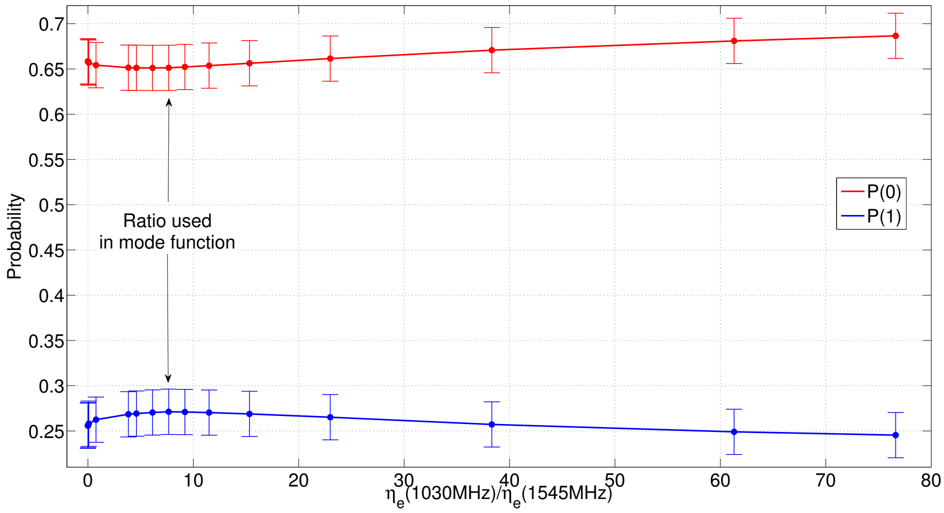

Figure 6.30: Photon number probabilities as a function of effective homodyne detection efficiency ratios used in the multi-frequency temporal mode function for projected state reconstruction. The detection efficiency ratio used for state reconstruction presented in this section is labelled in the figure. The single-photon probability is shown in blue and vacuum probability is shown in red; the lines connecting the data points is shown to illustrate the data trend and is not a theory curve.

ability and decrease in zero-photon and two-photon probabilities of the multi-FSR S-mode state compared to that of the 515 MHz S-mode state.

It is interesting to note that the three-photon probability of the multi-FSR symmetric mode shown in figure 6.31 is now larger than the two-photon probability by a statistically-significant margin. This is not the case for the 515 MHz projected S-mode state. As mentioned in chapter 1, this type of PND is only possible from photon-subtracted squeezed vacuum states, which are generally thought of as being produced from strictly *degenerate* PDC. We have experimentally demonstrated that applying a projection and state reconstruction measurement technique that cannot discern between the upper and lower side-bands leads to a photon-subtracted squeezed state from frequency *nondegenerate* PDC produced by a SS-NOPO.

Figure 6.32 shows the experimental PND corrected for $\eta_{HD} = 0.7368$ of the *projected* anti-symmetric side-band mode (A-mode Multi-FSR) reconstructed using the multi-frequency temporal mode function described by equation 5.6 for a *locked* pump phase. This PND was reconstructed from homodyne tomography data of the projected state using the parameters listed in tables 6.1 & 6.7. Figure 6.32 also shows the experimental PND corrected for $\eta_{HD} = 0.7368$ of the anti-symmetric side-band mode at 515 MHz (A-mode 1st FSR) reconstructed using the parameters listed in tables 6.1 & 6.2. These PNDs are shown together to illustrate the clear increase in the two-photon probability and decrease in one-photon probability of the

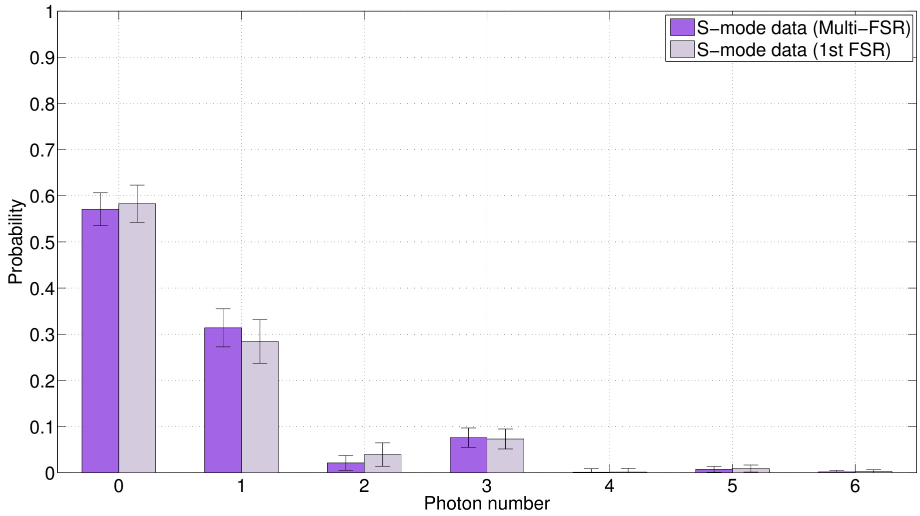

Figure 6.31: Comparison of experimental photon number distributions corrected for $\eta_{HD} = 0.7368$ of the state in the *projected* symmetric side-band mode (S-mode Multi-FSR) reconstructed using the multi-frequency temporal mode function to the experimental PND corrected for $\eta_{HD} = 0.7368$ of the state in the *projected* symmetric side-band mode at 515 MHz (S-mode 1st FSR) for a *locked* pump phase. The reconstruction parameters for the S-mode multi-FSR state are listed in tables 6.1 & 6.7, and for the S-mode 1st FSR state are listed in tables 6.1 & 6.2.

multi-FSR A-mode state compared to that of the 515 MHz A-mode state.

Figure 6.33 shows the corresponding Wigner functions corrected for $\eta_{HD} = 0.7368$ for the photon-subtracted squeezed vacuum state in the symmetric mode (figure 6.33A) and the squeezed vacuum state in the anti-symmetric mode (figure 6.33B) reconstructed using the multi-frequency temporal mode function described by equation 5.6 for a *locked* pump phase. These Wigner functions are more noticeably different to each other than compared to the states at 515 MHz (figure 6.10). The Wigner function of the projected symmetric mode state has a clear dip near $W(0,0)$, and has a distinct non-Gaussian shape compared to the Wigner function of the projected anti-symmetric mode state.

Figure 6.34 shows the efficiency-corrected (p_0, p_1) trajectory of the photon-subtracted squeezed vacuum state (symmetric mode) reconstructed using the multi-frequency temporal mode function described by equation 5.6 for a *locked* pump phase. This trajectory was obtained by applying the anti-squeezing operation to our experimental density matrix corrected for $\eta_{HD} = 0.7368$ obtained using the reconstruction parameters listed in table 6.7. The efficiency-corrected (p_0, p_1) trajectory of this multi-FSR state crosses both the classical boundary *and* the Gaussian boundary by a statistically-significant margin. Therefore, this corrected multi-FSR experimental state can be statistically classified as a quantum *non*-Gaussian state. Figure

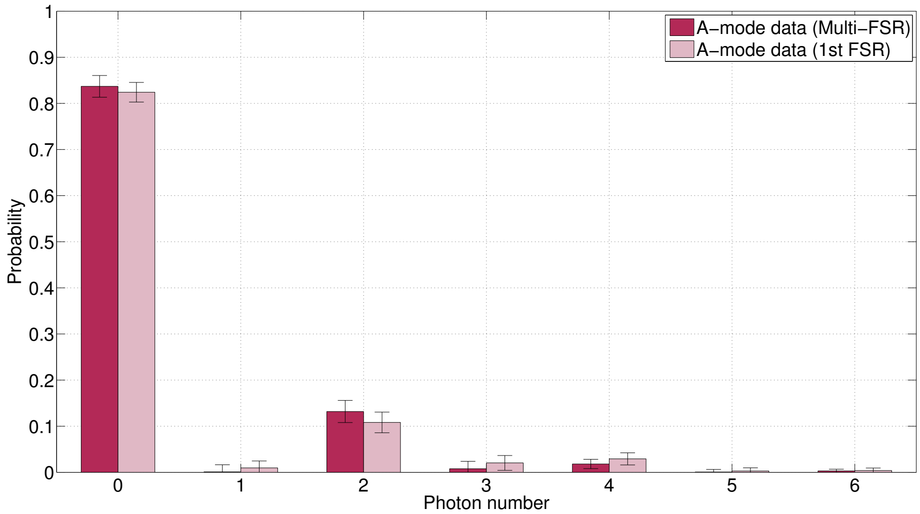

Figure 6.32: Comparison of experimental photon number distributions corrected for $\eta_{HD} = 0.7368$ of the *projected* anti-symmetric side-band mode state reconstructed using the multi-frequency temporal mode function (A-mode Multi-FSR) to the experimental PND corrected for $\eta_{HD} = 0.7368$ of the *projected* anti-symmetric side-band mode state at 515 MHz (A-mode 1st FSR) for a *locked* pump phase. The reconstruction parameters for the A-mode multi-FSR state are listed in tables 6.1 & 6.7, and the reconstruction parameters for the A-mode 1st FSR state are listed in tables 6.1 & 6.2.

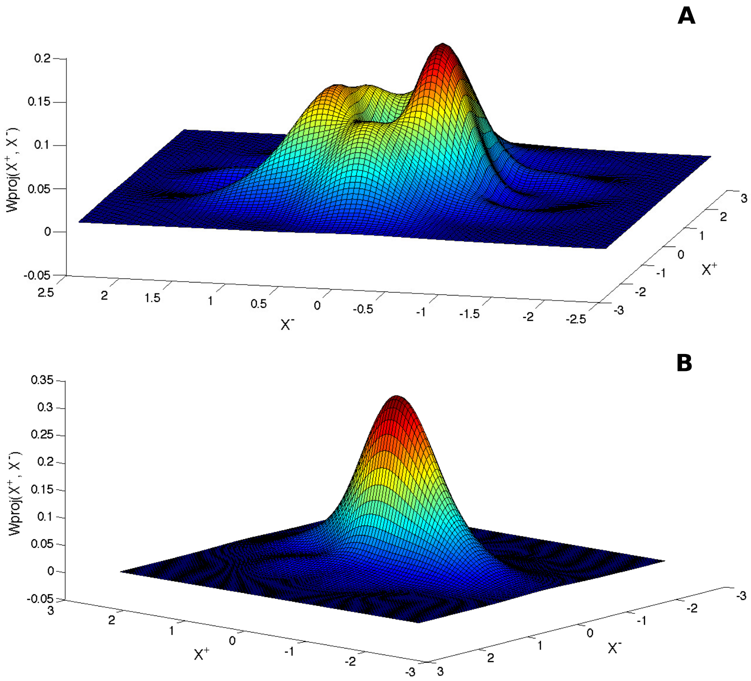

Figure 6.33: Experimental Wigner functions corrected for $\eta_{HD} = 0.7368$ reconstructed from *projected* data using the multi-frequency temporal mode function described by equation 5.6 for a *locked* pump phase. A) Photon-subtracted squeezed vacuum state (symmetric mode), and B) squeezed vacuum state (anti-symmetric mode). The reconstruction parameters are listed in tables 6.1 & 6.7.

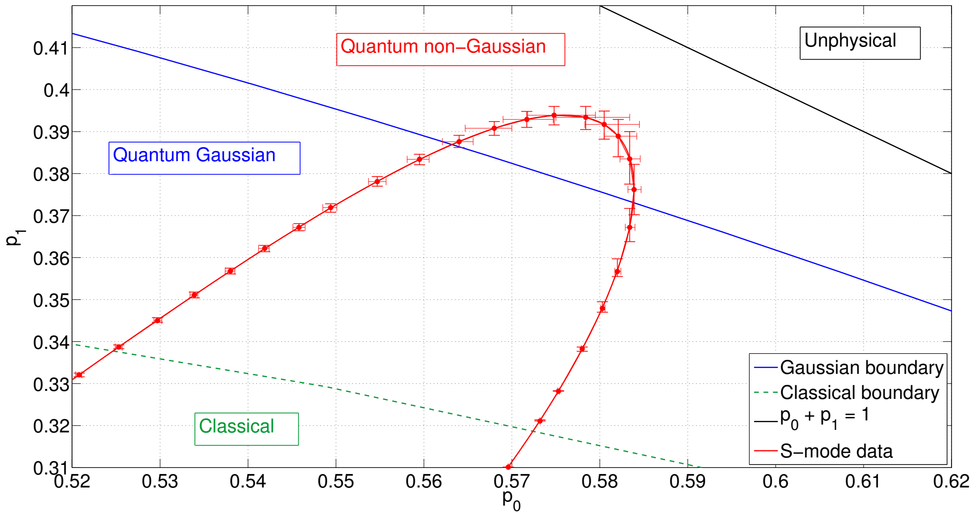

Figure 6.34: *Projected* symmetric mode (p_0, p_1) trajectory of our experimental data corrected for $\eta_{HD} = 0.7368$ reconstructed using the multi-frequency temporal mode function described by equation 5.6 for a *locked* pump phase. The efficiency-corrected trajectory crosses both the classical boundary *and* the Gaussian boundary by a statistically-significant margin, which means this experimental state can be statistically classified as a quantum *non*-Gaussian state.

6.35 shows the corresponding optimal quantum non-Gaussian character witness, $W(a_{opt}, s) - W_G(a_{opt})$, as a function of the anti-squeezing parameter, s.

We have seen that applying this multi-frequency mode function with the appropriate temporal and phase offsets reveals the entanglement between the FSR side-band pairs. This leads to an improvement in the quality of the quantum non-Gaussian state, as evident by the *uncorrected* photon-subtracted squeezed vacuum state reconstructed with the multi-frequency function crossing both the classical and Gaussian boundaries by a statistically-significant margin. We confirm that the quantum non-Gaussian character witness proposed in [313] demonstrates a powerful ability to identify non-classical and quantum non-Gaussian states.

Recall that the use of this mode function on the unprojected data resulted in a weighted-average of the quantum states at the three FSRs, which was worse due to the FSRs being uncorrelated. However, the FSRs became entangled in the projected state due to the spectral nature of the optical trigger mode, and the use of this mode function improved the quality of both the projected symmetric and projected anti-symmetric quantum states. Despite the relatively small contribution of the third FSR in the mode function, including this frequency component in the demodulation function had a significant effect on the quality of the reconstructed photon-subtracted squeezed vacuum state. It is interesting to note that an entangled spectrum of side-bands is necessary to produce a resource state for

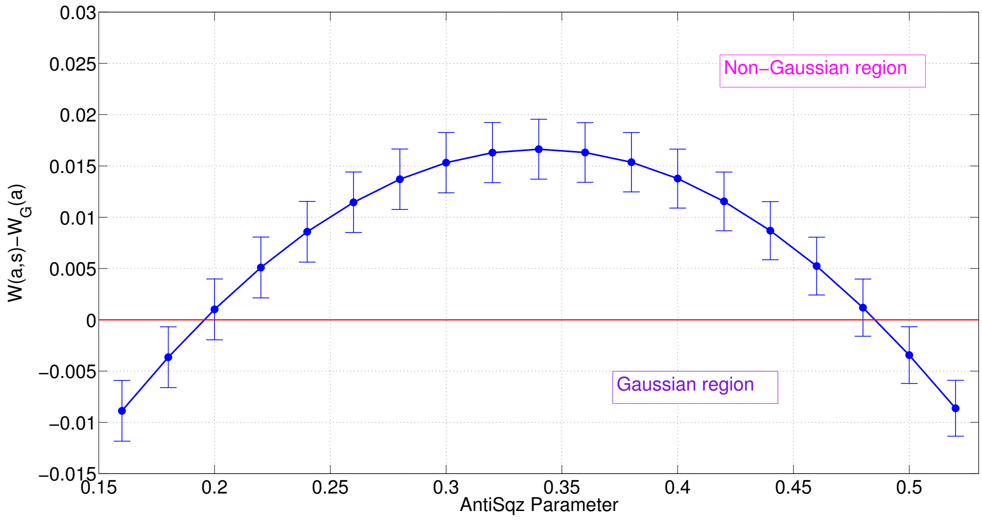

Figure 6.35: Quantum non-Gaussian character witness of our *projected* symmetric mode state corrected for $\eta_{HD} = 0.7368$ reconstructed using the multi-frequency temporal mode function described by equation 5.6 for a *locked* pump phase. As the peak of this corrected curve crosses the $W(a, s) - W_G(a) = 0$ boundary by a statistically-significant margin, this state can be classified as a quantum non-Gaussian state.

time-division-multiplexing (TDM) in which a channel is divided into several time bins. The number of entangled FSRs is only limited by the detection bandwidth of the APD, and the frequency transfer function of the optical filter system. Therefore, these quantum states could lead to ultra-fast TDM channels [163].

6.4 Impact of η_{APD} and P_{dc} on projected state

Although superconducting transition edge sensors (TESs) with photon-number-resolving ability are available [227,228], commercially available APDs are still widely used as photon-number detectors in Schrödinger kitten state generation experiments since cryogenic environments are required for TESs. Typical characteristics of commercially available telecommunication wavelength InGaAs-APDs (ID Quantique Ltd.) range between 10^{-4} to 10^{-5} for dark count probabilities (P_{dc}), and $\sim 10\% - 20\%$ for quantum detection efficiencies (η_{APD}). These quantities are orders of magnitude worse compared to typical $\sim$ 860 nm wavelength Si-APDs (Perkin Elmer Ltd.), which are $P_{dc} = 5 \times 10^{-6}$ to 2.5×10^{-7} for $\eta_{APD} = 45\%$ [304]. Si-APDs perform better than InGaAs-APDs due to their lower dark count probabilities and higher detection efficiencies.

We have established throughout this chapter and the previously chapter that we have a theoretical model that is consistent with our experimental results. Therefore

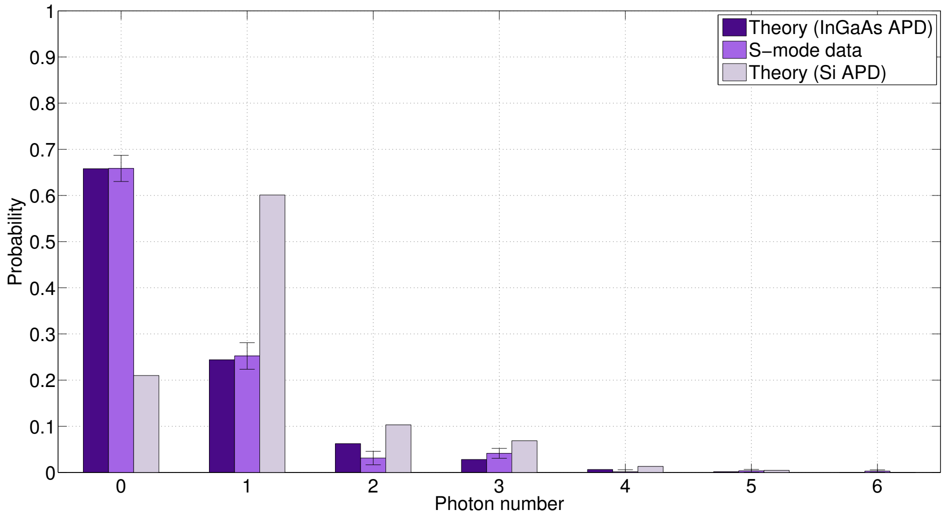

Figure 6.36: Comparison of uncorrected experimental and theoretical photon number distributions of the 515 MHz *projected* symmetric side-band mode (S-mode) for two different types of APDs. The reconstruction parameters are listed in tables 6.1 & 6.2, and the model parameters are listed in table 6.8.

Side-band mode	Pure squeezing level	Loss r_1	Tap-off r_2	η_{HD}	η_{APD}	P_{dc}
515 MHz S-mode (InGaAs-APD)	-3.474 dB	0.005	0.008	0.7368	0.08	0.00175
515 MHz S-mode (Si-APD)	-3.474 dB	0.005	0.008	0.7368	**0.45**	**0.00001**

Table 6.8: Summary of model parameters used to simulated symmetric mode (S-mode) for the 515 MHz states from the projected data results for two different projecting detectors (APDs).

we are able to use that model to predict the expected photon-subtracted squeezed vacuum state if the projecting detector (APD) had a higher quantum efficiency and a lower dark count rate. Table 6.8 lists the parameters of the two projecting detectors used to predict such a state using the model reviewed in §2.6. The InGaAs-APD parameters are the same as the ones used throughout this chapter when modelling the various projected states. The parameters for the Si-APD are of a typical Si device currently commercially available [304]. Figure 6.36 shows the uncorrected experimental photon number distribution (PND) of the projected symmetric side-band mode (S-mode) at 515 MHz for a *locked* pump phase. This PND was reconstructed from homodyne tomography data of the projected state using the parameters listed in tables 6.1 & 6.2. Figure 6.36 also shows two theoretical PNDs of photon-subtracted squeezed vacuum state projected using two different types of APDs: an InGaAs-APD and a Si-APD (parameters listed in table 6.8). This model predicts that if we were to connect a projecting detector to the *existing* experiment that had the characteristics of a standard Si-APD, we would expect a single-photon probability to be $\sim 60\%$, which would most likely correspond to negativity in the Wigner function. This figure illustrates how the qualities of the projecting detector have a significant influence over the quality of the projected state, and the various technical challenges that must be overcome in a hybrid experiment performed at 1550 nm.

6.5 Summary

Experimental results from a photon-subtracted two-mode squeezed vacuum state generated by a side-band-scale nondegenerate optical parametric oscillator (SS-NOPO) were presented. Measuring this state in a rotated basis revealed two distinct quantum states in independent side-band modes. These modes could be accessed and manipulated separately within a single optical mode. Despite its positive Wigner function, the photon-subtracted squeezed vacuum state was determined to be a *quantum non-Gaussian state* according to a recently formulated character witness. It is important to note that the detection of a trigger photon heralds the generation of both the quantum non-Gaussian *and* squeezed vacuum states, which is a unique property of working with distinguishable frequency side-bands. Utilising a multi-frequency temporal mode function revealed an improvement in the quality of the projected states. This demonstrated the presence of entanglement between the first, second, and third FSR states. The spectral shape of this multi-frequency temporal mode function was investigated. This investigation established that the ideal weightings between the FSR components were determined by the frequency characterisation measurements of the optical filter system, and homodyne detection efficiencies due to data aliasing effects. Finally, the detrimental effects on the quality of a photon-subtracted squeezed vacuum state caused by a high dark count probability and low quantum detection efficiency of the projecting detector were briefly discussed. We presented a model of the expected projected state if we were to use a projecting detector with the qualities of a Si-APD. It was established that we could theoretically achieve a projected state with a single-photon probability of $\sim 60\%$ if a commercial InGaAs-APD could be fabricated with a lower dark count rate and higher detection efficiency similar to a standard Si-APD.

Chapter 7

Conclusions

7.1 Summary

This thesis was focussed on the generation and characterisation of two-mode quantum states. These quantum states were generated by frequency nondegenerate parametric down-conversion produced by a side-band-scale nondegenerate optical paramateric oscillator (SS-NOPO). Time and effort were invested to improve the stability and nonlinearity of this experiment with the goal of generating a projected state with a higher single photon probability than previously achieved. We obtained this goal and, more importantly, experimentally demonstrated a photon-subtraction operation which affected the symmetric side-band mode without affecting the anti-symmetric side-band mode.

The vital components of the experiment that led to the experimental results highlighted in this thesis were discussed in detail. In particular, a simple and powerful technique for high-frequency characterisation of an optical system, such as measuring the linewidth and FSR of a cavity, was highlighted as an important experimental tool. An accurate measurement of the FSR of a cavity is experimentally challenging and usually requires a high-frequency photodetector. Our technique utilises a standard fibre amplitude modulator and a readily-available power meter to monitor the transmitted power through the system as a function of modulation frequency. This discovery allowed the frequency transfer function of the trigger mode filter cavities to be measured.

We demonstrated theoretically that a two-mode squeezed vacuum state can be decomposed into two single-mode squeezed vacuum states in the rotated side-band basis. We defined this basis as the symmetric and anti-symmetric modes, which are linear combinations of the upper and lower side-bands. Measuring a two-mode squeezed vacuum state generated by a SS-NOPO using a technique that probes the states in this rotated basis allowed us to reconstruct the two single-mode squeezed vacuum states. This novel technique combines phase-locked frequency demodulation with wide-bandwidth homodyne detection. We were able to reconstruct single-mode squeezed vacuum states at the first three FSR frequencies of our SS-NOPO due to the 2 GHz detection bandwidth of our homodyne detector. This was the first experimental demonstration of quantum state tomography of single-mode squeezed vacuum states from two-mode squeezed vacuum states produced by a SS-NOPO at multiple FSR frequencies.

We then discussed the projection of a photon-subtracted two-mode squeezed vacuum state using a photodetection technique that could not distinguish whether the subtracted photon originated from the upper or lower frequency side-band. State generation theory predicted that applying such a projector to the two-mode squeezed vacuum state would generate a photon-subtracted squeezed vacuum state in the symmetric mode without affecting the single-mode squeezed vacuum state in the orthogonal mode. We experimentally confirmed this prediction and demonstrated photon-subtraction from a two-mode squeezed vacuum state, which generated a powerful quantum resource state consisting of two distinguishable quantum states: a quantum non-Gaussian state in one side-band mode *and* a squeezed vacuum state in the orthogonal mode. These states exist as independent states in a *single* optical beam.

Due to the multi-frequency nature of our optical trigger mode, we were able to isolate and reconstruct both photon-subtracted squeezed vacuum states and squeezed vacuum states at the first three FSR frequencies of our SS-NOPO. We showed that we could improve the quality of the reconstructed quantum states by utilising a multi-frequency temporal mode function which best matched the spectral properties of our trigger mode and the data aliasing effects of the homodyne data. Therefore, the mode function depended on both the optical filtering system implemented before the APD, and on the data aliasing effects caused by digitally undersampling our high-frequency homodyne detection signal. Reconstructing the quantum states using this multi-frequency temporal mode function improved the quality of both the quantum non-Gaussian and squeezed vacuum states, and demonstrated entanglement between the three FSR side-band pairs. Such a frequency entangled quantum resource state could be useful in applications such as time-division-multiplexing.

Finally, we applied a theoretical model for impure squeezed vacuum and Schrödinger kitten state generation with imperfect experimental conditions to our experimental results. This model predicts that the single-photon probability of our photon-subtracted squeezed vacuum state would significantly increase if we were to use a projecting detector with a lower dark count probability and higher quantum efficiency.

7.2 Suggestions for Future Work

We have illustrated the power and flexibility possible in quantum optics experiments that capitalise on the frequency nondegenerate nature of SS-NOPOs. There are several improvements/extensions that could be made to this experiment, such us

- **Unresolved technical issues:** There are some technical issues that should be resolved, such as locating the source of the unknown phase drift that affects the pump phase. We have demonstrated how the amount of squeezing measured in the quantum state is related to the pump phase lock. Therefore, it would be better to experimentally phase-lock the pump phase to reduce the amount of homodyne data that needs to be rejected during post-processing.

- **Build a new optical parametric oscillator:** As discussed in chapter 4, the effective nonlinearities of our PPLN crystals are quite low compared to other nonlinear medium, such as PPKTP. One way to improve the system would be to replace the OPO with a new optical system that uses a PPKTP crystal and has a different cavity geometry with a much smaller beam waist at the crystal location. These changes should increase the effective nonlinearity of the crystal and lower the OPO threshold so that less 775 nm optical power is required to produce a similar level of squeezing.

- **Improving the projecting detector:** As mentioned towards the end of chapter 6, using an APD with a lower dark count rate and higher detection efficiency could improve the quality of our projected quantum states. We could test our prediction by sourcing a more efficient detector at 1550 nm and retake the projected state data.

- **Proof-of-principles CSQC experiments:** Once we have a better detector we could explore some proof-of-principles experiments on coherent state quantum computing with our unique quantum resource states.

- **Proof-of-principles quantum communication experiments:** Our ability to generated concurrent quantum resource states allows for numerous opportunities for proof-of-principles experiments to demonstrate basic quantum communication which could be explored in the future.

- **Construct filters to make TDM states:** We could design and construct a new optical filtering system that would purposely create quantum resource states for time-division-multiplexing.

- **Demonstrate FDM/TDM on CSQC and quantum communication experiments**

- **S-mode/A-mode 'tool kit:'** In order to explore the opportunities afforded by having independent access to the symmetric and the anti-symmetric modes, we would need to develop the appropriate 'tool kit.'

- **Derive new character witness based on p_0 & p_2:** We showed in chapter 6 that the quantum non-Gaussian character witness (which depends on p_0 & p_1) may not correctly identify a squeezed vacuum state as a quantum Gaussian state as the witness does not depend on p_2. Therefore a new character witness that depends on p_0 & p_2 could be investigated.

References

[1] John Preskill. Quantum computing: pro and con. *Proceedings of the Royal Society of London. Series A: Mathematical, Physical and Engineering Sciences*, 454(1969):469–486, 1998.

[2] J. J . Bollinger, Wayne M. Itano, D. J. Wineland, and D. J. Heinzen. Optimal frequency measurements with maximally correlated states. *Phys. Rev. A*, 54:R4649–R4652, Dec 1996.

[3] H. J. Kimble. The quantum internet. *Nature*, 453:1023–1030, 2008.

[4] Nicolas Gisin, Grégoire Ribordy, Wolfgang Tittel, and Hugo Zbinden. Quantum cryptography. *Rev. Mod. Phys.*, 74:145–195, Mar 2002.

[5] P. W. Shor. Algorithms for quantum computation: discrete logarithms and factoring. In *Proceedings of the 35th Annual Symposium on the Foundations of Computer Science*, pages 124–134. IEEE Computer Society Press, New York, 1994.

[6] Peter W. Shor. Polynomial-time algorithms for prime factorization and discrete logarithms on a quantum computer. *arXiv:quant-ph/9508027v2*, 1996.

[7] L. K. Grover. A fast quantum mechanical algorithm for database search. In *Proceedings of the 28th ACM Symposium on Theory of Computation*, page 212, 1996.

[8] Lov K. Grover. Quantum mechanics helps in searching for a needle in a haystack. *Phys. Rev. Lett.*, 79:325–328, Jul 1997.

[9] P. G. Kwiat, J. R. Mitchell, P. D. D. Schwindt, and A. G. White. Grover's search algorithm: An optical approach. *Journal of Modern Optics*, 47(2-3):257–266, 2000.

[10] Richard P. Feynman. Simulating physics with computers. *International Journal of Theoretical Physics*, 21:467–488, 1982.

[11] Seth Lloyd. Universal quantum simulators. *Science*, 273(5278):1073–1078, 1996.

[12] Christof Zalka. Simulating quantum systems on a quantum computer. *Proceedings of the Royal Society of London. Series A: Mathematical, Physical and Engineering Sciences*, 454(1969):313–322, 1998.

[13] Stephen Wiesner. Simulations of many-body quantum systems by a quantum computer. *arXiv:quant-ph/9603028*, 1996.

[14] David A. Meyer. Quantum mechanics of lattice gas automata: One-particle plane waves and potentials. *Phys. Rev. E*, 55:5261–5269, May 1997.

[15] Daniel A. Lidar and Ofer Biham. Simulating ising spin glasses on a quantum computer. *Phys. Rev. E*, 56:3661–3681, Sep 1997.

[16] Daniel S. Abrams and Seth Lloyd. Simulation of many-body fermi systems on a universal quantum computer. *Phys. Rev. Lett.*, 79:2586–2589, Sep 1997.

[17] Bruce M. Boghosian and Washington Taylor IV. Simulating quantum mechanics on a quantum computer. *Physica D: Nonlinear Phenomena*, 120(12):30 – 42, 1998. ¡ce:title¿Proceedings of the Fourth Workshop on Physics and Consumption¡/ce:title¿.

[18] V. Giovannetti, S. Lloyd, and L. Maccone. Quantum-enhanced measurements: Beating the standard quantum limit. *Science*, 360:1330–1336, 2004.

[19] M. J. Holland and K. Burnett. Interferometric detection of optical phase shifts at the heisenberg limit. *Phys. Rev. Lett.*, 71:1355–1358, Aug 1993.

[20] Z. Y. Ou. Fundamental quantum limit in precision phase measurement. *Phys. Rev. A*, 55:2598–2609, Apr 1997.

[21] R. A. Campos, Christopher C. Gerry, and A. Benmoussa. Optical interferometry at the heisenberg limit with twin fock states and parity measurements. *Phys. Rev. A*, 68:023810, Aug 2003.

[22] Agedi N. Boto, Pieter Kok, Daniel S. Abrams, Samuel L. Braunstein, Colin P. Williams, and Jonathan P. Dowling. Quantum interferometric optical lithography: Exploiting entanglement to beat the diffraction limit. *Phys. Rev. Lett.*, 85:2733–2736, Sep 2000.

[23] Paul Benioff. Quantum mechanical models of turing machines that dissipate no energy. *Phys. Rev. Lett.*, 48:1581–1585, Jun 1982.

[24] D. Deutsch. Quantum theory, the church-turing principle and the universal quantum computer. *Proceedings of the Royal Society of London. Series A, Mathematical and Physical Sciences*, 400(1818):pp. 97–117, 1985.

[25] Jeremy L. O'Brien. Optical quantum computing. *Science*, 318(5856):1567–1570, 2007.

[26] D.P. DiVincenzo and D. Loss. Quantum information is physical. *Superlattices and Microstructures*, 23(34):419 – 432, 1998.

[27] J. L. O'Brien, G. J. Pryde, A. G. White, T. C. Ralph, and D. Branning. Demonstration of an all-optical quantum controlled-not gate. *Nature*, 426:264–267, 2003.

[28] Charles H. Bennett. Quantum information and computation. *Physics Today*, 48(10):24–30, 1995.

[29] Charles H. Bennett, Gilles Brassard, Claude Crépeau, Richard Jozsa, Asher Peres, and William K. Wootters. Teleporting an unknown quantum state via dual classical and einstein-podolsky-rosen channels. *Phys. Rev. Lett.*, 70:1895–1899, Mar 1993.

[30] Dik Bouwmeester, Jian-Wei Pan, Klaus Mattle, Manfred Eibl, Harald Weinfurter, and Anton Zeilinger. Experimental quantum teleportation. *Nature*, 390:575–579, 1997.

[31] Daniel Gottesman and Isaac L. Chuang. Demonstrating the viability of universal quantum computation using teleportation and single-qubit operations. *Nature*, 402:390–393, 1999.

[32] S. J. van Enk. Discrete formulation of teleportation of continuous variables. *Phys. Rev. A*, 60:5095–5097, Dec 1999.

[33] Charles H. Bennett and Stephen J. Wiesner. Communication via one- and two-particle operators on einstein-podolsky-rosen states. *Phys. Rev. Lett.*, 69:2881–2884, Nov 1992.

[34] Klaus Mattle, Harald Weinfurter, Paul G. Kwiat, and Anton Zeilinger. Dense coding in experimental quantum communication. *Phys. Rev. Lett.*, 76:4656–4659, Jun 1996.

[35] T. C. Ralph and E. H. Huntington. Unconditional continuous-variable dense coding. *Phys. Rev. A*, 66:042321, Oct 2002.

[36] Isaac L. Chuang and Yoshihisa Yamamoto. Simple quantum computer. *Phys. Rev. A*, 52:3489–3496, Nov 1995.

[37] E. Knill, R. Laflamme, and G. J. Milburn. A scheme for efficient quantum computation with linear optics. *Nature*, 409:46–52, 2001.

[38] Pieter Kok, W. J. Munro, Kae Nemoto, T. C. Ralph, Jonathan P. Dowling, and G. J. Milburn. Linear optical quantum computing with photonic qubits. *Rev. Mod. Phys.*, 79:135–174, Jan 2007.

[39] Timothy C. Ralph and Robert W. Boyd. Better computing with photons. *Science*, 318:1251–1252, 2007.

[40] C. Monroe, D. M. Meekhof, B. E. King, W. M. Itano, and D. J. Wineland. Demonstration of a fundamental quantum logic gate. *Phys. Rev. Lett.*, 75:4714–4717, Dec 1995.

[41] J. I. Cirac and P. Zoller. Quantum computations with cold trapped ions. *Phys. Rev. Lett.*, 74:4091–4094, May 1995.

[42] H.-J. Briegel, T. Calarco, D. Jaksch, J. I. Cirac, and P. Zoller. Quantum computing with neutral atoms. *Journal of Modern Optics*, 47(2-3):415–451, 2000.

[43] B.B. Blinov, D. Leibfried, C. Monroe, and D.J. Wineland. Quantum computing with trapped ion hyperfine qubits. *Quantum Information Processing*, 3(1-5):45–59, 2004.

[44] J. Beugnon, M. P. A. Jones, J. Dingjan, B. Darqui, G. Messin, A. Browaeys, and P. Grangier. Quantum interference between two single photons emitted by independently trapped atoms. *Nature*, 440:779–782, 2006.

[45] P. Maunz, D. L. Moehring, S. Olmschenk, K. C. Younge, D. N. Matsukevich, and C. Monroe. Quantum interference of photon pairs from two remote trapped atomic ions. *Nat Phys*, 3:538–541, 2007.

[46] Philippe Grangier, Barry Sanders, and Jelena Vuckovic. Focus on single photons on demand. *New Journal of Physics*, 6(1), 2004.

[47] AlexanderN. Korotkov. Special issue on quantum computing with superconducting qubits. *Quantum Information Processing*, 8(2-3):51–54, 2009.

[48] D. G. Cory, A. F. Fahmy, and T. F. Havel. Nuclear magnetic resonance spectroscopy: an experimentally accesible paradigm for quantum computing. In *Proceedings of the 4th Workshop on Physics and Computation.* Boston: New England Complex Systems Institute, 1996.

[49] Neil A. Gershenfeld and Isaac L. Chuang. Bulk spin-resonance quantum computation. *Science*, 275(5298):350–356, 1997.

[50] Lieven M. K. Vandersypen, Isaac L. Chuang, and Dieter Suter. *Liquid-State NMR Quantum Computing.* John Wiley & Sons, Ltd, 2007.

[51] Charles Santori, David Fattal, Jelena Vuckovic, Glenn S. Solomon, and Yoshihisa Yamamoto. Indistinguishable photons from a single-photon device. *Nature*, 419:594–597, 2002.

[52] Toshimasa Fujisawa, Toshiaki Hayashi, Ritsuya Tomita, and Yoshiro Hirayama. Bidirectional counting of single electrons. *Science*, 312(5780):1634–1636, 2006.

[53] Michael N. Leuenberger. Fault-tolerant quantum computing with coded spins using the conditional faraday rotation in quantum dots. *Phys. Rev. B*, 73:075312, Feb 2006.

[54] S Braunstein and HK Lo. Experimental proposals for quantum computation - foreword. *FORTSCHRITTE DER PHYSIK-PROGRESS OF PHYSICS*, 48(9-11):767, 2000.

[55] R. J. Thompson, G. Rempe, and H. J. Kimble. Observation of normal-mode splitting for an atom in an optical cavity. *Phys. Rev. Lett.*, 68:1132–1135, Feb 1992.

[56] T. Pellizzari, S. A. Gardiner, J. I. Cirac, and P. Zoller. Decoherence, continuous observation, and quantum computing: A cavity qed model. *Phys. Rev. Lett.*, 75:3788–3791, Nov 1995.

[57] Q. A. Turchette, C. J. Hood, W. Lange, H. Mabuchi, and H. J. Kimble. Measurement of conditional phase shifts for quantum logic. *Phys. Rev. Lett.*, 75:4710–4713, Dec 1995.

[58] Takao Aoki, Barak Dayan, E. Wilcut, W. P. Bowen, A. S. Parkins, T. J. Kippenberg, K. J. Vahala, and H. J. Kimble. Observation of strong coupling between one atom and a monolithic microresonator. *Nature*, 443:671–674, 2006.

[59] Markus Hijlkema, Bernhard Weber, Holger P. Specht, Simon C. Webster, Axel Kuhn, and Gerhard Rempe. A single-photon server with just one atom. *Nat Phys*, 3:253–255, 2007.

[60] Hua Wei, Wan Li Yang, Zhi Jiao Deng, and Mang Feng. Many-qubit network employing cavity qed in a decoherence-free subspace. *Phys. Rev. A*, 78:014304, Jul 2008.

[61] Siyuan Han, Yang Yu, Xi Chu, Shih-I Chu, and Zhen Wang. Time-resolved measurement of dissipation-induced decoherence in a josephson junction. *Science*, 293(5534):1457–1459, 2001.

[62] W. Tittel, J. Brendel, N. Gisin, and H. Zbinden. Long-distance bell-type tests using energy-time entangled photons. *Phys. Rev. A*, 59:4150–4163, Jun 1999.

[63] Richard J. Hughes, George L. Morgan, and C. Glen Peterson. Quantum key distribution over a 48 km optical fibre network. *Journal of Modern Optics*, 47(2-3):533–547, 2000.

[64] T C Ralph. Quantum optical systems for the implementation of quantum information processing. *Reports on Progress in Physics*, 69(4):853, 2006.

[65] Samuel L. Braunstein and Peter van Loock. Quantum information with continuous variables. *Rev. Mod. Phys.*, 77:513–577, Jun 2005.

[66] Leonard Mandel and Emil Wolf. *Optical Coherence and Quantum Optics*. Cambridge University Press, 1995.

[67] Charles H. Bennett. Quantum cryptography using any two nonorthogonal states. *Phys. Rev. Lett.*, 68:3121–3124, May 1992.

[68] Anton Zeilinger, Herbert J. Bernstein, and M.A. Horne. Information transfer with two-state two-particle quantum systems. *Journal of Modern Optics*, 41(12):2375–2384, 1994.

[69] David P. DiVincenzo. Quantum computation. *Science*, 270(5234):255–261, 1995.

[70] Seth Lloyd. Quantum-mechanical computers. *Scientific American*, 273:140–145, 1995.

[71] R Loudon. Non-classical effects in the statistical properties of light. *Reports on Progress in Physics*, 43(7):913, 1980.

[72] W. H. Louisell, A. Yariv, and A. E. Siegman. Quantum fluctuations and noise in parametric processes. i. *Phys. Rev.*, 124:1646–1654, Dec 1961.

[73] J. P. Gordon, W. H. Louisell, and L. R. Walker. Quantum fluctuations and noise in parametric processes. ii. *Phys. Rev.*, 129:481–485, Jan 1963.

[74] William G. Wagner and R. W. Hellwarth. Quantum noise in a parametric amplifier with lossy modes. *Phys. Rev.*, 133:A915–A920, Feb 1964.

[75] S. E. Harris, M. K. Oshman, and R. L. Byer. Observation of tunable optical parametric fluorescence. *Phys. Rev. Lett.*, 18:732–734, May 1967.

[76] Douglas Magde and Herbert Mahr. Study in ammonium dihydrogen phosphate of spontaneous parametric interaction tunable from 4400 to 16 000 å. *Phys. Rev. Lett.*, 18:905–907, May 1967.

[77] David C. Burnham and Donald L. Weinberg. Observation of simultaneity in parametric production of optical photon pairs. *Phys. Rev. Lett.*, 25:84–87, Jul 1970.

[78] H. J. Kimble, M. Dagenais, and L. Mandel. Photon antibunching in resonance fluorescence. *Phys. Rev. Lett.*, 39:691–695, Sep 1977.

[79] M. Dagenais and L. Mandel. Investigation of two-time correlations in photon emissions from a single atom. *Phys. Rev. A*, 18:2217–2228, Nov 1978.

[80] R. Short and L. Mandel. Observation of sub-poissonian photon statistics. *Phys. Rev. Lett.*, 51:384–387, Aug 1983.

[81] M. C. Teich and B. E. A. Saleh. Observation of sub-poisson franck-hertz light at 253.7 nm. *J. Opt. Soc. Am. B*, 2(2):275–282, Feb 1985.

[82] John F. Clauser. Experimental distinction between the quantum and classical field-theoretic predictions for the photoelectric effect. *Phys. Rev. D*, 9:853–860, Feb 1974.

[83] P. Grangier, G. Roger, and A. Aspect. Experimental evidence for a photon anticorrelation effect on a beam splitter: A new light on single-photon interferences. *EPL (Europhysics Letters)*, 1(4):173, 1986.

[84] H. Paul. Photon antibunching. *Rev. Mod. Phys.*, 54:1061–1102, Oct 1982.

[85] S. Friberg, C. K. Hong, and L. Mandel. Measurement of time delays in the parametric production of photon pairs. *Phys. Rev. Lett.*, 54:2011–2013, May 1985.

[86] C. K. Hong and L. Mandel. Experimental realization of a localized one-photon state. *Phys. Rev. Lett.*, 56:58–60, Jan 1986.

[87] Paul G. Kwiat, Klaus Mattle, Harald Weinfurter, Anton Zeilinger, Alexander V. Sergienko, and Yanhua Shih. New high-intensity source of polarization-entangled photon pairs. *Phys. Rev. Lett.*, 75:4337–4341, Dec 1995.

[88] F. Devaux and E. Lantz. Spatial and temporal properties of parametric fluorescence around degeneracy in a type i lbo crystal. *The European Physical Journal D*, 8(1):117–124, 2000.

[89] Christian Kurtsiefer, Markus Oberparleiter, and Harald Weinfurter. High-efficiency entangled photon pair collection in type-ii parametric fluorescence. *Phys. Rev. A*, 64:023802, Jul 2001.

[90] Alfred B. U'Ren, Christine Silberhorn, Konrad Banaszek, and Ian A. Walmsley. Efficient conditional preparation of high-fidelity single photon states for fiber-optic quantum networks. *Phys. Rev. Lett.*, 93:093601, Aug 2004.

[91] T.B. Pittman, B.C. Jacobs, and J.D. Franson. Heralding single photons from pulsed parametric down-conversion. *Optics Communications*, 246(46):545 – 550, 2005.

[92] S. Castelletto, I. Degiovanni, V. Schettini, and A. Migdall. Spatial and spectral mode selection of heralded single photons from pulsed parametric down-conversion. *Opt. Express*, 13(18):6709–6722, Sep 2005.

[93] Peter J. Mosley, Jeff S. Lundeen, Brian J. Smith, Piotr Wasylczyk, Alfred B. U'Ren, Christine Silberhorn, and Ian A. Walmsley. Heralded generation of ultrafast single photons in pure quantum states. *Phys. Rev. Lett.*, 100:133601, Apr 2008.

[94] G S Buller and R J Collins. Single-photon generation and detection. *Measurement Science and Technology*, 21(1):012002, 2010.

[95] G. Brida, I. P. Degiovanni, M. Genovese, A. Migdall, F. Piacentini, S. V. Polyakov, and I. Ruo Berchera. Experimental realization of a low-noise heralded single-photon source. *Opt. Express*, 19(2):1484–1492, Jan 2011.

[96] Sylvain Fasel, Olivier Alibart, Sébastien Tanzilli, Pascal Baldi, Alexios Beveratos, Nicolas Gisin, and Hugo Zbinden. High-quality asynchronous heralded single-photon source at telecom wavelength. *New Journal of Physics*, 6(1):163, 2004.

[97] S Castelletto, I P Degiovanni, V Schettini, and A Migdall. Optimizing single-photon-source heralding efficiency and detection efficiency metrology at 1550nm using periodically poled lithium niobate. *Metrologia*, 43(2):S56, 2006.

[98] A. Zavriyev, A. Leverrier, V. Denchev, and A. Trifonov. Improving the performance of quantum key distribution apparatus. *Journal of Modern Optics*, 54(2-3):305–313, 2007.

[99] Jing Zhang. Einstein-podolsky-rosen sideband entanglement in broadband squeezed light. *Phys. Rev. A*, 67:054302, May 2003.

[100] O. Glöckl, U. L. Andersen, S. Lorenz, Ch. Silberhorn, N. Korolkova, and G. Leuchs. Sub-shot-noise phase quadrature measurement of intense light beams. *Opt. Lett.*, 29(16):1936–1938, Aug 2004.

[101] E. H. Huntington, G. N. Milford, C. Robilliard, T. C. Ralph, O. Glöckl, U. L. Andersen, S. Lorenz, and G. Leuchs. Demonstration of the spatial separation of the entangled quantum sidebands of an optical field. *Phys. Rev. A*, 71:041802, Apr 2005.

[102] S. A. Castelletto and R. E. Scholten. Heralded single photon sources: a route towards quantum communication technology and photon standards. *The European Physical Journal Applied Physics*, 41:181–194, 2 2008.

[103] Charles Santori, David Fattal, Jelena Vuckovic, Glenn S Solomon, and Yoshihisa Yamamoto. Single-photon generation with inas quantum dots. *New Journal of Physics*, 6(1):89, 2004.

[104] M Hennrich, T Legero, A Kuhn, and G Rempe. Photon statistics of a nonstationary periodically driven single-photon source. *New Journal of Physics*, 6(1):86, 2004.

[105] M Keller, B Lange, K Hayasaka, W Lange, and H Walther. A calcium ion in a cavity as a controlled single-photon source. *New Journal of Physics*, 6(1):95, 2004.

[106] T Gaebel, I Popa, A Gruber, M Domhan, F Jelezko, and J Wrachtrup. Stable single-photon source in the near infrared. *New Journal of Physics*, 6(1):98, 2004.

[107] W E Moerner. Single-photon sources based on single molecules in solids. *New Journal of Physics*, 6(1):88, 2004.

[108] Jérémie Fulconis, Olivier Alibart, Jeremy L. O'Brien, William J. Wadsworth, and John G. Rarity. Nonclassical interference and entanglement generation using a photonic crystal fiber pair photon source. *Phys. Rev. Lett.*, 99:120501, Sep 2007.

[109] J. Leuthold, C. Koos, and W. Freude. Nonlinear silicon photonics. *Nat Photon*, 4:535–544, 2010.

[110] Jian-Wei Pan, Christoph Simon, Caslav Brukner, and Anton Zeilinger. Entanglement purification for quantum communication. *Nature*, 410:1067–1070, 2001.

[111] T. B. Pittman, B. C. Jacobs, and J. D. Franson. Demonstration of nondeterministic quantum logic operations using linear optical elements. *Phys. Rev. Lett.*, 88:257902, Jun 2002.

[112] T. B. Pittman, M. J. Fitch, B. C Jacobs, and J. D. Franson. Experimental controlled-not logic gate for single photons in the coincidence basis. *Phys. Rev. A*, 68:032316, Sep 2003.

[113] T. C. Ralph, A. G. White, W. J. Munro, and G. J. Milburn. Simple scheme for efficient linear optics quantum gates. *Phys. Rev. A*, 65:012314, Dec 2001.

[114] J. D. Franson, M. M. Donegan, M. J. Fitch, B. C. Jacobs, and T. B. Pittman. High-fidelity quantum logic operations using linear optical elements. *Phys. Rev. Lett.*, 89:137901, Sep 2002.

[115] Peter P. Rohde and Timothy C. Ralph. Frequency and temporal effects in linear optical quantum computing. *Phys. Rev. A*, 71:032320, Mar 2005.

[116] Michael Varnava, Daniel E. Browne, and Terry Rudolph. How good must single photon sources and detectors be for efficient linear optical quantum computation? *Phys. Rev. Lett.*, 100:060502, Feb 2008.

[117] D. Boschi, S. Branca, F. De Martini, L. Hardy, and S. Popescu. Experimental realization of teleporting an unknown pure quantum state via dual classical and einstein-podolsky-rosen channels. *Phys. Rev. Lett.*, 80:1121–1125, Feb 1998.

[118] Yoon-Ho Kim, Sergei P. Kulik, and Yanhua Shih. Quantum teleportation of a polarization state with a complete bell state measurement. *Phys. Rev. Lett.*, 86:1370–1373, Feb 2001.

[119] Jian-Wei Pan, Sara Gasparoni, Markus Aspelmeyer, Thomas Jennewein, and Anton Zeilinger. Experimental realization of freely propagating teleported qubits. *Nature*, 421:721–725, 2003.

[120] Seth Lloyd and Jean-Jacques E. Slotine. Analog quantum error correction. *Phys. Rev. Lett.*, 80:4088–4091, May 1998.

[121] Samuel L. Braunstein. Error correction for continuous quantum variables. *Phys. Rev. Lett.*, 80:4084–4087, May 1998.

[122] Samuel L. Braunstein. Quantum error correction for communication with linear optics. *Nature*, 394:47–49, 1998.

[123] Lev Vaidman. Teleportation of quantum states. *Phys. Rev. A*, 49:1473–1476, Feb 1994.

[124] Samuel L. Braunstein and H. J. Kimble. Teleportation of continuous quantum variables. *Phys. Rev. Lett.*, 80:869–872, Jan 1998.

[125] A. Furusawa, J. L. Srensen, S. L. Braunstein, C. A. Fuchs, H. J. Kimble, and E. S. Polzik. Unconditional quantum teleportation. *Science*, 282:706–709, 1998.

[126] P. van Loock and Samuel L. Braunstein. Multipartite entanglement for continuous variables: A quantum teleportation network. *Phys. Rev. Lett.*, 84:3482–3485, Apr 2000.

[127] Warwick P. Bowen, Nicolas Treps, Ben C. Buchler, Roman Schnabel, Timothy C. Ralph, Hans-A. Bachor, Thomas Symul, and Ping Koy Lam. Experimental investigation of continuous-variable quantum teleportation. *Phys. Rev. A*, 67:032302, Mar 2003.

[128] Seth Lloyd and Samuel L. Braunstein. Quantum computation over continuous variables. *Phys. Rev. Lett.*, 82:1784–1787, Feb 1999.

[129] Carlton M. Caves. Quantum-mechanical noise in an interferometer. *Phys. Rev. D*, 23:1693–1708, Apr 1981.

[130] Carlton M. Caves. Quantum limits on noise in linear amplifiers. *Phys. Rev. D*, 26:1817–1839, Oct 1982.

[131] D. F. Walls. Squeezed states of light. *Nature*, 306:141–146, 1983.

[132] C. K. Hong and L. Mandel. Higher-order squeezing of a quantum field. *Phys. Rev. Lett.*, 54:323–325, Jan 1985.

[133] S.M. Barnett and P.L. Knight. Squeezing in correlated quantum systems. *Journal of Modern Optics*, 34(6-7):841–853, 1987.

[134] K. Wódkiewicz. On the quantum mechanics of squeezed states. *Journal of Modern Optics*, 34(6-7):941–948, 1987.

[135] M. S. Kim, F. A. M. de Oliveira, and P. L. Knight. Properties of squeezed number states and squeezed thermal states. *Phys. Rev. A*, 40:2494–2503, Sep 1989.

[136] R. E. Slusher, L. W. Hollberg, B. Yurke, J. C. Mertz, and J. F. Valley. Observation of squeezed states generated by four-wave mixing in an optical cavity. *Phys. Rev. Lett.*, 55:2409–2412, Nov 1985.

[137] Ling-An Wu, H. J. Kimble, J. L. Hall, and Huifa Wu. Generation of squeezed states by parametric down conversion. *Phys. Rev. Lett.*, 57:2520–2523, Nov 1986.

[138] Min Xiao, Ling-An Wu, and H. J. Kimble. Precision measurement beyond the shot-noise limit. *Phys. Rev. Lett.*, 59:278–281, Jul 1987.

[139] P. Grangier, R. E. Slusher, B. Yurke, and A. LaPorta. Squeezed-light - enhanced polarization interferometer. *Phys. Rev. Lett.*, 59:2153–2156, Nov 1987.

[140] Y. H. Shih and C. O. Alley. New type of einstein-podolsky-rosen-bohm experiment using pairs of light quanta produced by optical parametric down conversion. *Phys. Rev. Lett.*, 61:2921–2924, Dec 1988.

[141] E. S. Polzik, J. Carri, and H. J. Kimble. Spectroscopy with squeezed light. *Phys. Rev. Lett.*, 68:3020–3023, May 1992.

[142] H. J. Kimble. Squeezed states of light: an (incomplete) survey of experimental progress and prospects. *Physics Reports*, 219:227–234, 1992.

[143] G. Breitenbach, T. Müller, S. F. Pereira, J.-Ph. Poizat, S. Schiller, and J. Mlynek. Squeezed vacuum from a monolithic optical parametric oscillator. *J. Opt. Soc. Am. B*, 12(11):2304–2309, Nov 1995.

[144] S. Schiller, G. Breitenbach, S. F. Pereira, T. Müller, and J. Mlynek. Quantum statistics of the squeezed vacuum by measurement of the density matrix in the number state representation. *Phys. Rev. Lett.*, 77:2933–2936, Sep 1996.

[145] G. Breitenbach, S. Schiller, and J. Mlynek. Measurement of the quantum states of squeezed light. *Nature*, 387:471–475, 1997.

[146] Klaus Schneider, M. Lang, J. Mlynek, and Stephan Schiller. Generation of strongly squeezed continuous-wave light at 1064 nm. *Opt. Express*, 2(3):59–64, Feb 1998.

[147] P K Lam, T C Ralph, B C Buchler, D E McClelland, H-A Bachor, and J Gao. Optimization and transfer of vacuum squeezing from an optical parametric oscillator. *Journal of Optics B: Quantum and Semiclassical Optics*, 1(4):469, 1999.

[148] Y. J. Lu and Z. Y. Ou. Optical parametric oscillator far below threshold: Experiment versus theory. *Phys. Rev. A*, 62:033804, Aug 2000.

[149] Yun Zhang, Hai Wang, Xiaoying Li, Jietai Jing, Changde Xie, and Kunchi Peng. Experimental generation of bright two-mode quadrature squeezed light from a narrow-band nondegenerate optical parametric amplifier. *Phys. Rev. A*, 62:023813, Jul 2000.

[150] U.L. Andersen, B.C. Buchler, P.K. Lam, J.W. Wu, J.R. Gao, and H.-A. Bachor. Four modes of optical parametric operation for squeezed state generation. *The European Physical Journal D - Atomic, Molecular, Optical and Plasma Physics*, 27(2):181–191, 2003.

[151] Simon Chelkowski, Henning Vahlbruch, Boris Hage, Alexander Franzen, Nico Lastzka, Karsten Danzmann, and Roman Schnabel. Experimental characterization of frequency-dependent squeezed light. *Phys. Rev. A*, 71:013806, Jan 2005.

[152] Takao Aoki, Go Takahashi, and Akira Furusawa. Squeezing at 946nm with periodically poled ktiopo4. *Opt. Express*, 14(15):6930–6935, Jul 2006.

[153] M. Lassen, V. Delaubert, C.C. Harb, P.K. Lam, N. Treps, and H-A. Bachor. Generation of squeezing in higher order hermite-gaussian modes with an optical parametric amplifier. *Journal of the European Optical Society - Rapid publications*, 1(0), 2006.

[154] Yuishi Takeno, Mitsuyoshi Yukawa, Hidehiro Yonezawa, and Akira Furusawa. Observation of -9 db quadrature squeezing with improvement of phasestability in homodyne measurement. *Opt. Express*, 15(7):4321–4327, Apr 2007.

[155] Henning Vahlbruch, Moritz Mehmet, Simon Chelkowski, Boris Hage, Alexander Franzen, Nico Lastzka, Stefan Goßler, Karsten Danzmann, and Roman Schnabel. Observation of squeezed light with 10-db quantum-noise reduction. *Phys. Rev. Lett.*, 100:033602, Jan 2008.

[156] Moritz Mehmet, Henning Vahlbruch, Nico Lastzka, Karsten Danzmann, and Roman Schnabel. Observation of squeezed states with strong photon-number oscillations. *Phys. Rev. A*, 81:013814, Jan 2010.

[157] Moritz Mehmet, Stefan Ast, Tobias Eberle, Sebastian Steinlechner, Henning Vahlbruch, and Roman Schnabel. Squeezed light at 1550 nm with a quantum noise reduction of 12.3 db. *Opt. Express*, 19(25):25763–25772, Dec 2011.

[158] Christian Weedbrook, Stefano Pirandola, Raúl García-Patrón, Nicolas J. Cerf, Timothy C. Ralph, Jeffrey H. Shapiro, and Seth Lloyd. Gaussian quantum information. *Rev. Mod. Phys.*, 84:621–669, May 2012.

[159] T. C. Ralph and P. K. Lam. Teleportation with bright squeezed light. *Phys. Rev. Lett.*, 81:5668–5671, Dec 1998.

[160] Samuel L. Braunstein, Christopher A. Fuchs, and H. J. Kimble. Criteria for continuous-variable quantum teleportation. *Journal of Modern Optics*, 47(2-3):267–278, 2000.

[161] U. L. Andersen and G. Leuchs. *Lectures on Quantum Information.* Wiley-VCH, Berlin, 2007.

[162] H Vahlbruch, S Chelkowski, K Danzmann, and R Schnabel. Quantum engineering of squeezed states for quantum communication and metrology. *New Journal of Physics*, 9(10):371, 2007.

[163] M. Heurs, J. G. Webb, A. E. Dunlop, C. C. Harb, T. C. Ralph, and E. H. Huntington. Multiplexed communication over a high-speed quantum channel. *Phys. Rev. A*, 81:032325, Mar 2010.

[164] Boris Hage, Aiko Samblowski, and Roman Schnabel. Towards einstein-podolsky-rosen quantum channel multiplexing. *Phys. Rev. A*, 81:062301, Jun 2010.

[165] H. Zaidi, N.C. Menicucci, S.T. Flammia, R. Bloomer, M. Pysher, and O. Pfister. Entangling the optical frequency comb: Simultaneous generation of multiple 2 x 2 and 2 x 3 continuous-variable cluster states in a single optical parametric oscillator. *Laser Physics*, 18(5):659–666, 2008.

[166] Nicolas C. Menicucci, Steven T. Flammia, and Olivier Pfister. One-way quantum computing in the optical frequency comb. *Phys. Rev. Lett.*, 101:130501, Sep 2008.

[167] Matthew Pysher, Alon Bahabad, Peng Peng, Ady Arie, and Olivier Pfister. Quasi-phase-matched concurrent nonlinearities in periodically poled ktiopo4 for quantum computing over the optical frequency comb. *Opt. Lett.*, 35(4):565–567, Feb 2010.

[168] Matthew Pysher, Yoshichika Miwa, Reihaneh Shahrokhshahi, Russell Bloomer, and Olivier Pfister. Parallel generation of quadripartite cluster entanglement in the optical frequency comb. *Phys. Rev. Lett.*, 107:030505, Jul 2011.

[169] Johanna L. Miller. Entanglement gets scaled up in an optical frequency comb. *Physics Today*, 64(9):21–24, 2011.

[170] Olivier Pinel, Pu Jian, Renné Medeiros de Araújo, Jinxia Feng, Benoˆ Chalopin, Claude Fabre, and Nicolas Treps. Generation and characterization of multimode quantum frequency combs. *Phys. Rev. Lett.*, 108:083601, Feb 2012.

[171] Stephen D. Bartlett, Barry C. Sanders, Samuel L. Braunstein, and Kae Nemoto. Efficient classical simulation of continuous variable quantum information processes. *Phys. Rev. Lett.*, 88:097904, Feb 2002.

[172] M.G.A. Paris, M.B. Plenio, S. Bose, D. Jonathan, and G.M. D'Ariano. Optical bell measurement by fock filtering. *Physics Letters A*, 273(3):153 – 158, 2000.

[173] Kae Nemoto and W. J. Munro. Nearly deterministic linear optical controlled-not gate. *Phys. Rev. Lett.*, 93:250502, Dec 2004.

[174] S. D. Barrett, Pieter Kok, Kae Nemoto, R. G. Beausoleil, W. J. Munro, and T. P. Spiller. Symmetry analyzer for nondestructive bell-state detection using weak nonlinearities. *Phys. Rev. A*, 71:060302, Jun 2005.

[175] W. J. Munro, Kae Nemoto, R. G. Beausoleil, and T. P. Spiller. High-efficiency quantum-nondemolition single-photon-number-resolving detector. *Phys. Rev. A*, 71:033819, Mar 2005.

[176] W J Munro, K Nemoto, and T P Spiller. Weak nonlinearities: a new route to optical quantum computation. *New Journal of Physics*, 7(1):137, 2005.

[177] T P Spiller, Kae Nemoto, Samuel L Braunstein, W J Munro, P van Loock, and G J Milburn. Quantum computation by communication. *New Journal of Physics*, 8(2):30, 2006.

[178] P. van Loock, W. J. Munro, Kae Nemoto, T. P. Spiller, T. D. Ladd, Samuel L. Braunstein, and G. J. Milburn. Hybrid quantum computation in quantum optics. *Phys. Rev. A*, 78:022303, Aug 2008.

[179] Daniel Gottesman, Alexei Kitaev, and John Preskill. Encoding a qubit in an oscillator. *Phys. Rev. A*, 64:012310, Jun 2001.

[180] Thierry Paul. Discrete-continuous and classical-quantum. *Mathematical Structures in Computer Science*, 17:177–183, 3 2007.

[181] P. van Loock. Optical hybrid approaches to quantum information. *Laser & Photonics Reviews*, 5(2):167–200, 2011.

[182] C. Cabrillo, J. I. Cirac, P. García-Fernández, and P. Zoller. Creation of entangled states of distant atoms by interference. *Phys. Rev. A*, 59:1025–1033, Feb 1999.

[183] L.-M. Duan, M. D. Lukin, J. I. Cirac, and P. Zoller. Long-distance quantum communication with atomic ensembles and linear optics. *Nature*, 414:413–418, 2001.

[184] A. Kuzmich, I. A. Walmsley, and L. Mandel. Violation of bell's inequality by a generalized einstein-podolsky-rosen state using homodyne detection. *Phys. Rev. Lett.*, 85:1349–1353, Aug 2000.

[185] E. Shchukin and W. Vogel. Universal measurement of quantum correlations of radiation. *Phys. Rev. Lett.*, 96:200403, May 2006.

[186] Valentina Parigi, Alessandro Zavatta, Myungshik Kim, and Marco Bellini. Probing quantum commutation rules by addition and subtraction of single photons to/from a light field. *Science*, 317(5846):1890–1893, 2007.

[187] Nitin Jain, S. R. Huisman, Erwan Bimbard, and A. I. Lvovsky. A bridge between the single-photon and squeezed-vacuum states. *Opt. Express*, 18(17):18254–18259, Aug 2010.

[188] P. van Loock, T. D. Ladd, K. Sanaka, F. Yamaguchi, Kae Nemoto, W. J. Munro, and Y. Yamamoto. Hybrid quantum repeater using bright coherent light. *Phys. Rev. Lett.*, 96:240501, Jun 2006.

[189] J. B. Brask, I. Rigas, E. S. Polzik, U. L. Andersen, and A. S. Sørensen. Hybrid long-distance entanglement distribution protocol. *Phys. Rev. Lett.*, 105:160501, Oct 2010.

[190] Nicolas Sangouard, Christoph Simon, Nicolas Gisin, Julien Laurat, Rosa Tualle-Brouri, and Philippe Grangier. Quantum repeaters with entangled coherent states. *J. Opt. Soc. Am. B*, 27(6):A137–A145, Jun 2010.

[191] Ulrik L. Andersen and Jonas S. Neergaard-Nielsen. Heralded generation of a micro-macro entangled state. *Phys. Rev. A*, 88:022337, Aug 2013.

[192] H.-J. Briegel, W. Dür, J. I. Cirac, and P. Zoller. Quantum repeaters: The role of imperfect local operations in quantum communication. *Phys. Rev. Lett.*, 81:5932–5935, Dec 1998.

[193] Alexei Ourjoumtsev, Aurélien Dantan, Rosa Tualle-Brouri, and Philippe Grangier. Increasing entanglement between gaussian states by coherent photon subtraction. *Phys. Rev. Lett.*, 98:030502, Jan 2007.

[194] Hiroki Takahashi, Jonas S. Neergaard-Nielsen, Makoto Takeuchi, Masahiro Takeoka, Kazuhiro Hayasaka, Akira Furusawa, and Masahide Sasaki. Entanglement distillation from gaussian input states. *Nat Photon*, 4:178–181, 2010.

[195] Ruifang Dong, Mikael Lassen, Joel Heersink, Christoph Marquardt, Radim Filip, Gerd Leuchs, and Ulrik L. Andersen. Continuous-variable entanglement distillation of non-gaussian mixed states. *Phys. Rev. A*, 82:012312, Jul 2010.

[196] Jonas S. Neergaard-Nielsen, Makoto Takeuchi, Kentaro Wakui, Hiroki Takahashi, Kazuhiro Hayasaka, Masahiro Takeoka, and Masahide Sasaki. Optical continuous-variable qubit. *Phys. Rev. Lett.*, 105:053602, Jul 2010.

[197] R. E. S. Polkinghorne and T. C. Ralph. Continuous variable entanglement swapping. *Phys. Rev. Lett.*, 83:2095–2099, Sep 1999.

[198] Toshiki Ide, Holger F. Hofmann, Takayoshi Kobayashi, and Akira Furusawa. Continuous-variable teleportation of single-photon states. *Phys. Rev. A*, 65:012313, Dec 2001.

[199] Toshiki Ide, Holger F. Hofmann, Akira Furusawa, and Takayoshi Kobayashi. Gain tuning and fidelity in continuous-variable quantum teleportation. *Phys. Rev. A*, 65:062303, May 2002.

[200] Ulrik L. Andersen and Timothy C. Ralph. High-fidelity teleportation of continuous-variable quantum states using delocalized single photons. *Phys. Rev. Lett.*, 111:050504, Aug 2013.

[201] Saikat Guha. Structured optical receivers to attain superadditive capacity and the holevo limit. *Phys. Rev. Lett.*, 106:240502, Jun 2011.

[202] Kenji Tsujino, Daiji Fukuda, Go Fujii, Shuichiro Inoue, Mikio Fujiwara, Masahiro Takeoka, and Masahide Sasaki. Quantum receiver beyond the standard quantum limit of coherent optical communication. *Phys. Rev. Lett.*, 106:250503, Jun 2011.

[203] Amine Laghaout, Gunnar Björk, and Ulrik L. Andersen. Realistic limits on the nonlocality of an n-partite single-photon superposition. *Phys. Rev. A*, 84:062127, Dec 2011.

[204] S. A. Babichev, B. Brezger, and A. I. Lvovsky. Remote preparation of a single-mode photonic qubit by measuring field quadrature noise. *Phys. Rev. Lett.*, 92:047903, Jan 2004.

[205] Anders Tipsmark, Ruifang Dong, Amine Laghaout, Petr Marek, Miroslav Ježek, and Ulrik L. Andersen. Experimental demonstration of a hadamard gate for coherent state qubits. *Phys. Rev. A*, 84:050301, Nov 2011.

[206] A. I. Lvovsky, H. Hansen, T. Aichele, O. Benson, J. Mlynek, and S. Schiller. Quantum state reconstruction of the single-photon fock state. *Phys. Rev. Lett.*, 87:050402, Jul 2001.

[207] M. Dakna, T. Anhut, T. Opatrný, L. Knöll, and D.-G. Welsch. Generating schrödinger-cat-like states by means of conditional measurements on a beam splitter. *Phys. Rev. A*, 55:3184–3194, Apr 1997.

[208] Agata M. Brańczyk and T. C. Ralph. Teleportation using squeezed single photons. *Phys. Rev. A*, 78:052304, Nov 2008.

[209] Erwin Schrödinger. Die gegenwärtige situation in der quantenmechanik. *Die Naturwissenschaften*, 23:807–812, 823–828, 844–849, 1935.

[210] V. Bužek and P. Knight. *Progress in Optics XXXIV*. Elsevier, Amsterdam, 1995.

[211] Jérôme Wenger, Rosa Tualle-Brouri, and Philippe Grangier. Non-gaussian statistics from individual pulses of squeezed light. *Phys. Rev. Lett.*, 92:153601, Apr 2004.

[212] Alessandro Zavatta, Silvia Viciani, and Marco Bellini. Quantum-to-classical transition with single-photon-added coherent states of light. *Science*, 306(5696):660–662, 2004.

[213] H. Jeong, A. P. Lund, and T. C. Ralph. Production of superpositions of coherent states in traveling optical fields with inefficient photon detection. *Phys. Rev. A*, 72:013801, Jul 2005.

[214] Stefano Olivares and Matteo G A Paris. Squeezed fock state by inconclusive photon subtraction. *Journal of Optics B: Quantum and Semiclassical Optics*, 7(12):S616, 2005.

[215] Asoka Biswas and G. S. Agarwal. Nonclassicality and decoherence of photon-subtracted squeezed states. *Phys. Rev. A*, 75:032104, Mar 2007.

[216] J. S. Neergaard-Nielsen, B. Melholt Nielsen, C. Hettich, K. Mølmer, and E. S. Polzik. Generation of a superposition of odd photon number states for quantum information networks. *Phys. Rev. Lett.*, 97:083604, Aug 2006.

[217] Alexei Ourjoumtsev, Rosa Tualle-Brouri, Julien Laurat, and Philippe Grangier. Generating optical schrödinger kittens for quantum information processing. *Science*, 312(5770):83–86, 2006.

[218] J. S. Neergaard-Nielsen, B. M. Nielsen, H. Takahashi, A. I. Vistnes, and E. S. Polzik. High purity bright single photon source. *Opt. Express*, 15(13):7940–7949, Jun 2007.

[219] A. Soujaeff, S. Takeuchi, K. Sasaki, T. Hasegawa, and M. Matsui. Heralded single photon source at 1550nm from pulsed parametric down conversion. *Journal of Modern Optics*, 54(2-3):467–471, 2007.

[220] Alexei Ourjoumtsev, Hyunseok Jeong, Rosa Tualle-Brouri, and Philippe Grangier. Generation of optical 'schrödinger cats' from photon number states. *Nature*, 448:784–786, 2007.

[221] Kentaro Wakui, Hiroki Takahashi, Akira Furusawa, and Masahide Sasaki. Photon subtracted squeezed states generated with periodically poled ktiopo4. *Opt. Express*, 15(6):3568–3574, Mar 2007.

[222] Scott Glancy and Hilma Macedo de Vasconcelos. Methods for producing optical coherent state superpositions. *J. Opt. Soc. Am. B*, 25(5):712–733, May 2008.

[223] Masahiro Takeoka, Hiroki Takahashi, and Masahide Sasaki. Large-amplitude coherent-state superposition generated by a time-separated two-photon subtraction from a continuous-wave squeezed vacuum. *Phys. Rev. A*, 77:062315, Jun 2008.

[224] Hiroki Takahashi, Kentaro Wakui, Shigenari Suzuki, Masahiro Takeoka, Kazuhiro Hayasaka, Akira Furusawa, and Masahide Sasaki. Generation of large-amplitude coherent-state superposition via ancilla-assisted photon subtraction. *Phys. Rev. Lett.*, 101:233605, Dec 2008.

[225] Christopher C. Gerry and Trung Bui. Approximate phase-coherent states and their generation. *Phys. Rev. A*, 80:033831, Sep 2009.

[226] Alexei Ourjoumtsev, Franck Ferreyrol, Rosa Tualle-Brouri, and Philippe Grangier. Preparation of non-local superpositions of quasi-classical light states. *Nat Phys*, 5:189–192, 2009.

[227] Thomas Gerrits, Scott Glancy, Tracy S. Clement, Brice Calkins, Adriana E. Lita, Aaron J. Miller, Alan L. Migdall, Sae Woo Nam, Richard P. Mirin, and Emanuel Knill. Generation of optical coherent-state superpositions by number-resolved photon subtraction from the squeezed vacuum. *Phys. Rev. A*, 82:031802, Sep 2010.

[228] Naoto Namekata, Yuta Takahashi, Go Fujii, Daiji Fukuda, Sunao Kurimura, and Shuichiro Inoue. Non-gaussian operation based on photon subtraction using a photon-number-resolving detector at a telecommunications wavelength. *Nat Photon*, 4:655–660, 2010.

[229] M. Takeoka, J.S. Neergaard-Nielsen, M. Takeuchi, K. Wakui, H. Takahashi, K. Hayasaka, and M. Sasaki. Engineering of optical continuous-variable qubits via displaced photon subtraction: multimode analysis. *Journal of Modern Optics*, 58(3-4):266–275, 2011.

[230] Jonas S. Neergaard-Nielsen, Makoto Takeuchi, Kentaro Wakui, Hiroki Takahashi, Kazuhiro Hayasaka, Masahiro Takeoka, and Masahide Sasaki. Photon subtraction from traveling fields - recent experimental demonstrations. *Progress in Informatics*, 8:5–18, 2011.

[231] Jonas S. Neergaard-Nielsen, Yujiro Eto, Chang-Woo Lee, Hyunseok Jeong, and Masahide Sasaki. Quantum tele-amplification with a continuous-variable superposition state. *Nat Photon*, 7:439–443, 2013.

[232] A. P. Lund, H. Jeong, T. C. Ralph, and M. S. Kim. Conditional production of superpositions of coherent states with inefficient photon detection. *Phys. Rev. A*, 70:020101, Aug 2004.

[233] T. C. Ralph, W. J. Munro, and G. J. Milburn. Quantum computation with coherent states, linear interactions and superposed resources. *arXiv:quant-ph/0110115v2*, 2001.

[234] H. Jeong, M. S. Kim, and Jinhyoung Lee. Quantum-information processing for a coherent superposition state via a mixed entangled coherent channel. *Phys. Rev. A*, 64:052308, Oct 2001.

[235] S. J. van Enk and O. Hirota. Entangled coherent states: Teleportation and decoherence. *Phys. Rev. A*, 64:022313, Jul 2001.

[236] H. Jeong and M. S. Kim. Efficient quantum computation using coherent states. *Phys. Rev. A*, 65:042305, Mar 2002.

[237] T. C. Ralph, A. Gilchrist, G. J. Milburn, W. J. Munro, and S. Glancy. Quantum computation with optical coherent states. *Phys. Rev. A*, 68:042319, Oct 2003.

[238] A Gilchrist, Kae Nemoto, W J Munro, T C Ralph, S Glancy, Samuel L Braunstein, and G J Milburn. Schrödinger cats and their power for quantum information processing. *Journal of Optics B: Quantum and Semiclassical Optics*, 6(8):S828, 2004.

[239] A. P. Lund and T. C. Ralph. Coherent-state linear optical quantum computing gates using simplified diagonal superposition resource states. *Phys. Rev. A*, 71:032305, Mar 2005.

[240] A. P. Lund, T. C. Ralph, and H. L. Haselgrove. Fault-tolerant linear optical quantum computing with small-amplitude coherent states. *Phys. Rev. Lett.*, 100:030503, Jan 2008.

[241] P.A.M. Dirac. *The Principles of Quantum Mechanics.* Clarendon, 1984.

[242] Hans-A. Bachor and Timothy C. Ralph. *A Guide to Experiments in Quantum Optics.* Wiley-VCH, 2004.

[243] Ulf Leonhardt. *Measuring the Quantum State of Light.* Cambridge University Press, 1997.

[244] W. Heisenberg. über den anschaulichen inhalt der quantentheoretischen kinematik und mechanik. *Zeitschrift für Physik*, 43:172, 1927.

[245] A I Lvovsky. Iterative maximum-likelihood reconstruction in quantum homodyne tomography. *Journal of Optics B: Quantum and Semiclassical Optics*, 6(6):S556, 2004.

[246] E. Wigner. On the quantum correction for thermodynamic equilibrium. *Phys. Rev.*, 40:749–759, Jun 1932.

[247] J. Bertrand and P. Bertrand. A tomographic approach to wigners function. *Foundations of Physics*, 17:397, 1987.

[248] N. Lütkenhaus and S. M. Barnett. Nonclassical effects in phase space. *Physical Review A*, 51:3340, 1995.

[249] D. Leibfried, D. M. Meekhof, B. E. King, C. Monroe, W. M. Itano, and D. J. Wineland. Experimental determination of the motional quantum state of a trapped atom. *Physical Review Letters*, 77:4281, 1996.

[250] D. Dragoman. Phase space correspondence between classical optics and quantum mechanics. *Progress in Optics*, 43:433, 2002.

[251] B. Yurke and M. Potasek. Obtainment of thermal noise from a pure quantum state. *Phys. Rev. A*, 36:3464–3466, Oct 1987.

[252] Horace P. Yuen. Two-photon coherent states of the radiation field. *Phys. Rev. A*, 13:2226–2243, Jun 1976.

[253] R. Friedberg. The squeezing operator in quasinormal form. *Laser Physics*, 12:1171–1176, 2002.

[254] G. Breitenbach and S. Schiller. Homodyne tomography of classical and non-classical light. *Journal of Modern Optics*, 44(11-12):2207–2225, 1997.

[255] Richard A. Campos, Bahaa E. A. Saleh, and Malvin C. Teich. Quantum-mechanical lossless beam splitter: Su(2) symmetry and photon statistics. *Phys. Rev. A*, 40:1371–1384, Aug 1989.

[256] C. K. Hong, Z. Y. Ou, and L. Mandel. Measurement of subpicosecond time intervals between two photons by interference. *Phys. Rev. Lett.*, 59:2044–2046, Nov 1987.

[257] E H Huntington and T C Ralph. Separating the quantum sidebands of an optical field. *Journal of Optics B: Quantum and Semiclassical Optics*, 4(2):123, 2002.

[258] U Leonhardt, M Munroe, T Kiss, Th Richter, and M.G Raymer. Sampling of photon statistics and density matrix using homodyne detection. *Optics Communications*, 127(13):144 – 160, 1996.

[259] U. Leonhardt and H. Paul. Realistic optical homodyne measurements and quasiprobability distributions. *Phys. Rev. A*, 48:4598–4604, Dec 1993.

[260] M.J. Collett, R. Loudon, and C.W. Gardiner. Quantum theory of optical homodyne and heterodyne detection. *Journal of Modern Optics*, 34(6-7):881–902, 1987.

[261] W. Schleich. *Quantum optics in phase space*. Wiley-VCH New York, 2001.

[262] O. Alibart, D. B. Ostrowsky, P. Baldi, and S. Tanzilli. High-performance guided-wave asynchronous heralded single-photon source. *Opt. Lett.*, 30(12):1539–1541, Jun 2005.

[263] A. I. Lvovsky and M. G. Raymer. Continuous-variable optical quantum-state tomography. *Rev. Mod. Phys.*, 81:299–332, Mar 2009.

[264] J Clausen, M Dakna, L Knöll, and D G Welsch. Conditional quantum-state transformation at a beam splitter. *Journal of Optics B: Quantum and Semiclassical Optics*, 1(3):332, 1999.

[265] Shigenari Suzuki, Kenji Tsujino, Fumihiko Kannari, and Masahide Sasaki. Analysis on generation schemes of schrödinger cat-like states under experimental imperfections. *Optics Communications*, 259(2):758 – 764, 2006.

[266] Mikio Nakahara and Tetsuo Ohmi. *Quantum Computing: From Linear Algebra to Physical Realizations*. CRC Press Taylor & Francis Group, 2008.

[267] Hwang Lee, Ulvi Yurtsever, Pieter Kok, George M. Hockney, Christoph Adami, Samuel L. Braunstein, and Jonathan P. Dowling. Towards photostatistics from photon-number discriminating detectors. *Journal of Modern Optics*, 51(9-10):1517–1528, 2004.

[268] Masashi Ban. Photon statistics of conditional output states of lossless beam splitter. *Journal of Modern Optics*, 43(6):1281–1303, 1996.

[269] M. S. Kim, E. Park, P. L. Knight, and H. Jeong. Nonclassicality of a photon-subtracted gaussian field. *Phys. Rev. A*, 71:043805, Apr 2005.

[270] M. J. Collett and C. W. Gardiner. Squeezing of intracavity and traveling-wave light fields produced in parametric amplification. *Phys. Rev. A*, 30:1386–1391, Sep 1984.

[271] E.S. Polzik, J. Carri, and H.J. Kimble. Atomic spectroscopy with squeezed light for sensitivity beyond the vacuum-state limit. *Applied Physics B*, 55(3):279–290, 1992.

[272] R. Kumar, E. Barrios, A. MacRae, E. Cairns, E.H. Huntington, and A.I. Lvovsky. Versatile wideband balanced detector for quantum optical homodyne tomography. *Optics Communications*, 285(24):5259 – 5267, 2012.

[273] W. H. Press, S. A. Teukolsky, W. T. Vetterling, and B. P. Flannery. *Numerical Recipes in Fortran 77.* Cambridge University Press, 1992.

[274] Y. Vardi and D. Lee. From image deblurring to optimal investments: Maximum likelihood solutions for positive linear inverse problems. *Journal of the Royal Statistical Society. Series B (Methodological)*, 55:569, 1993.

[275] Jonas Schou Neergaard-Nielsen. *Generation of single photons and Schrödinger kitten states of light.* PhD thesis, Danish National Research Foundation Center for Quantum Optics Quantop Niels Bohr Institute, 2008.

[276] M. Munroe, D. Boggavarapu, M. E. Anderson, and M. G. Raymer. Photon-number statistics from the phase-averaged quadrature-field distribution: Theory and ultrafast measurement. *Physical Review A*, 52:924, 1995.

[277] Alessandro Zavatta, Silvia Viciani, and Marco Bellini. Tomographic reconstruction of the single-photon fock state by high-frequency homodyne detection. *Phys. Rev. A*, 70:053821, Nov 2004.

[278] J. Fiurášek. Maximum-likelihood estimation of quantum measurement. *Physical Review A*, 64:024102, 2001.

[279] Jaroslav Řeháček, Zdeněk Hradil, E. Knill, and A. I. Lvovsky. Diluted maximum-likelihood algorithm for quantum tomography. *Phys. Rev. A*, 75:042108, Apr 2007.

[280] K. Banaszek, G. M. D'Ariano, M. G. A. Paris, and M. F. Sacchi. Maximum-likelihood estimation of the density matrix. *Phys. Rev. A*, 61:010304, Dec 1999.

[281] Carlton M. Caves and Bonny L. Schumaker. New formalism for two-photon quantum optics. i. quadrature phases and squeezed states. *Phys. Rev. A*, 31:3068–3092, May 1985.

[282] Bonny L. Schumaker and Carlton M. Caves. New formalism for two-photon quantum optics. ii. mathematical foundation and compact notation. *Phys. Rev. A*, 31:3093–3111, May 1985.

[283] J. Gea-Banacloche and G. Leuchs. Squeezed states for interferometric gravitational-wave detectors. *Journal of Modern Optics*, 34(6-7):793–811, 1987.

[284] Michael Vasilyev, Sang-Kyung Choi, Prem Kumar, and G. Mauro D'Ariano. Tomographic measurement of joint photon statistics of the twin-beam quantum state. *Phys. Rev. Lett.*, 84:2354–2357, Mar 2000.

[285] Christian Schori, Jens L. Sørensen, and Eugene S. Polzik. Narrow-band frequency tunable light source of continuous quadrature entanglement. *Phys. Rev. A*, 66:033802, Sep 2002.

[286] Paul Voss, Tae-Gon Noh, Sarah Dugan, Michael Vasilyev, Prem Kumar, and G. M. D'ariano. Experimental realization of 'universal homodyne tomography' with a single local oscillator. *Journal of Modern Optics*, 49(14-15):2289–2296, 2002.

[287] Ondřej Haderka, Jan Peřina Jr, and Martin Hamar. Simple direct measurement of nonclassical joint signal-idler photon-number statistics and the correlation area of twin photon beams. *Journal of Optics B: Quantum and Semiclassical Optics*, 7(12):S572, 2005.

[288] Julien Laurat, Gaëlle Keller, José Augusto Oliveira-Huguenin, Claude Fabre, Thomas Coudreau, Alessio Serafini, Gerardo Adesso, and Fabrizio Illuminati. Entanglement of two-mode gaussian states: characterization and experimental production and manipulation. *Journal of Optics B: Quantum and Semiclassical Optics*, 7(12):S577, 2005.

[289] V. D'Auria, S. Fornaro, A. Porzio, S. Solimeno, S. Olivares, and M. G. A. Paris. Full characterization of gaussian bipartite entangled states by a single homodyne detector. *Phys. Rev. Lett.*, 102:020502, Jan 2009.

[290] Andreas Eckstein, Andreas Christ, Peter J. Mosley, and Christine Silberhorn. Highly efficient single-pass source of pulsed single-mode twin beams of light. *Phys. Rev. Lett.*, 106:013603, Jan 2011.

[291] T. C. Ralph, E. H. Huntington, and T. Symul. Single-photon side bands. *Phys. Rev. A*, 77:063817, Jun 2008.

[292] Girish S. Agarwal. *Quantum Optics.* Cambridge University Press, 2012.

[293] S. M. Barnett and P. L. Knight. Thermofield analysis of squeezing and statistical mixtures in quantum optics. *J. Opt. Soc. Am. B*, 2(3):467–479, Mar 1985.

[294] S. M. Barnett and P. L. Knight. Comment on "obtainment of thermal noise from a pure quantum state". *Phys. Rev. A*, 38:1657–1658, Aug 1988.

[295] Michael Vasilyev, Sang-Kyung Choi, Prem Kumar, and G. M. D'Ariano. Investigation of the photon statistics of parametric fluorescence in a traveling-wave parametric amplifier by means of self-homodyne tomography. *Opt. Lett.*, 23(17):1393–1395, Sep 1998.

[296] J. Wenger, A. Ourjoumtsev, R. Tualle-Brouri, and P. Grangier. Time-resolved homodyne characterization of individual quadrature-entangled pulses. *Eur. Phys. J. D*, 32:391–396, 2005.

[297] E. H. Huntington, G. N. Milford, C. Robilliard, and T. C. Ralph. Coherent analysis of quantum optical sideband modes. *Opt. Lett.*, 30(18):2481–2483, Sep 2005.

[298] James G. Webb. *The measurement, creation and manipulation of quantum optical states via photodetection*. PhD thesis, The University of New South Wales, 2009.

[299] M. Heurs, I. R. Petersen, M. R. James, and E. H. Huntington. Homodyne locking of a squeezer. *Opt. Lett.*, 34(16):2465–2467, Aug 2009.

[300] E.H. Huntington, M.R. James, and I.R. Petersen. Laser-cavity frequency locking using modern control. In *Decision and Control, 2007 46th IEEE Conference on*, pages 6346–6351, 2007.

[301] Anthony E. Siegman. *Lasers*. University Science Books, 1986.

[302] R.W.P. Drever, J.L. Hall, F.V. Kowalski, J. Hough, G.M. Ford, A.J. Munley, and H. Ward. Laser phase and frequency stabilization using an optical resonator. *Applied Physics B*, 31(2):97–105, 1983.

[303] Eric D. Black. An introduction to pound–drever–hall laser frequency stabilization. *American Journal of Physics*, 69(1):79–87, 2001.

[304] Hongbin Song, Katanya B Kuntz, and Elanor H Huntington. Limitations on the quantum non-gaussian characteristic of schrödinger kitten state generation. *New Journal of Physics*, 15(2):023042, 2013.

[305] Radim Filip and Ladislav Mišta, Jr. Detecting quantum states with a positive wigner function beyond mixtures of gaussian states. *Phys. Rev. Lett.*, 106:200401, May 2011.

[306] H. Kogelnik and T. Li. Laser beams and resonators. *Appl. Opt.*, 5(10):1550–1567, Oct 1966.

[307] Bahaa E. A. Saleh and Malvin Carl Teich. *Fundamentals of Photonics, Second Edition*. Wiley, 2007.

[308] C. E. Shannon. Communication in the presence of noise. *Proc. Institute of Radio Engineers*, 37:10–21, 1949.

[309] Anne E. B. Nielsen and Klaus Mølmer. Single-photon-state generation from a continuous-wave nondegenerate optical parametric oscillator. *Phys. Rev. A*, 75:023806, Feb 2007.

[310] Klaus Mølmer. Non-gaussian states from continuous-wave gaussian light sources. *Phys. Rev. A*, 73:063804, Jun 2006.

[311] Anatole Kenfack and Karol Życzkowski. Negativity of the wigner function as an indicator of non-classicality. *Journal of Optics B: Quantum and Semiclassical Optics*, 6(10):396, 2004.

[312] Miroslav Ježek, Ivo Straka, Michal Mičuda, Miloslav Dušek, Jaromír Fiurášek, and Radim Filip. Experimental test of the quantum non-gaussian character of a heralded single-photon state. *Phys. Rev. Lett.*, 107:213602, Nov 2011.

[313] M. Ježek, A. Tipsmark, R. Dong, J. Fiurášek, L. Mišta, Jr., R. Filip, and U. L. Andersen. Experimental test of the strongly nonclassical character of a noisy squeezed single-photon state. *Phys. Rev. A*, 86:043813, Oct 2012.

Analogue circuitry used in the experiment

This Appendix gives the analogue electronic circuit diagram of 'QMATE' that was used in the experiment during data collection as described in this thesis.

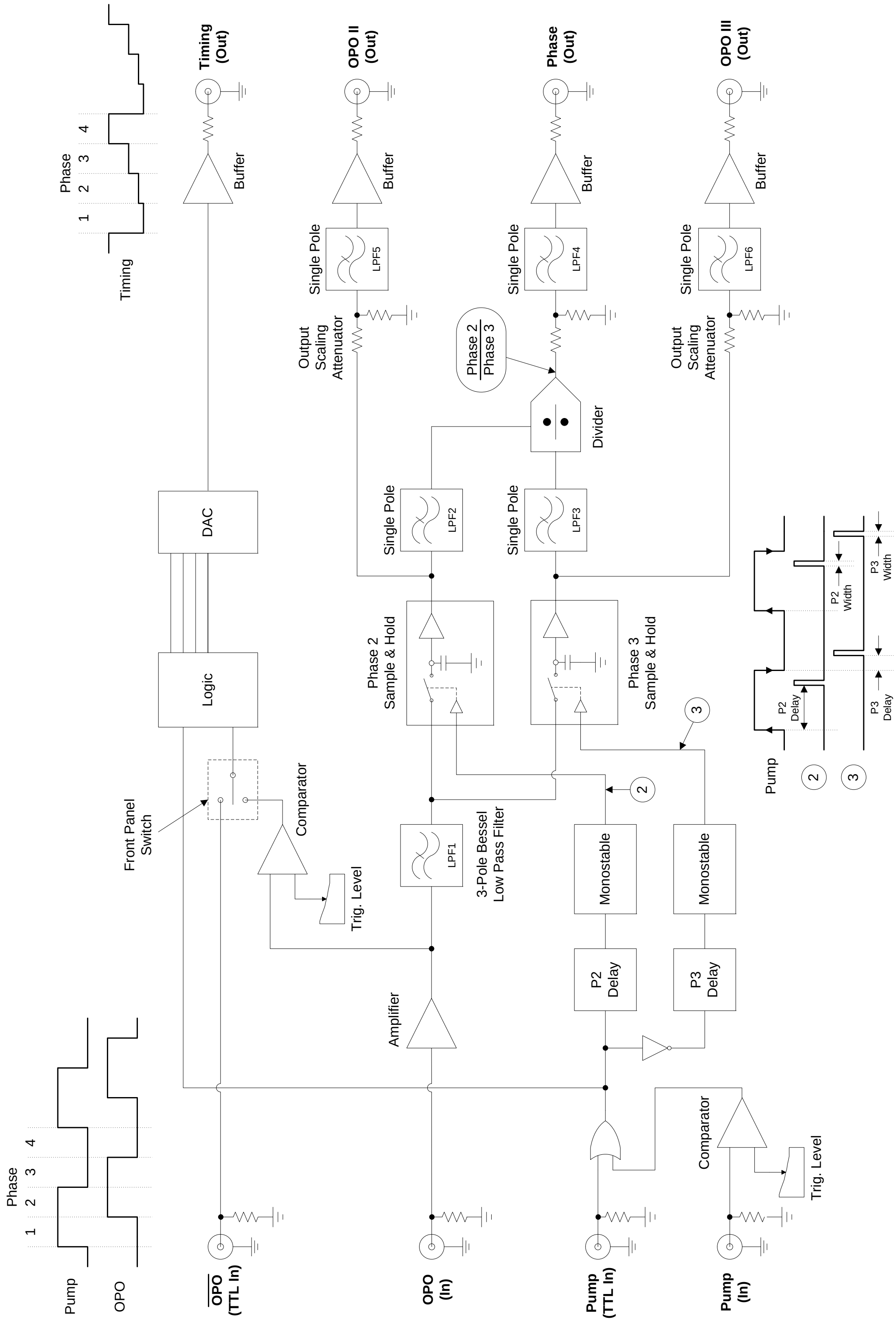

Figure 1: Simplified electronic circuit diagram of 'QMATE'.

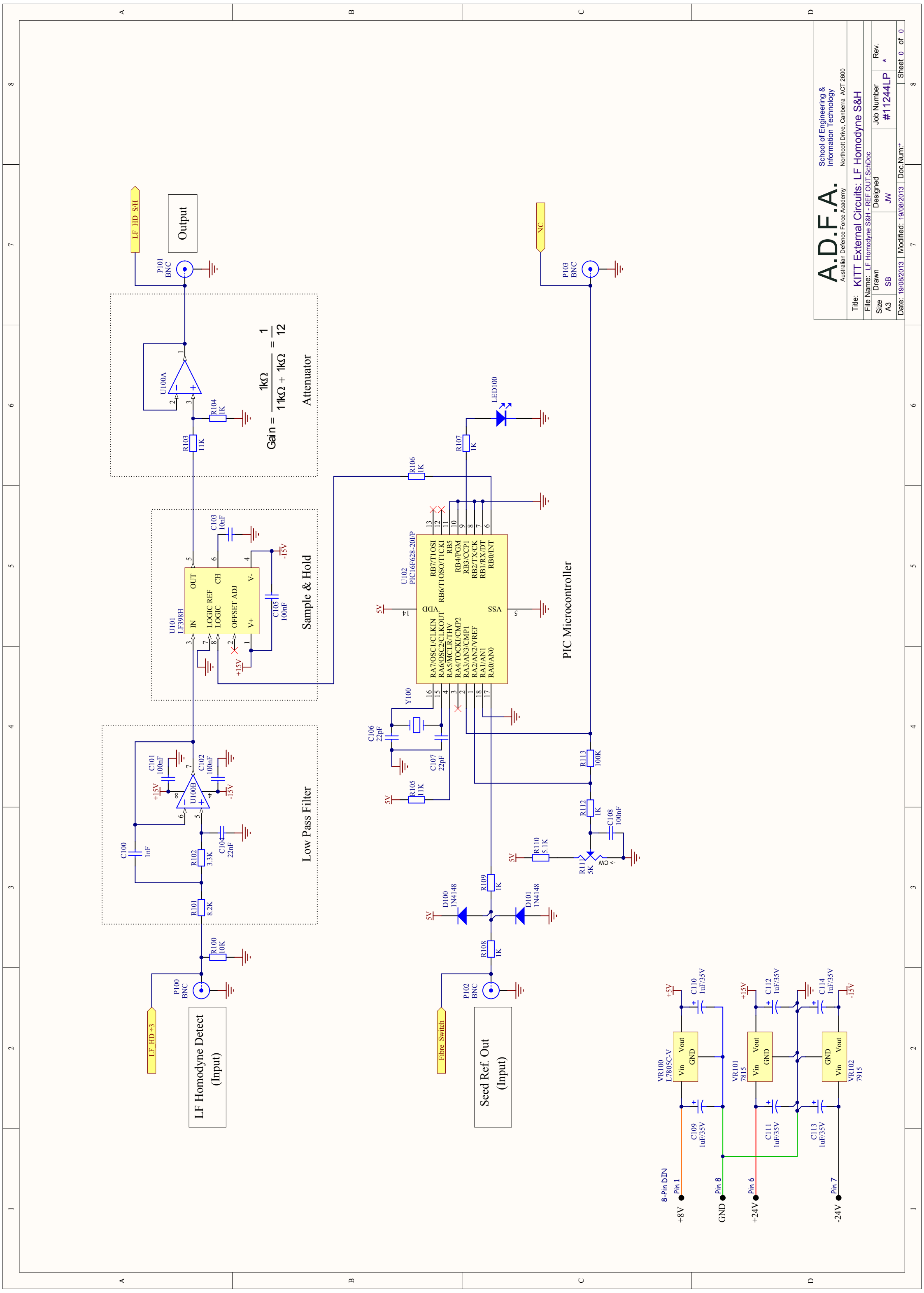

Figure 2: Simplified schematic of the sample-and-hold circuit used to estimate the LO optical phase during data collection of the experiment.